Gold Nanoparticles for Biosensor Development

A thesis presented in partial fulfillment of the degree of

Doctor of Philosophy in

Chemistry

Institute of Fundamental Science, Massey University

Palmerston North, New Zealand

Xiuqian Jiang

2009

ABSTRACT

Gold nanoparticles, are one of the most widely investigated nanoparticles (NP) and are normally synthesized by the reduction of metal salts in citrate solution. The reason for studying this nanostructured material from a technological standpoint is mainly the anticipated application in different areas based on optical properties explained with plasmon resonance. The main work of this study was to develop different sensing systems using gold nanoparticles. Three techniques have been utilized, being lateral flow immunoassay (LFIA), surface plasmon resonance (SPR), and surface-enhanced Raman scattering (SERS).

A one-step semi-quantitative LFIA strip test was developed using colloidal gold coated by a partially-purified polyclonal antibody (pAb) raised in sheep as a signal generator, and bovine serum albumin-Estriol-16-glucuronide (BSA-E3-16G) conjugates as the capture agent spotted onto a nitrocellulose membrane as the test line. In this system, gold nanoparticles were applied for visualising the response. The application of the strip sensor to urinary samples from pregnant woman proved successful.

A quantitative evaluation of low levels of E3-16G in liquid media was developed based on SPR, which used the same pAb-nanogold conjugates employed for the LFIA analysis. The assay can be carried out directly on any urine samples without sample pretreatment. In this system, gold nanoparticles were utilized as high mass label to improve the sensitivity of the assay.

A SERS probe was developed which comprised of Raman reporter molecules (RRM) and gold NPs. Results showed that the conducting polymer materials of 3’-[(E)-2-(4-R-phenyl)ethenyl]-2’2’:5’,2”-terthiophene (R-pe3T, where R is NO_2 or NH_2) showed significant enhancement. Moreover, high bio-activity groups included in the compounds make them potential candidates for the development of a SERS based sensing system.

ACKNOWLEDGMENTS

I would like to take this opportunity to offer my heart felt thanks to a number of people without whose help and support this thesis would never have been possible. I must start with my supervisor **Dr. Mark Waterland** who has given me the chance to come to New Zealand and work here. I am sure there are only a few students who ever have the pleasure of working for as wonderful a researcher and educator as I have had. I will always be grateful for all his guidance, understanding and support. I must also express great gratitude to **Assoc. Prof. Len Blackwell**. It has been a great pleasure working with and learning from him. I appreciate his assistance in writing this thesis. A very special thanks for **Assoc. Prof. Ashton Partridge** who has supported me throughout my study with his patience and knowledge whilst allowing me the room to work in my own way. In addition I would like to thank the MacDiarmid Institute for providing me with financial support to conduct my studies, and the Institute of Fundamental Science at Massey University providing the support and equipments I have needed to produce and complete my thesis.

I have had the pleasure of working with a number of very talented and knowledgeable people in the MacDiarmid Institute at Massey University. I would like to deeply thank Dr. Wayne Campbell, giving me so many advices about conducting polymers and providing compounds for SERS work, Dr. Krishanthi Jayasundera who synthesized the ligand (E3-16G-OEG) for SPR study. Dr. Steve Kirk, Adam Stephenson, Gaile Dombroski, Nyree Parker, Helen Hsu, Indu Sharma and Emad Al-Imarah, it is my pleasure to work with them.

A number of people in the collaboration have provided invaluable support and information. I would therefore like to thank Dr. Jenness Guthrie, Dr. Delwyn Cooke, Dr. Yinqiu Wu, and Dr. Jing Yuan.

My parents have always been an important source of encouragement and support. Nothing I can say can do justice to how I feel about their support throughout all my entire life. I must acknowledge my mum and my fiancé in particular. Without their care, their support and their love in the last few months this thesis would never have started much less finished.

Table of Contents

Chapter 3: Lateral flow immunoassay

Chapter 4: SPR Biosensor-based immunoassay

Chapter 5: Surface-enhanced Raman scattering

Abbreviations

E3-16G	**Estriol-16-glucuronide**
SPR	**Surface plasmon resonance**
SERS	**surface-enhanced Raman scattering**
LFIA	**Lateral flow immunoassay**
BSA	**bovine serum albumin**
RRM	**Raman reporter molecule**
R-pe3T	**3’-[(E)-2-(4-R-phenyl)ethenyl]-2’2’:5’,2”-terthiophene**
NP	**nanoparticle**
NR	**NanoRod**
MTP	**multiple twinned particles**
CTAB	**cetyltrimethylammonium bromide**
R	**aspect ratio**
GS	**growth solution**
LFA	**Lateral flow assay**
RU	**Reaction Unit or Resonance Unit**
DDC	**Direct Digital Control**
TEM	**transmission electron microscopy**
Ab	**antibody**

pAb	**polyclonal primary antibody**
Au-Ab	**nanogold-antibody**
2˚AS	**anti-sheep serum raised in rabbit**
E1-3G	**Estrone-3-glucuronide**
E3-3G	**Estriol-3-glucuronide**
E3-17G	**Estriol-17-glucuronide**
LOD	**low limit of detection**
TM	**Tris-maleate**
CV	**coefficient of variation**
RIA	**radio immunoassay**
HPLC	**high performance liquid chromatography**
LC	**liquid chromatography**
MS	**mass spectroscopy**
OVA	**ovalbumin**
OEG	**oligoethylene glycol**
FC	**flow cell**
FR	**flow rate**
EDC	**1-ethyl-3-(3-dimethylaminopropyl) carbodiimide**
NHS	**N-hydroxysuccinimide**

EAH	**ethanolamine-HCl**
RelResp	**relative response**
OD	**optical density**
PEG	**poly ethylene glycol**
PdG	**pregnanediol glucoronide**
PVP	**polyvinylpyrrolidone**
EDOT	**2,3-dihydrothieno[3,4-b]-1,4-dioxin**
PEDOT	**poly(2,3-dihydrothieno-1,4-dioxin)**
DCM	**dichloromethane**
ZnTXP	**5,10,15,20-Tetrakis(3',5'-dimethylphenyl)porphyrinato zinc(II)**
ZnTPP	**5,10,15,20-Tetraphenylporphyrinato zinc(II)**

List of Figures

FIGURE ***PAGE***

List of Tables

TABLE ***PAGE***

List of Publications

1. The first paper based on the SPR work discussed in Chapter Four has been published in Steroids.

   Jiang, X. Q., Waterland, M., Blackwell, L., Wu, Y. Q., Jayasundera, K. P., & Partridge, A. (2009). Sensitive determination of estriol-16-glucuronide using surface plasmon resonance sensing. *Steroids, 74*(10-11), 819-824.

2. The second paper based on the applications of Lateral flow immunoassay and SPR assay in human urinary samples (discussed in Chapter Three and Four) has been published in Analytical methods.

   Jiang, X. Q., Waterland, M., Blackwell, L., & Partridge, A. (2009). Determination of Estriol 16-glucuronide in human urine with surface plasmon resonance and lateral flow immunoassays. *Analytical Methods*, 2010, **2**, 368-374.

3. The third paper based on the surface enhanced Raman scattering (Chapter Five) has been finished and is going to be submitted to Small soon.

   Jiang, X. Q., Waterland, M., & Partridge, A. (2010).

Chapter One

Introduction

1.1 Background theory of gold nanoparticles

Gold colloids, a typical kind of nanoparticle (NP), have been used to stain glass ever since ancient times. The gold colloid was first investigated in detail around 1857 by the distinguished English physicist and chemist Michael Faraday [1]. In recent decades, nanoscale properties of NPs have attracted more and more attention[1]. Currently the NPs are used in different fields like optics [2, 3], electronics [4-6], optoelectronics [7, 8] and bio-sensor techniques [9, 10].

Fig 1-1: Michael Faraday was born on 22.09.1791.

1.1.1 The formation of spherical nanoparticles

The formation of nanoparticles in solution can be explained in terms of a model which describes nucleation-growth transition[11]. The nucleation process is a formation of a new phase [12]. External energy is required to enlarge the boundary since it takes energy to form stable interfaces. The free energy change ΔG is [13]:

$$\Delta G = \Delta G_V + \Delta G_S \qquad (1\text{-}1)$$

ΔG_V : change of volume free energy

ΔG_S : change of surface free energy.

Assuming the radius of the formed nuclei is r, the change of volume free energy is:

$$\Delta G_V = (4/3)\,\pi r^3 \Delta G_v \quad , \qquad (1\text{-}2)$$

where ΔG_v is the change of free energy per unit volume of the solid phase. Furthermore, the contribution from the change of surface energy should also be taken into account. The formation of a new phase leads to an increase of surface free energy:

$$\Delta G_S = 4\pi r^2 \gamma \,, \qquad (1\text{-}3)$$

where γ is the surface energy per unit area (surface tension). The total change of free energy is given by:

$$\Delta G = (4/3)\,\pi r^3 \Delta G_v + 4\pi r^2 \gamma \qquad (1\text{-}4)$$

$$\Delta G_v = (-k_B T/\Omega)^* \ln(C/C_0) = (-k_B T/\Omega) * \ln(S) = (-k_B(T_E - T_R)/\Omega) * \ln(S), \qquad (1\text{-}5)$$

where k_B is Boltzmann constant, T is the difference of transformation temperature and reacting temperature, C is the concentration of the solute (activity product), C_0 is the concentration in equilibrium, Ω is the atomic volume of Au, and S is the relative supersaturation described by C/C_0 [13].

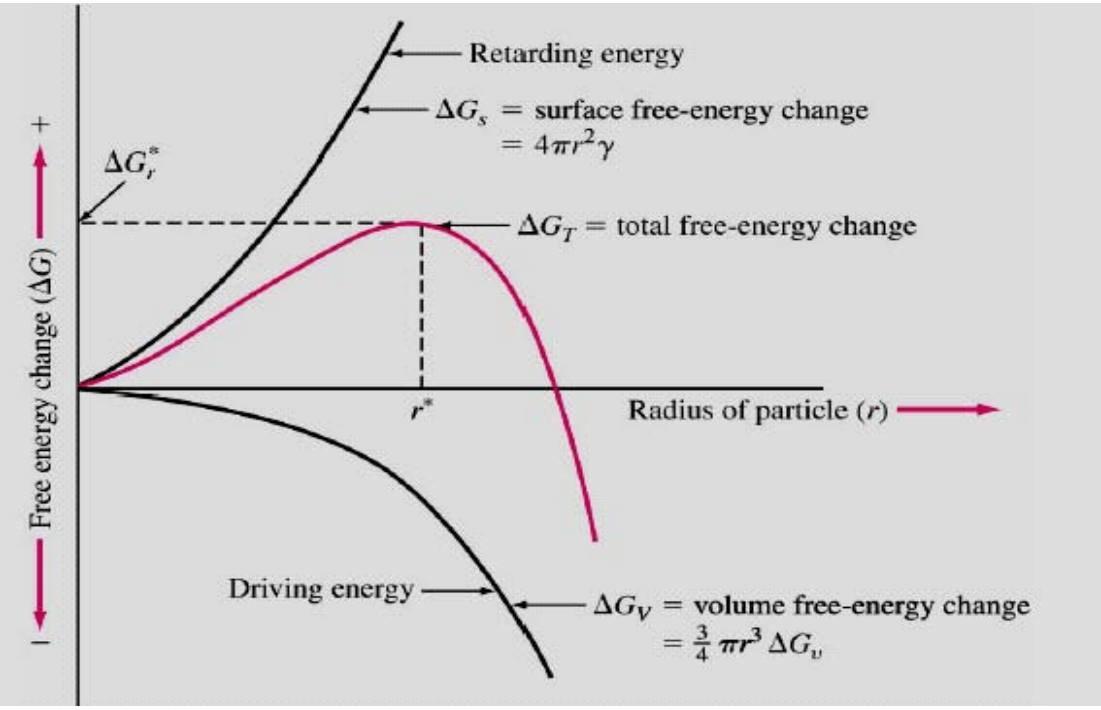

Fig 1-2 : Change of total free energy, volume free energy and surface free energy as a function of nucleus size. The interfacial contribution opposes nucleation while the volume free energy propels nucleation. In the smaller size range the surfacial term (retarding energy) dominates, so the nucleation is prevented. In the larger size range the volumetric term (driving energy) dominates, so the nucleation progresses. Picture from [13].

It can be seen from Fig 1-2 that the freshly formed nucleus is only stable when its radius exceeds a critical radius r^*, otherwise, the formed nucleus will dissolve into solution to reach a situation with lower energy. Nuclei, equal to or larger than the critical size, are stable and can grow continuously to form the nano crystal. At the critical size, the change of the total free energy (ΔG) reaches a maximum value, namely the energy barrier of ΔG_r^*.

The critical size and barrier ΔG_r^* are calculated as following:

$$\frac{\partial \Delta G}{\partial r} = 4\pi r^2 \Delta G_v + 8\pi r\gamma$$

$$\frac{\partial \Delta G}{\partial r} = 0, \qquad r^* = \frac{-2\gamma}{\Delta G_v}$$

$$r^* = \frac{2\gamma\Omega}{kT\ln(S)}$$

The critical barrier: $$\Delta G_r^* = \frac{16\pi\gamma^3}{3(\Delta G_v)^2} \quad (1\text{-}7)$$

The critical size r^* and the energy barrier ΔG_r^* are influenced by the surface energy of the new phase γ, temperature T, atomic volume Ω and the relative supersaturation S (C/C_0). Here, the influence of the relative supersaturation S and temperature T are discussed. Nucleation occurs when the supersaturation reaches or exceeds a level of which the corresponding energy is equal to the energy barrier. Growth of the nucleus reduces the concentration of solute C and the relative supersaturation S. Growth stops when the relative supersaturation S is equal to one, i.e. the concentration of solute equals the equilibrium concentration. A higher reacting temperature gives larger nuclei (Fig 1-3) under the condition of constant supersaturation [13].

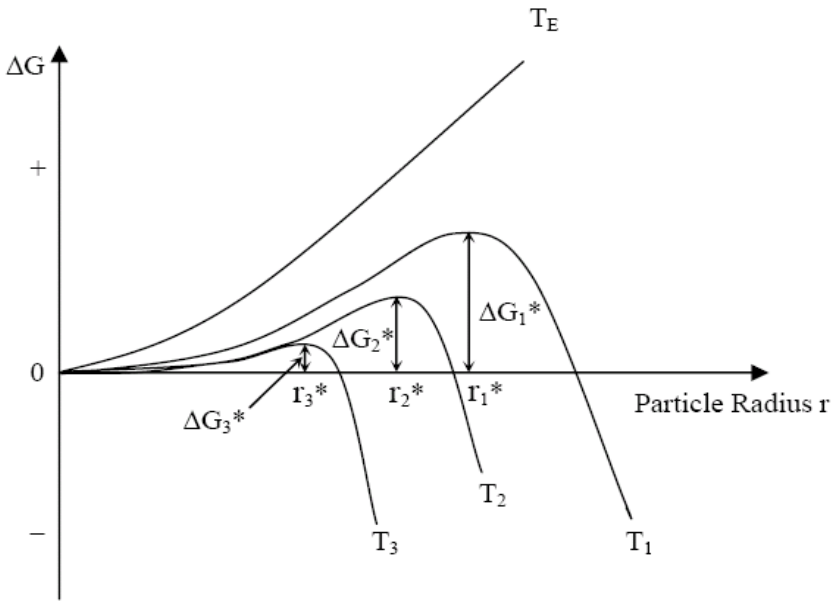

Fig 1-3: The critical radius increase with increasing the reacting T. T_E represents the transformation temperature where the energy of solid and liquid phase are the same. $T_E > T_1 > T_2 > T_3$, the corresponding critical size is $r_1 > r_2 > r_3$. Picture from [13].

1.1.2 The formation of rod-shaped nanoparticles

The model reported by P. L. Gai and co-worker [14] explains that growth of NanoRods (NRs) is due to the minimization of surface energy. The formation of NRs can be discussed as a stepwise process [14] (Fig 1-4). The first step (Fig 1-4

a) is the self assembling of 5 or 20 similar fcc tetrahedral NPs to form the multiple twinned particles (MTP) with weaker binding in twin boundary areas where two crystals of the same type intergrow. Then diffusion of Au to these twin sites leads to the growth of NRs. The NRs are prepared with wet chemical synthesis [15] in the presence of surfactant of cetyltrimethylammonium bromide (CTAB). Taking into account weaker atomic binding at (110) surfaces of Au, CTAB binds to these surfaces as stabilizing agent [14]. According to the reasons described above, the Au has no chance to diffuse to the (110) surfaces and can only diffuse to (111) surfaces along [100] direction (Fig 1-4 b). Aspect ratio (R), as an important parameter describing NRs, is defined as a ratio of the length of NR to the diameter of NR.

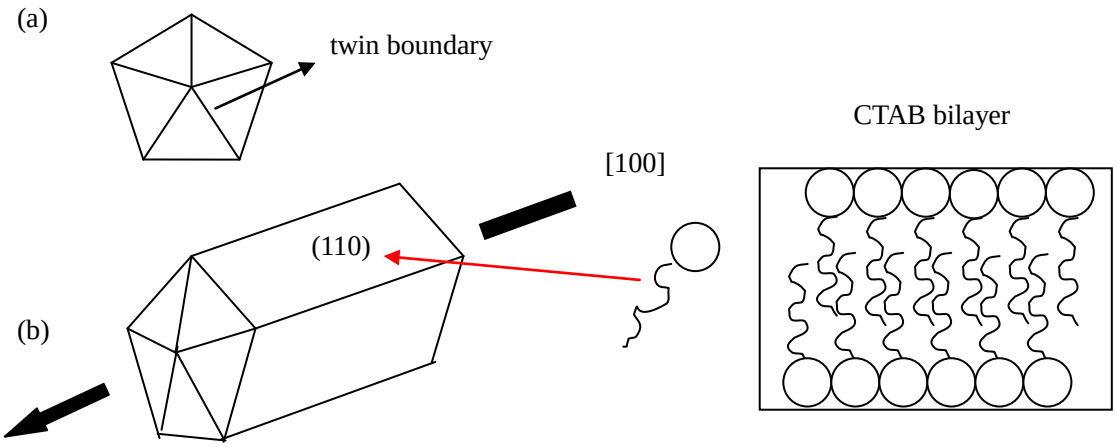

Fig 1-4: The growth of NRs. a) The multiple twinned particles (MTP) composed of 5 fcc tetrahedral NPs. b) Bilayer of CTAB binds to (110) surface and Au diffuse to the twin sites along [100] direction.

1.1.3 Plasmon resonance

The optical properties of noble metals are largely determined by the presence of the plasmons. When light (electromagnetic wave) is incident on the metal, the photons cause the collective oscillation of the free electron gas i.e. plasma. A quantum of the plasma oscillation is known as a plasmon [16]

$$\omega_p = (4\pi Ne^2/m)^{1/2}, \qquad (1\text{-}8)$$

where N is the density of electrons, e is the electronic charge and m is the mass of

an electron. When the frequency of incident light equals to plasmon frequency, the incident photons are resonant absorbed, leading to an absorption band in the UV/Visble spectrum [13]. Fig 1-5 and Fig 1-6 show typical absorption spectra of spherical and rod-shaped Au NPs, respectively.

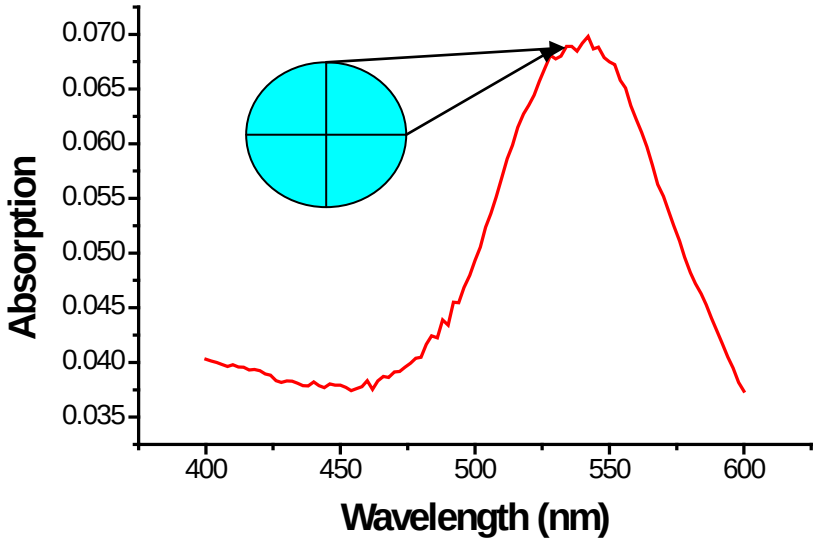

Fig 1-5: A typical absorption spectrum of spherical NPs. The peak around 540 nm is caused by the isotropic oscillations which are the same in all directions.

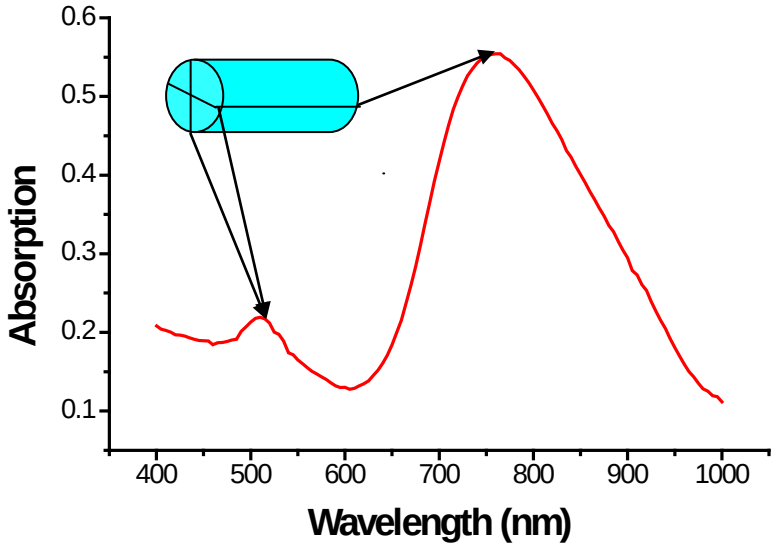

Fig 1-6: A typical absorption spectrum of rod-shaped NPs. The peak at 510 nm is the transversal plasmon peak which is caused by oscillations perpendicular to the rod axis. The peak situated around 760 nm is longitudinal plasmon peak corresponding to oscillations along the rod axis.

1.2 Application of gold nanoparticles to biological sensing

This thesis focuses on the application of Au NPs to affinity based biosensing. Three types of sensing techniques are considered: lateral flow immunoassay (LFIA), surface plasmon resonance (SPR) and surface-enhanced Raman scattering (SERS). In LFIA Au NPs are used simply as a color indicator and both SPR and SERS use the plasmonic resonance as the determination mechanism.

1.2.1 Lateral flow assay

Lateral flow assays (LFAs) are currently an easy and therefore popular assay format which is a general one-step format and easy to perform [17]. Major advantages are speed, cost and that no trained personnel or special apparatus is necessary, and thus they are well suited for applications outside the laboratory. LFA provides a binary yes/no response. Furthermore, the prepared strips can be stored for a long period without refrigeration, giving the tool an advantage in resource-poor settings.

Currently LFAs are based on the movement of liquid samples passing the detection area where molecules are attached for specific interaction with analyte and then giving signals. A typical LFA format consists of membrane strips, sample pad, conjugate pad and absorbent pad like the one depicted in Fig 1-7 The membrane can be produced from nitrocellulose [18, 19], nylon [20], polyethersulfone [21], or polyethylene [22]. The most commonly used membrane is a nitrocellulose membrane for which the pore size ranges from 0.05 to 12 μm. Considering the non-randomly distributed pores due to the manufacturing process, capillary flow time (the time for the fluid front to travel into the strip material) with a unit of s/cm is preferred for description of the materials. The sample pad is attached to the bottom part of the membrane and normally produced with cellulose or cross-linked silica. The conjugate pad is in contact with the sample pad and the membrane. Labeled analyte or recognition element(s) are dried on this pad and will specifically interact with the materials present in liquid samples. The

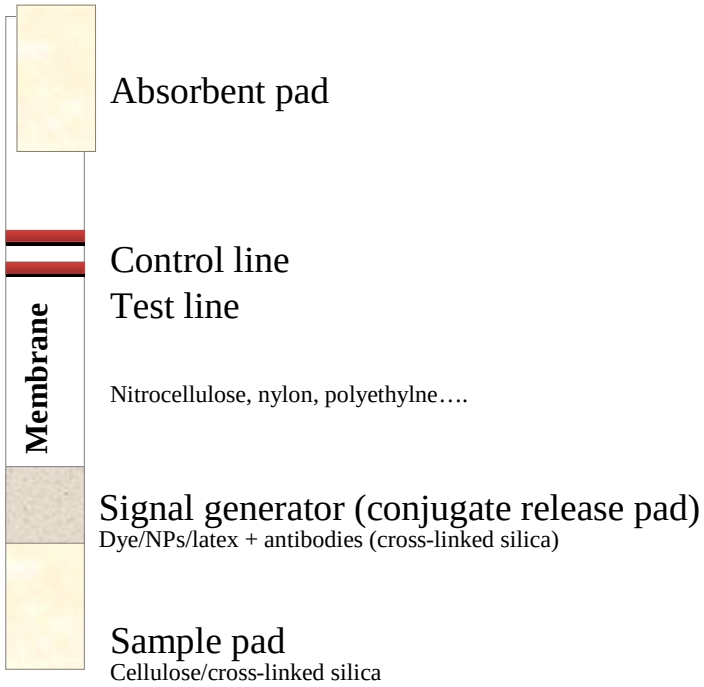

Fig 1-7: Schematic diagram of the analytical device for a lateral flow assay. The strip is composed of sample pad, conjugate release pad, membrane where the test and control lines are spayed, and absorbent pad.

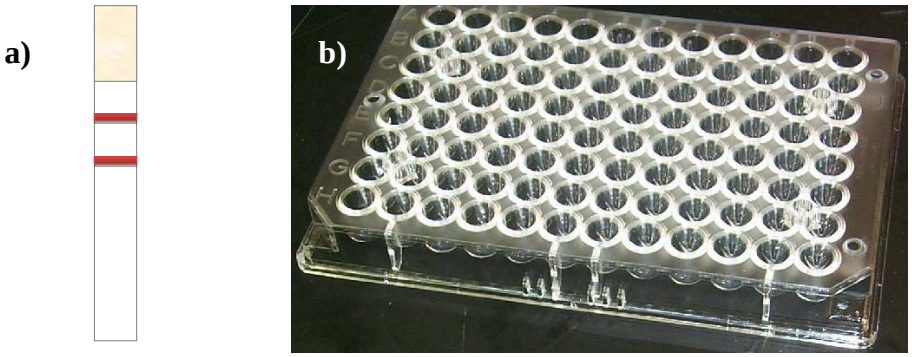

Fig 1-8: a) Half strip used for our study. b) Mircotiter plate for assay development.

labels for visualization can be colloidal Au [21, 23], dried latexes [24], selenium [25], carbon [18, 26] or liposomes [27]. The use of colloidal particles was first reported by Leuvering et al [23] in 1980 and nowadays is the most often used label. For single analyte determination, two lines are sprayed on the strip: a test line giving the test answer and a control line confirming a proper flow of the liquid through the strip. For multiple analytes, more test lines could be applied. The liquid moves upwards because of the capillary force of the strip materials and

is stopped by the absorbent pad at the top end of the strip. In our experiments, the bottom part of the membrane for attaching the conjugate release pad and sample pad were cut away and thus named as half strip (Fig 1-8 A). For application, the strip was directly applied to one well of a microtiter plate (Fig 1-8 B) where the conjugates and analytes were mixed.

When antibodies are used exclusively as recognition elements, the tests were called “lateral flow immunoassays” (LFIA). They are designed to confirm the presence or absence of an (un)wanted compound. Therefore, the analyte can be the compound of interest, or a metabolic derivative. In recent years, lateral flow test strips as a popular diagnostic tool are commercially available for detecting hormones [23, 26], viruses [19], toxic compounds [28, 29] and metabolic disorder [22]. Two common formats can be chosen. The sandwich format (positive assay) is designed for analytes with more than one epitope which is recognized by the immune system, specially by antibodies. In this format, the test line is prepared using one analyte-specific antibody and its intensity is directly proportional to the amount of analyte in the sample. Competitive assay (negative assay) is designed for analytes with a molecular weight smaller than 1000 Da and only one epitope. The test line in this format could be either anti-analyte antibody or analyte-protein conjugates depending on which is applied to strips. In this format, the response at the test line is most intensely coloured in the absence of analyte because of the inverse relationship between the analyte concentration and the colour development. For this study, the LFIA was developed for the determination of E3-16G in liquid samples. Based of the use of an analyte of low molecular weight, a competitive assay was applied by using a primary anti-E3-16G-IgG-Au conjugate. The details will be discussed in chapter three.

The LFIA technology reduces development time and brings applications faster to market. Moreover, the assay is superior to other immunoassay, such as radioimmunoassay and enzyme-linked immunoassay, with respect to its overall speed [17].

1.2.2 Surface plasmon resonance sensing

Surface plasmon resonance (SPR) is a physical optical phenomenon and its first application for biosensing was published by Liedberg in 1983 [30] determining the interaction between an IgG and its antigen. Since then SPR sensing has been receiving more and more attention from the scientific community and a great deal of work has been done with it including protein binding [31, 32], association / dissociation kinetics [33, 34], determination of affinity constants [35, 36] and so on. In all these work SPR, as a surface oriented method, allows real-time analysis of interactions without any labeled molecules. In addition, compared to the traditional methods such as chromatographic and spectroscopic methods, the identification and quantification of small molecules has been much improved by SPR with low detection limits [37, 38], selectivity, speed and reliability in analysis. It is believed that the development and application of SPR will continue to grow rapidly.

In 1902, Wood [39] described abnormal diffraction from diffraction gratings which was the earliest recorded observation of the electromagnetic effect of SPR. In 1941, Fano [40] found that the abnormal phenomenon was caused by surface plasma waves. In the late 1960s and early 1970s, Otto [41] and Kretschmann [42] demonstrated the optical excitation of surface plasmons using total reflection. Most commercialized SPR sensors are developed using the configuration described by Kretschmann.

When light travels from a medium with a higher refractive index to one with a lower refractive index, such as from glass to air, and the incident angle, Θ, is larger than a particular critical angle, no light is refracted and all incident light is reflected. This optical phenomenon is total internal reflection. Although the entire incident wave is reflected back, there is partial penetration into another medium at the boundary which is the evanescent wave. It travels along the boundary (in x direction) for about half wavelength with z-direction amplitude (perpendicular to

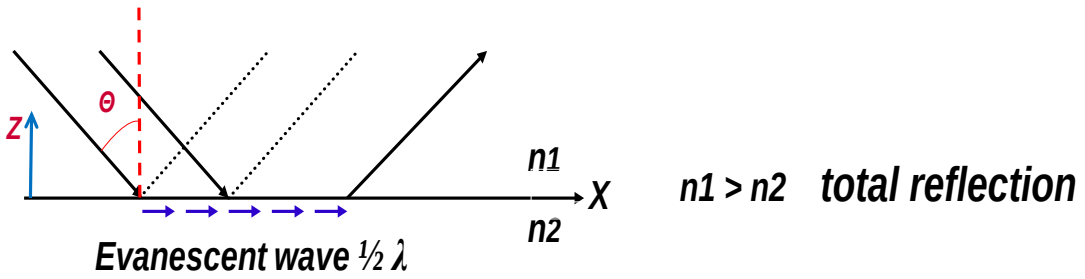

Fig 1-9: Schematic explanation of the total internal reflection and the evanescent wave under this condition.

the interface of two media) and then returns back to the first medium (with higher refractive index) shown in Fig 1-9. It causes surface plasmon resonance which is explained as a charge density oscillation at the interface of the two media. Because the field is maximal at the interface and decays exponentially with the penetrating depth from the interface, SPR is preferred for the study of interaction on the surface of thin films.

In general, an SPR sensor is mainly comprised of a polarized light source, a detector, a transducer face (for example Au film), a prism and a flow system (Fig 1-10). A thin Au film of 50-100 nm on a glass slide is the most often used transducer surface because of chemical stability and free electron behaviour of Au. In the SPR system, the detector measures the resulting reflected light against the incident light angle. Under the condition of constant incident light (wavelength and polarization state are not changed), the resonance condition associated with the critical angle is quite sensitive to the refractive index of the sample coupled to the metal surface. Therefore, the SPR biosensor can guarantee the real-time determination of any interaction occurring on the transducer film by monitoring the resonance angle change. SPR is applied to investigate the adsorption of biomolecules on the surface and the structure or configuration change of immobilized molecules. All changes are monitored over time and converted into a sensorgram. In the SPR system, the response is measured in units of resonance angle (RU) which could be understood as a reaction unit or resonance unit and 1 RU=10^{-4} degrees. From experience, adsorption of 1 ng/mm^2 protein causes a

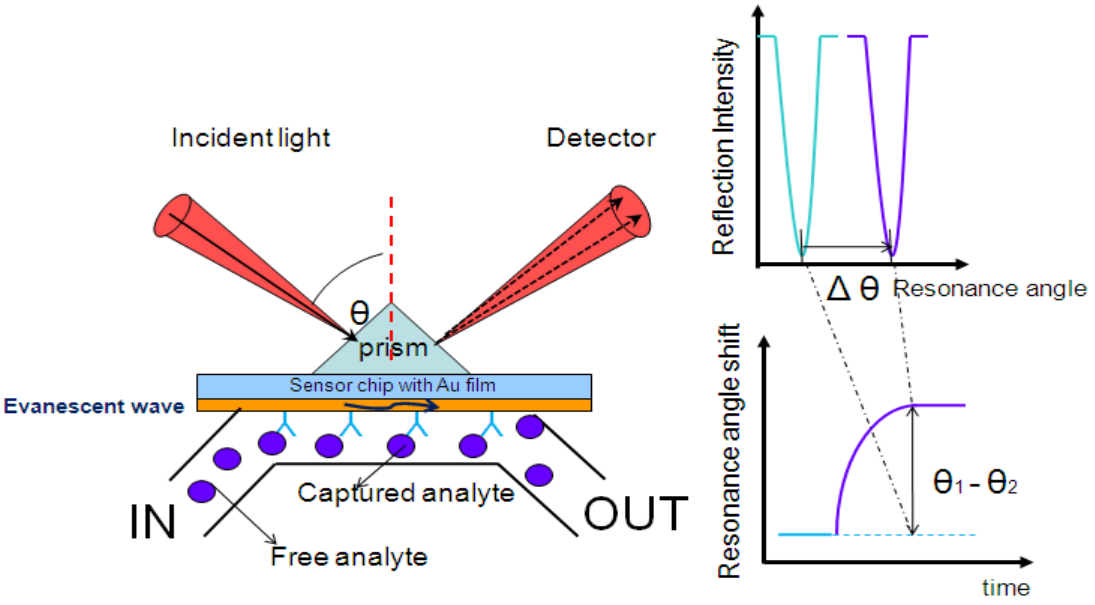

Fig 1-10: Schematic illustration of a Surface Plasmon Resonance sensor. Under the condition of total reflection, an evanescent wave is generated in the Au thin film. As the antigen (analyte) binds to the antibodies immobilized on the chip surface, the refractive index shifts and the resonance angle shifts consequently. The angle shift over time forms the sensorgram.

resonance angle increase of 1000 RU. Thus, the resonance angle shift can give a clue to how many analyte molecules are binding to the surface, the affinity and the association kinetics between the biomolecules. In some cases, a dextran layer (100-200 nm) is introduced to the SPR system and coupled on the surface of a thin Au film, and then the acceptor for interactions is coupled to the layer. In this way, the density of acceptors on surface is much more increased.

The high sensitivity, accuracy and the low degree of sample preparation in the SPR assay highlight its advantages over many other techniques for studies in the area of biology, clinical studies and immunology. Furthermore, the high specific detection of small molecules makes the SPR immunoassay an ideal candidate for researches in the areas of food and environment since most analytes of interest have low molecular weight (less than about 1000 Da). In the current study, the SPR biosensor was used to develop immunoassays for determination of low-levels of E3-16G in liquid samples (such as urine and waste water) which will be discussed in chapter four.

1.2.3 Surface-enhanced Raman scattering

Raman scattering is a light scattering technique. Major types of light scattering are elastic Rayleigh scattering, inelastic Brillouin scattering and Raman scattering. Raman scattering photons are scattered by the interaction with vibrational and rotational transitions in molecules. Depending on the excitation frequency, Raman scattered light can be in the UV to near infrared frequency range. However, the cross section of Raman scattering is quite small, typically around 10^{-30} to 10^{-25} cm^2 per molecule [43, 44], and that means a large number of analyte molecules are required for sufficient Raman photons. Therefore, usually, Raman spectroscopy has been considered a technique for analysis of chemical composition and molecule structure.

The aggressive and explosive development in the field of surface-enhanced Raman Scattering (SERS) was started from the work published by Fleischmann et al [45] in 1974 showing intense Raman signals from pyridine on a rough silver electrode. They initially thought that the increased surface area caused by the electrochemical roughening procedure resulted in the intense signal of pyridine. Efficiency of the signal enhancement is expressed with signal enhancement factor which is estimated by comparing the surface enhanced Raman signals and the normal Raman scattering, considering the contribution by the different concentrations of analyte molecules [46, 47]. Independently, Vanduyne and Jeanmaire [48] confirmed the SERS enhancement factor of 10^5 - 10^6 for pyridine. It can be further enhanced on nanometer-structured surfaces especially. At such a high enhancement level, the number of required molecules in the SERS sample was obviously lowered, thus, the surface-enhanced Raman scattering offers high sensitivity and possibility to detect monolayer of molecules and even to single molecule level [49]. The discovery of SERS transforms Raman spectroscopy from a structural analytical tool to a sensitive single-molecule and nanoscale probe. Nowadays it has been widely used in trace analysis [50, 51], medicinal chemistry [52], environmental science [53], biological and medicinal system [54, 55],

nano-materials and sensors [56]. Moreover, SERS as one of the best techniques to study interface effects has also been used in studying orientation [57] and adsorption behaviour of molecules on the surface [58].

SERS enhancements arise mainly by two mechanisms, chemical and electromagnetic effects [59, 60]. The former can be understood in terms of various possible electronic interactions between molecule and metal leading to changes in the electronic structure of molecules that can cause resonant Raman scattering, in which either (a) the electronic states of the adsorbate are shifted and broadened by the chemisorption interaction [57, 61] or (b) new electronic states resulted from photon-driven charge-transfer, and serve as resonant intermediate states in Raman scattering [61-63]. The latter one arises from the electromagnetic field of the light, resulted from increased electric field strength $|E|^2$ [64],

$$|E|^2 = |E_0|^2 \left|\frac{\varepsilon_m - \varepsilon_0}{\varepsilon_m - 2\varepsilon_0}\right|^2 \quad (1\text{-}9)$$

where $|E_0|$ is the incident field magnitude, ε_m is the frequency dependent dielectric function of the metal, and ε_0 is the relative permittivity of the ambient phase. From the above equation, it can be understood that the electromagnetic effects can be greatly enhanced under conditions of surface plasmon resonance (collective electron resonance) for “free electron” metals [65], i.e. $\varepsilon_m = 2\varepsilon_0$. Therefore, the electromagnetic enhancement is due to the metal’s ability to sustain surface plasmons of high resonance quality. Strong SERS enhancement comes about as a combination of the two effects. For Ag and Au systems, the electromagnetic field enhancement generated by nanostructures plays a dominant role. Apart from the two important mechanisms mentioned above, there is another effect able to contribute to the signal enhancement, i.e. resonances within the molecule itself [65]. It can occur when the excitation wavelength equals the wavelength of an electronic transition of the molecule [65]. As a result, the Raman scattering intensity from vibrations associated with the electronic chromophore, and having the correct symmetry, may be increased remarkably over

non-resonance intensities.

Considering the high electron density, coinage metals of Ag, Au and Cu can provide ideal conditions for surface plasmon resonance and promise enhancement of localized electromagnetic field considerably [66, 67]. As a consequence, Ag, Au and Au are the most often used active SERS substrates, on the surface of which enhancement of up to 10^6 can be obtained [47]. SERS from colloidal particles was first verified by Creighton, Blatchford and Albrecht in silver and Au hydrosols [68, 69]. Since then, they have been widely used in part due to the attractive simplicity of the experiment and the stable SERS enhancement from them under fairly reproducible conditions. Enormous improvement was achieved when “hot-spots” were recognized in 1994 by Moskovits and Shalaev [70]. Independently, Nie and Emery [50] used citrate reduced silver sols comprising mostly un-aggregated NPs of various sizes and shapes for SERS study. Surprisingly, extraordinarily high enhancement was observed around a small number of slightly aggregated particles. They were named as “hot” particles. The increase of SERS enhancement factors due to “hot-spots” (aggregates) is up to 10 orders of magnitude in the case of Au sol [71]. The large increase is explained by the electromagnetic field being strongly localized in the inter-particle region of aggregates which leads to trapping of the molecule in the hot-spots [46, 52]. The field enhancement in the hot spots is extremely sensitive to the distance between the particles and the frequency and polarization of the excitation laser [72-74].

The extremely efficient SERS enhancement mainly associated with the electromagnetic field indicates that silver and Au aggregates are appropriate substrates for Raman signal detection. In the early stage of this study, both Ag and Au were utilized and the model is described in Fig 1-11. However, in the future, the SERS may be combined with the SPR work to develop a biosensor with the sensitivity of SPR and the specificity of SERS. Thus, later studies were focused on Au sol considering its biocompatibility along with the favourable enhancing properties and the details will be discussed in chapter five.

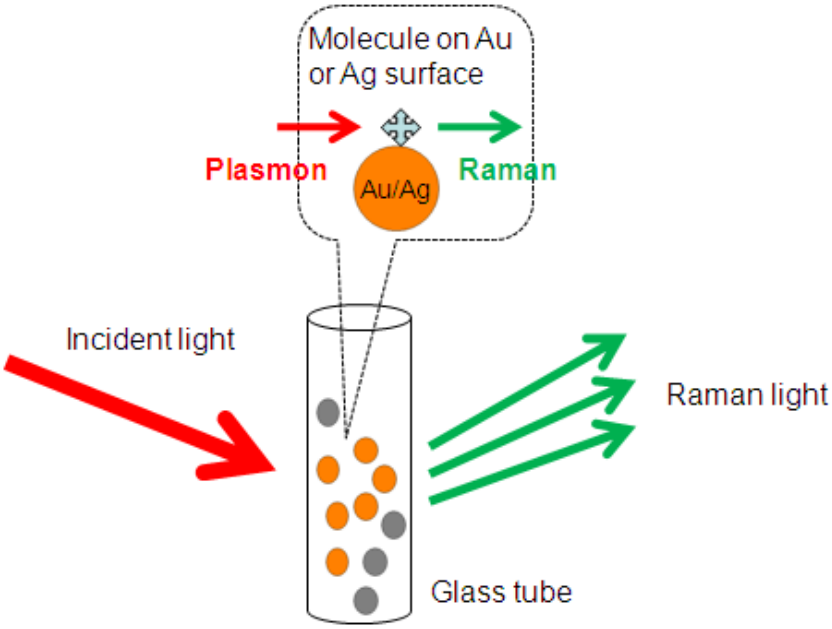

Fig 1-11: Schematic illustration of surface-enhanced Raman scattering (SERS) experiment. The molecules of interest are mixed with hydro sol of Ag or Au in a glass tube. The sample is excited by a laser (red) and the scattered light (green) is detected by DDC camera.

1.3 Thesis overview

The remaining chapters in this thesis describe in details the synthesis and the application of Au NPs to biological sensing.

Chapter two describes synthesis and characterization of spherical and rod-shaped Au NPs, and the synthesis of biomolecule-Au conjugates.

Chapter three describes a sensing system developed based on the LFIA technique using the conjugates introduced in chapter two and the validation of immunoassays developed in urinary samples with molecules of estriol-16-glucuronide.

Chapter four describes a sensing system developed with a SPR biosensor, the application of simple SPR-based immunoassays in clinical samples and a comparison between LFIA and SPR respectively.

Chapter five introduces preliminary investigations for a new sensing system using the SERS technique, in which 8 compounds from 3 different families, substituted porphyrin, thiophene and substituted terthiophene, are introduced and examined as Raman reporter molecules (RRM).

At the end, a summary and a brief discussion of the results presented in this thesis are provided. This part also discusses possible future research that could be carried out based on the current results.

Chapter Two

Gold nanoparticles and conjugates

2.1 Gold Nanostructure

2.1.1 Introduction

It is well known that the special physicochemical and optical properties of nanomaterials are quite dependent on both their size and shape [67, 75, 76]. As a result, one of the most challenging and important tasks of nanotechnology is to control the size and shape of NPs, while their size is in a range of 10 - 100 nm. There are many methods to produce Au nanoparticles [77-87], however, not all of them can be easily carried out in lab. The most common and efficient method is to use wet chemical synthesis (liquid-phase method).

In this approach, many different reductants have been used, such as sodium citrate first used by Turkevich and Frens [77, 80], phosphorus developed by Zsigmondy [87], and sodium borohydride reported by Brust et al. [79]. One method used here was to reduce dissolved $HAuCl_4$ with sodium citrate which acted as both reductant and surfactant. It produced Au nanospheres in a range of

12-20 nm with a relatively narrow size distribution [77, 88]. The formation of particles is achieved in a few steps [89]. The first step is the oxidation of citrate with dicarboxy acetone ($-CH_2-C(=O)-CH_2-$) as the product [89]. The next step is the reduction from auric ions (Au^{3+}) to aurous ions (Au^{+}). Finally is the step of disproportionation of aurous ions to Au atoms ($3Au^{+} \rightarrow 2Au^{0} + Au^{3+}$), in which Au^{+} ions are simultaneously reduced and oxidized. The overall stoichiometry can be described as

$$2AuCl_3 + 3(^{-}OCCH_2)_2C(OH)CO^{-} \rightarrow 2Au^{0} + 3(^{-}OCCH_2)_2C{=}O + 6Cl^{-} + 3H^{+} + 3CO_2$$

In addition, the stronger reductant $NaBH_4$ has also been tried to produce smaller sized nanospheres using sodium citrate as a stabilizing agent [15].

For preparation of the rod-shaped NPs, two common strategies are the electrochemical method reported by Yu et al. [78] and the wet chemical method described by Jana et al. [15]. Considering cost and equipment, wet chemical synthesis was selected. The model reported by Gai et al. [14] explains that the formation of NRs is caused by a diffusion of spherical NPs to the Au (111) surface along the [110] direction. Therefore, for NRs preparation spherical NPs as nucleation centres are necessary and called seed solution in this process. Solution for subsequent growth is called growth solution (GS). The strategy is therefore named as seed-mediated synthesis. In some cases, $AgNO_3$ is added to the growth solution to control the aspect ratio of NRs [15].

a) Seed solution

Colloidal Au NPs are achieved using a reductant of $NaBH_4$ in the presence of surfactant. Citrate stabilized Au colloids are negatively charged while those capped by CTAB are positively charged.

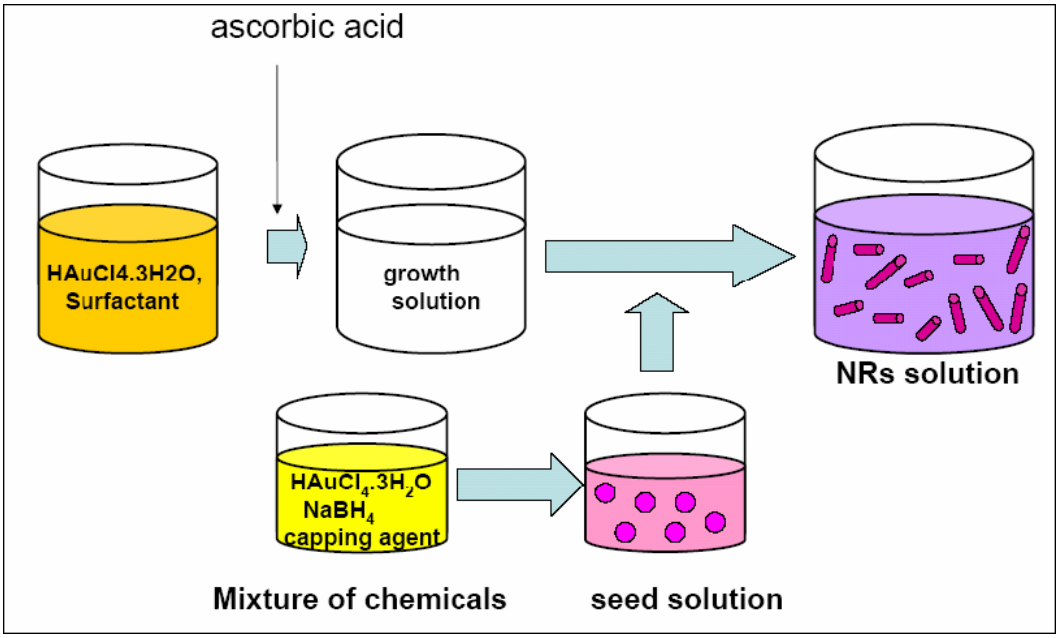

Fig 2-1: One-step seed mediated synthesis. The Au ions were reduced by ascorbic acid. The colour of the solution changes from dark yellow to colourless, by ascorbic acid reducing Au^{3+} to Au^{+}. To achieve final reduction from Au^{+} to Au^{0}, the seed solution was added to the growth solution. The colour of the mixture changes to purple due to formation of NRs.

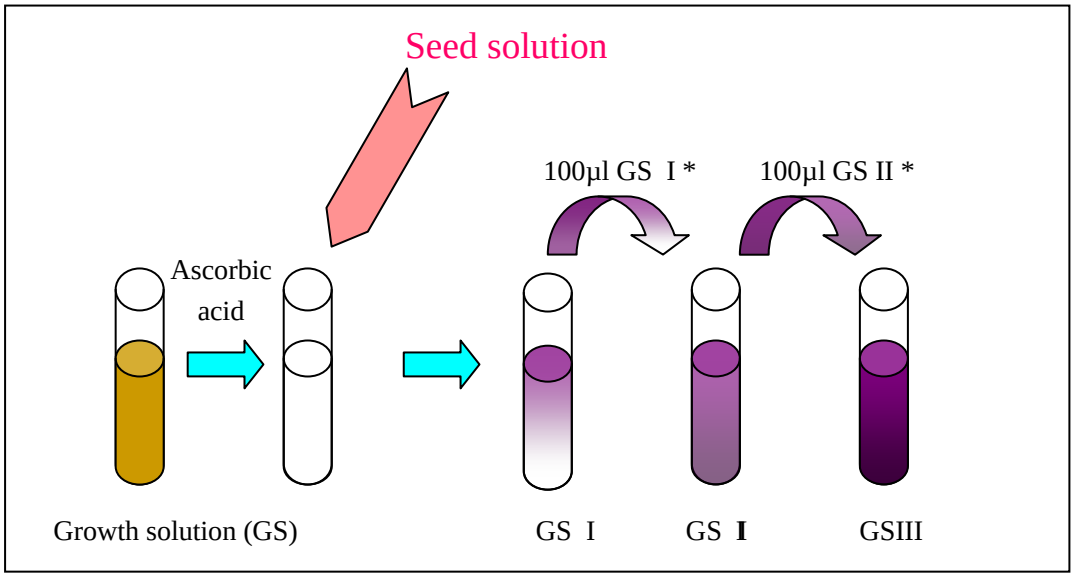

Fig 2-2: Three-step seed-mediated synthesis. The first step was to add seed solution into GS I to obtain GS I *. The second step was to add 100 µl GS I * into GS II about 3 minutes later and the GS II* was formed. The last step was to add 100 µl GS II * to GSIII. The GS III* was the final NRs solution.

b) Growth solution

Mixing the Au salt and surfactant CTAB leads to the colour change of the

solution from bright yellow to dark yellow (Fig 2-1), which can be explained by the formation of a CTA^+AuCl^- complex [90]. After adding the freshly prepared ice-cold ascorbic acid, it turns to colourless. This change indicates that ascorbic acid can only reduce Au^{3+} to Au^+ [91]. The further reduction is completed by the seed solution. The colour of the growth solution changes from colourless to different shades of red depending on the aspect ratio of formed NRs.

c) Mixing seed solution and growth solution

There are two ways to add seed solution into a growth solution. One way is to add the seed solution directly as described in Fig 2-1. Another way is to add the seed solution stepwise to 3 growth solutions as described in Fig 2-2. After adding the seed solution to the first growth solution, part of the mixed solution is added to the second growth solution. The generated mixture is then added to the third growth solution to form the final NRs solution. In the final solution, spherical and rod-shaped NPs co-exist which can be separated using centrifugation.

In the experiments, both spherical and rod-shaped Au NPs were synthesized according to the liquid-phase method introduced before. The NPs were characterized with UV-Vis spectrophotometry and transmission electron microscope (TEM).

2.1.2 Spherical nanoparticles

2.1.2.1 Amount of reductant and particle size

The NPs were negatively charged due to the citrate ions on the Au NPs' surface. In the experiments, six samples (a-d) were prepared using different amounts of the reductant according to the method described in Appendix I – 4.1.1. Table 2-1 shows information of the six samples. The mole ratios of Au^{3+} to the reductant were 1:1, 1:1.36, 1:2, 1:2.04, 1:3.4 and 1:4. The absorption spectra of the samples are shown in Fig 2-3, indicating that for a constant amount of Au^{3+} the size of spheres is controlled by the amount of citrate.

Sample / Information	a	b	c	d	e	f
Au^{3+} : citrate	1:1	1:1.36	1:2	1:2.04	1:3.4	1:4
Wavelength (nm)	534.5	534	525.5	526	523.5	521
Diameter (nm)	24±2	17±1	18±5	15±2	9±2	8±1

Table 2-1: Six Au NP batches prepared according to different mole ratios of Au^{3+} to reductant. Wavelength is the plasmon resonance wavelength of Au NPs and the diameter was determined by TEM.

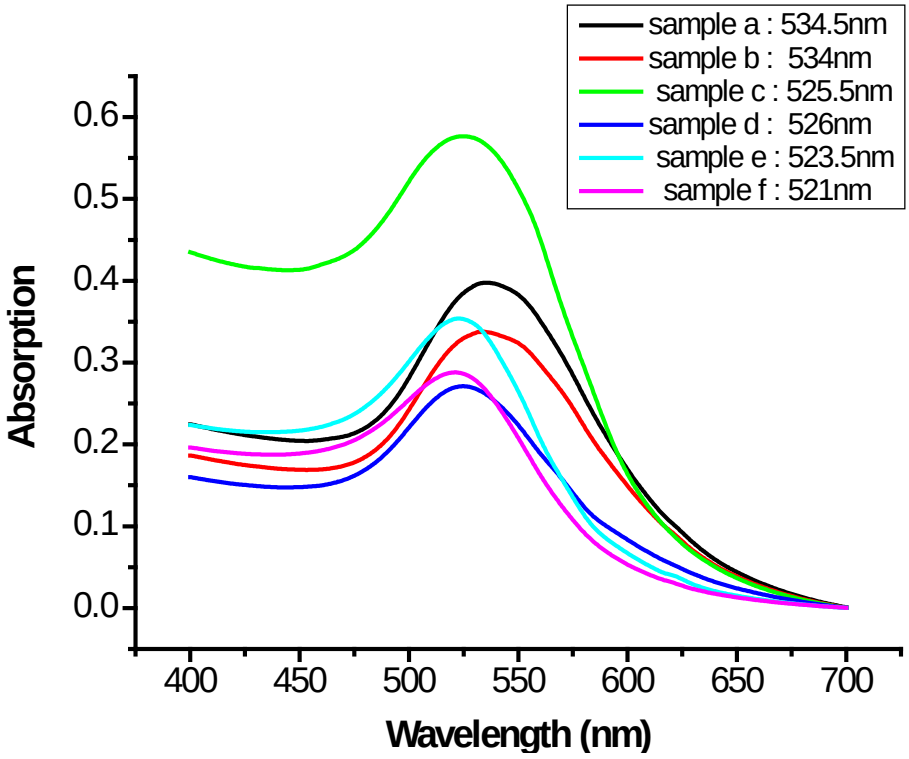

Fig 2-3: Absorption spectra of the six spherical NPs samples produced with different amount of reductant. All samples were 1:20 diluted with Milli.Q water.

To illustrate this relationship, the plasmon resonance wavelength of the nanospeheres was plotted versus the mole ratio in Fig 2-4. The regression line shows that the size of NPs increased with the mole ratio of Au^{3+} : citrate according to a linear relation. This conclusion was supported by the TEM images (Fig 2-5) as well. All images are displayed in a scale of 100 nm. The colloids were larger at the higher ratio of Au salt to sodium citrate (i.e. less reductant).

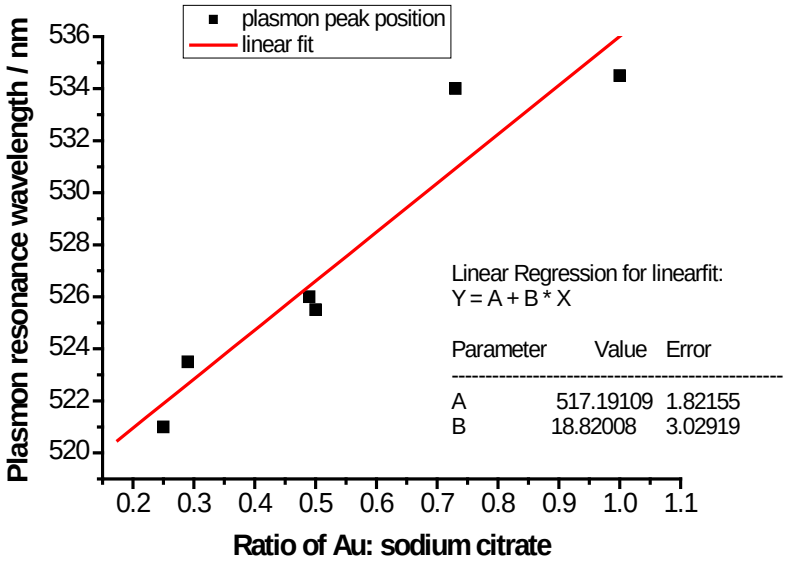

Fig 2-4: Correlation between the plasmon resonance wavelength of the Au nanospheres and the mole ratio of Au^{3+} to reductant. The regression line was calculated with the six samples prepared with different amounts of sodium citrate.

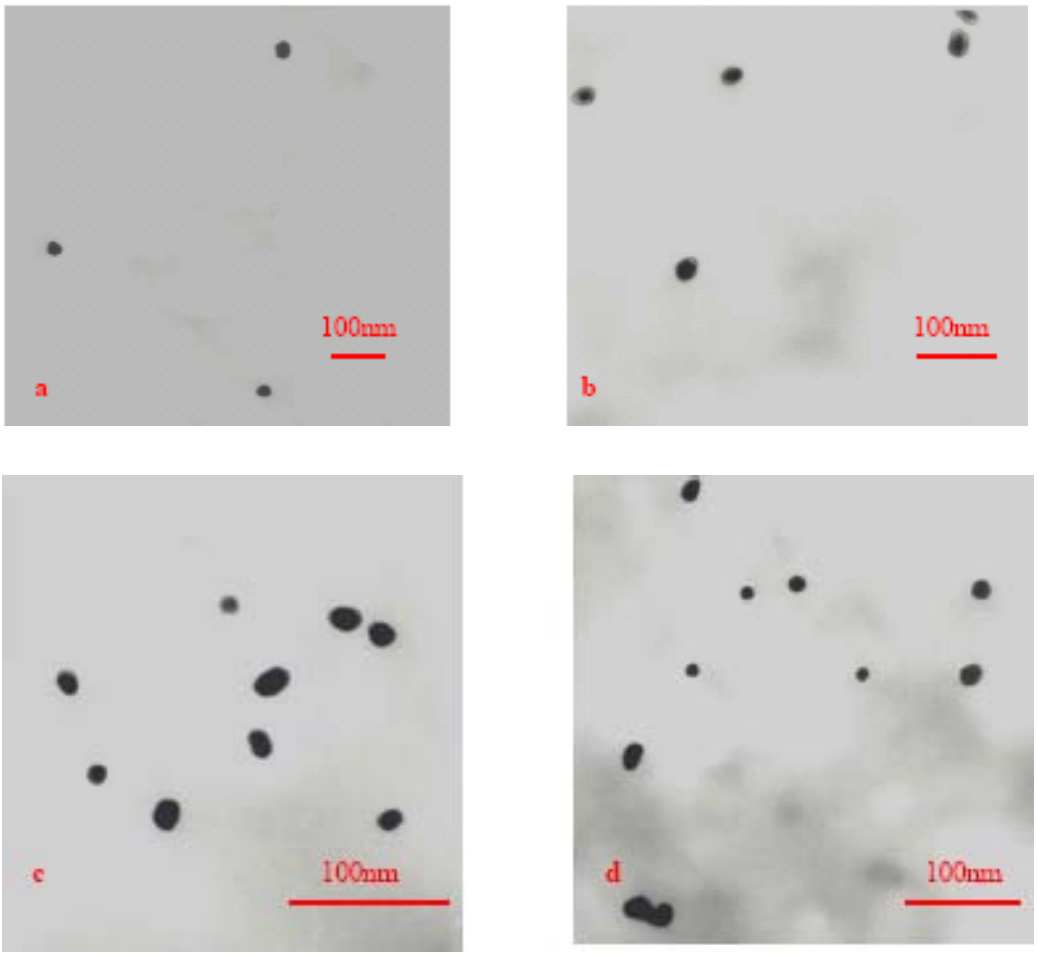

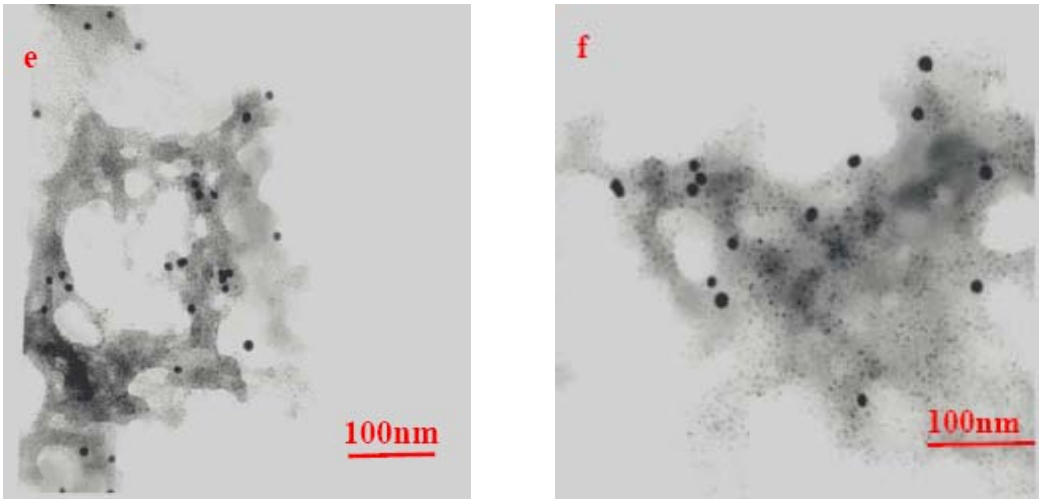

Fig 2-5: TEM images of six nano-spheres' samples. Diameters of six samples are a) 24±2 nm, b) 17±1 nm, c) 18±5 nm, d) 15±2)nm, e) 9±2 nm, f) 8±1 nm. Scale in all images are 100 nm.

2.1.2.2 The stability of NPs

Theoretically the NPs tend to be fairly unstable and to aggregate easily. The capping (stabilizing) agent is required to suppress the aggregation. In this work, Au nanospheres were generated and stabilized by citrate that formed a negatively charged layer on spheres' surfaces. The repulsion force between the NPs keep them stable in suspension for long time without serious aggregation. The plasmon

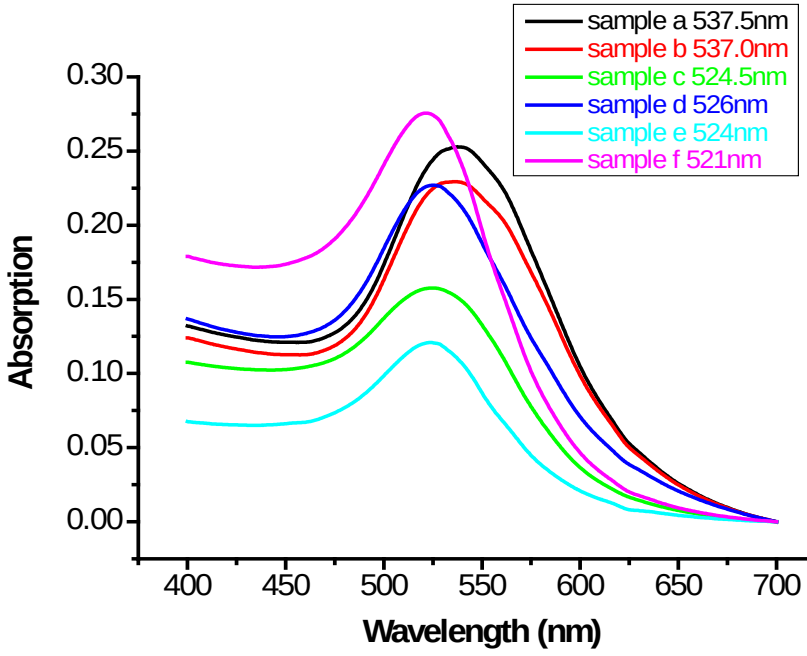

Fig 2-6: Absorption spectra of two-week old samples. All samples were 1:20 diluted with Milli.Q water.

sample	a	b	c	d	e	f
λ (Fresh) nm	534.5	534	525.5	526	523.5	521
λ (2 weeks old) nm	537.5	537	524.5	526	524	521

Table 2-2: Plasmon resonance wavelength of fresh and two weeks old samples.

resonance peak position is related to several factors [13, 92], however, the size of the noble metal particles is one of the most important factors causing the peak shift. Therefore, UV-Vis spectrophotometry is an efficient way to determine the stability of NPs' suspension. Two weeks later, the six samples were measured again (Fig 2-6) and the reported plasmon resonance wavelengths were compared to the data of the related fresh samples in Table 2-2. The maximum shift around 3 nm, which is presumably due to the slightly aggregated but still stable NPs in suspensions, indicates that the sodium citrate capped NPs are at least stable for two weeks.

2.1.2.3 Dynamic Light Scattering

To estimate the size of the particles, a Malvern Zetasizer was used based on the principle of dynamic light scattering (Appendix I – 4.1.3). In total there are three numbers reported by a Zetasizer which are size distributions by number, volume and intensity. The relation between them is described with the following equation

$$\mathbf{Size}_{\text{reported by number}} = (\mathbf{Size}_{\text{reported by volume}})^{1/3} = (\mathbf{Size}_{\text{reported by intensity}})^{1/9}. \quad \textbf{(2-1)}$$

Therefore, only the size by number represents the correct size determined by Zetasizer. Although the data shown in Fig 2-7 support that larger Au NPs correspond to less reductant, for all samples the sizes by number reported here are much smaller than those measured by TEM. To validate accuracy of the measurements of the Zetasizer, 20 nm sized commercial spherical Au NPs were tested and the reported size by number was 1.54 nm smaller than its real size. Fig 2-8 represents the main size by intensity is 36 nm of which the ninth root is 1.48

similar to the size by number, consistent with the relation described in Equation (2-1). Although the reason for that is not clear yet, it is not recommended to use Zetasizer to estimate the size of Au colloids.

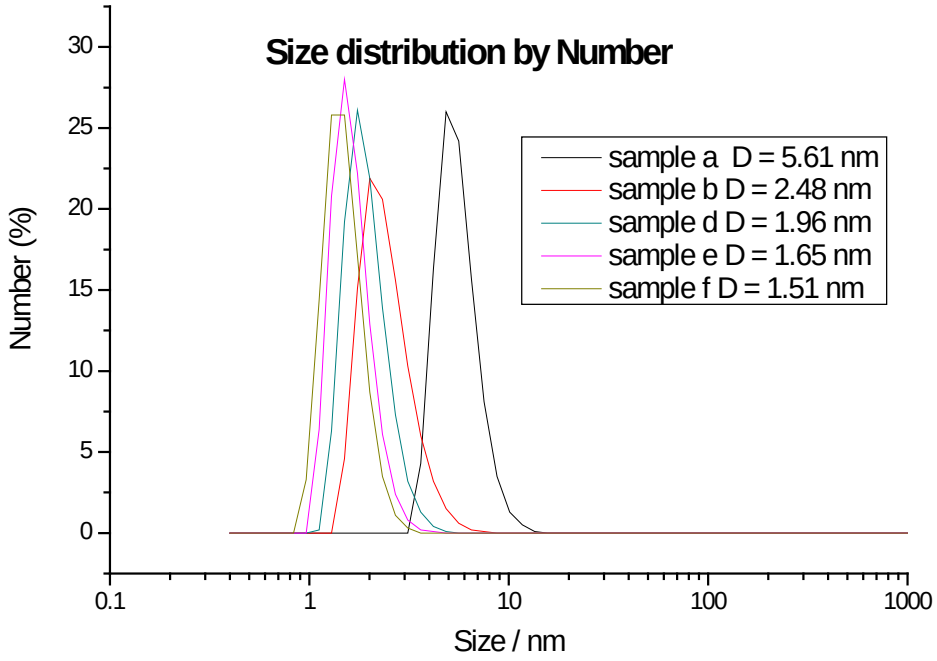

Fig 2-7: Size distributions by number of the spherical NPs reduced by sodium citrate. D represents the diameter of the nanospheres in detected sample.

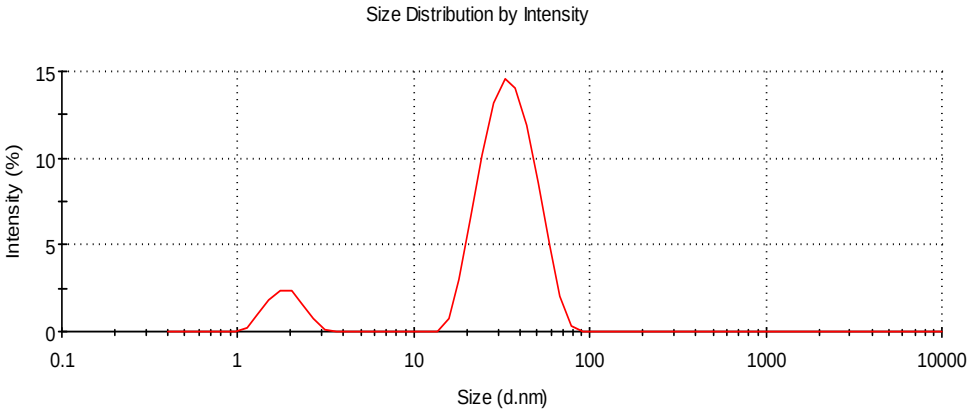

Fig 2-8: Size distribution by intensity of 20 nm sized commercial Au NPs determined by the Malvern Zetasizer.

2.1.3 Rod-shaped nanoparticles

2.1.3.1 Seed mediated synthesis

As described previously, there are two ways to add the seed solution to the growth solution, directly or stepwise (Appendix I – 4.1.2.1). The difference between them can be illuminated with the following TEM images. In the samples formed with the direct addition, it was observed that the percentage of spherical NPs was quite high and their size was not uniform. According to measurements of 150 spheres, it was found, 16.7 % of them were around 5 nm, similar to the seed size, 8.3 % were around 8.5 nm and 75 % were around 11.5 nm. Fig 2-9 shows the

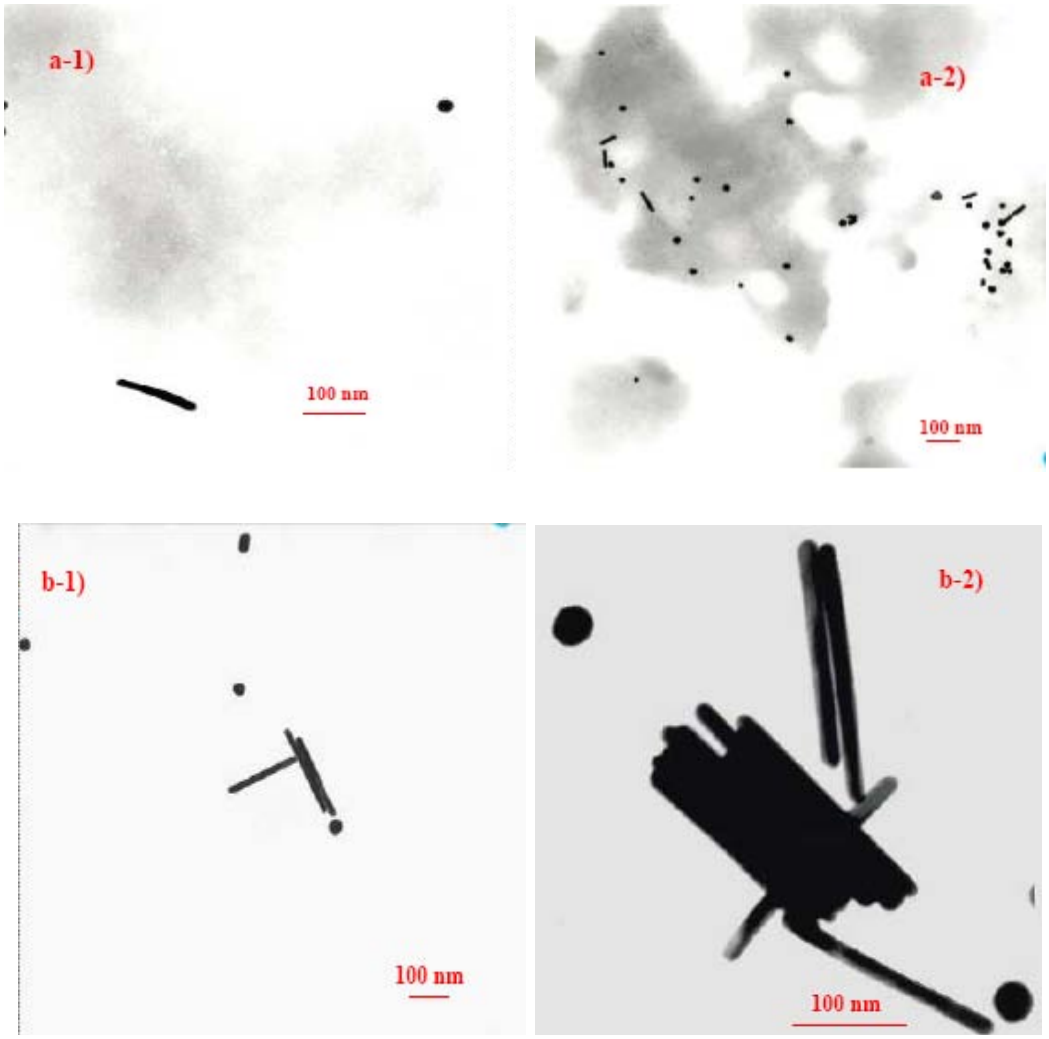

Fig 2-9 a): NR1– direct seed mediated synthesis. Most NPs are spherical and the average R is in a range of 4~6. b): NR2– three step seed mediated synthesis, the average R ranges from 13 to 16. All data were calculated by measuring more than 50 particles.

average aspect ratio (R) of NRs produced with the one-step seed mediated synthesis is around 4 to 6 and the maximum is 9 while the average aspect ratio of NRs synthesized with the step by step enlargement is higher and in a range of 13-16. In the case of adding the seed solution directly, the ratio of seed solution to growth solution was relatively small (25 μl to 10 mL). Under this condition, the added seeds induced further nucleation rather than growth of NRs and thus resulted in multiple sized nucleation centres. Therefore, in the final samples, the size distribution of NPs was broad and the aspect ratio of NRs was low.

2.1.3.2 Synthesis in the presence of $AgNO_3$

Another way to produce the NRs is to use $AgNO_3$ as an "assisting agent" controlling the aspect ratio in the growth solution. In this strategy (Appendix I – 4.1.2.2), the seed was positively charged by adding CTAB. In the experiments, the $AgNO_3$ (4 mM), of which the volume was in a range of 0.15 mL and 0.5 mL (Table 2-3), was added to the growth solution after the Au^{3+} were reduced to Au^{+} by ascorbic acid. The final reduction from Au^{+} to Au^{0} was completed by 12 μl seed solution. Considering the definition of the aspect ratio (length to diameter of NRs) and the size- / shape-dependence of the plasmon resonance wavelength, it could be understood that any change of the aspect ratio will result in shifts of either the longitudinal plasmon resonance wavelength or the transversal plasmon resonance wavelength.

Information in Table 2-3 and spectra in Fig 2-10 show that the longitudinal wavelength of the 8 NRs – 3 samples continuously shift to longer wavelength range with further addition of Ag^{+} ions except the 2^{nd} and 6^{th} sample. At the same time, the transversal wavelength blue shifts when the volume of Ag^{+} is less than 0.35 mL and red shifts above this critical volume. It is suggested that the aspect ratio of NRs increased as more Ag^{+} ions were added to the growth solution.

NRs / Information	3.1	3.2	3.3	3.4	3.5	3.6	3.7	3.8
V_{Ag+} (mL)	0.15	0.20	0.25	0.30	0.35	0.40	0.45	0.50
$\lambda_{transversal}$ (nm)	515	521	513	512	510	517	514.5	515
$\lambda_{longitudinal}$ (nm)	697	685	796	844	822.5	848.5	882	899.5

Table 2-3: NRs-3 samples prepared by adding $AgNO_3$ of different volumes to the growth solution. The $\lambda_{transversal}$ and $\lambda_{longitudinal}$ represent the transversal and the longitudinal plasmon resonance wavelength.

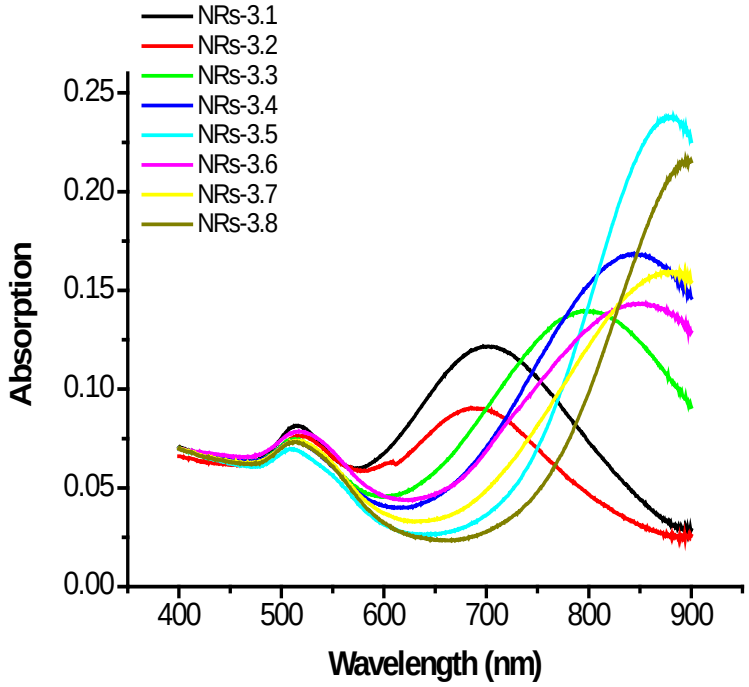

Fig 2-10: Absorption spectra of 8 NRs – 3 samples synthesized with 4 mM $AgNO_3$ of different volumes.

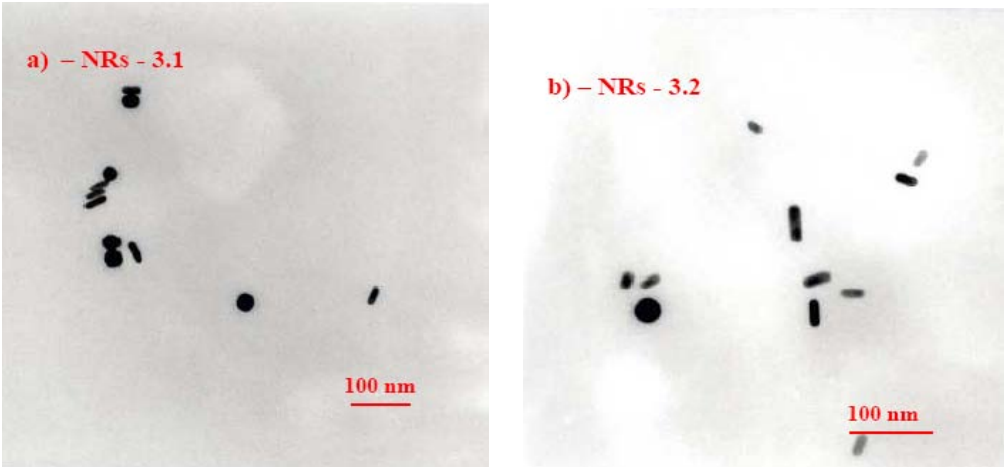

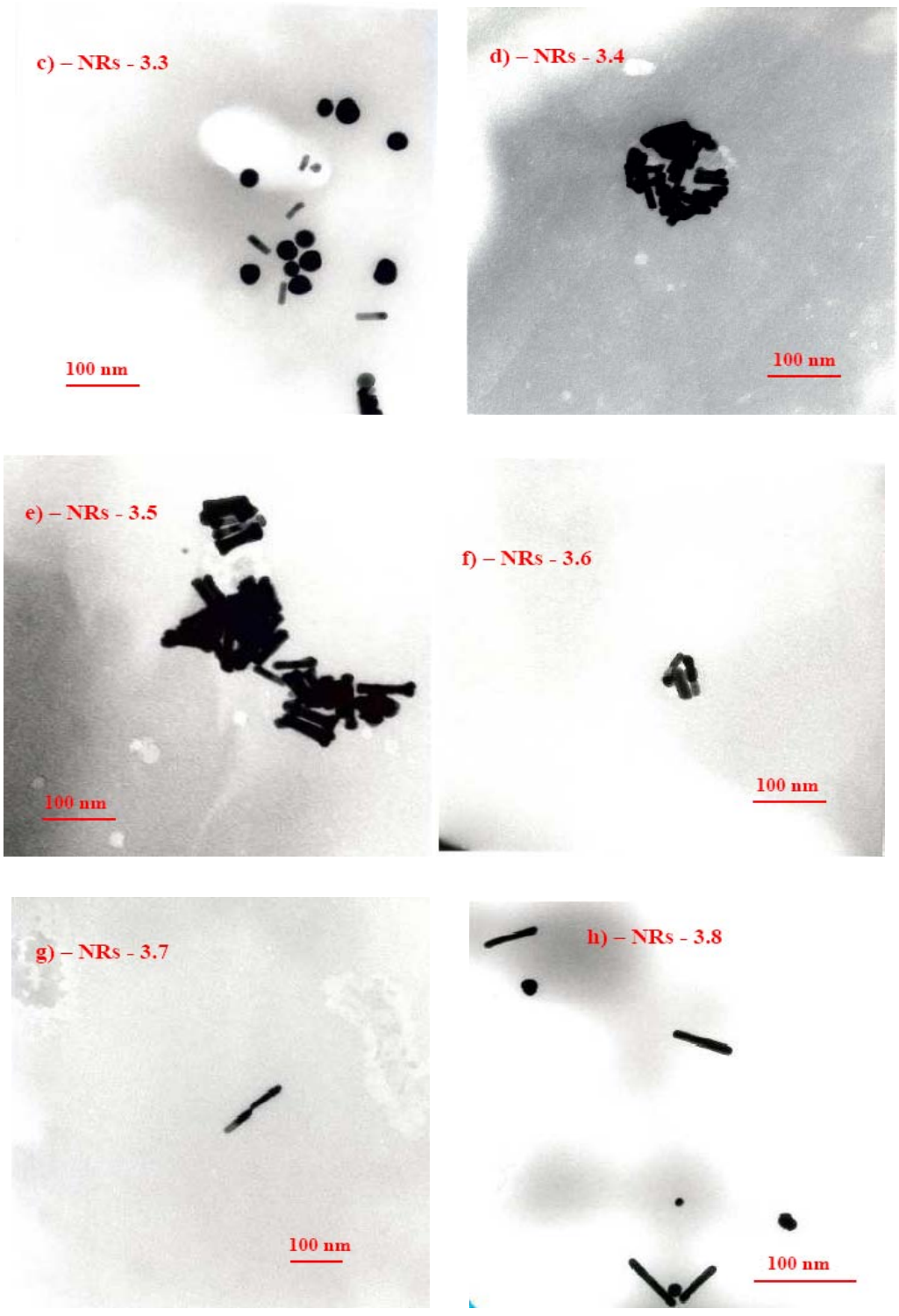

Fig 2-11: TEM images of NRs – 3 synthesized in the presence of $AgNO_3$. The scale bar in all images is 100 nm. The aspect ratios of the 8 samples are 2.6±0.2, 2.8±0.5, 4.0±0.3, 4.8±0.5, 4.8±0.5, 5.3±0.3, 6.2±0.5 and 7.0±0.5.

The aspect ratios of the 8 samples were determined with TEM images (Fig 2-11) and are shown in Table 2-4. Fig 2-12 depicts a linear correlation between

the longitudinal plasmon resonance wavelength and the aspect ratio that is λ_{max} = 575.53 nm + 51.695 * R nm. The regression is in good agreement with the previous publication [93] reporting an equation of

$$\lambda_{max} = 570 \text{ nm} + 51 * R \text{ nm} \qquad (2\text{-}2)$$

for estimation of the aspect ratios using the longitudinal wavelength. The aspect ratios of the 8 samples calculated using Equation (2-2) are also shown in Table 2-4. It is found the maximal difference between the two sets of data is less than 9%.

NRs / R	3.1	3.2	3.3	3.4	3.5	3.6	3.7	3.8
R_{TEM}	2.6±0.2	2.8±0.5	4.0±0.3	4.8±0.5	4.8±0.5	5.3±0.3	6.0±0.5	7±0.5
$R_{Equation}$	2.5	2.3	4.4	5.4	4.9	5.5	6.1	6.5

Table 2-4: Aspect ratios of the 8 samples determined by TEM (R_{TEM}) and calculated with the Equation (2-2) ($R_{Equation}$).

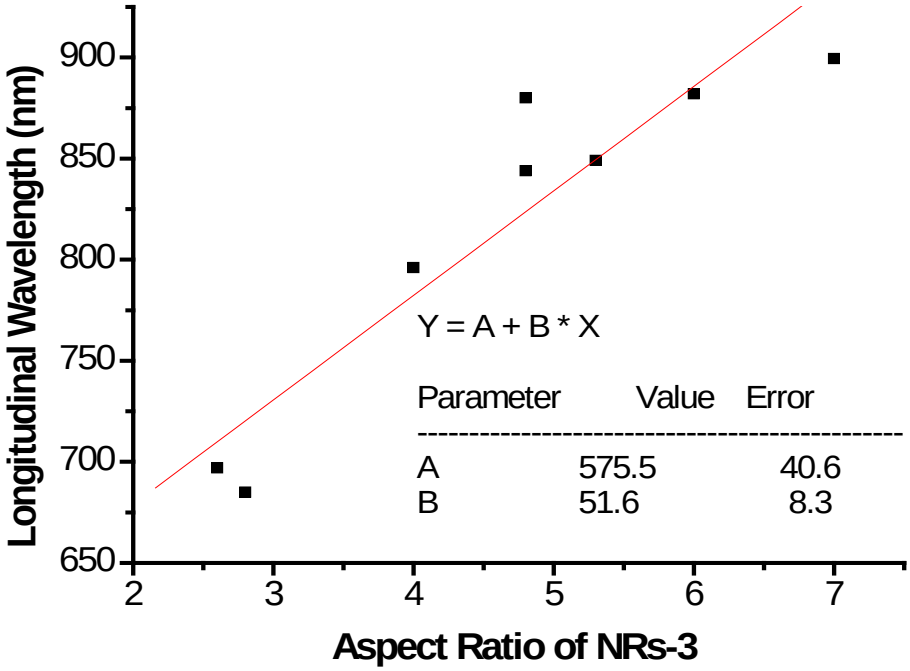

Fig 2-12: Correlation between the aspect ratios (TEM) determined experimentally and longitudinal plasmon resonance wavelength of NRs (UV-Vis). The regression line was calculated with the 8 samples prepared with different amounts of $AgNO_3$.

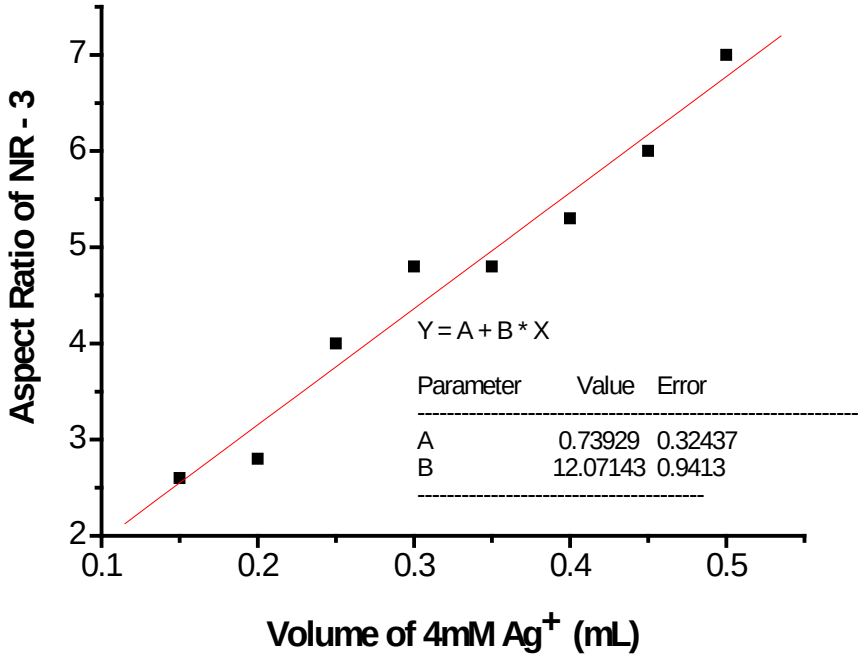

Fig 2-13: Correlation between the experimentally determined aspect ratio (TEM) and volume of the applied $AgNO_3$. The regression line was calculated with the 8 data points.

Based on the above analysis, it can be concluded that the aspect ratio is linearly dependent upon the total Ag^+ ions in growth solution as that shown in Fig 2-13.

2.2 Gold conjugate

The application of noble metal NPs in the biological field is a new and important direction of research. The biological molecule – metal NPs conjugates are applied in different areas，such as molecular electronics [94, 95], acting as signal reporters for fluorescence and dark-field microscopy [96, 97], biological sensing [98-100], and as nano-devices for diagnosis, medical diagnostics and drug delivery [101]. The purpose of this work is to generate small conjugates composed of nanometer (nm) sized Au colloids and antibodies (Ab) for the determination of E3-16G at low concentrations existing in liquid media, such as urine and waste water, using lateral flow immuno-tests and SPR sensors which will be discussed in chapter three and four.

The use of colloidal particles as versatile and efficient templates for the

immobilization of biomolecules has been recognized since the early 1980s [102]. Examples of colloidal particle–biomolecule conjugates include immuno-micro-spheres, that can react in a very specific way with antibodies [100], target cell [103], or viruses [104, 105], depending on the type of antigen adsorbed on the microspheres. Usually the pH of the negatively charged Au colloids is adjusted to the range of 8 to 9. Under this condition, the antibody molecule binds successfully to the Au particles despite the fact that it is believed the big antibody molecules will be overall negatively charged.

The nanogold-antibody (Au-Ab) conjugates were prepared with different sized Au NPs stabilized by sodium citrate and polyclonal primary anti-E3-16G Ab (pAb) of different concentrations raised in sheep or rabbit anti-sheep serum. The optimal conditions for the synthesis of conjugates including the pH of the Au NPs used and the amount of Ab required for stabilizing the Au colloids were confirmed by titration.

2.2.1 Finding optimal conditions

Synthesis of stable conjugates is related to the size, concentration and pH of the Au colloids and to the concentration of the molecules applied. Colloidal Au sol carries an overall charge which confers a stabilizing effect due to mutual repulsion of the particles. Flocculation of the particles occurs in the presence of strong electrolytes, such as NaCl. The flocculated Au NPs show red-shifted plasmon resonances due to strong interactions between individual NPs. It is pointed out that the flocculation can be prevented by coating the particles with macromolecules possessing polar groups [102], such as antibodies. Also the Au NPs coated with antibodies show a plasmon resonance wavelength close to that of the unconjugated Au colloids even with the stress of a concentrated salt solution (10 % NaCl). A titration experiment using a series of antibodies of different concentrations and Au colloids of different pH-values is therefore commonly performed to determine the optimal synthesis conditions. The aim of the titration is to put the Au-Ab system under stress with salt.

2.2.1.1 Titration for synthesis of pAb-Au conjugates

The antibody used in the present work was a partially purified polyclonal primary anti-E3-16G IgG raised in sheep preparation in phosphate buffer (10 mM pH=7) (Appendix I – 4.2.1) for which the concentration of the stock solution was 4.8 mg/mL. It was diluted with sodium borate buffer to a range of 0 to 0.23 mg/mL for titration. To determine the optimum conditions for synthesis of the pAb-Au conjugates, the plasmon resonance wavelengths of the NPs coated by pAbs obtained in the presence of 10 % NaCl were plotted versus the concentrations of pAb in the final mixtures (in Fig 2-14) which were calculated by dividing by a factor of 11 considering the dilution caused by the Au suspension. Experimental details see Appendix I – 4.2.2.

Considering the previous discussion that a small shift (generally lower than 10 nm) of the plasmon resonance wavelength obtained in the presence of high stress of salt indicates the formation of stable conjugates, it can be concluded from Fig 2-14 that pH values of 8.5 and 9.0 are appropriate since fluctuations of the

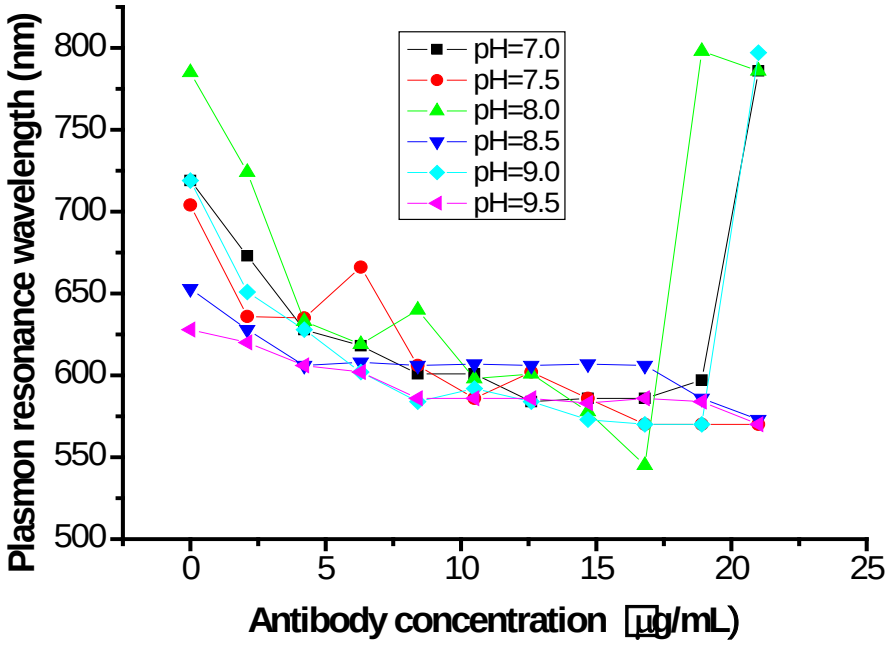

Fig 2-14: Correlation between the plasmon resonance wavelengths of pAb coated Au NPs and the concentrations of the coating pAb at different pH values.

wavelength shift are quite narrow once the pAb concentration are sufficiently high to stabilize the Au colloids. At pH of 8.5 the minimum amount of required pAb to stabilize Au NPs was around 4.2 µg/mL while it was 8.4 µg/mL at pH of 9.0.

2.2.1.2 Titration for synthesis of 2° antiserum-Au conjugates

A commercial available anti-sheep serum raised in rabbit (2° antiserum) was also used for synthesis of nanogold conjugates. The concentration of the secondary antibody which was specific to the pAb raised in sheep was given by the suppliers as 3.5 mg/mL and the total protein concentration as 69 mg/mL. Before titrating, it was necessary to determine whether the non-specific serum proteins could bind to the Au surface. If we assume all proteins bind, then 69 mg/mL is the concentration of the stock solution. Otherwise, the specific antibody concentration must be taken as 3.5 mg/mL. At the beginning of the experiments, the total protein concentration of 69 mg/mL was assumed to be correct. A relatively simple titration (Appendix I – 4.2.2) was done using the Au colloids (pH from 7-10) and 3 different amounts of 2° antiserum (2°AS) which were calculated using 69 mg/mL as the stock concentration. The concentrations of 2°AS in the final samples were therefore believed to be 5.5, 9.1 and 18.2 µg/mL. Fig 2-15 shows only the absorption spectra of the conjugates for which the 2°AS concentration was calculated to be 18.2 µg/mL. Instead of the normal sharp plasmon resonance peaks, only broad bands were observed that suggested unstable conjugates in suspension. The huge shift, from the plasmon resonance wavelength of the unconjugated Au (530 nm) to the wavelength corresponding to the maximal absorbance of the bands, indicates that the protein molecules present in the samples were not able to stabilize the Au NPs. This means there was no reaction between the Au colloids and the proteins in serum at these concentrations and hence the concentration of specific antibody (3.5 mg/mL) was the correct one to use in calculation.

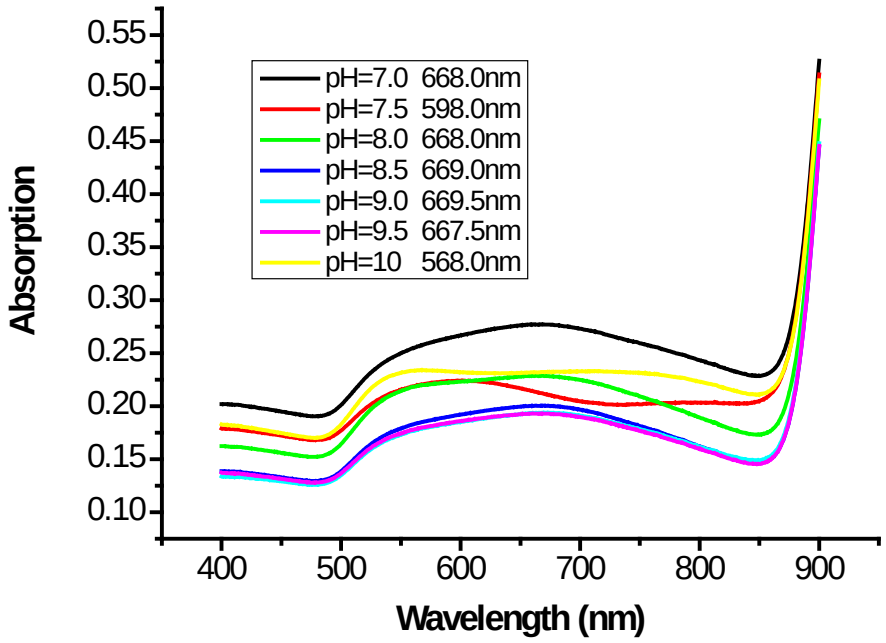

Fig 2-15: Absorption spectra of the 2°AS-Au conjugates synthesized using Au NPs of different pH. The 2°Ab concentration in mixtures was estimated to be 18.2 μg/mL.

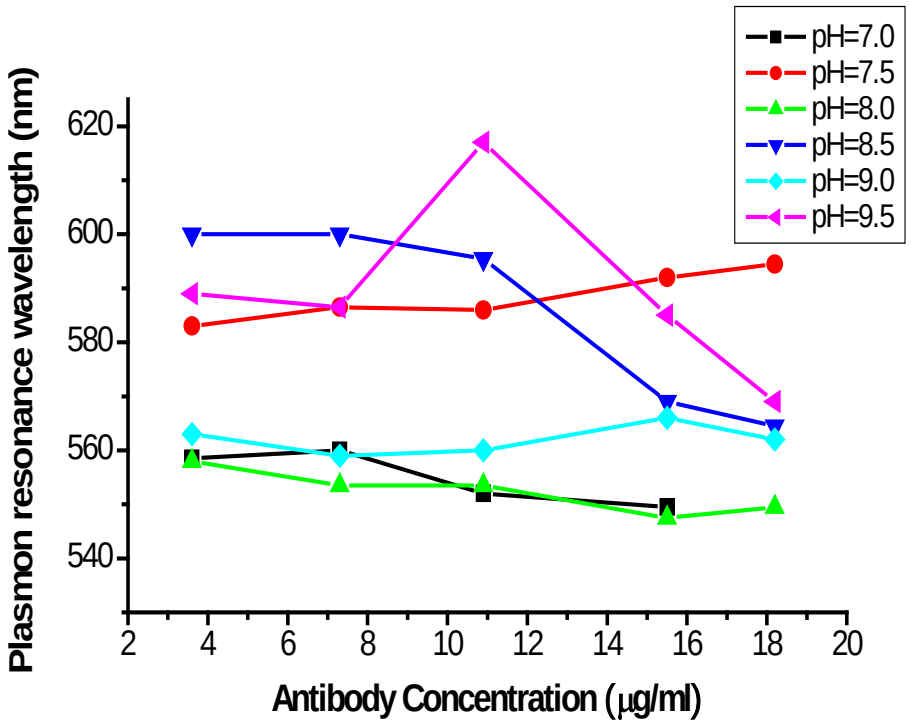

Fig 2-16: Correlation between the plasmon resonance wavelengths of conjugates and the concentrations of coating 2°AS at different pH values.

After the correct concentration of molecules for coating the Au NPs was confirmed, another titration set was carried out following the procedure described in Appendix I – 4.2.2. The plasmon resonance wavelengths of all the samples were plotted versus the concentration of 2°AS present in the conjugates as shown in Fig 2-16 from which it was observed that relatively small shifts, from the plasmon resonance wavelength of un-conjugated Au (530 nm), were obtained when the pH of the Au sol was adjusted to 7.0 or 8.0. In the case of pH 8.0, the lowest 2°AS concentration required for formation of stable conjugates was 7.3 μg/mL while it was 10.9 μg/mL under the condition of adjusting the pH of the Au colloids to 7.0. Therefore, pH 8.0 was chosen as optimum for the synthesis of the 2°AS-Au conjugates.

2.2.2 Antibody/antiserum-Au conjugates

2.2.2.1 pAb-Au conjugates

Based on the information confirmed with the titration, two conjugates were produced with different amounts of pAb according to the procedure shown in Appendix I – 4.2.3. The final concentrations of pAb in the two conjugates were estimated to be 73 μg/mL and 187 μg/mL respectively. Compared to the absorption spectrum of unconjugated Au shown in Fig 2-17, it was found that the plasmon resonance wavelengths of the two conjugates were red-shifted 8 nm and 10 nm respectively (around 1.8 %) presumably as a result of the binding of the pAb and the blocking agent of BSA onto the colloidal Au surface. The maximal absorbances of the final conjugate solutions were 17.2 and 15.3 respectively, calculated by multiplying the absorbance by a dilution factor of 20. Considering that the volume of the conjugate solution (2.2 mL) was about 1/9 of the initial volume of the colloids (20 mL) Au NPs were added for synthesis and the absorbance of the unconjugated Au was 2.3 (0.23x10), it was estimated that maximal 26 % (=100% - 15.3/(2.3*9)) of the colloids were lost during the synthesis of the conjugates.

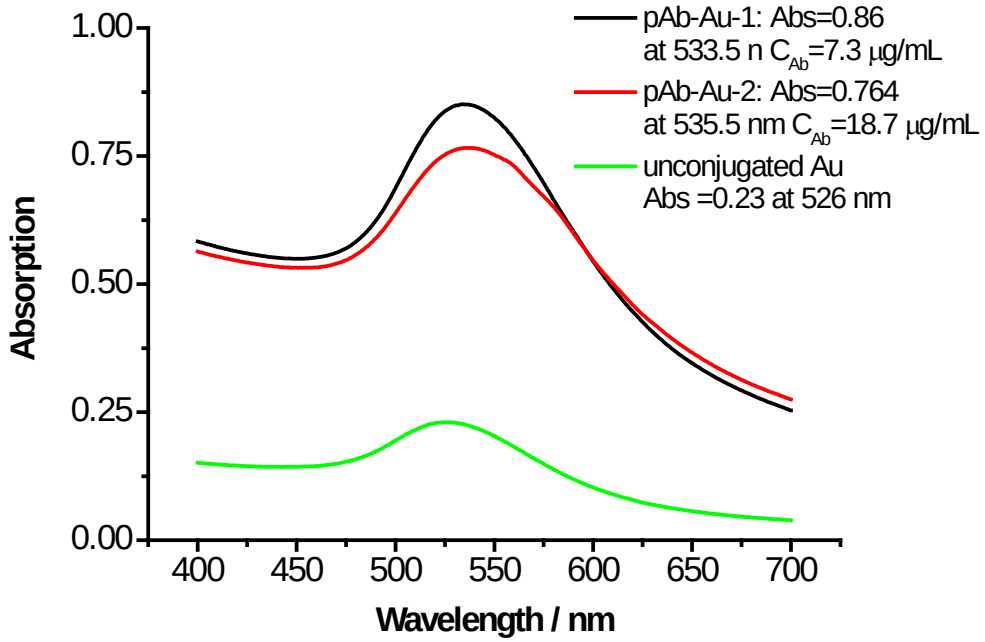

Fig 2-17: Absorption spectra of the unconjugated Au NPs and two pAb-Au conjugates synthesized using pAb of different concentrations. The spectra of the conjugates were performed using 1:20 dilution of the conjugates and the spectrum of the unconjugated Au was collected using 1:10 dilution of the sample.

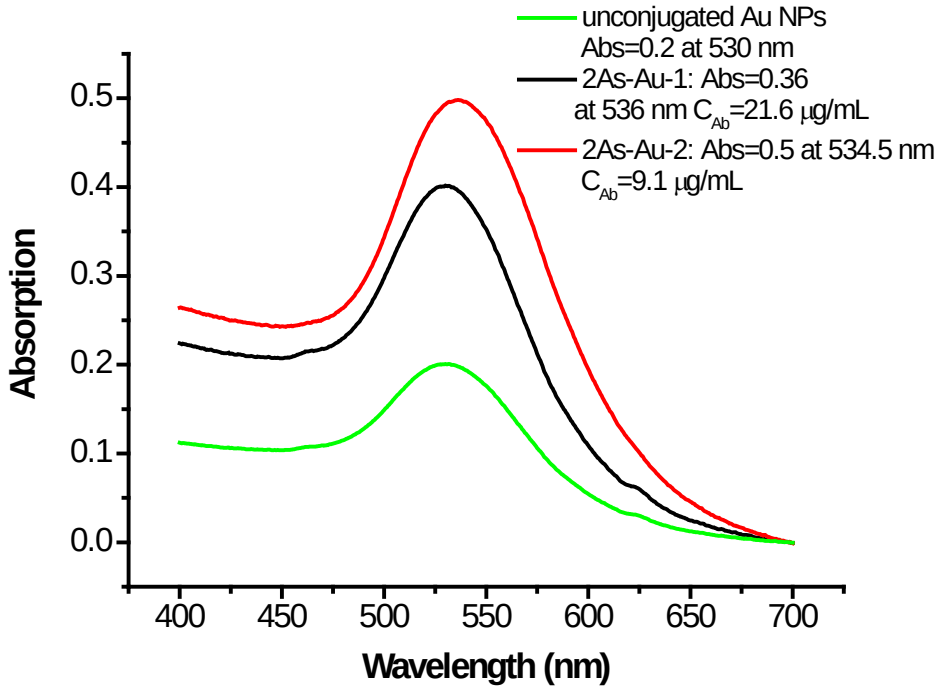

Fig 2-18: Absorption spectra of the unconjugated Au NPs and two 2°AS-Au conjugates synthesized using different amounts of antiserum. The spectra of the conjugates were performed using 1:20 dilution of the conjugates and the spectrum of the unconjugated Au was collected using 1:10 dilution of the sample.

2.2.2.2 2°antiserum-Au conjugates

The 2°AS-Au conjugates were synthesized according to the same strategy as for the pAb-Au conjugates. Fig 2-18 shows the absorption spectra of two 2°AS-Au conjugates synthesized using bigger sized Au NPs, for which the plasmon resonance wavelength was 530 nm. The final concentrations of 2°Ab in the 2°AS-Au conjugates were calculated as 216 and 91 μg/mL, respectively. Both conjugates showed the intense plasmon resonance peaks with red-shifts of around 5 nm due to the large molecules attached to the Au spheres' surface. The maximal absorbances of the formed conjugates were 7.27 and 10.00 respectively (absorbance times the dilution factor of 20). Considering the absorbance of 2.03 for the unconjugated Au, it was estimated that the 2°AS-Au conjugates were produced with a higher loss of Au NPs close to 65 % (calculated according to the absorbance of the conjugates and the unconjugated Au NPs). This was presumed to be a result of the Au colloids stuck to the centrifuge tube wall. To reduce losses related to centrifugation, different sized Au NPs and different centrifuge speeds were tried. However, no reproducible method was found, the best being 26 % loss of the NPs.

2.3 Conclusion

In the first part of my work, spherical and rod-shaped NPs were generated with wet chemical strategies. They were stable for several weeks with the help of capping agents. The negatively charged nanospheres were produced and stabilized by sodium citrate. For a constant amount of the Au salt, their size increased with decreased sodium citrate concentration in solution. The slight aggregation of NPs ($n(Au) \rightarrow (Au)_n$) caused a red shift of the plasmon resonance wavelength.

For the NRs preparation, two different seed solutions were used which were negatively charged with sodium citrate as surfactant and positively charged using CTAB as stabilizing agent. With a three-step seed mediated synthesis, NRs of higher aspect ratio were produced with a small size distribution. Furthermore, the

addition of the Ag^+ ions was also an option to control the aspect ratio of NRs. When the volume of Ag^+ ions was less than 0.5 mL, the aspect ratio increased linearly with further addition of Ag^+ ions (4 mM).

The conjugates were synthesized with antibodies or antiserum (pAb or 2ºAS) and colloidal Au reduced by sodium citrate under the optimal conditions, appropriate pH of the Au colloids and minimum of the required antibodies or antiserum, were confirmed by titration. The antibodies and the blocking agent BSA on the Au surface caused red shifts of the plasmon resonance wavelength. During the synthesis, Au loss, estimated by the maximum absorbance of the plasmon resonance band, could not be avoided and it was much worse in the case of 2º AS-Au conjugates.

Chapter Three

Lateral flow immunoassay

3.1 Introduction

Strip tests are potentially cost-effective and easily performed assays providing more user friendly analysis than most laboratory based assays. Moreover, they can be brought to market extremely fast with a relatively small investment. The application of colloidal particles to strip was first reported in 1980 [23]. In recent years, lateral flow test strips as a popular diagnostic tool are commercially available for detecting hormones [23, 26], viruses [19, 106], toxic compounds [28, 29] and metabolic disorders [22]. In our study, the first sensing system developed with the Au NPs was based on this technique. To validate the developed immunoassays, Estriol-16-glucuronide (E3-16G) was chosen as analyte molecules.

E3-16G is a steroid derived from ovarian estradiol by hepatic hydroxylation and conjugation and has been proposed as an alternative urinary metabolite to estrone glucuronide for the monitoring of ovarian function [107]. Metabolism of estradiol produces three estriol glucuronides shown in Fig 3-1, one conjugated at

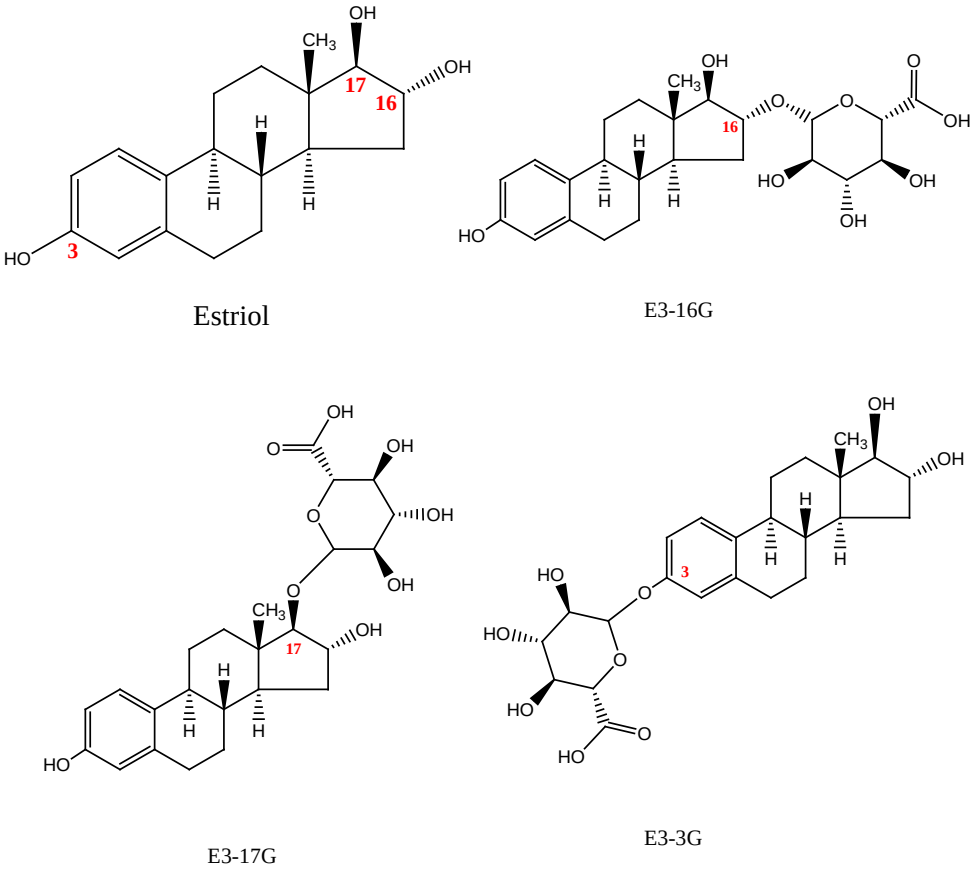

Fig 3-1: Chemical structures of Estriol, E3-16G, E3-17G and E3-3G

position 3, one at position 16 and one at position 17. Of the three, E3-16G is the preferred metabolite for monitoring fertility since it is excreted rapidly whereas the 3 glucuronide undergoes a complex entero-hepatic re-circulation before excretion and hence is delayed with respect to E3-16G [108]. E3-16G is also produced by the feto-placental unit during pregnancy and is the predominant estrogen in the urine of pregnant women increasing in parallel with the healthy growth of the foetus [109]. E3-16G has also been associated with breast cancer [110].

For the determination of E3-16G in liquid samples, here we represent the lateral flow strip sensor developed using the Ab-Au conjugates which were introduced in chapter two. Instead of full strips, where all reagents are present in dried form, here the assays were developed with half strips for which the part used to attach a sample pad and conjugate pad was cut away. Details for preparation of

the half strips are described in Appendix I 4.3.1. The sample and conjugate were introduced by dipping the half strip into a premixed solution, usually in a well of a microtiter plate.

A major aim of our study with LFIA was to develop a non-laboratory urinary hormone assay, therefore urine samples were collected both from pregnant and non-pregnant female volunteers to validate the use of LFIA with clinical samples. All urine samples were collected overnight or at any convenient time during a day but the collection period was an interval of a minimum of 3 hours. The minimum collection period of 3 hr was specified to reduce error caused by unpassed urine [111]. Depending on the duration of the collection period and the volume of urine passed over this period, all urine samples were diluted using tap water to represent a constant urine excretion rate of 150 mL/hr (i.e. 3.6 L/24 hr). The diluted urine was thoroughly mixed and approximately 2 mL was added to a 3 mL plastic tube and then stored in a freezer (-20 ºC) [112]. Samples collected as described are referred to as time-diluted samples. The aim of using time diluted urinary samples is to minimize variations in urine volume with time and in the pipettes used for dispensing fluid volumes, and hence to guarantee an accurate reflection of hormone production [111]. The concentration used to describe the time diluted urinary samples is nmol/24 hr which includes information of time, volume, and concentration. A common unit used in SPR experiments is g/L. The unit of nmol/24 hr is converted to g/L by converting it firstly to nM by dividing by 3.6 L/24 hr, and then multiplying by the molecular weight of E3-16G (464.15 g/mol), namely

$$\text{nmol/24 hr} = (\text{nmol/24 hr}) / (3.6\ \text{L/24 hr})$$

$$= 0.278\ \text{nM} \times 464.15\ \text{g/mol}$$

$$= 0.129\ \text{ng/mL}$$

Matrix effects are quite common in applications of immunoassays since modern methods usually require no cleanup or pretreatment for the aqueous

samples. Matrix effects in urine are serious since urine has much more variable composition than does serum or plasma. Potentially all direct urinary immunoassays for steroid glucuronides and blood assays for steroids are subject to matrix effects particularly at low analyte concentrations [113, 114]. A blank urine sample, so called analyte free urine, would be desirable to assess matrix effects in the immunoassay. Urine collected from a 2 years and 11 months aged young girl was used in the present work as a blank based on the belief that the amount of E3-16G in the urine of a little girl should be quite low and the urine can be treated as E3-16G free.

3.2 Lateral flow immunoassays

Considering the low molecular weight of E3-16G (465 Da), competitive assays, in which an analyte-protein conjugate (E3-16G-BSA) as test line is sprayed onto commercial nitrocellulose cards, were developed with two different signal generators. The binding of the small molecule (E3-16G) to the nitrocellulose membrane was affected by the polymer molecule BSA due to its multiple binding sites (amine group). The actual model of binding of proteins to nitrocellulose is not well understood. The E3-16G-BSA conjugates were sprayed onto a nitrocellulose membrane as a test line (as capture materials) in all formats as shown in Fig 3-2 and Fig 3-3.

The first format is a one-step assay using a pAb-Au conjugate as the signal generator and the 2ºAS located above the test line as the control line. Fig 3-2

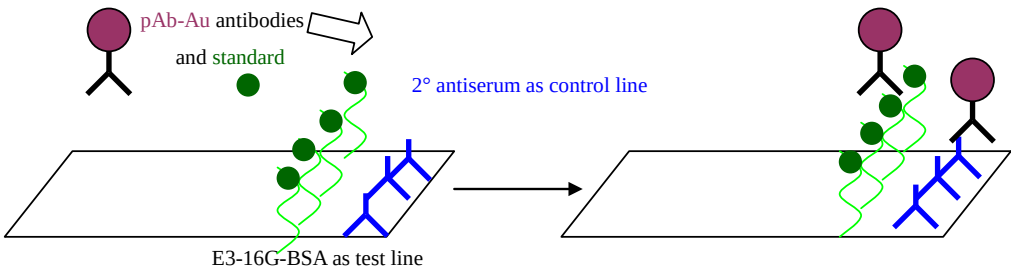

Fig 3-2: One-step assay developed with pAb-Au conjugates. E3-16G-BSA ( ) and 2°antiserum ( ) serve as test and control lines. The pAb-Au is represented with , the free E3-16G is shown with .

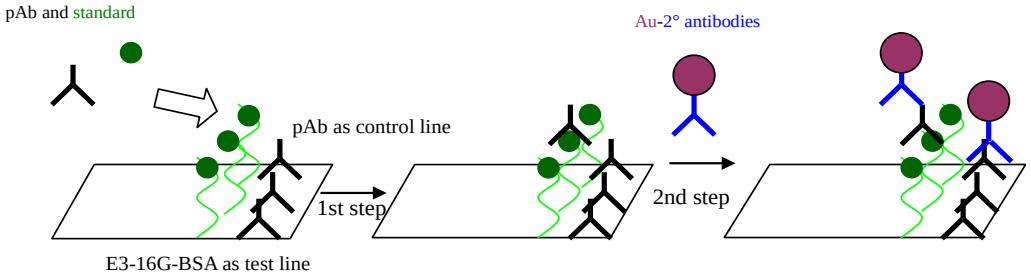

Fig 3-3: Two-step assay developed with 2°AS-Au conjugates. E3-16G-BSA ( ) and pAb ( ) serve as test and control lines. The pAb-Au is represented with , the free E3-16G is shown with . The mixtures of free standards and pAb are run first, followed by the 2°AS-Au conjugates.

shows that mixtures including the pAb-Au conjugates and free E3-16G standards of different concentrations, are going to compete with the E3-16G-BSA located at the test line for binding of the antibody when applied to the strip. As a result, the pAb on the Au surface becomes partially neutralized, the extent depending on the concentration of analyte, and hence the numbers of the pAb-Au captured by the E3-16G-BSA are reduced and the line intensity decreases as a function of analyte concentration.

In the second format (Fig 3-3) tests are carried out in two steps using 2ºAS-Au conjugates. In the first step, the pAb solutions mixed with an appropriate standard series are run first. Due to the competition between the E3-16G-BSA at the test lines and the free E3-16G of different concentrations present in mixtures, different amounts of pAb are left un-neutralised and hence able to be located at the test line. As a result, a new test line is formed containing a mixture of unbound E3-16G-BSA and E3-16G-BSA-pAb (in Fig 3-3). The latter complex can capture the 2ºAS-Au conjugates in a following step and produce a red band whose intensity is inversely proportional to the E3-16G concentration. The excess 2ºAS-Au conjugates were captured by pAb sprayed at the control line. Finally, the signals are given by the 2º AS-Au œnjugates.

The intensity of the control and test line on strips is quantified with an in-house system, strip reader 2.00, using the images obtained with a photoscanner (Fig 3-4). For statistical analysis, the absolute intensity of the test line or the ratio

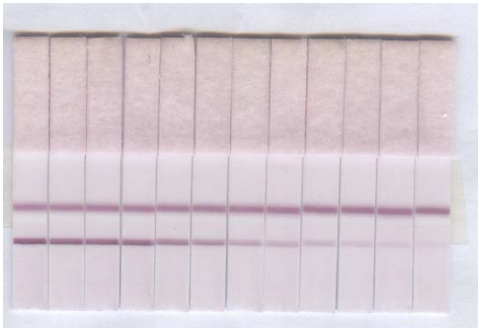

Fig 3-4: Strip tests performed using a series of standards (12 different concentrations). The image was obtained with a photoscanner.

of the intensity of the test line to the sum of the control and the test line (T / (T+C)) are generally plotted versus log-scale concentration of the standards with the graphic package of GraphPad Prism 5. The fitting equation is a Boltzmann Sigmoidal plot. For the discussion of the standard curves, three important parameters are the IC_{50}, defined as the concentration giving half-maximal effect, EC20 and EC80, defined as the lowest and highest concentration that can be distinguished from background noise [115]. As an important datum, the IC_{50} indicates the most accurate working area of an assay and is given as a parameter with the curve fitting from software. The EC20 value describing the low limit of detection is commonly represented as LOD. The linear range between LOD and EC80 is denoted as the working range. To compare data sets on different scale, standard curves are normalized by dividing all data of a set with the maximal datum of the set. By this way, all data sets can be brought to a common scale.

3.2.1 Assays developed with pAb-Au conjugates

For investigation of the assays developed with the pAb-Au conjugates, several conjugates were synthesized and then tested using the strips (Appendix I 4.3.2.1-A). Fig 3-5 depicts normalized standard curves with two pAb-Au conjugates introduced in chapter two, for which the nominal pAb concentrations were calculated to be 73 and 187 µg/mL. Both of them were plotted with mean ± SD of duplicate measurements of 12 standard samples spiked in 10 mM Tris-maleate (TM) buffer (pH=7). The IC_{50} of the curve (a) performed with

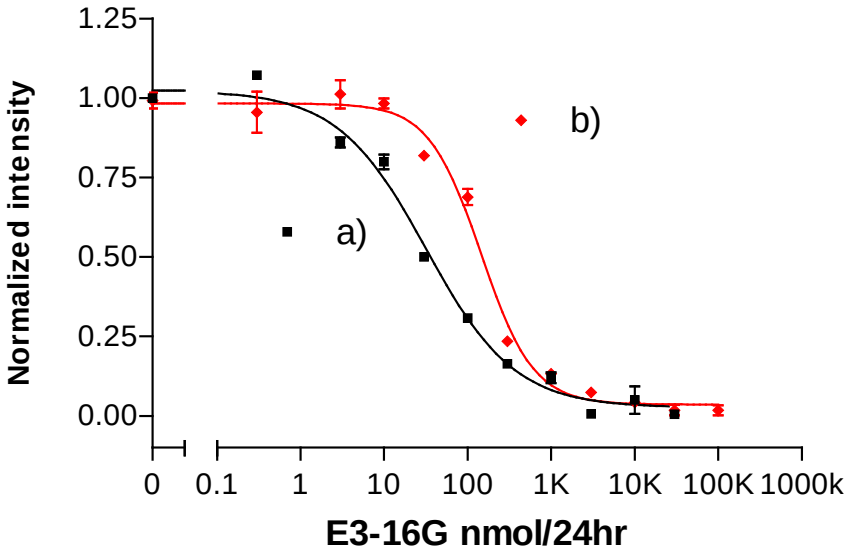

Fig 3-5: Standard curves performed using pAb-Au conjugates, for which the concentrations of pAb were 73 µg/mL (■) and 187 µg/mL (◆), and the standards of E3-16G spiked in TM buffer. All values shown here are mean ± SD from duplicate measurements of each sample.

conjugates containing less pAb (73 µg/mL) was 25.1 nmol/24 hr which was much lower than that of curve (b) (IC_{50} = 145.3 nmol/24 hr). The slope of the linear range shown in the curve (b) is quite high resulting in a relatively narrow working range (53.6 – 394.5 nmol/24 hr) compared to the curve (a) (3.7 – 176.0 nmol/24 hr). The lower $IC_{50,}$ lower LOD and wider working range of curve (a) suggest that the sensitivity of the one-step assay can be improved by using the conjugates containing less coating pAb. Baker (1979) [116] showed that the mean value of the mid cycle peak of E3-16G excretion in a normal human menstrual cycle using a direct radioimmunoassay method was approximately 75 nmol/24 hr. Therefore, the assays performed with both conjugates may be applied in principle to clinical samples.

Before using the assays to measure urinary samples, the urine matrix effects in the format were assessed and corrected with urine collected from a young girl, which was used as a blank standard with low concentrations of endogenous steroids (blank urine). Experimental details see Appendix I 4.3.2.1-B.

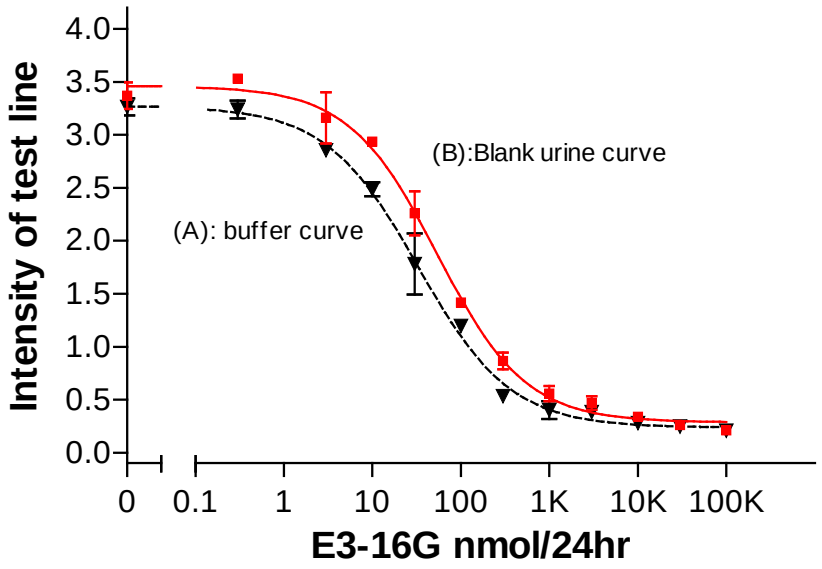

Fig 3-6**:** Urine blank (■) and buffer (▼) standard curves obtained from test strips, calibrated with duplicate measurements. Error bars represent the SD of the measurements.

Fig 3-6 shows two standard curves performed with E3-16G standards spiked in 10 mM TM buffer and the blank urine (pH=6.77). Both curves were plotted with the mean ± SD of duplicate measurements. Surprisingly, the presence of the blank urine led to a higher intensity of the colour on the test strips that was expected to be lowered due to the presence of some E3-16G in the urine samples no matter how diluted they are. For the buffer curve, the linear regression range (working range) was from 5.2 to 153.7 nmol/24 hr (R^2=0.99) with an IC_{50} value of 33.1 nmol/ 24 hr. For the curve in the presence of urine, the working range was between 11.1 nmol/24 hr and 266.8 nmol/24 hr (R^2=0.99) with an IC_{50} of 54.2 nmol/24 hr. The intra-assay (within assay) coefficient of variation (CV : Standard Deviation divided by the mean and multiplied by 100 %) was lower than 15 % (buffer curve) and 13.7% (blank urine curve).

The pH of the time-diluted blank urine was lower than that of the TM buffer. Thus, to study the pH-dependence of the matrix effect of the blank urine, four samples containing zero standard (i.e. the concentration of the analyte is zero) spiked in blank urine of different pH values were tested in triplicate (Table 3-1). The test line intensities of the strips were compared with that obtained with the zero standard spiked in TM buffer and showed that the higher intensity of the test

Sample information	TM buffer pH=7.10	Urine blank pH=6.77	Urine blank pH=5.00	Urine blank pH=9.00	Urine blank pH=7.10
Intensity	0.81 ± 0.08	1.06 ± 0.12	0.98 ± 0.08	1.06 ± 0.04	1.01 ± 0.10
CV (%)	9.34	11.52	7.80	3.59	9.67

Table 3-1: pH dependence study of the urine matrix effect in the first format. Intensity of each sample is explained as mean ± SD of duplicate measurement and the CV is intra-assay CV.

Sample information	TM buffer pH=7.10 C=2.17mS	Urine pH=7.10 C=3.48mS	Urine pH=7.10 C=2.18mS
Intensity	2.06 ± 0.07	2.08 ± 0.11	2.16 ± 0.04
CV (%)	3.54	5.45	1.65

Table 3-2: Conductivity (C) dependence study of the urine matrix effect in the first format. Intensity of each strip is explained as mean ± SD of duplicate measurement and the CV is intra-assay CV.

line in the presence of the blank urine was independent of the pH of the blank urine.

Furthermore, the conductivity of the urine blank and the 10 mM TM buffer was measured and it was found that the conductivity of the urine blank was 3.45 mS which was higher than that of TM buffer (2.17 mS). To investigate the conductivity dependence, the experiment was carried out in triplicate using three zero standard samples present in different solvent surroundings shown in Table 3-2. The test line intensity seems to be independent of the solvent surroundings and no evidence was found that suggested the urine matrix effect could be reduced by keeping a consistency of the conductivity. Although the urinary matrix effect was not removable in the one-step format, the changes caused by the presence of blank urine was still acceptable since the two standard curves were almost parallel.

In a preliminary evaluation of the reproducibility of the test strips and the reliability of the synthesis of the Au-pAb conjugates for applying the first format to real samples, two sets of conjugates were synthesized with different amounts of pAb (3 of each set) and tested with strips cut from six different membrane cards. A set of six standard curves was generated with each conjugate and the LOD, IC_{50}

Conjugates	Set A (C_{pAb} = 187 µg/mL)				Set B (C_{pAb} = 73 µg/mL)			
	Conj A1	Conj A2	Conj A3	Inter-CV	Conj B1	Conj B2	Conj B3	Inter-CV
IC_{50} (nmol/24hr)	121.9	121.1	116.0	2.67%	24.37	25.12	28.78	9.04%
LOD (nmol/24hr)	43.44	37.87	40.83	6.85%	2.55	3.69	5.20	34.86%

Table 3-3. Reproducibility of test strips and synthesis of the conjugates. Two sets of conjugates (3 each) were synthesized with pAb. The concentration of pAb was estimated to be 187 µg/mL in set A and 73 µg/mL in set B. All IC_{50} and LOD values shown in table are mean value of triplicate performances. Inter-CV of IC_{50} and LOD were calculated using the mean value of three standard curves performed with three different membrane cards.

and the inter-assay CV (CV of assays run on different days) of the six conjugates were computed and shown in Table 3-3. For the conjugates of set A, the highest intra-assay CV (not shown) was 9.6 %, the inter-assay CV of the LOD (40.7 ± 2.8 nmol/24 hr) and IC_{50} (119.7 ± 3.2 nmol/24 hr) were 2.7 % and 6.9 % respectively. For the tests carried out with the conjugates of set B, the intra-assay CV was in the range of 0.2 % to 11.9 % (not shown), the inter-assay CV of the LOD (3.8 ± 1.3 nmol/24 hr) and IC_{50} (26.1 ± 2.4 nmol/24 hr) were 9.0 % and 34.9 % respectively. These data demonstrate the high stability and reproducibility of the LFIA format using the pAb-Au conjugates as signal generators. The lower LOD and IC_{50} of the set B conjugates showed that the assay sensitivity was improved by applying a lower concentration of the pAb coating as could be expected. Thus conjugates B were used for the generation of the standard curves and measurement of the E3-16G excretion rates in the collected urine samples.

3.2.2 Assays developed with 2˚antiserum-Au conjugates

Another format was developed using 2ºAS-Au conjugates and tests were carried out in two steps. The mixtures of pAb and a series of standards (in TM buffer) were applied to the test strips and followed by the application of 2ºAS-Au conjugates (Appendix I 4.3.2.2).

For the same series of standards, the higher the concentration of the pAb, the more molecules can bind to the test line, hence the more 2ºAS-Au conjugates can be captured and more intense the test line is. However, the presence of more pAb

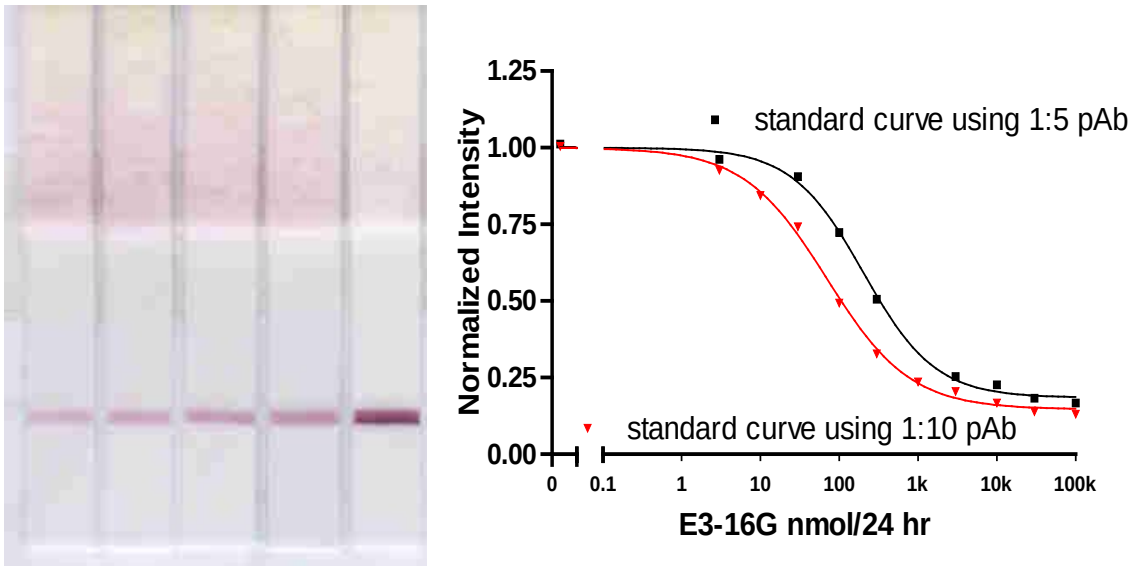

Fig 3-7: a) Strip tests for the determination of the correct dilution factor (left to right: 1:1, 1:2, 1:5, 1:10 and buffer) of the pAb introduced in the first step. b) Two standard curves performed using 1:5 pAb (■) and 1:10 pAb (▼) in the first step. The data shown here is the average of duplicate measurements.

reduced the sensitivity of the assay. Therefore, an optimum concentration of pAb, guaranteeing both the intensity of the test line and the sensitivity of the assay, has to be determined. The experiments were carried out using strips, of which the test line was pAb and with no control line. Mixtures containing the 2°AS-Au conjugates and different dilutions of pAb (1:1, 1:2, 1:5, 1:10 and TM buffer) were pipetted to sample wells. The competition between the pAb present in the mixtures and the pAb sprayed at the test line caused different amounts of neutralized 2°AS-Au conjugates due to the different pAb concentrations, and thus intensity at test lines was different (Fig 3-7 a). The test line intensity is required to be around 1.0-1.5, therefore the dilutions of 1:5 and 1:10 were appropriate. They were further investigated by processing the two-step tests with the two dilutions of pAb chosen for the first step. Fig 3-7 b) suggests that the curve performed with the pAb of lower concentration (1:10 dilution) was more sensitive with a IC_{50} of 69.5 nmol/24 hr compared to the curve performed using 1:5 diluted pAb with a IC_{50} of 202.5 nmol/24 hr. Not only the IC_{50}, but also the LOD was improved by using the pAb of lower concentration in the first step, from 58.5 (1:5 dilution) to 13.4 nmol/24 hr (1:10 dilution). In the early stage of the work, the two dilutions of

pAb were tested for several times using the conjugates from different batches. All data suggested that the sensitivity of the two-step assay was improved by reducing the amount of pAb in the first step. This is easily understood. If the pAb used in the first step is too concentrated, then not only the free E3-16G in solution completely bound but also all the E3-16G-BSA at the test line is bound by the pAb. Therefore, the test line totally changes to pAb-E3-16G-BSA which can capture the entire 2ºAS-Au conjugates in suspension and hence lower the sensitivity of an assay. For further investigation, the dilution of 1:10 was used.

In the experiments, two different sized Au colloids, indicated by the plasmon resonance wavelengths of 530 and 537 nm, were used for the synthesis of the conjugates with the same amount of coating 2ºAS in each case. Fig 3-8 depicts two normalized standard curves related to the two conjugates and shows that the assay carried out with the conjugates synthesized using bigger sized Au NPs is more sensitive, with an IC_{50} of 44.5 nmol/24 hr which was only half of 81.3 nmol/24 hr (the IC_{50} of the curve using the conjugate synthesized with smaller NP). Furthermore, the working range was wider. Thus, it could be concluded that

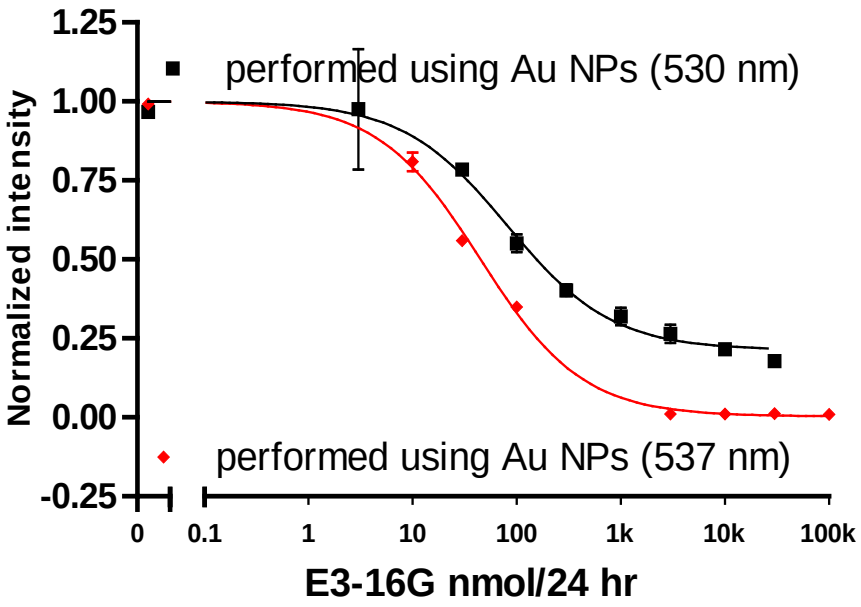

Fig 3-8: Standard curves performed using the conjugates synthesized with different sized Au NPs for which the plasmon resonance wavelengths were 530 nm (■) and 537 nm (◆). The data shown here is the mean ± SD of duplicate measurement.

larger sized Au NP improved the sensitivity and broadened the working range in this format.

The influence from the concentration of the Au suspension was investigated with two conjugates which were synthesized using the Au NPs of different concentrations (0.25 mM and 1 mM) with the same amount of antiserum. The IC_{50} of the standard curves (not shown here) performed with the two conjugates were 88.8 and 81.3 nmol/24 hr, respectively. The comparable IC_{50} values of the two standard curves indicated that the assay sensitivity (IC_{50}) was unlikely to be dependent on the concentration of the Au suspension. Considering the strong dependence on the concentration of coating pAb of the assay sensitivity in the one-step format, the concentration of the 2°Ab in the antiserum for stabilizing the Au NPs was investigated as well (standard curves not shown). Unlike the first format, there was no clear dependence on the concentration of the 2°Ab in the antiserum. That means the assay sensitivity in the second format was only clearly dependent on the concentration of the pAb introduced in the first step. Therefore, the concentration of the 2°Ab only needed to be sufficient to stabilize the Au colloids. Based on this conclusion, the concentration of the 2°Ab in the final samples was kept at 91 μg/mL.

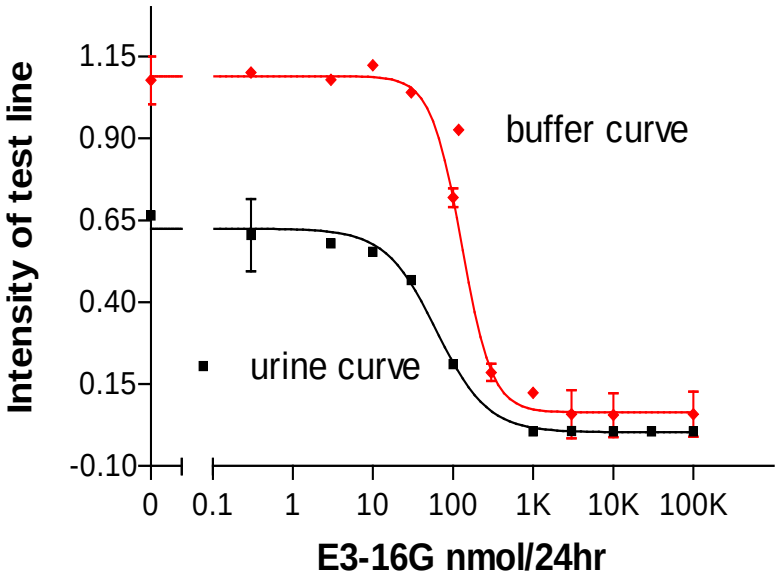

Fig 3-9: Buffer (◆) and urine blank (■) standard curves obtained from test strips calibrated with duplicate measurements. Error bars represent the SD of the measurements.

In the second assay format, the matrix effect of the urine samples was estimated by comparing the standard curves (Fig 3-9) obtained with the TM buffer and the urine blank, respectively. In the standard curve performed with the TM buffer, the test line intensity of the zero standard was 1.1 and it was reduced to 0.6 by the presence of the blank urine. This phenomenon was different from that observed in the one-step format (Fig 3-6), where the test line intensity change caused by the blank urine was increased about 5 % (from 3.3 to 3.5). In addition, the presence of the urine shifted the IC_{50} from 127.6 to 61.9 nmol/24 hr (nearly half) along with changing the shape of the standard curve (non-parallelism). All of these facts demonstrated that the format developed with 2ºAS-Au conjugates was not suitable for the determination of E3-16G in urine samples.

3.3 Application of LFIA

Based on the above discussions, the determination of E3-16G in urine samples was carried out with the first format using pAb-Au conjugates. In order to validate the application, urinary samples collected both from pregnant (Volunteer C) and non-pregnant women (Volunteer A and B) were tested using the pAb-Au conjugates with the smallest concentration of coating pAb (73 μg/mL). The excretion in the samples was calculated with a standard curve performed with test strips cut from a membrane that was also used for the sample measurement.

The accuracy of the strip assay (Appendix I 4.3.2.1-C) was determined by measuring three control samples spiked in the blank urine, of which the concentrations were known to be 10, 30 and 50 nmol/24 hr. The data calibrated from the reference standard curve (urine curve in Fig 3-6) were compared to the known concentrations to validate the accuracy of the assay. The ratio of the value of the measured concentration over the known spiked concentration of E3-16G is defined as the recovery (R) and is expected to be in the 90 % to 110 % range. The recoveries of these three controls from the strip assay were from 97 % to 120 % (Table 3-4) and were acceptable with the possible exception of the 10 nmol/24 hr

Spiked E3-16G (nmol/24 hr)	Lateral flow test		
	Mean ± SD (nmol/24 hr)	Recovery (%)	Intra-assay CV (%)
10 nmol/24 hr	12.04± 1.9	120	15.9
30 nmol/24 hr	29.2 ± 3.3	97	11.4
50 nmol/24 hr	49.2 ± 3.1	98	6.4

Table 3-4: Recovery and precision of the LFIA. The mean value, SD and intra-assay CV were obtained with triplicate measurements.

control value. This sample had an apparent absorption value that was close to the lower end of the straight-line portion of the calibration curve (shown in Fig 3-6) which may explain the higher recovery (120 %) and greater variance (16 %).

The assay was firstly used to assess the excretion of E3-16G in a menstrual cycle which was contributed by volunteer A. The pattern of the excretion of 30 days is depicted in Fig 3-10. The excretion through the cycle was in a range of 0.2 (day 5) to 9.2 nmol/24 hr (day 17) which is much lower than the anticipated values as previously reported by Baker et al. [116]. This was presumed to be due to the matrix effects of the adult urine sample being different from that from the child's urine, and hence the blank urine standard curve being inappropriate for the samples. To verify the result shown in Fig 3-10, another cycle volunteered by non-pregnant woman (B) was tested according to the same procedure with the same conjugates. The excretion rates for the second menstrual cycle (not shown) gave a maximum excretion rate on the peak day of 11 nmol/24 hr which is close to the peak data shown in Fig 3-10. The excretion rates reported by the strip sensor were mainly out of the linear regression range (11.1 to 266.8 nmol/24 hr) of the blank urine calibration curve, and therefore the intra-assay CV was high and the reported data lacked accuracy.

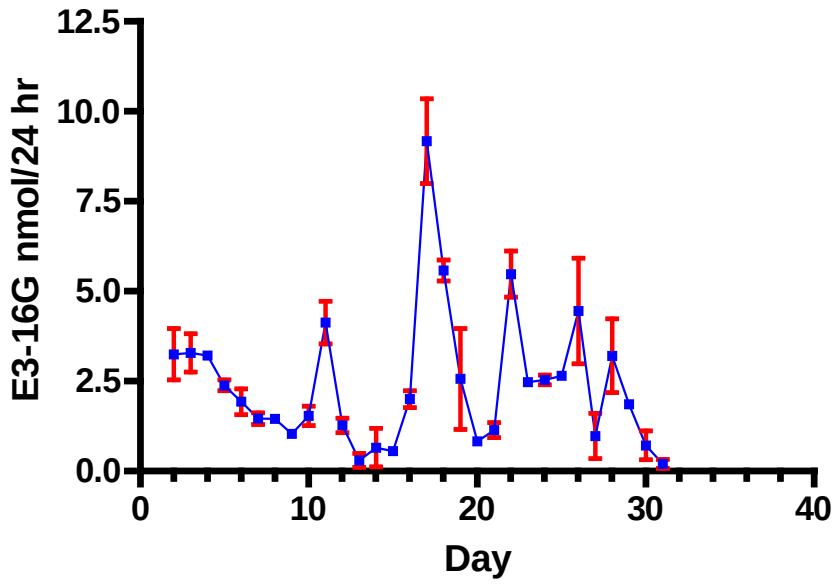

Fig 3-10: E3-16G excretion pattern obtained using the LFIA strips (■). The mean intra-assay CV of strip pattern are 11.7 ± 8.8 %. All values are mean ± SD from triplicate measurements of each sample.

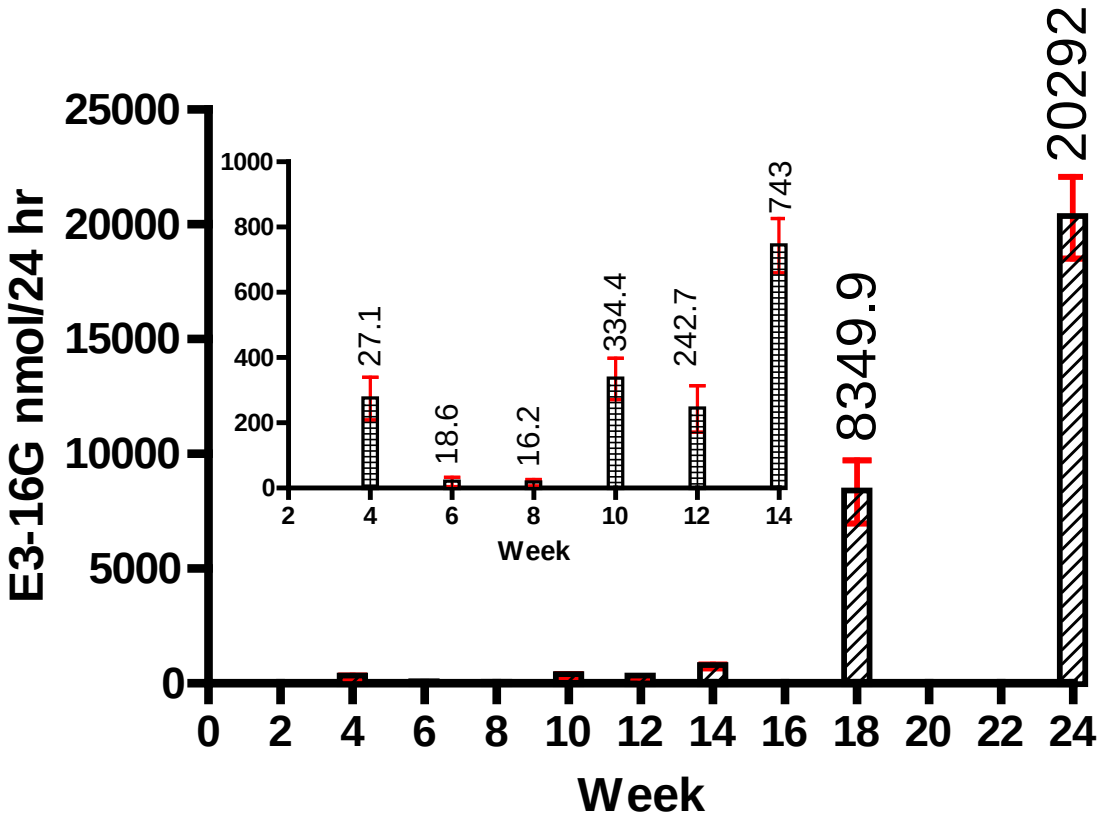

Fig 3-11: Excretion rates of E3-16G during the first and second trimester determined using the test strips. All values are mean ± SD from triplicate measurements of each sample.

Besides the application to urinary samples from a normal menstrual cycle, the strip sensor was also applied to test eight weekly urine samples from the first two trimesters of a pregnant woman (volunteer C). The daily production of E3-16G before delivery is some 2000 fold greater than normal menstrual cycle luteal-phase excretion levels [116]. Thus, the analyte concentration of urine samples from pregnant women vastly exceeds the working range of the calibration curve shown in Figure 3-6 (11.1 nmol/ 24 hr to 266.8 nmol/24 hr). Thus, the determination of E3-16G in these samples necessitated pre-dilution. Samples of week 4 and 10 were diluted 1:10, samples of week 6 and 8 were diluted 1:5, sample of week 12 was diluted 1:50 and samples of week 14, 18, 24 were diluted 1:100. Figure 3-11 shows the pattern of E3-16G excretion throughout the first and second trimester of the pregnancy. The insert displays the pattern for week 4 to week 14 since the excretion of E3-16G in the first trimester was much lower than that in the second trimester and hence a separate scale is necessary for these data. The excretion of E3-16G in the first trimester was much lower than that in the second trimester and there are two intervening lower values between week 4 and week 10 which were reported to be 18.6 (week 6) and 16.2 nmol/24hr (week 8) respectively. The data clearly show how the excretion of E3-16G rises steadily from week 14 onwards.

3.4 Conclusion

Two assay formats were developed using the LFIA technique. In the first format, a sensitive and repeatable lateral flow assay was achieved with a LOD of 3.8 ± 1.3 nmol/24 hr in time diluted urine using a low coating concentration of the pAb, which has not been reported before in this format. However, the unavoidable matrix effects of the adult female urine samples masked the response to E3-16G, and precluded its application for monitoring menstrual cycle levels of E3-16G. But the application to urine samples of pregnant women was successful and revealed the increasing tendency of E3-16G levels in urine from the end of second

trimester during pregnancy. Although the two-step assay performed with 2°AS-Au conjugates showed the potential to be used with clinical samples, the big difference of the standard curve caused by the presence of the blank urine, including the apparent absorbance, the IC_{50} and the standard curve shape, precluded its use for analysis of the clinical samples.

Compared with other immunoassays, such as radioimmunoassay and enzyme-linked immunoassay, LFIA is potentially superior with respect to its overall speed and simple sample preparation. These characteristics make the LFIA-based test strip described here an ideal candidate for further development of a portable and hand-held detection kit that helps pregnant women to monitor fetal growth at home. This development is being carried out in a parallel study.

Chapter Four

SPR Biosensor-based immunoassay

4.1 Introduction

The strip sensors developed with the LFIA technique were semi-quantitative. For quantitative results, the second sensing system was developed using SPR technique relying on plasmonic resonance and high density of Au. Estriol-16-glucoronide (E3-16G, referred to page 41 to 42) was kept as analyte molecules for later comparisons with the LFIA sensing system. Compared to the methods reported previously, such as, radioimmunoassay (RIA) for E3-16G using [^{3}H] [117] or [^{125}I] [118] labeled radio ligands, high pressure liquid chromatography (HPLC) [119], and liquid chromatography (LC) coupled with fluorescence measurement [120], mass spectrometry (MS) [121] or UV spectrophotometry [122], the limit of detection (LOD) of the SPR sensing system is sufficiently low (compared to RIA assay) even for detections of environmental concentrations [123] along with simple sample preparation (compared to RIA, HPLC, and LC/MS assay).

In this chapter, different quantitative formats developed using an SPR

biosensor are presented including non-enhanced and enhanced assays for the determination of E3-16G in liquid samples. E3-16G was conjugated to ovalbumin (OVA) through an oligoethylene glycol (OEG) linker to form protein conjugates (E3-16G-OEG-OVA), which were then immobilized on a carboxymethyl dextran-coated sensor chip via amine coupling to develop inhibition immunoassays. Urinary samples from both pregnant and non-pregnant women were tested to validate the application of a SPR assay.

4.2 Development of SPR assays

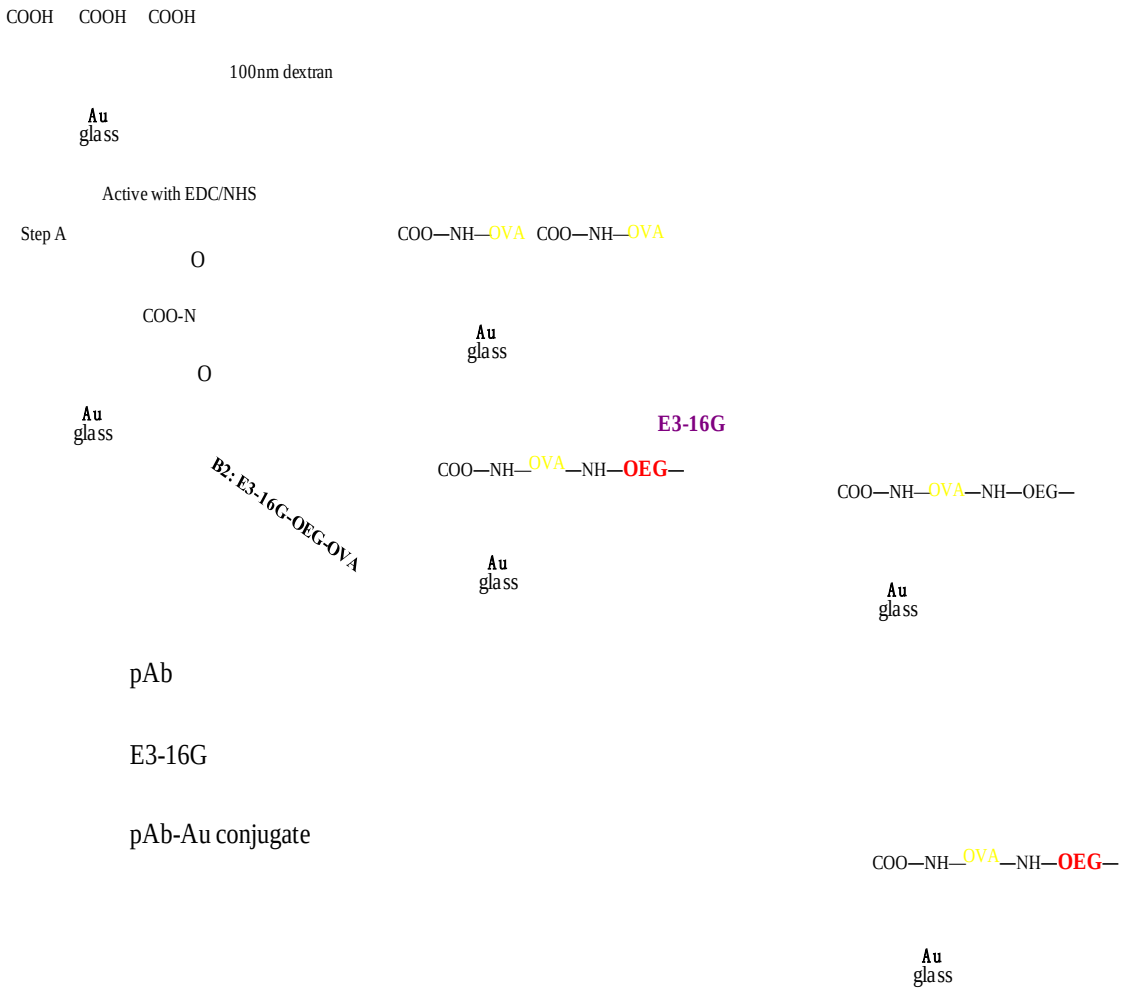

Fig 4-1: Development of biosensor-based inhibition assay. Step A represents the activation of the chip surface using EDC/NHS. Step B1 depicts immobilization of OVA onto the reference surface of FC1. Step B2 depicts the coupling of E3-16G-OEG-OVA ligands onto the chip surface of FC2. Step C1 and step C2 describe the developments of non- and enhanced assays respectively. Here the described enhanced assay is the one developed with pAb-Au conjugates.

For the development of an SPR immunoassay (model described in Fig 4-1), two flow cells (FC) are required in general, a reference FC (FC1) and a binding FC (FC2). The reference FC measures the non-specific binding of analytes to the chip surface. In the binding experiments, samples were passed over both FC1 and FC2 and responses were measured by subtracting the reference response (binding at FC1) from the binding response collected from the reaction surface (FC2). Thus, the results represented only the specific binding to the chip surface. A dextran layer around 100 nm is coupled to the surface of the chip used currently, providing sufficient carboxylic acid groups. These groups can be activated (step A) by a 1:1 (v/v) mixture of 0.4 M 1-ethyl-3-(3-dimethylaminopropyl) carbodiimide in water and 0.1 M N-hydroxysuccinimide in water (i.e. EDC/NHS). In the next step (step B), OVA molecule and the synthesized ligand of E3-16G-OEG-OVA are coupled covalently onto the activated surfaces of FC1 and FC2, respectively. Then (step C), both non-enhanced and enhanced immunoassays were developed with pAb (step C1) and pAb-Au conjugates (step C2). Details for each step will be discussed later.

4.2.1 Synthesis of E3-16G-OEG-OVA conjugates

Due to the relatively small size of the E3-16G molecule (464.51 Da), it was linked chemically to OVA via a 23-atom polyethylene oxide spacer to reduce steric effects on the chip surface and to promote extension away from the surface thus facilitating antibody binding (Appendix I 4.4.1). OVA was chosen as the carrier molecule because it contains multiple amino acid residues for linking with E3-16G-OEG and it also allows for efficient immobilization of the conjugate (E3-16G-OEG-OVA) onto the chip surface through amine coupling. The E3-16G density on the chip surface was approximately 11 steroid moieties per OVA molecule, estimated by the worker who synthesized the conjugate [98]. The extended 23-atom long OEG as a spacer molecule lowered non-specific binding of the antibodies or antibody-Au conjugates to the dextran surface [98, 99]. An advantage of binding the OEG-OVA conjugate to the sensor surface rather than

the antibody-E3-16G was the high stability of the resulting surface [124]. Regeneration conditions are quite harsh and multiple exposure of the surface to these conditions damages the structural integrity of the antibody binding sites. On the other hand denaturation of OVA molecules is irrelevant since functional properties are not being utilized. The capability to bind antibodies or antibody-gold conjugates showed no significant drop in sensor response after more than 1000 binding/regeneration cycles, when OVA conjugates were used bound to the sensor surface.

4.2.2 Immobilization of ligands onto the CM5 chip surface

Sodium-acetate buffer (10 mM) as diluent was used to prepare solutions of the ligand for immobilization. The pH of the sodium-acetate buffer played an important role in this step, as explained with Fig 4-2. If the pH of the buffer is lower than the pK of the dextran matrix (left image), both the dextran and the ligands are positively charged, therefore the ligands can not be immobilized. If the pH of the buffer is higher than the pI of the ligands (right image), both the ligands and the dextran are negatively charged, thus no ligands are coupled to the surface either. The ligands can be immobilized successfully only when the pH of the buffer is between the pK of the dextran and the pI of the ligands (middle image). The experimental procedures are described in Appendix I 4.4.2.1.

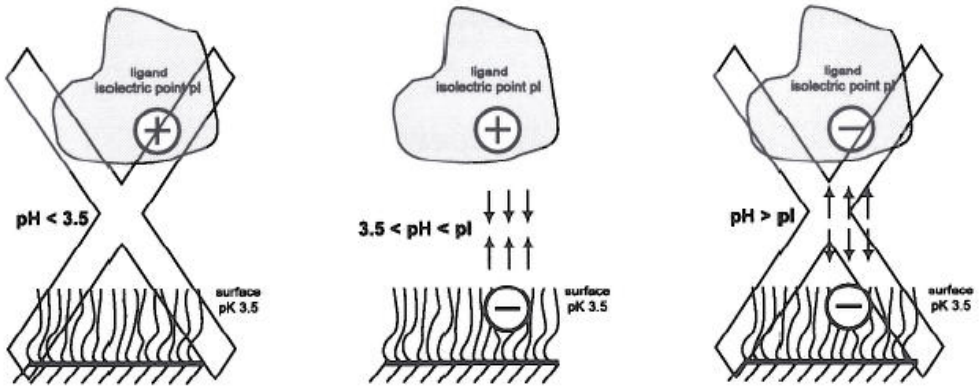

Fig 4-2: Buffer conditions for successful immobilization of ligands onto a CM5 chip surface. Left) pH of the buffer lower than the pK of the dextran layer. Middle) pH of the buffer between the pI of the ligands and the pK of the dextran layer. Right) pH of the buffer higher than the pI of the ligands. Picture from user manual.

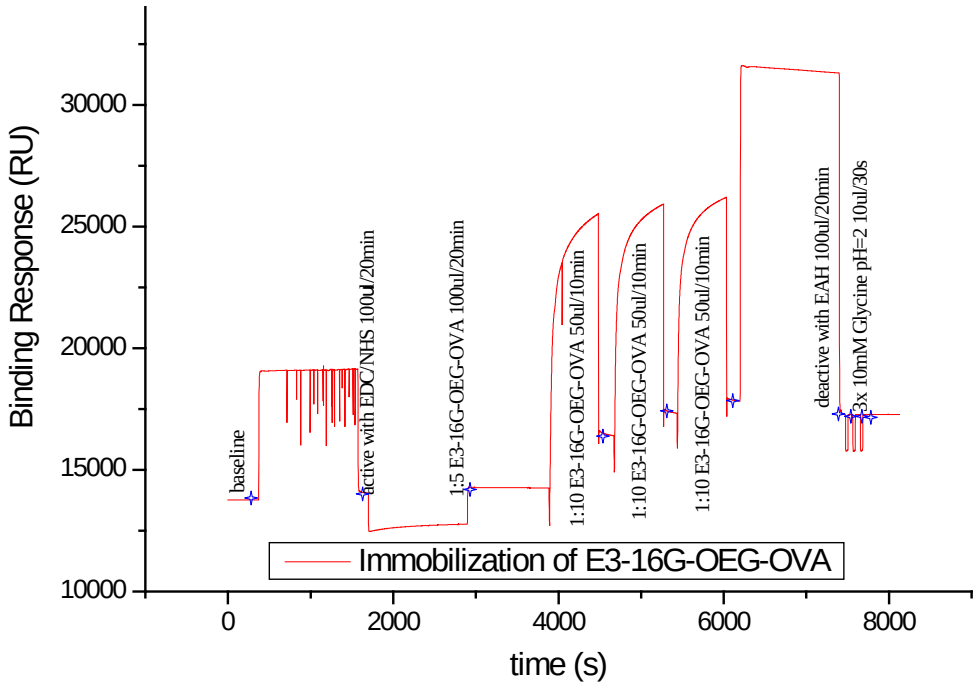

FC	time	Absresp	slope	baseline	RelResp	Id
2	366.5	13757.6	-0.02	yes	0	baseline
2	1608.5	14091.5	-1.24	no	333.9	EDC/NHS 100ul/20min
2	2930.5	14279.0	0.09	no	521.4	1:5 E3-16G-OEG-OVA 100ul/20min
2	4518.5	16543.4	-2.07	no	2785.8	1:10 E3-16G-OEG-OVA 50ul/10min
2	5308.5	17432.0	-1.35	no	3674.5	1:10 E3-16G-OEG-OVA 50ul/10min
2	6069.5	17907.3	-1.19	no	4149.7	1:10 E3-16G-OEG-OVA 50ul/10min
2	7436.5	17278.2	-4.67	no	3520.6	EAH 100ul/20min
2	7521.5	17268.5	0.13	no	3511	10mM Glycine pH=2 10ul/30s
2	7614.5	17273.8	-0.01	no	3516.2	10mM Glycine pH=2 10ul/30s
2	7704.5	17278.8	-0.08	no	3521.2	10mM Glycine pH=2 10ul/30s

Fig 4-3: Sensorgram for the process of activating the surface with EDC/NHS, immobilizing E3-16G-OEG-OVA with four injections, deactivating the surface using EAH and washing the surface with 10 mM Glycine (pH = 2).

Fig 4-3 shows a sensorgram (obtained from FC2) presenting processes related to activation of the chip surface, immobilizing ligands onto the chip surface, deactivation of the surface and cleaning of the chip surface. After the injection of EDC/NHS (100 µl over 20 min, i.e. 5 µl/min), the relative response (RelResp) was 333.9 RU suggesting a successful surface activation (according to instruction from supplier that the response is required to be higher than 200 RU). The immobilization of ligands was firstly performed with a solution of ligands diluted 1:5 (v/v) (100 µl/20 min). The resulting response was about 200 RU (= 521.4 – 333.9), indicating that only a few ligands were coupled to the chip surface (according to instruction that the immobilized level is at least around 1200 RU).

Next, a 1:10 (v/v) dilution of the ligand was tried. After the first 50 µl injection, the RelResp increased to 2275 RU (= 2785.8 - 521.4). The 10 times higher response indicated that too high a concentration of the solution lowered the efficiency of the immobilization. That was also supported by the fact that the response of 15 RU reported from FC1 corresponding to an injection of 100 µl 0.5 % OVA was much lower than the response of 1400 RU caused by 100 µl of 0.05 % OVA. The second and third 50 µl injections of a 1:10 dilution of E3-16G-OEG-OVA ensured enough ligands were immobilized on the chip surface. The redundant carboxylic acid groups were deactivated with ethanolamine-HCl (EAH) buffer of pH 8.5. The binding level was kept in a constant range (around 3510 RU) after three times washing with 10 mM glycine (pH=2) suggesting that immobilization of the ligands on the chip surface was stable.

4.2.3 Binding performance of pAb/pAb-Au conjugates on the chip surface

The purpose of this SPR sensing study is to create a calibration curve to determine the concentration of pAb/pAb-Au and the best injection time required for appropriate responses on the chip surface (Appendix I 4.4.2.2). One calibration series is required to include at least 5 samples of different antibody concentrations and a zero standard. In addition, at least one of these five samples needs to be tested in duplicate. In our study, a series of pAb samples of 7 different

pAb µg/ml	pAb performance				pAb in conjugates µg/ml	pAb-Au performance			
	Specific response (RU)			CV (100%)		Specific response (RU)			CV (100%)
10.0	287.1	289	285	0.70	*9.970*	*281.2*	*310*	*298.8*	4.89
5.0	138.7	139.0	137.0	0.78	4.990	193.9	194.8	194.3	0.23
2.5	77.8	80.1	80.8	1.97	2.490	119.4	119.5	120.3	0.41
1.0	37.6	38.7	39.6	2.59	1.250	71.2	70.1	70.3	0.83
0.5	24.3	24.8	25.3	2.02	0.623	39.8	39.0	41.1	2.65
0.1	11.3	10.9	11.6	3.12	0.312	23.5	24.2	24.1	1.58
0	2.2	2.8	2.8	13.32	0.156	14.4	14.2	14.8	2.11
					0.078	10.9	11.0	11.5	2.89
					0	3.1	3.1	3.4	5.41

Table 4-1: Binding response (FC2-1) according to the concentration of pAb in the samples. The pAb concentrations in the conjugates were estimated by the dilution factors (18.8, 37.5, 75, 150, 300, 600, 1200 and 2400). The specific response is the difference of binding on FC1 and FC2. CV shown here is the intra-assay CV of triplicate measurement.

concentrations and a series of pAb-Au conjugates with 9 different concentrations were used. The pAb concentration in the conjugates was calculated according to the dilution factors. Each sample was tested in triplicate (Table 4-1). For the pAb samples with concentrations in a range of 0 to 10 µg/mL, the binding performance on the chip surface was quite stable and was supported with a low intra-assay CV (≤ 3.12 %). When the conjugates for which the concentration of pAb was estimated to be 9.97 µg/mL were applied to the chip surface, the response showed a high fluctuation indicating non-reproducible binding. Considering the corresponding dilution factor of 18.8, it is suggested that the pAb-Au conjugates used currently have to be at least diluted 1:37.5 for reproducible response.

In Fig 4-4, the binding response is plotted versus the calculated pAb concentration assumed to be present in the samples. In both formats, the binding response was linear with increasing concentration of antibody in the samples. The higher slope of the calibration curve in the NPs enhanced format suggests that the response was improved by the increased mass due to the presence of the high

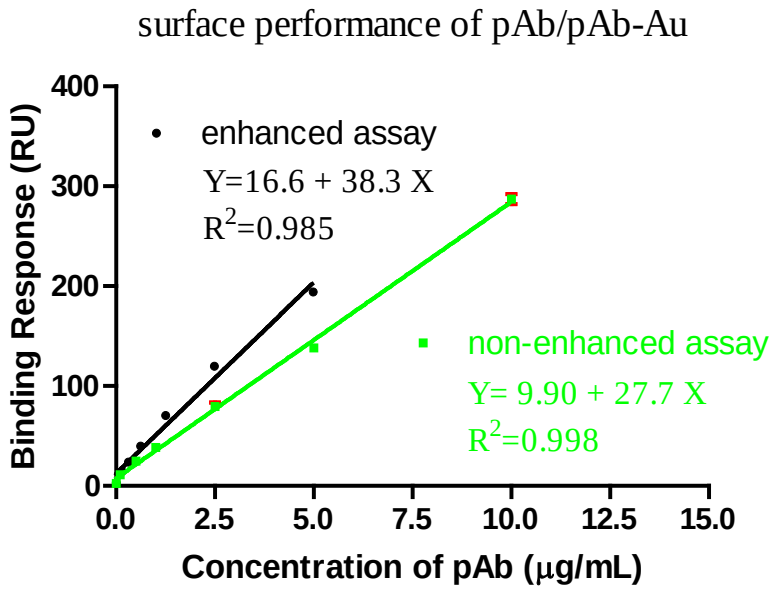

Fig 4-4: Correlation between the concentration of pAb in the samples and the sensor response. The regression line of antibody (■) was calculated by injecting pAb of 7 different concentrations. The regression line for antibody-Au (●) was obtained with measurements of 8 samples containing different concentrations of pAb. Each data point represents the mean and SD of three measurements.

mass probe of Au NPs, and therefore required less pAb for the same response. The ratio of the slope of the two linear regressions (enhanced assay / non-enhanced assay) suggests that for samples containing the same concentration of antibody the binding response could be theoretically enhanced 1.38-fold by conjugating the antibody to the Au NPs. To obtain the same level of response on the chip surface, less pAb was needed in the enhanced assay. As a result, the amount of the analyte required to saturate the pAb was reduced. Hence, this enhancement has the potential to give a more sensitive assay.

4.2.4 Inhibition assay developed with pAb

Firstly an SPR assay was developed using the biosensor response on binding of just the pAb (Appendix I 4.4.2.3). An advantage of this format was that the result could be obtained in less than 10 minutes. In addition, since only the pAb molecule was bound to the biosensor surface the distance from the chip surface to the analyte was minimized with a corresponding increase in the SPR signal. Fig 4-5 shows two standard curves performed with solutions containing concentrations of 5 µg/mL and 1 µg/mL pAb.

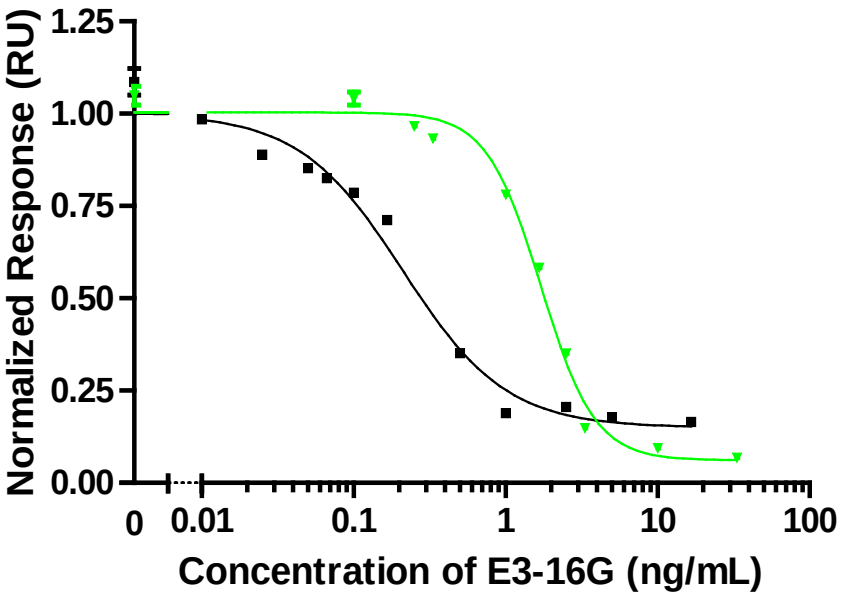

Fig 4-5: Standard curves developed with samples containing 1 µg/mL (■) and 5 µg/mL (▼) pAb. Values are the means ± SD from triplicate injections of each sample.

As expected on theoretical grounds, the IC_{50} and the LOD were both improved using solutions containing pAb at lower concentrations and supports the conclusion given in chapter three (chapter 3.2.1). A LOD value of 76 pg/mL was obtained with the solutions containing 1 µg/mL pAb whereas it was 969 pg/mL for the 5 µg/mL pAb solutions. Compared to the immunoassay developed with the pAb-Au using the strip test format, the LOD (1 µg/mL pAb assay) has been improved at least 6.5-fold (491 pg/mL (3.8 nmol/24hr buffer curve shown in Fig 3-6) / 76 pg/mL) in the absence of Au NPs. The intra-assay CV of the triplicate measurements for each sample was lower than 3.9 % for the 1 µg/mL curve and 4.4 % for the 5 µg/mL curve. The inter-assay CV (obtained from 3 separate assays) of the LOD was 12.3 % (1 µg/mL) and 9.6 % (5 µg/mL). The inter-assay CV of IC_{50} was 0.8 % for the 1 µg/mL antibody standard curves and 5.9 % for the 5 µg/mL antibody standard curves. All these data show the high reproducibility of the developed inhibition assay.

4.2.5 Enhanced assay developed with pAb-Au conjugates

In an attempt to develop an even more sensitive assay, a high molecular weight probe is introduced. Considering the fact that the antibody is a polyclonal antibody, the first enhanced assay was developed by directly conjugating the Au NPs to the pAb (Appendix I 4.4.2.4). Thus potential non-specific binding caused by the secondary antiserum (to the polyclonal primary antibody) was avoided. The system brought the Au NPs even closer to the chip surface and provided a greater SPR effect since there were no secondary antibodies involved. In addition, results were obtained in one step, therefore the time to achieve a result and the cost were also reduced. In the present study, colloidal Au NPs of 15.8 ± 2.7 nm diameter reduced by sodium citrate were employed.

The results shown in section 4.2.3 indicate that the concentrated pAb-Au conjugates lead to high intra-assay variation of response, therefore the conjugate series were prepared with a dilution factor from 37.5 using HBS-EP running buffer as diluent. The standard curves performed with the series of conjugates are

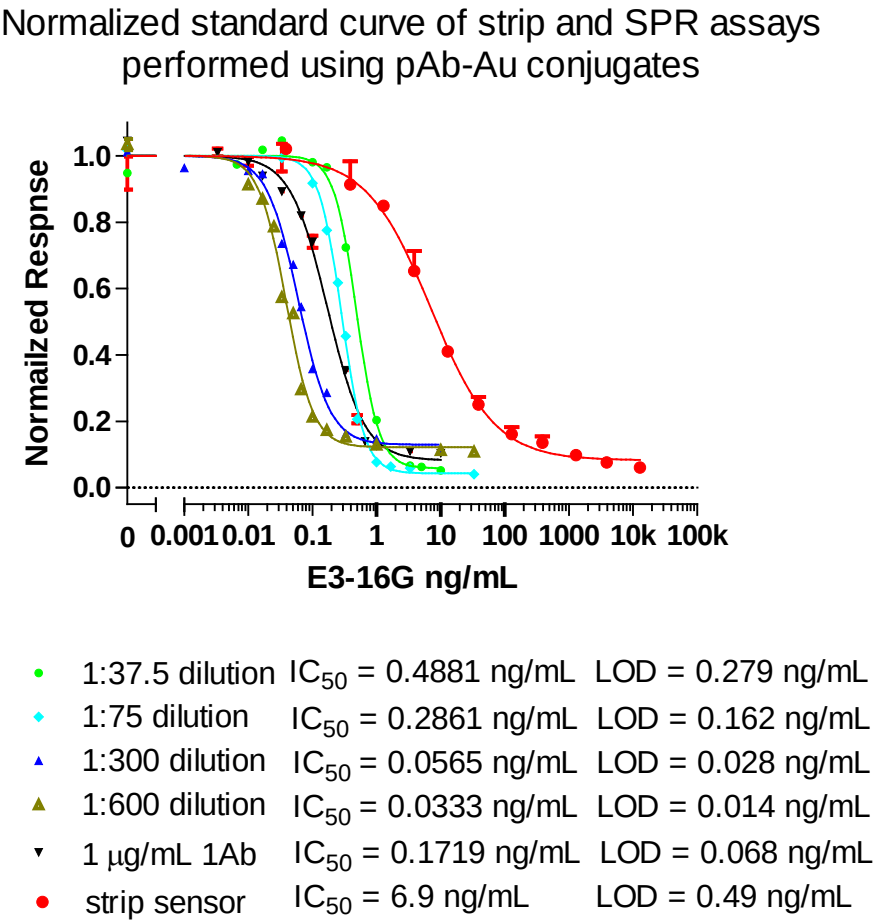

Fig 4-6: Standard curves performed with SPR and strip sensor. All data are mean ± SD (N=2). The highest CV of all measurement is 8.2 %. Error bars represent SD.

presented in Fig 4-6. Both the LOD and IC_{50} shifted to the lower value side as the dilution factor was increased (lowering the concentration of pAb in samples). The most sensitive and reproducible curve is the one performed with 1:600 diluted conjugates with a LOD of 14 pg/mL which is 5.5 fold more sensitive than the non-enhanced assay and 30 fold more sensitive than LFIA.

4.2.6 Enhanced assays developed with 2°Ab-Au and 2° antiserum

Besides using Au colloids as signal enhancement probe, 2°Ab and 2°Ab-Au can be two other options [125, 126] for increasing the mass on the sensor surface. The discussion in chapter three (section 3.2.2) indicated that the urine matrix effects on the immune reaction were quite severe when the 2°AS-Au conjugates were used for signal generation. We consider that the effects may be caused by

some unknown interactions between the proteins included in the serum or the urine. Therefore, for the SPR assay commercial secondary antibody conjugates (from BBInternational), synthesized using monoclonal anti-sheep IgG and Au colloids, were used in an attempt to lower the matrix effects and also the non-specific binding to the pAb by using a 2°Ab of high purity. Based on the belief that the introduction of high mass labels can lower the amount of pAb required to get a suitable level of signal and thus improve the sensitivity of the assay, the concentration of the pAb is commonly used at concentration lower than 1 μg/mL. The optimal binding response caused by injecting the enhancement probe should be around 150 RU.

The commercial 2°Ab-Au conjugates had an optical density (OD, i.e. maximum absorbance of plasmon resonance band) of 4.2 and hence were diluted 1:4 using HBS-EP running buffer before injection (20 μl/120s) based on the performance of the pAb (1 μg/mL, 20 μl/120s) (Appendix I 4.4.2.5). The RU of 321.3 (FC2-1) caused by binding of the 2°Ab-Au conjugates suggested that either the pAb or the 2°Ab-Au could be further diluted. Following this, several concentrations of pAb and dilutions of the 2°Ab-Au were tried to find the optimal combination with which the response caused by binding of the 2°Ab-Au was around 150 RU. Table 4-2 shows the responses obtained according to the OD of the 2°Ab-Au conjugates and the concentrations of the pAb. No obvious relation was found between the concentration of the pAb and the assay response. In some cases, the response was even abnormally lower in the presence of more pAb

C_{pAb} (μg/mL)	0	0.04	0.05	0.06	0.075	0.0767	0.10
OD of 2°Ab-Au	0.25	0.3	0.25	0.5	0.125	0.167	0.25
Response (RU)	70.8	89	86	134	52	49	74

Table 4-2: Relative responses on FC2-1 caused by the 2°Ab-Au conjugates in the presence of pAb of different concentrations. The OD of the conjugates was estimated using the initial OD of 4.2 and the dilution factors.

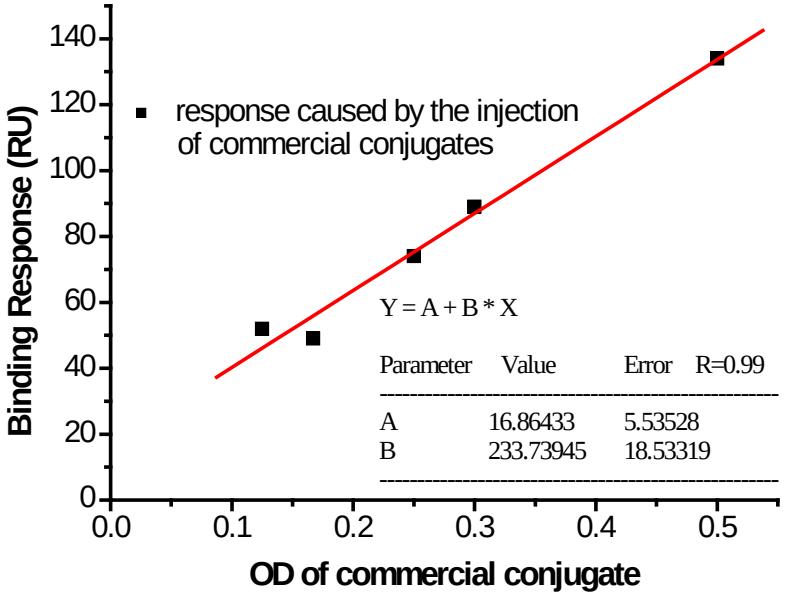

Fig 4-7: Correlation between the OD of the 2°Ab-Au conjugates and the related binding response. The linear regression is calculated based on the average of duplicate measurement.

(highlighted with gray) and the responses obtained in the absence and presence of the pAb were comparable (underlined) as the OD of the 2°Ab-Au was the same. In addition, Fig 4-7 depicts a linear relation between the OD of the 2°Ab-Au conjugates and the assay responses. All of these results illustrate that the responses arise from the non-specific binding of the 2°Ab-Au conjugates to the chip surface even when using conjugates synthesized with monoclonal IgG. Therefore, the non-specific binding could not be lowered by increasing the purity of the antibody applied.

In a previous study [127, 128], it was mentioned that the non-specific binding of 2°Ab to the chip surface was improved using reagents, such as NaCl, OVA and Poly Ethylene Glycol-400 (PEG). Here six different combinations were tried as running buffer using the three reagents and HBS-EP buffer. Table 4-3 shows the binding responses from FC1 and FC2 caused by the 2°AS of 25 µg/mL prepared in the 6 different running buffers. The RU of 376.3 on FC1 and 1396.1 on FC2 indicate that the best running buffer to lower the non-specific binding of 2°Ab to the chip surface was the one containing 0.05 % OVA, 0.5 M NaCl and 1% PEG.

Reagents in running buffer of HBS-EP	Response of 2°AS (25 µg/mL) in different buffers	
	FC1	FC2
A: HBS-EP buffer	345.8	1703.7
B: 0.5 M NaCl	361.6	1604.6
C: 0.5 M NaCl, 0.05% OVA	370.5	1535.7
D: 0.5 M NaCl, 1% PEG	389.3	1448.1
E: 0.5 M NaCl, 0.05% OVA and 1% PEG	376.3	1396.1
F: 0.3 M NaCl, 1% PEG	314.4	1766.3

Table 4-3: Non-specific binding in FC1 and FC2 caused by the 2°AS of 25 µg/mL in different running buffers (A to F). Commercial HBS-EP buffer was used as diluent for all buffer preparations.

C_{pAb} (µg/mL)	Response of FC2-1 (RU)						
	pAb	2°AS (25µg/mL)	**R**	2°AS (10µg/mL)	**R**	2°AS (5µg/mL)	**R**
1	20 RU	10 RU	**0.5**	19.2 RU	**2.0**	8 RU	**0.4**
5	85 RU	99.9 RU	**1.2**	140.5 RU	**1.8**	38.8 RU	**0.44**
10	167 RU	120.5 RU	**0.72**	212.6 RU	**1.3**	65.6 RU	**0.39**

Table 4-4: Specific binding of 2°AS of different concentrations prepared with running buffer E obtained in the presence of pAb. All responses were measured by subtracting the reference response (binding at FC1) from the binding response collected from the reaction surface (FC2). R represents the ratio of the response caused by the 2°AS to the response related to the pAb.

To get optimal enhancement of binding at the sensor surface, 2°AS samples of different concentrations were prepared with running buffer E (Appendix I 4.4.2.5). The efficiency of the enhancement was estimated with a ratio of the specific binding response of the 2°AS to response of the pAb. Table 4-4 shows that the specific binding of the 2°AS increased in the presence of more pAb. Although a maximal ratio of 2 was observed with a 20 µl/120s injection of the 2°AS of 10 µg/mL after the application of 1 µg/mL pAb (20 µl/120s), the pAb concentration of 1 µg/mL is not suggested since the corresponding response of the

2°AS was too low and could be easily affected by some unknown factors in the experiment. Therefore, the condition for optimal enhancement from the 2°AS was to inject a pAb of 5 μg/mL and followed by 20 μl/120s 2°AS of 10 μg/mL.

Although the enhancement from binding of the 2°AS was confirmed, considering the much higher non-specific binding on the chip surface compared to the pAb and pAb-Au conjugates alone, the relatively higher intra-assay CV and lower efficiency of enhancement, the assays developed with pAb or pAb-Au conjugates were considered more appropriate for the determination of E3-16G in clinical samples.

4.3 Determination of E3-16G in urinary samples

In section 4.2.5, a sensitive SPR inhibition assay using nanogold particle enhancement was described with a LOD of 14 pg/mL (0.11 nmol/24 hr). This high sensitivity in principle allows direct measurement of E3-16G in a range of (14 pg/mL to 75 pg/mL) both in wastewaters and in the urine of non-pregnant female subjects. The SPR assay therefore provides an opportunity to develop a direct reference assay for E3-16G that is rapid, precise and sensitive.

4.3.1 Cross-reactivity of the polyclonal anti-E3-16G antibody

When using the SPR assay for measurement of E3-16G excretion rates in urine samples from menstrual cycles of nonpregnant women, it must be considered that there are a number of metabolites excreted into the urine from metabolism of estradiol which is the primary steroid produced by the ovary. These metabolites may interfere in the assays if they cross-react with the antibodies being used. Low cross-reactivity is one pre-requisite for a reliable assay. Thus estrone-3-glucoronide (E1-3G), E3-3G and E3-17G, all having similar chemical structures related to E3-16G, could potentially interfere with the determination of E3-16G levels. The percentage of cross-reactivity by E1-3G and E3-17G was defined as the IC_{50} of the standard curve generated with E3-16G standards divided by the corresponding IC_{50} values for the two related steroids times 100 %.

Compounds	IC_{50} (ng/mL)	Cross-reactivity (%)
E3-16G	0.9	100
E3-17G	$5.2x10^{4}$	$1.8x10^{-2}$
E1-3G	$1.8x10^{9}$	$5.3x10^{-8}$

Table 4-5: Cross-reactivity of anti-E3-16G pAb to similar compounds. Each IC_{50} value is the mean based on three standard curves calibrated at different times and performed in triplicate.

Table 4-5 shows the responses of the E1-3G and E3-17G estradiol metabolites for the polyclonal E3-16G antibody, compared to that for E3-16G. The mean IC_{50} for E3-17G was $5.2x10^{4}$ ng/mL and it was even higher ($1.8x10^{9}$ ng/mL) for E1-3G. These low values for the cross reactivity (not higher than 0.0018 %) showed that neither E1-3G nor E3-17G, would interfere to a significant extent in the assay. Unfortunately E3-3G was not available for testing in the assay and that introduces an uncertainty into the assay results since E3-3G is produced in approximately twice the concentration of E3-16G throughout the menstrual cycle. However, given the extremely low cross reactivity for E1-3G and the similarity of the two structures it seems unlikely that E3-3G would be a significant cross reactor.

4.3.2 The matrix effect of the urine in the SPR immunoassay

Considering the low excretion of E3-16G in the urine of non-pregnant females, the colloidal Au enhanced SPR assay was selected for determination of the excretion rate in urinary samples of a normal cycle (volunteer A) and carried out using a 1:100 dilution of the Au-pAb conjugates.

The matrix effects of the urine samples were estimated by measuring the binding response in the assay with respect to different dilutions of time-diluted blank urine (Table 4-6) compared with buffer controls (Appdendix I 4.4.2.7) . The results for the 1:5 dilution showed a decrease in binding of approximately 50 % (115.2-57.7)/115.2) when compared to the control, and indicated the extent of interference by the matrix. This shows clearly that components in the urine are a competing factor in the assay. The difference due to the urine matrix effects was

samples	Response of samples (RU)		
	1:5 dilution	1:10 dilution	1:30 dilution
TM sample	115.2 ± 4.4	129.1 ± 2.7	144.3 ±3.0
Urine sample	57.7 ± 2.8	81.5 ± 0.4	138.3 ± 0.5

Table 4-6: The effect of diluting urine samples on the response to E3-16G binding in an SPR assay. The response is the mean ± SD based on triplicate measurements.

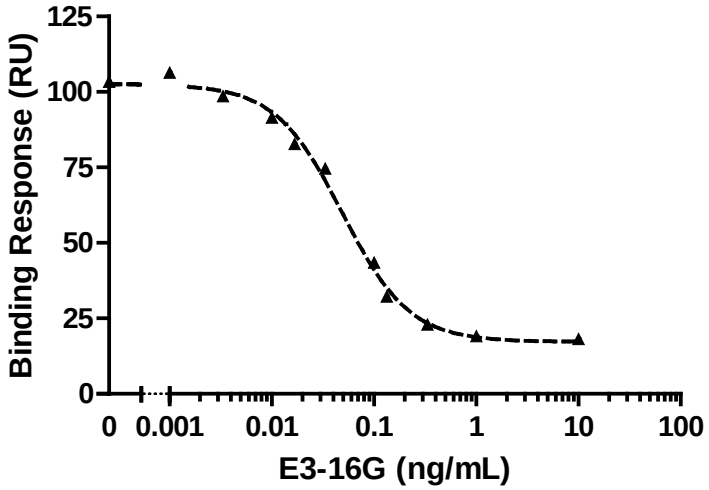

Fig 4-8: SPR reference calibration curve performed in the presence of the time-diluted blank urine. All values shown here are mean ± SD from triplicate measurements of each sample.

lowered to 36.9 % of the control value by changing to a dilution factor of 10, and then to 4.2 % of the control value with a further dilution (1:30). Thus, the lower assay response caused in the presence of the blank urine was reduced to acceptable (near zero) levels by increasing the dilution factor. The low coefficients of variation (0.4 - 4.8 %) demonstrated the excellent precision of these assay results. Subsequent assays were carried our using a dilution factor of at least 1:30.

A reference calibration curve (standard curve Fig 4-8) was generated using the pAb-Au conjugates (1:100 dilution), the time-diluted blank urine (1:30 dilution) and a series of E3-16G standards prepared in HEP-BS buffer. The sensitivity (LOD) of the curve was 16 pg/mL and the IC_{50} value was 49 pg/mL. These values were similar to the values reported previously for the buffer-only

Spiked E3-16G (ng/mL)	SPR immunoassay		
	Mean ± SD (ng/mL)	Recovery (%)	Intra-assay CV (%)
1.29 ng/mL	1.191 ± 0.008	92	0.71
3.87 ng/mL	4.172 ±0.014	108	0.34
6.45 ng/mL	6.96 ± 0.039	108	0.56

Table 4-7: Recovery and precision of SPR assay. The mean value, SD and intra-assay CV were obtained with triplicate measurements.

standard curve (for which the LOD was 14 pg/mL) shown in section 4.2.5 and the intra-assay coefficient of variation (CV) was ≤ 3.8 %. Thus, there was no discernible matrix effect in the presence of the diluted blank urine standard.

4.3.3 Precision and accuracy of the immunoassay

To determine the accuracy of the assay (Appendix 4.4.2.8), E3-16G standards of 1.29, 3.87, and 6.45 ng/mL (10, 30, and 50 nmol/24 hr) spiked in blank urine were prepared and diluted 1:30 with HBS-EP buffer, and the recoveries were measured in triplicate by calculation from the reference curve (Figure 4-8). The recoveries ranged from 92 % to 108 % with the highest CV of 0.71 % (Table 4-7). The acceptable recovery of the pure standard samples spiked in blank urine showed a high repeatability and accuracy of the SPR assay.

4.3.4 Determination of E3-16G

Cilinical samples contributed by voluteers (A and C) were measured using the Au NPs enhanced inhibition assay (Appendix 4.4.3) and the results were compared to the results reported with strip tests discussed in chapter three. Participant A contributed daily urine samples for a complete menstrual cycle. The E3-16G excreation rates were determined each day. Figure 4-9 A shows the correlation between the LFIA and SPR assays, and for comparison Figure 4-9 B depicts the corresponding excretion rates of pregnanediol glucuronide (PdG), determined with the Ovarian Monitor as described by Cooke et al [112] against that of E3-16G data obtained via the SPR.

The measured range of E3-16G excretion rates (from 27 nmol/24 hr (day5) to 90 nmol/24 hr (day 17)) reported by the SPR assay was consistent with the results reported by Baker et al.[116]. Although the absolute values of the E3-16G excretion rates obtained using the two techniques were different, the profiles were remarkably similar. Both patterns showed that the E3-16G excretion rate reached a maximum (around 90 nmol/24 hr in the SPR pattern and 10 nmol/24 hr in LFIA pattern) on day 17. Moreover, several common

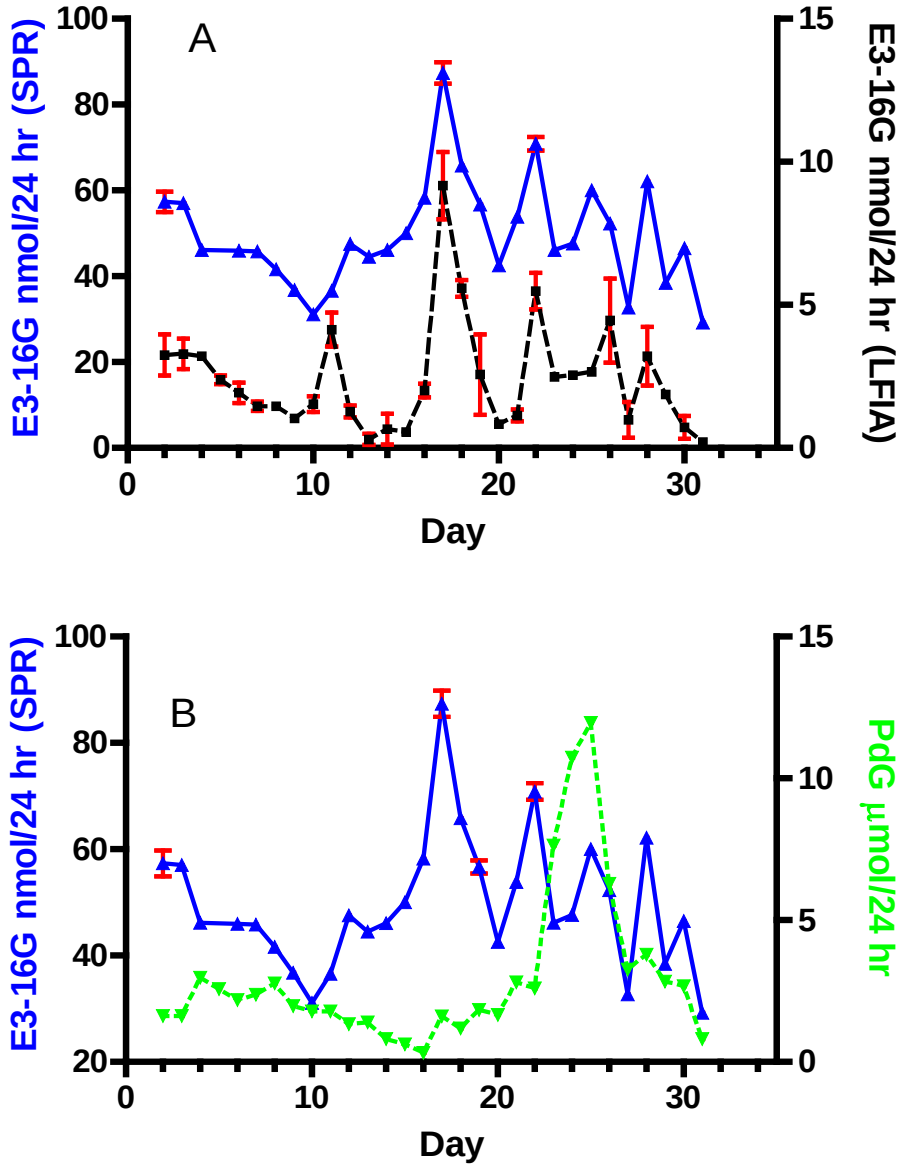

Fig 4-9: A) E3-16G concentration obtained using the SPR biosensor (▲, left Y axis) and LFIA strips (■, right Y axis). The mean intra-assay CV of strip pattern was 11.7 ± 8.8 %. All values are mean ± SD from triplicate measurements. B) Excretion pattern of PdG (▼, right Y axis) compared with E3-16G concentration values obtained from the SPR biosensor (▲, left Y axis).

smaller peaks occurred after the main peak. The rise in E3-16G excretion rate on day 12 that led to the pre-ovulatory peak on day 17 identified the beginning of the fertile window [116]. The PdG excretion rate exceeded the threshold value of 7 µmol/24 hr identifying the end of the fertile window on day 23 giving a fertile period of 11 days [129]. This threshold also confirms that the E3-16G peak on day 17 is the ovulatory estrogen peak. The smaller post-ovulatory peaks are consistent with the fact that the excretion levels of E3-16G in the luteal phase are usually higher than that in the follicular phase [116]. The decline in E3-16G levels for the first 3 days is consistent with the observations that in some cycles the levels are still declining after bleeding commences as a continuation of the previous luteal phase [116]. The luteal phase length defined as the number of days from the mid-cycle estrogen peak to the day before the next bleed was 14 days, and is in agreement with the fact that the mean luteal phase length in normal menstrual cycles is 14±2 days [130]. The likely day of ovulation is the day after the E3-16G peak, thus the direct assay for E3-16G identifies the key cycle parameters equally as well as measurements reported for E1-3G [111].

The comparison of the SPR and strip results revealed that the matrix effects of the adult urine sample was markedly different from that in the “blank” child’s urine, and highlights the difficulties associated with acquiring a truly blank adult urine sample. The matrix effects were probably more predominant in the strip assay since higher concentrations of urine were necessary because of the lower sensitivity. The higher sensitivity of the SPR assay gave reliable responses at a greater dilution factor for the urine sample. As a consequence, the matrix effect of the adult urine was removed for the SPR assay but in LFIA format it was not removed. The matrix effects of the urine samples used in the LFIA experiments indicated that the blank urine effect noted in the preliminary experiments did not compensate for the adult urine.

Time-diluted samples of week:	4	6	8	10	12	14	18	24
Dilution Factors:	300	60	300	1500	4k	1k	12k	25k

Table 4-8. Further pre-dilution of time-diluted urinary samples of pregnant volunteer C.

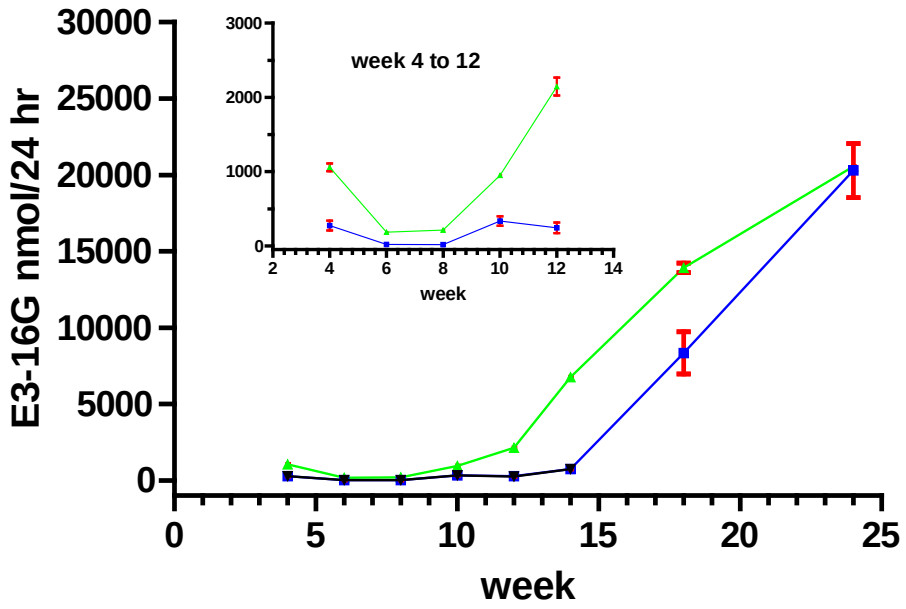

Fig 4-10: Excretion of E3-16G during the first two trimesters determined using the SPR biosensor (▲) and LFIA (■). All values are mean ± SD from triplicate measurements of each sample. The intra-assay CV of 3 measurements was lower than 4.9 % in SPR format.

Considering the high excretion of E3-16G during pregnancy daily production of E3-16G [116], the determination of E3-16G in these samples necessitated pre-dilution (see Table 4-8) to bring them within the range of the calibration curve (shown in Fig 4-8) and Figure 4-10 shows the patterns of E3-16G excretion throughout the first and second trimester of the pregnancy measured using both LFIA and SPR techniques. The insert in Figure 4-10 displays the patterns for weeks 4 to 12. Both patterns show the expected much higher excretion of E3-16G in the second trimester and the lower values of weeks 6 and 8. The mean concentrations of E3-16 in the two samples were 183 and 213 nmol/24 hr respectively reported by the SPR assay which are around 10 times higher than those calculated with the LFIA assay (18.6 and 16.2 nmol/24hr). That the gap between the two sets of data reported with the two techniques was close to zero in

the sample of week 24 validates that the strong matrix effect of adult urine in LFIA can be reduced by increasing the dilution factor. The insert to the figure suggests that the excretion of E3-16G rose steadily from the end of the first trimester (week 8) almost doubling every 2 weeks and the increase was six weeks earlier than that reported by the LFIA assay.

The above discussions demonstrate that the SPR biosensor-based assay can be applied to the measurement of E3-16G in any urine specimen, to give a rapid, precise and accurate result. This makes it suitable as an analytical tool that requires minimal sample preparation. It has the potential to be used as a reference assay for E3-16G, however a larger sample set of menstrual cycles would need to be analysed for complete validation of the system. No estriol assay for the menstrual cycle levels of E3-16G was available for a comparison of the present results with a reference assay.

4.4 Conclusion

In this chapter, the immunoassays for determination of E3-16G were developed using a SPR biosensor which is both rapid and sensitive compared to the technique of LFIA introduced in chapter three. It is also simple to apply and does not require any complicated sample pre-treatment, such as hydrolysis, extraction, or derivatization. Quantification of E3-16G was performed in aqueous samples by means of a competition between injected free E3-16G (pre-mixed with pAb) and E3-16G conjugate (E3-16G-OEG-OVA) immobilized on a CM5 chip surface. The non-enhanced assay was developed using a pAb with a LOD of 76 pg/mL which is improved to 14 pg/mL by using Au NPs for signal enhancement. Furthermore, both the commercial conjugates, synthesized with the monoclonal anti-sheep IgG, and the antiserum containing specific anti-sheep IgG were tried as enhancement probes. The non-specific binding by them to the chip surface was quite high no matter how pure the applied IgG was and it was difficult to remove it completely.

The application to urine samples was carried out using the Au NPs enhanced inhibition assay which reported the concentrations of E3-16G during a menstrual cycle that agreed with those previously reported [116]. The comparison to the strip test data suggests that the lower-reported excretion rate of E3-16G in the LFIA format were caused by the strong urinary matrix effect in adult urine. In addition, although only samples for the first two trimesters of a pregnancy were measured, the rapidly increasing levels of E3-16G in pregnancy urine were clearly observed starting from the end of the first trimester. The high sensitivity, accuracy and the low degree of sample preparation in the SPR assay highlighted its advantages over the more traditional techniques, with the levels measured being relevant also to environmental monitoring and the monitoring of steroidal metabolites in veterinary science.

Further work is required to convert this assay developed for sensitive determination of E3-16G in liquid samples into a routine or commercial assay.

Chapter Five

Surface-enhanced Raman scattering

5.1 Introduction

In the previous chapters, two sensor assay systems have been discussed, which were developed with LFIA and SPR techniques based on the specific binding between antibodies and analytes. Matrix effects have to be considered as the two immunoassays are applied to urinary samples. The effects could not be removed completely due to lack of selectivity of the two techniques. In this chapter, a new sensor system is introduced, which is developed based on Raman spectroscopy.

Although Raman spectroscopy can provide a finger-print signal for analytes in solution and thereby offers the selectivity, normal Raman scattering is a very weak effect and the sensitivity of Raman is very poor. The sensitivity of Raman can be improved in two ways, both of which rely on resonance enhancement of the Raman scattering process. The general strategy for improving the Raman

scattering efficiency is to resonantly couple the Raman scattering with strongly allowed (i.e. very efficient) processes that are driven by the laser radiation field. If we consider a system consisting of a molecule bound to the surface of a plasmonic nanostructure (Au and Ag sols were used in this study), then the first resonance enhancement mechanism uses resonance with the localized surface plasmon to increase the magnitude of Raman scattering by several orders of magnitude. Independently of this mechanism, the second resonance enhancement mechanism uses resonance with strongly-allowed electronic dipole transitions of the adsorbed molecules. In practice this means selecting a molecule that has a strong transition in the visible region, preferably towards the green or red end of the visible spectrum. This mechanism also increases the magnitude of Raman scattering by several orders of magnitude. If a strongly-allowed charge-transfer transition occurs between the molecules and the metallic nanostructure then further resonance enhancement of the Raman scattering can occur through this process, which may further multiply the enhancement by several orders of magnitude again. The ideal combination of metallic nanostructure and molecular chromophore, sometimes called the Raman Reporter Molecule (RRM) is described as a “SERS probe” [131].

In the new sensor system, the proposed structure for the SERS probe consists of the metal nanostructure with an adsorbed monolayer of the RRM or polymer. The RRM are chemically functionalized to allow attachment to the biologically active element (e.g. antibody) and the model is described in Fig 5-1. Strong binding between the RRM and metal surface is required for stability of

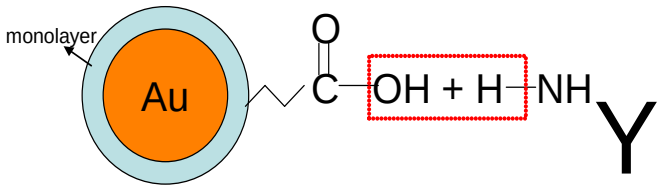

Fig 5-1: Model of SERS probe. Au NP is covered by a monolayer of Raman Reporter Molecule (RRM). Analyte biological molecules are linked to the signal generators via covalent reaction.

the SERS probe and for silver and gold substrates strong binding is achieved with the use of sulfur atoms in the structure of the molecule. Aromatic compounds with extensive delocalised π-electron systems possess very intense π–π* electronic transitions. Therefore appropriately substituted porphyrin systems or thiophene and thiophene oligomers are potential candidates for RRMs. For analytical applications of SERS probes, some chemical functionality must be included in the SERS probe. When using proteins and antibodies a convenient method to attaching the probe to the biologically active component is through either a carboxylic acid or amine functional group. Both the porphyrin and thiophene probes can be substituted in a relatively straightforward manner compared to other strong chromophores such as Rhodamine6G or other dye materials.

Here preliminary investigations are presented that examine the Raman spectroscopy of porphyrins and thiophenes as RRMs on Au nanostructures and the detection limits of these systems are measured. Thiophene monomers and oligomers are investigated and studies of the in situ polymerization of the oligomers on Au nanoparticle surfaces are presented. Analysis of the Raman spectra suggest that limited polymerization of the oligomers occurs.

5.2 Structures of Raman reporter molecules

All compounds used in this study are shown in scheme I. Three utilized classes of compounds were (1) substituted porphyrin, **5.1-5.3,** (2) thiophene class, **5.4** and **5.5,** and (3) substituted terthiophene, **5.6-5.8**. Compounds **5.1-5.3** and **5.6-5.8** were obtained from the MacDiarmid Institute at Massey University. Compounds **5.4** and **5.5** were commercial chemicals and used without further purification.

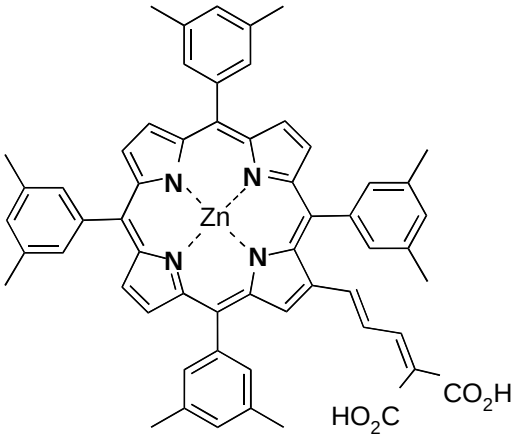

Compound **5.1**

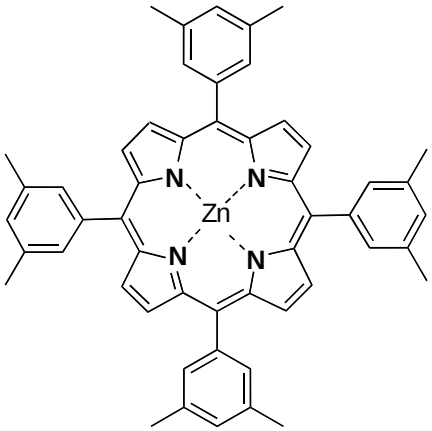

Compound **5.2**

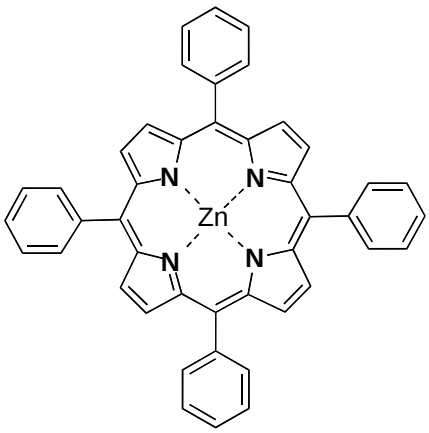

Compound **5.3**

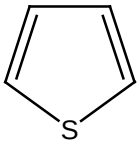

Compound **5.4**

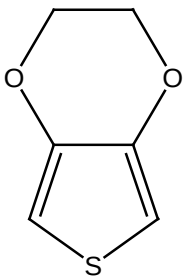

Compound **5.5**

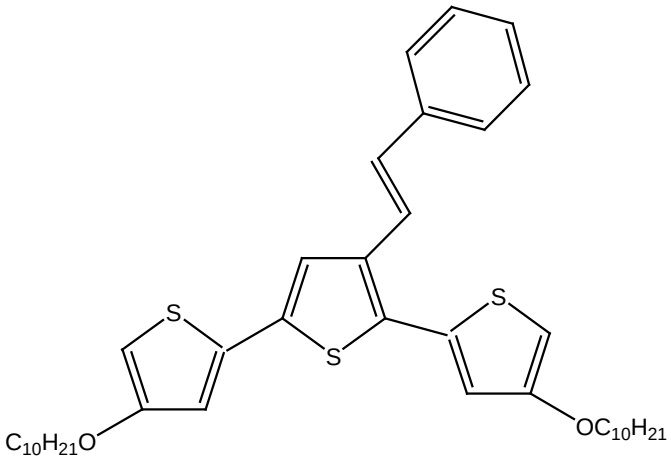

Compound **5.6**

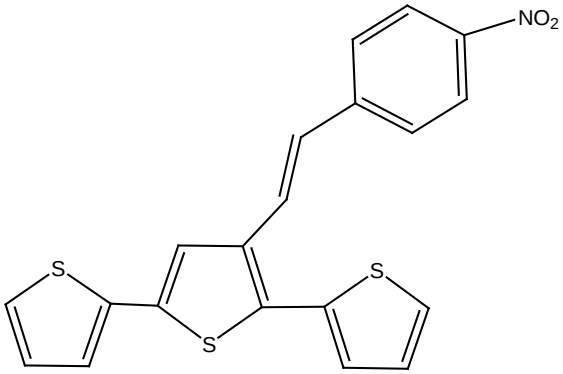

Compound **5.7**

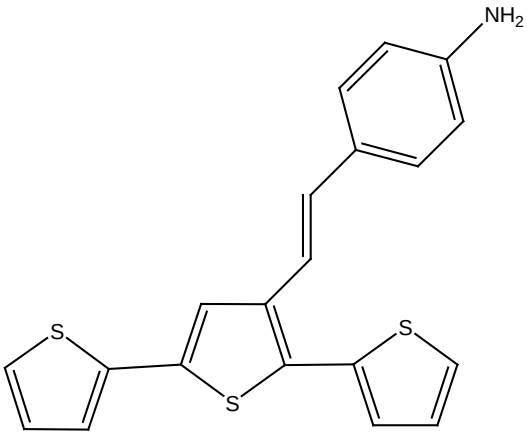

Compound **5.8**

Scheme I: Chemical structures of compounds **5.1** to **5.8** used for studies of Raman reporter molecules (RRM).

5.1 is 2-Carboxy-5-{2'-[5',10',15',20'-tetra(3",5"-dimethylphenyl)porphyrinato zinc(II)]yl}-penta-2,4-dienoic acid (Zn malonic acid porphyrin).

5.2 is 5,10,15,20-Tetrakis(3',5'-dimethylphenyl)porphyrinato zinc(II) (ZnTXP).

5.3 is 5,10,15,20-Tetraphenylporphyrinato zinc(II) (ZnTPP).

5.4 is Thiophene.

5.5 is 3,4-ethylenedioxythiophene (EDOT)

5.6 is 4,4"-bis(decyloxy)-3'-[(1E)-2-phenylethenyl]- 2,2':5',2"-terthiophene

5.7 is 3'-[(E)-2-(4-NO_2-phenyl)ethenyl]-2'2':5',2"-terthiophene (NO_2-pe3T).

5.8 is 3'-[(E)-2-(4-NH_2-phenyl)ethenyl]-2'2':5',2"-terthiophene (NH_2-pe3T).

5.3 Study of substituted porphyrins

This work started with substituted porphyrin, initially produced for the solar cell industry, by considering the well known Raman signals caused by the effect of conformational distortions of the π-electron system of the porphyrin macrocycle shown in Fig 5-2.

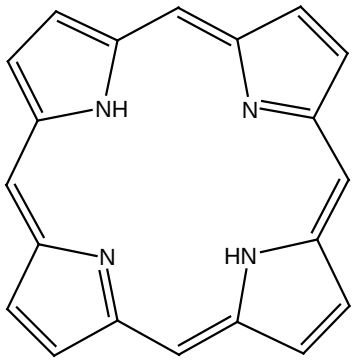

Fig 5-2: Chemical structure of porphyrin.

5.3.1 Compound 5.1

From the structure shown in Scheme I, it was known that the substituted functional group of **5.1** is a carboxylic acid group, opening a door to the biological area via the interaction with amino groups of biological molecules. In its visible absorption spectrum (Fig 5-3), the most intense band around 429 nm, known as the Soret band, was a strongly allowed π-π* transition, perturbed by the presence of the conjugated double-bond substituent [132]. Other two weak bands in longer wavelength range were the Q-bands that gain intensity through a vibronic mechanism. Experimental procedures related to **5.1** were described in Appendix I 4.5.1.

5.3.1.1 SERS signals from Au and Ag sols

Since the SERS effect from colloidal NPs was revealed in 1979 [69], metal colloids have become the most commonly used nanostructures as a substrate. Colloidal metal NPs have allowed to test theoretical models of SERS phenomenon as well as opened the window to its application as an analytical tool

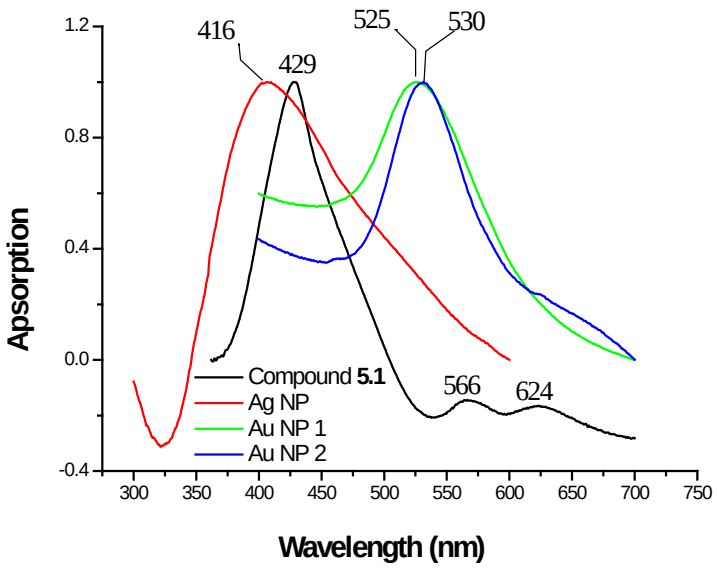

Fig 5-3: Normalized UV-Vis absorption spectra of **5.1** and Ag/Au NPs. The Plasmon resonance peaks of three metal sols are at 416 nm, 525 nm and 530 nm.

in chemistry and biological sciences. Grounds for using Ag or Au sol in our study are: (1) Compared to planar substrate, NPs provide more surface area for adsorption of molecules. (2) The localized surface plasmon resonance introduces a very strong electromagnetic near field close to particles and especially high around the "hot-spot" formed by aggregation of NPs. One Ag and two Au samples were synthesized with sodium citrate, and their absorption spectra, shown in Fig 5-3, reveal that the plasmon resonance wavelengths of three hydrosols were 416, 525 and 530 nm, respectively.

It is well known that the SERS efficiency of Ag sol as substrate can be improved by KCl, which causes aggregation of Ag NPs and resultant hot-spot. To determine the optimum concentration of KCl for signal enhancement and the limit of detection (LOD) of **5.1**, a set of SERS experiments were carried out with **5.1** of different concentrations (nM to μM) using KCl (10 to 50 mM) as an aggregating agent.

Sediments caused by excess aggregation of Ag NPs were found in samples, when the concentration of KCl in sample was higher than 3 mM. Experiments confirmed that the concentration of 2.5 mM was the optimum for signal enhancement (Details not shown here). From Fig 5-4 it can be revealed that (1)

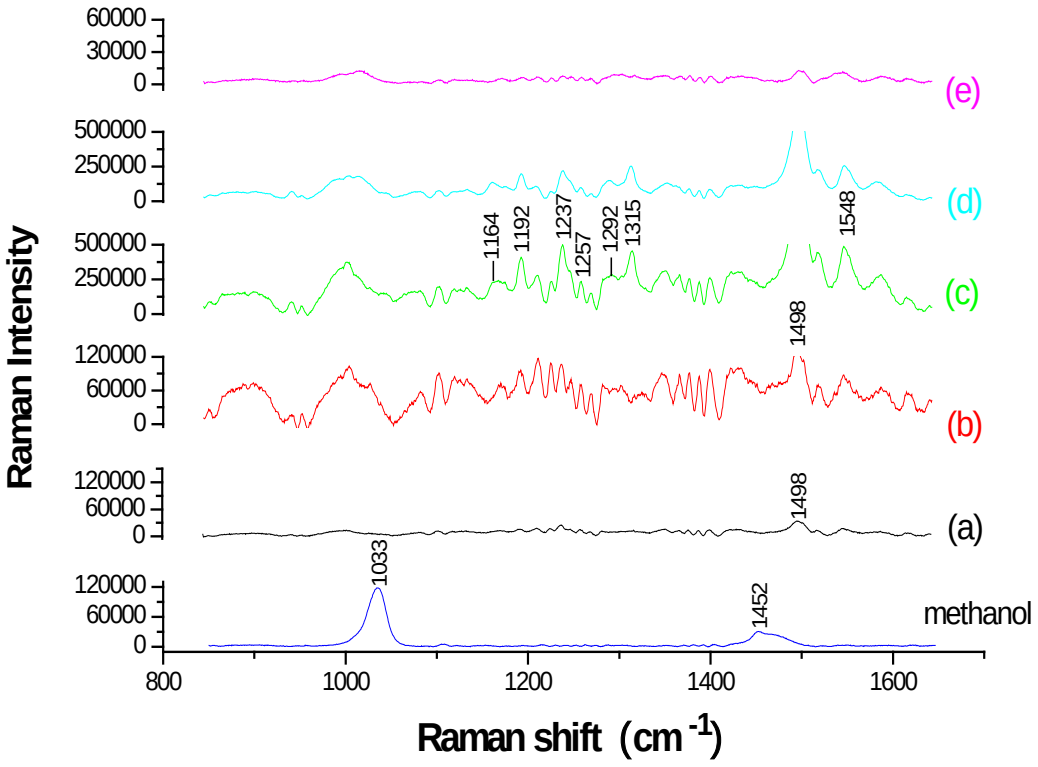

Fig 5-4: Raman spectra of methanol, a) **5.1** (200 µM) prepared in methanol, b) **5.1** (250 nM) in Ag sol, c) **5.1** (250 nM) in Ag sol in the presence of 2.5 mM KCl, d) **5.1** (250 nM) in Au sol, and e) **5.1** (250 nM) in Au sol in the presence of 2.5 mM KCl. The excitation wavelength was 632.5 nm.

the signal enhancement was obtained from Ag sol (spectrum b), (2) KCl of 2.5 mM promoted the signal enhancement (spectrum c), (3) and under the condition of using 2.5 mM KCl the LOD of **5.1** was lowered to nM level, much lower than the µM level obtained in the absence of noble NPs (spectrum a). In the spectrum of methanol, two intense bands of 1033 cm^{-1} and 1452 cm^{-1}, associated to the C-O stretching mode and symmetrical C-H bending mode of methanol respectively [133], have been demonstrated but not observed in signal enhanced spectra. The solvent peaks provided an intensity calibration reference and revealed that the strong signals must be caused by a true enhancement due to the SERS effect. The intense bands at 1164 cm^{-1} and 1192 cm^{-1} represented C-H deformation of the phenyl group while 1498 cm^{-1} and 1548 cm^{-1} bands were assigned to C=C stretching mode of phenyl group. The presence of carboxylic acid group was explained with bands at 1237 cm^{-1}, 1257 cm^{-1}, 1292 cm^{-1} and 1315 cm^{-1}, associated to the C(=O)O stretching vibration coupled to the OH in-plane

deformation calculated in the region of 1250 ± 80 cm^{-1} [134], and the band at 1003 cm^{-1} caused by the out-of-plane OH deformation [135], calculated in the range of 905 ± 65 cm^{-1}.

Au sol was also introduced for the investigation of SERS from **5.1**. Experiments were carried out with and without the aggregating agent of KCl (2.5 mM) respectively. Different from the behaviour of the Ag-sol, the presence of KCl of 2.5 mM led to serious aggregation in suspension and lowered the signal enhancement that was explained with the spectra (d) and (e) shown in Fig 5-4. Comparing the spectrum (c) and (d) depicted on the same scale, it can be concluded that for the same analyte molecules the signal enhancement from Ag-sol was more efficient. However, considering the toxicity of Ag to biological analytes, it was decided to use Au-sol for following work.

5.3.1.2 Concentration and size dependence studies of Au sol

Previous studies [70, 136, 137] have stated that the Raman signals can be affected by the size, shape and concentration of NPs. To obtain the maximum

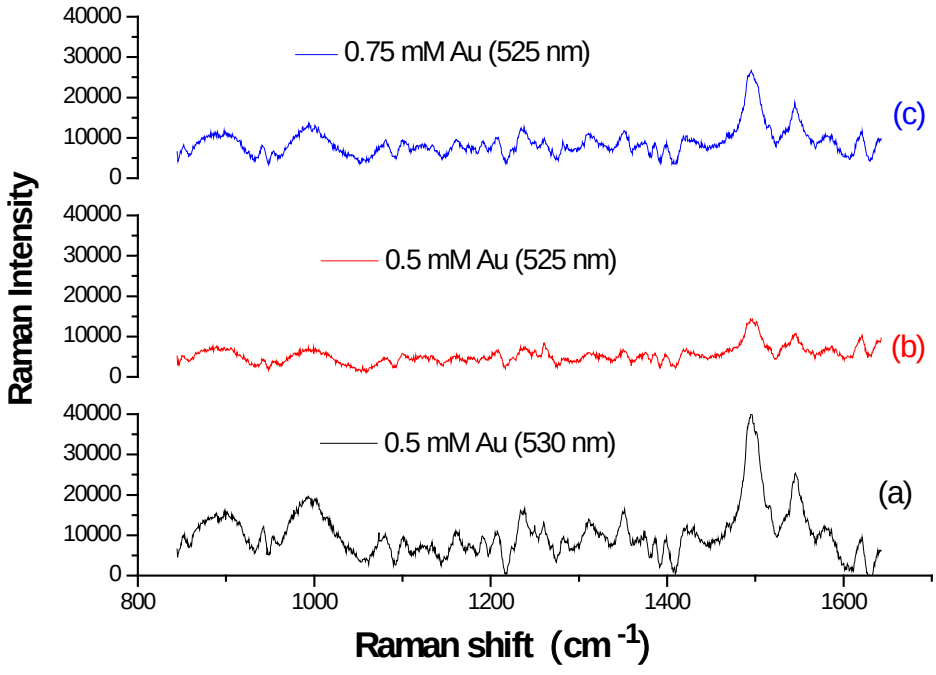

Fig 5-5: Raman spectra of **5.1** obtained under the condition of a) using 0.5 mM Au-NP2 as substrate, b) 0.5 mM Au-NP1 as substrate and c) 0.75 mM Au-NP2 as substrate.

enhancement, two different sized Au NPs, of which the corresponding plasmon resonance wavelengths were 525 and 530 nm (Fig 5-3), and Au NPs of different concentrations (0.5 mM and 0.75 mM) were used. The Raman spectra (a) and (b) shown in Fig 5-5 suggested that bigger-sized Au NPs could improve efficiency of the signal enhancement. In addition, Au NPs of higher concentration was another option to improve the efficiency explained with spectra of (b) and (c).

5.3.1.3 pH dependence study of SERS

Surface charge of NPs as an important factor affecting signal enhancement has been studied by Lecomte et al [138] who reported the surface charge of Ag NPs produced by citrate as a function of the concentration of the analyte molecules added, and by Faulds et al [139] who reported the relation between the rate of aggregation of these NPs and their surface charge. To obtain strong Raman signals in SERS experiment, one prerequisite condition is the efficient adsorption of analyte molecules onto the surface of NPs, which is strongly dependent on the charges of analyte molecules and NPs. Therefore, the surface charge dependence of Raman signals was studied by monitoring the absorption and SERS spectra of **5.1** over pH value of the Au sol.

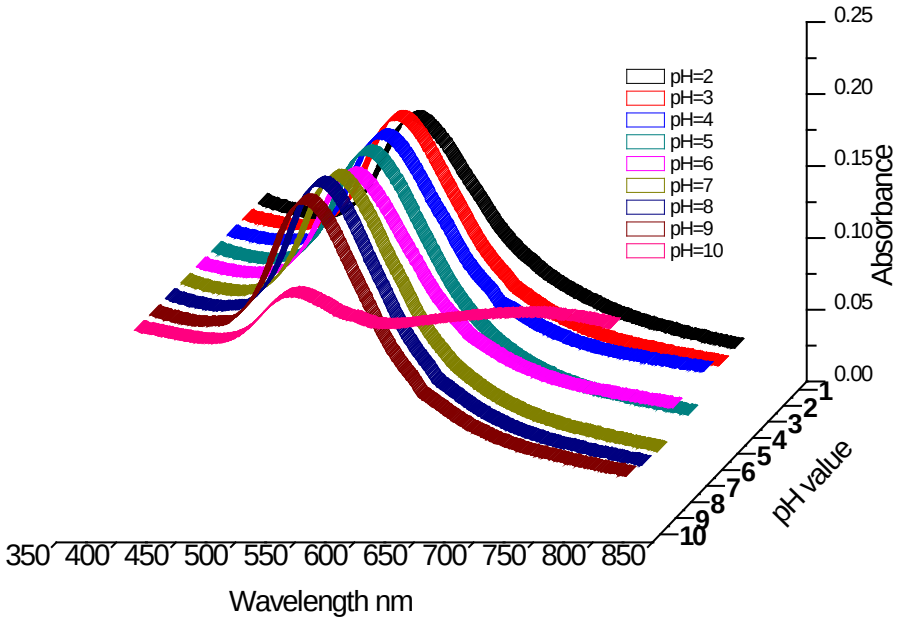

Fig 5-6: UV-Vis absorption spectra of the Au NP 2 at different pH value.

The initial pH of Au sol was around 5.5. The pH value was adjusted from 1 to 14 with 10 mM HCl and 20 mM K_2CO_3. It was found that the Au NPs can only be stable while the pH was in a range of 2 to 10. The absorption spectra (Fig 5-6) didn't show any shift of the plasmon resonance wavelength (525 nm) of the Au NPs from pH 2 to 9, indicating the high stability of the Au NPs under both acidic and basic conditions. At pH 10, it shifted to 530 nm along with a remarkable drop of band intensity. In addition, a new broad band appeared freshly in the lower energy range (around 730 nm). All these were likely due to the decrease of their stability and consequent formation of aggregates which led to shift in plasmon frequency.

The pH dependence of the Raman signals in the Au solution was studied and is discussed in two parts with UV-Vis absorption spectra and SERS Raman spectra. Fig 5-7 a) shows the absorption spectra of samples prepared using the Au NPs (pH 2 to 5). The peak at 429 nm was corresponding to the absorbance of the Soret band due to the porphyrin ring structure. The peak representing the plasmon resonance absorbance of Au NPs red shifted from 525 nm to 530 nm due to the adsorption of **5.1** onto the surface of NPs. Different from the behaviour of the Au sol shown in the Fig 5-6, intensity of the peak (around 530 nm) decreased as the

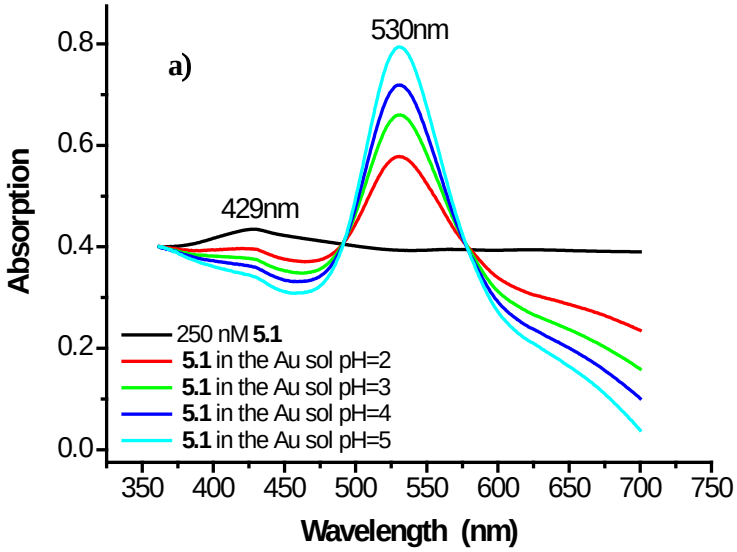

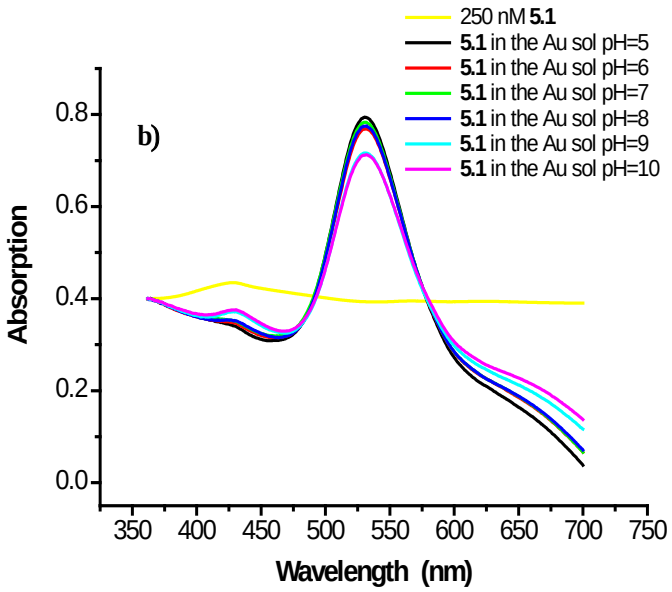

Fig 5-7: UV-Vis absorption spectra of samples prepared with **5.1** and the Au-sol of pH 2 to 5 (a) and the Au-sol of pH 5 to 10 (b). Moreover, the absorption spectrum of 250 nM compound **5.1** is also shown in two figures.

pH of the Au sol was lowered while the intensity of a broad band in the range of 600 nm to 700 nm increased. All these differences were related to an aggregating process of $nAu \rightarrow (Au)_n$ caused by an interaction with the analyte molecules. Independently, the aggregating process was proved by an isosbestic point at 491 nm of absorption spectra as well. Fig 5-7 b) showed the absorption spectra of samples prepared using the Au NPs of pH ranging 6 to 10. The intensity of either the peak corresponding to the monodispersed Au NPs, or the band caused by the aggregated Au NPs has not changed so much in this case, similar to the case in the absence of analyte molecules and suggesting depressed interaction with **5.1**. Taking into account the laser wavelength of 632.5 nm which matches the plasmon wavelength of the aggregated clusters (600-700 nm shown in Fig 5-7 a), it can be assumed that the SERS effect will be much stronger in the presence of H^+ and its efficiency should be increased as the amount of H^+ is increased.

Fig 5-8 shows the Raman spectra of the related samples discussed above, as a function of pH of the Au sol. The signal enhancement was only observed in the case of pH lower than the normal pH of the NPs (around 5.5) (Fig 5-8 a), i.e. pH of the Au sol after synthesis, indicating effective adsorption of **5.1** onto the Au

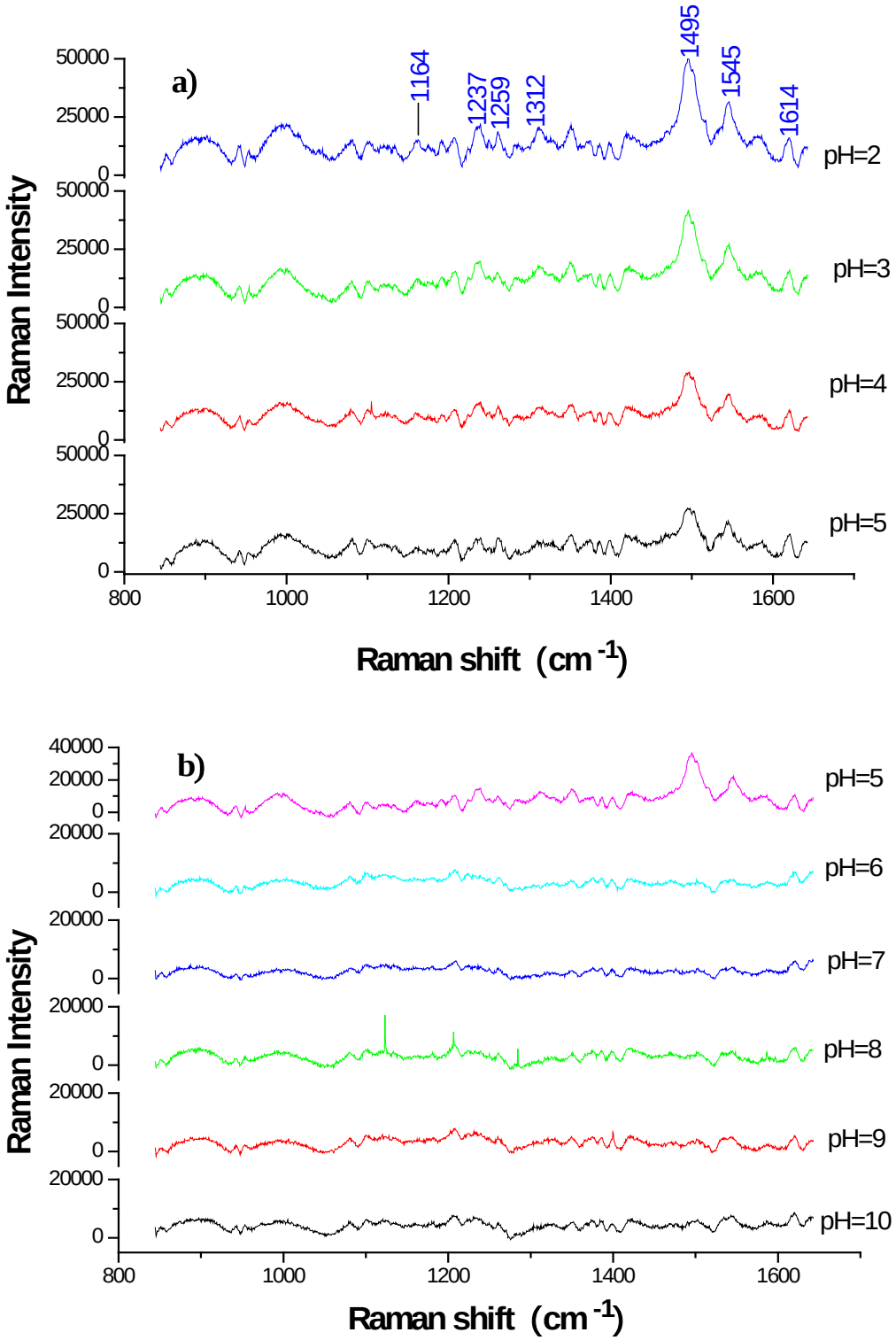

Fig 5-8: a) Raman spectra of the samples prepared with **5.1** and the Au sol of pH 2 to 5. b) Raman spectra of the samples prepared with **5.1** and the Au sol of pH 5 to 10.

surface. The presence of partially aggregated NPs in samples was another reason for efficient signal enhancement. Moreover, in this case, Raman signals increased as pH was reduced. It was likely due to the promoted adsorption of the analyte

molecules as a result of the decreased repulsion between **5.1** and the Au NPs. In the case of the pH value higher than the normal pH of the NPs (Fig 5-8 b), no signal enhancement was observed. It was attributed to the unsuccessful adsorption of the analyte molecules onto the Au surface. All phenomena observed from the Raman spectra are consistent with the assumption based on the absorption spectra.

5.3.2 Compound 5.2 and 5.3

Compound **5.2** (Zn-TXP), with xylyl groups at meso positions and without the malonic acid group, and **5.3** (Zn-TPP), also without the malonic acid group and with phenyl groups at the meso positions, were another two compounds used for this study (related experiment procedures in Appendix I 4.5.2). Their absorption spectra were shown in Fig 5-9. Nearly identical spectra were resulted by the similar structures of the two compounds. The sharp peaks at 421 nm showed a typical Soret band profile consistent with the absence of the extended double bond substituents explained with Woodward rule [140].

In a similar manner as **5.1**, mixtures of 250 nM solutions of **5.2** or **5.3** (prepared with methanol) and the Au NPs of 0.5 mM were measured by Raman spectroscopy. Spectra shown in Fig 5-10 demonstrated that Raman signals of both

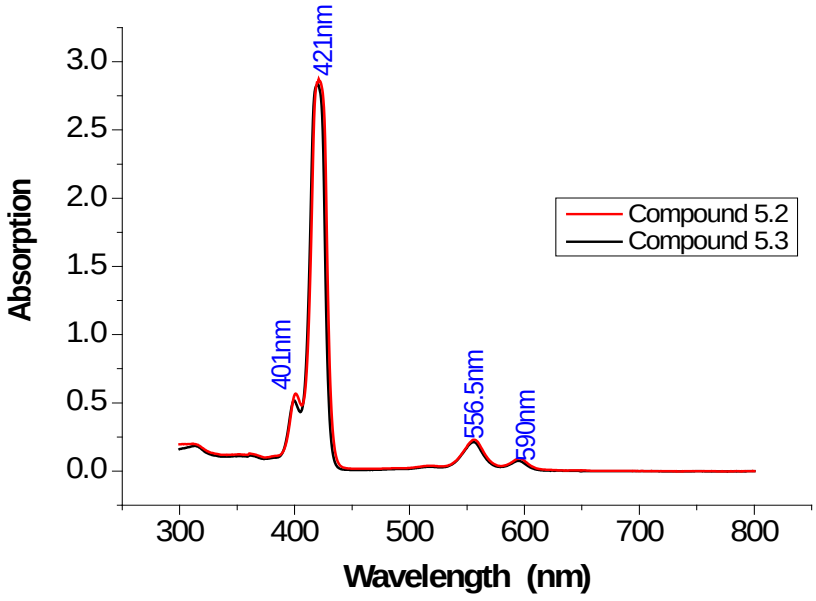

Fig 5-9: UV-Vis absorption spectra of **5.2** and **5.3**.

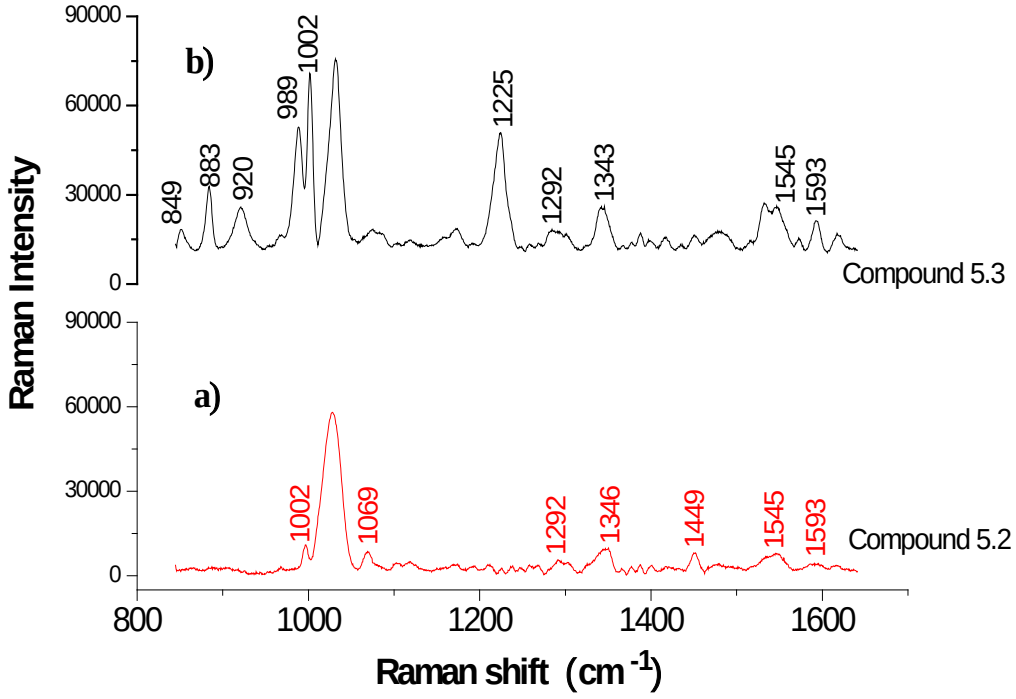

Fig 5-10: Raman spectra of a) **5.2** (250 nM) and b) **5.3** (250 nM) obtained using Au-sol substrate (0.5 mM).

compounds can be enhanced efficiently by the Au-sol even though there were no acid groups. The common bands localized around 1002 cm^{-1}, 1292 cm^{-1}, 1343 cm^{-1}, 1545 cm^{-1} and 1593 cm^{-1} were believed due to the common structures of the two compounds. More intense common bands shown in the Raman spectra of **5.3** indicated that the common structures were rather far from the Au NP surfaces as using **5.2,** resulted by the longer tail of dimethyl group of the compound **5.2** [141]. Intense Raman band at 989 cm^{-1} assigned to the skeletal C-C vibration of the phenyl group [142] was observed only in the spectrum b), independently corroborates that the dimethyl group of **5.2** acting as a spacer increased the distance from the surface of NPs to the common structure and consequently lowered the signal enhancement. Moreover, it was also indicated that the orientation of **5.2** must to be perpendicular to the surface of Au NPs, explained with scheme shown in Fig 5-11. If we assume the orientation of the compounds could be different, there should be 4 possibilities. If both compounds have horizontal orientations (Fig 5-11 a), the distance between the analyte molecules and the Au surface should be the same and intensities of common bands should be

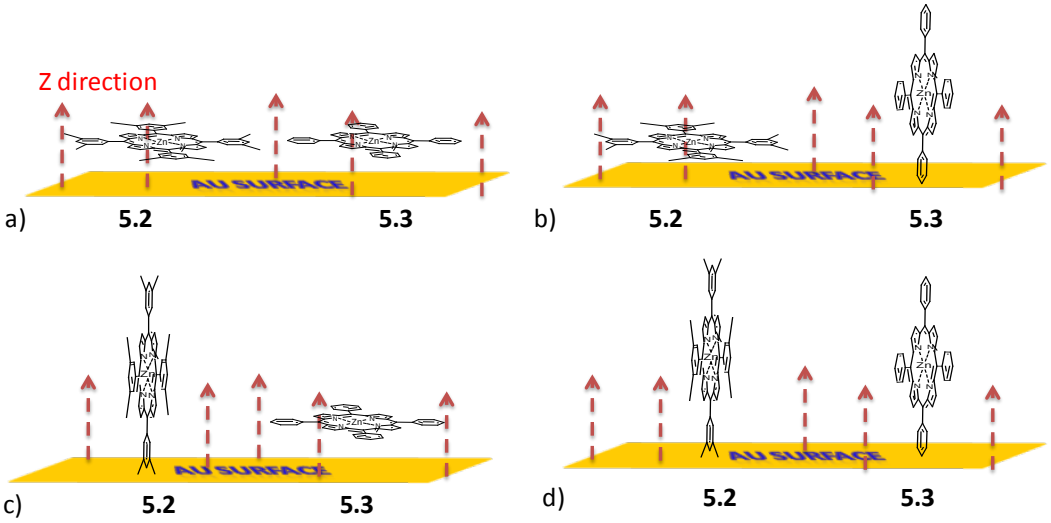

Fig 5-11: Schematic explanation of the orientation of **5.2** and **5.3** on the Au surface. a) both are horizontal, b) **5.2** is horizontal and **5.3** is perpendicular, c) **5.2** is perpendicular and **5.3** is horizontal, d) both are perpendicular. Red arrow represents the excitation laser in z direction.

the same since plasmon enhancement (E-field) is in z-direction (i.e. perpendicular to the surface). If the orientations of **5.2** and **5.3** are horizontal and perpendicular respectively (Fig 5-11 b), the common signals in the Raman spectrum of **5.2** should be stronger due the shorter distance to the surface. However, the observation from Raman spectra precluded these two possibilities. Therefore, the phenomena can be explained only when the orientation of **5.2** is vertical to the Au surface (Fig 5-11 c and d).

Based on the results obtained from the experiments with **5.1**, pH-dependence studies of **5.2** and **5.3** were carried out using the Au sol with the pH value in a range of 3 to 10 and the Raman spectra are shown in Fig 5-12. Signal enhancement of both compounds was obviously better under the acid conditions, and was more efficient as more protons were added into the samples. In the presence of alkali ions only solvent peak (labelled with star) observed in Raman spectra. All behaviours were same as those of **5.1**, and therefore the loss of the Raman signal as pH of the sol higher than 5 was believed caused by the depressed adsorption of analyte molecules onto the Au NPs surface and not related to the different substituted groups.

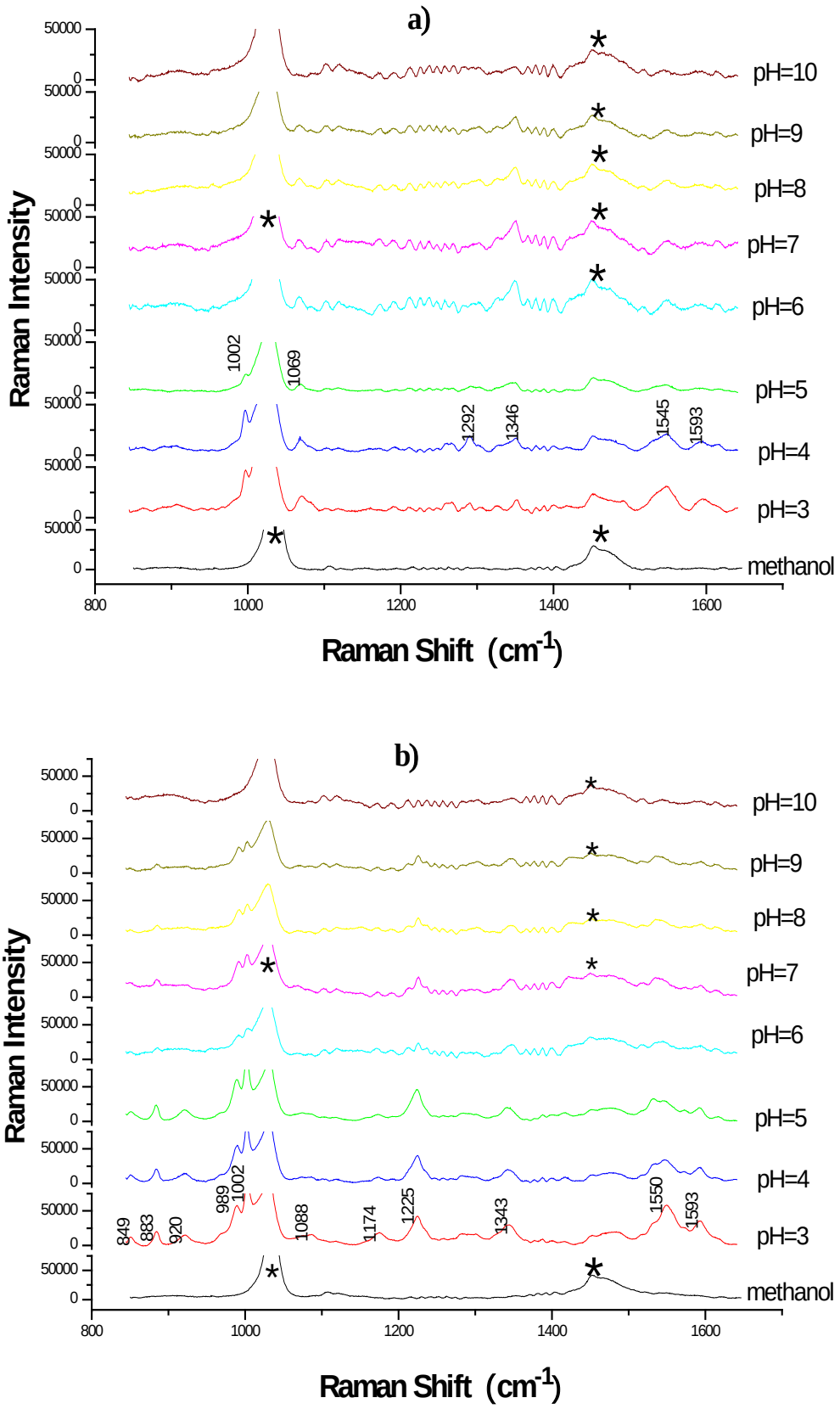

Fig 5-12: pH dependence study of Raman signals. a) Raman spectra **5.2** performed with the Au sol of different pH. b) Raman spectra of **5.3** performed with the Au sol of different pH.

5.3.3 Conclusion

Study of the porphyrin compounds suggested that the SERS from the Ag sol was more efficient than from the Au sol. However, Au sol was kept to be used by considering its biocompatibility along with the high stability (stable in the pH range of 2 to 9). When Au sol was used as the substrate, the SERS effect could be improved by either applying larger NPs or using Au suspension with higher concentration. For all three compounds (**5.1**-**5.3**), the interactions with the Au sol were promoted by adding H^+. Plasmon frequency of the resultant aggregated clusters and the laser frequency are in a similar range, guaranteeing efficient signal enhancement under this condition (i.e. acid condition).

5.4 Study of thiophene class

5.4.1 Compound 5.4

Thiophene is an aromatic herterocyclic compound (**5.4** in scheme I) which consists of four carbon atoms and one sulfur atom in a five-membered ring. It is used as reporter molecule for a number of reasons. First of all, the C-C bonds are electron-rich and easily polarized by the incident laser radiation and thereby strong Raman signals can be observed in Raman spectra of thiophene (Fig 5-13 a). Moreover, the sulfur atom has high affinity to the Au surface guaranteeing effective adsorption of analyte molecules which is necessary for SERS from the Au NPs surface. Thiophene can be readily polymerized in situ to form polythiophene with the help of an oxidant, such as $FeCl_3$, creating a possibility to set up Au-polythiophene core-shell particle that possess the Raman scattering ability of an Au sol system along with the chemical properties of polythiophene. Experimental procedures are described in Appendix I 4.5.3.

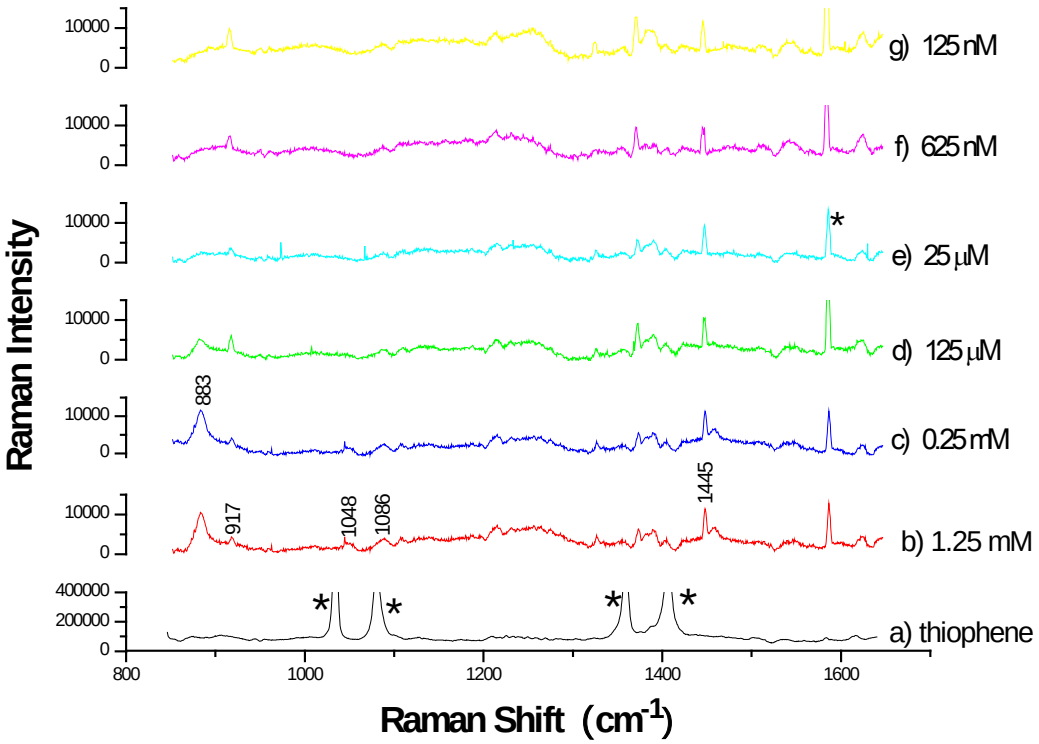

Fig 5-13: a) Raman spectra of **5.4** (100 %). b-g) Raman spectra of **5.4** of different concentrations using the Au-sol as substrate.

5.4.1.1 Concentration dependence study of Raman signals

The Raman signal is concentration dependent since it is believed that most signal enhancements in Raman spectra are from the analyte molecules adsorbed directly onto the surface of the Au NPs. That means the maximum signal enhancement can be achieved theoretically by covering the Au NPs' surface with a monolayer of the analyte molecules. To find the critical number of molecules (critical concentration of **5.4**) for the monolayer, a set of samples were prepared using the Au sol of pH 5.5 and thiophene solutions of different concentrations (nM to mM) prepared with ethanol and detected with Raman spectroscopy. Not all of them are shown in Fig 5-13 since they were quite similar. Peak intensity of the band at 1445 cm^{-1}, assigned to the C=C vibration of terthiophene [142], was analysed using the Origin 7.0 software package and is plotted versus the concentration of **5.4** in samples (Fig 5-14). It was found that the intensity varied irregularly at concentration lower than 25 μM, assumed due to either nonhomogeneous location of molecules in the specific places of the Au sol or random irregular formation of hot spot, and increased continuously after the critical point of 25 μM. Therefore, the concentration of 25 μM was chosen for the following polymerization study.

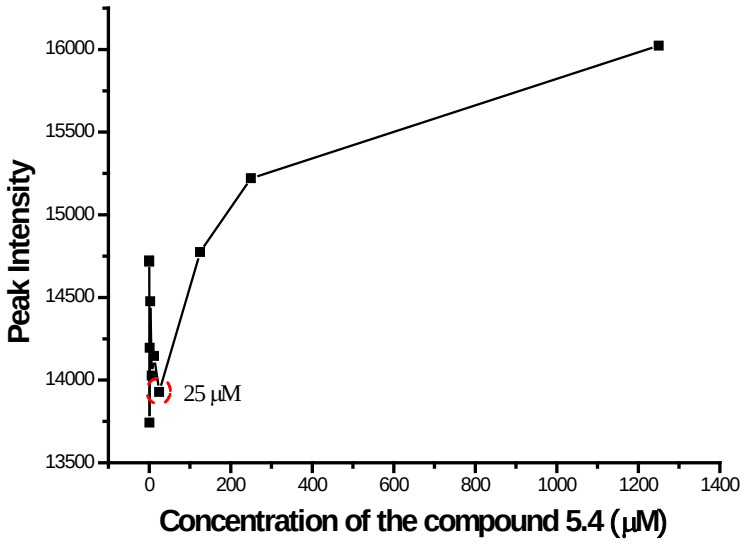

Fig 5-14: Correlation between the intensity of the band at 1445 cm^{-1} and the concentration of **5.4.** All data were calculated with software package of Origin 7.0.

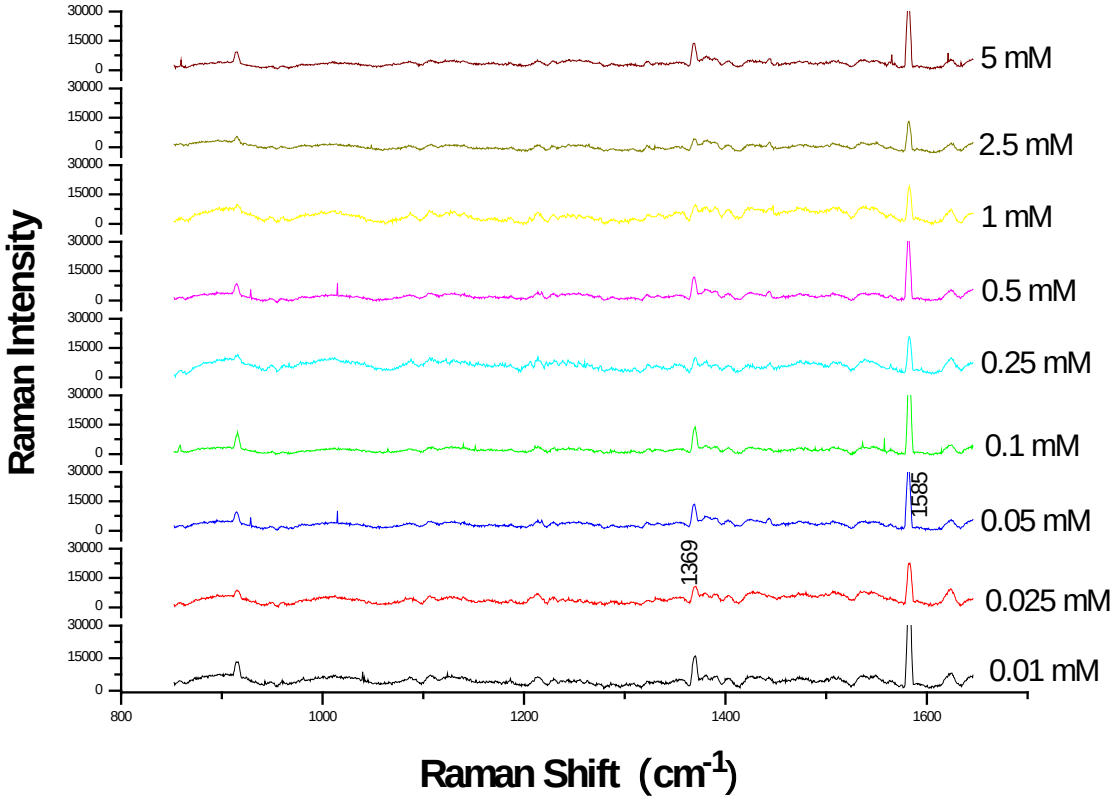

Fig 5-15: Raman spectra of **5.4** (25 μM) in the Au sol with KCl of different concentrations. The two numbered bands are laser lines.

5.4.1.2 Signal enhancement in the presence of KCl

To improve the signal enhancement of the band at 1445 cm^{-1}, KCl was added to the mixtures of the Au sol and the thiophene solution. Different concentrations of KCl were tried and the Raman spectra are shown in Fig 5-15. All spectra indicated that the addition of strong salt of KCl led to disappearance of the band at 1445 cm^{-1}. Two intense bands at 1369 and 1585 cm^{-1} were caused by laser excitation. That means the oxidation of thiophene was depressed by the salt of KCl.

5.4.1.3 Oxidation caused by $FeCl_3$

The experiments discussed in 5.5.1 and 5.5.2 suggested that the oxidation of thiophene on the surface of Au NPs should be processed in the absence of KCl. Fig 5-16 showed the spectra of **5.4** (25 μM) recorded in the absence (a) and

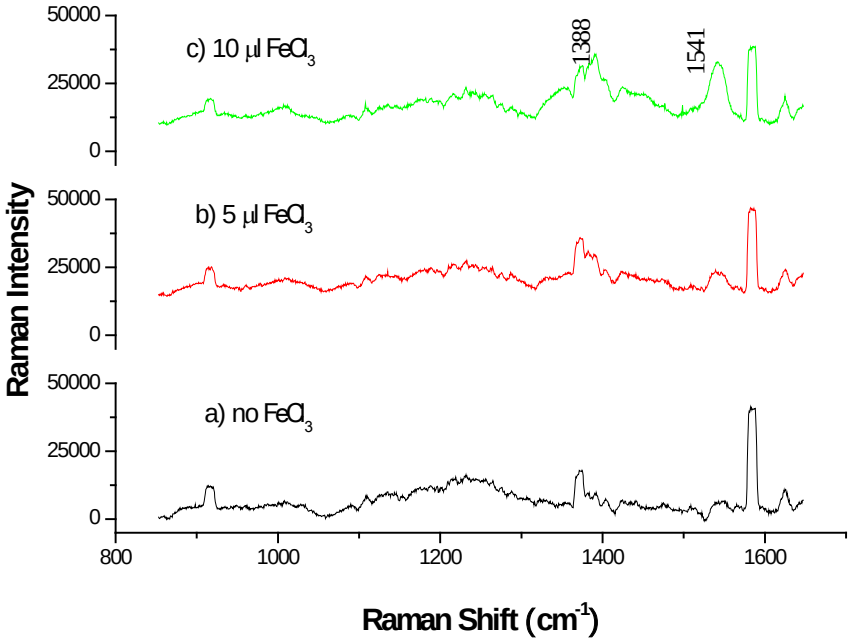

Fig 5-16: Raman spectra of **5.4** recorded a) before adding the oxidant of $FeCl_3$, b) after adding 5 µl $FeCl_3$ (0.1 M) and c) after adding 10 µl $FeCl_3$.

presence (b and c) of the oxidant of $FeCl_3$. The band between 1360 to 1413 cm^{-1} (Fig 5-16), caused by the C-C vibration of terthiophene [142], indicated the interaction of the thiophene molecules and Au NPs. The intense band at 1541 cm^{-1}, associated with the asymmetrical vibration of C=C band of terthiophene [143], demonstrated that thiophene molecules were oxidized by $FeCl_3$ with terthiophene as the product. Moreover, intensity of the band 1541 cm^{-1} increased along with the increased amount of oxidant (from spectrum a to c).

5.4.2 Compound 5.5

It has been reported that EDOT is capable of reducing Au salt and yielding PEDOT coating on the surface of Au NPs [144, 145]. Hence, we assumed that EDOT should be a good option as the Raman signal reporter for our investigation (experimental procedures in Appendix I 4.5.4). Spectrum (a) shown in Fig 5-17 is the absorption spectrum of a sample prepared by mixing EDOT solution with the Au sol. Monodispersed and aggregated Au NPs were present, with weak bands at 525 nm and intense band around 701 nm respectively. Meanwhile, two tiny peaks at 560 and 583 nm beside the plasmon resonance band of the Au NPs were

observed, which were also found in absorption spectrum of commercial PEDOT solution (spectrum c in Fig 5-17). Therefore, it was assumed that the EDOT molecules interacted with Au sol, and oligomers of EDOT were possible products.

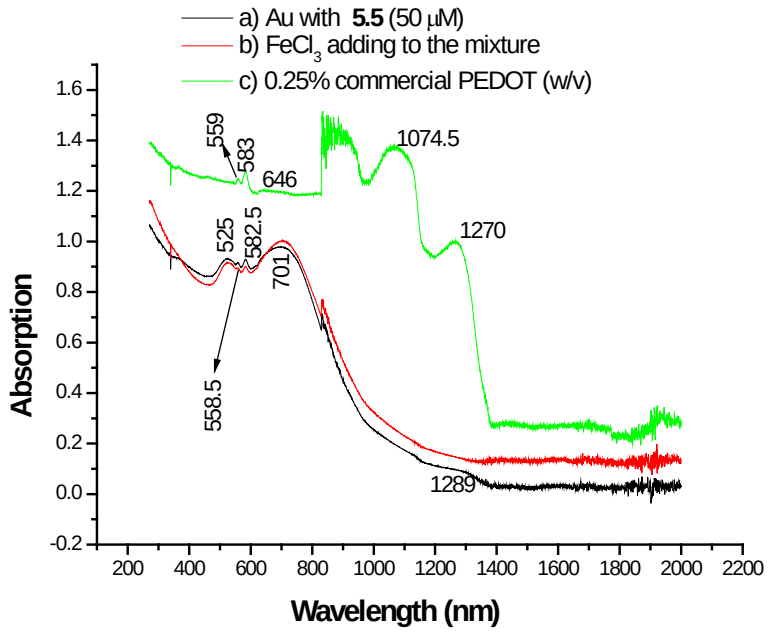

Fig 5-17: UV-Vis absorption spectra of a) sample comprising **5.5** and the Au-sol, b) the sample after adding the oxidant of $FeCl_3$ and c) 0.25 % commercial PEDOT (w/v). The noise in the range of 830-970 nm (spectrum c) was caused by grating change.

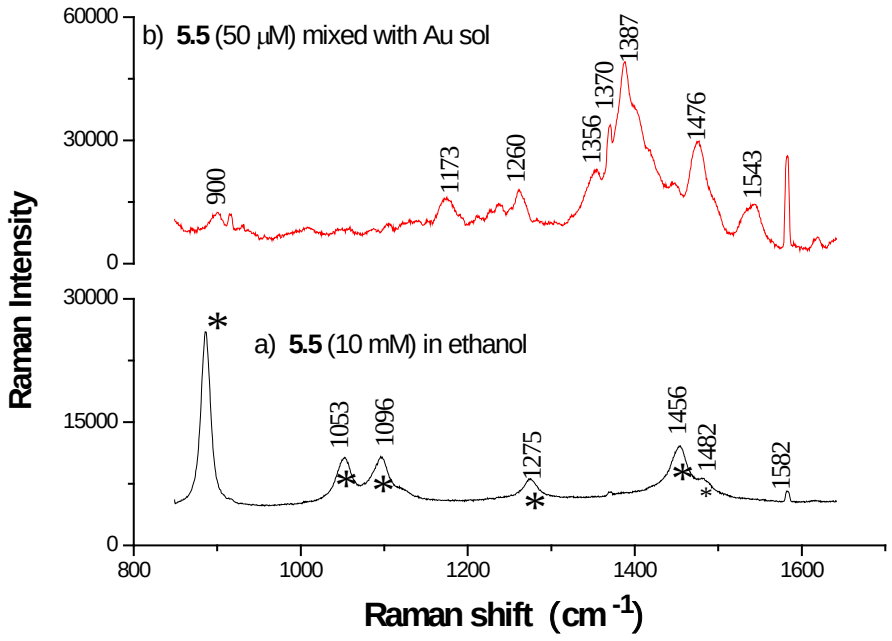

Fig 5-18: Raman spectra of **5.5** (10 mM) prepared with ethanol and the mixture of **5.5** (50 μM) and the substrate of the Au sol. Band at 1582 cm^{-1} is a laser line. Solvent bands are labelled with star.

Fig 5-18 shows Raman spectrum of 10 mM EDOT in ethanol and spectrum of the sample including the Au sol and 50 μM EDOT solution. Except the signals associated to the solvent of ethanol, no fingerprint band of EDOT was observed in spectrum (a) by comparing to the Raman spectrum of EDOT in a literature [146], and it was possible due to the low concentration of **5.5**. Spectrum (b) collected in the case of using Au sol as substrate was obviously different from the spectrum (a). Several intense bands were observed, such as 1173, 1260, 1370, 1387, and 1543 cm^{-1} band, indicating efficient signal enhancement by the Au sol. All of these bands were comparable to the Raman bands of PEDOT shown in literatures [147, 148], suggesting the polymerization of EDOT achieved by Au^{3+} ions.

5.4.2.1 Concentration dependence study of Raman signals

The concentration dependence was studied with a series of EDOT solutions (10 μM to 1 mM) using ethanol as diluents by Raman spectroscopy (spectra not shown here). Intensities (calculated with Origin 7.0) of the bands around 1173 and 1476 cm^{-1}, assigned to the C-S vibration and the C-H bending of the terthiophene molecules [142], and the symmetrical C=C vibration of phenyl group respectively, were plotted against the concentration of **5.5** in sample (Fig 5-19). Both patterns

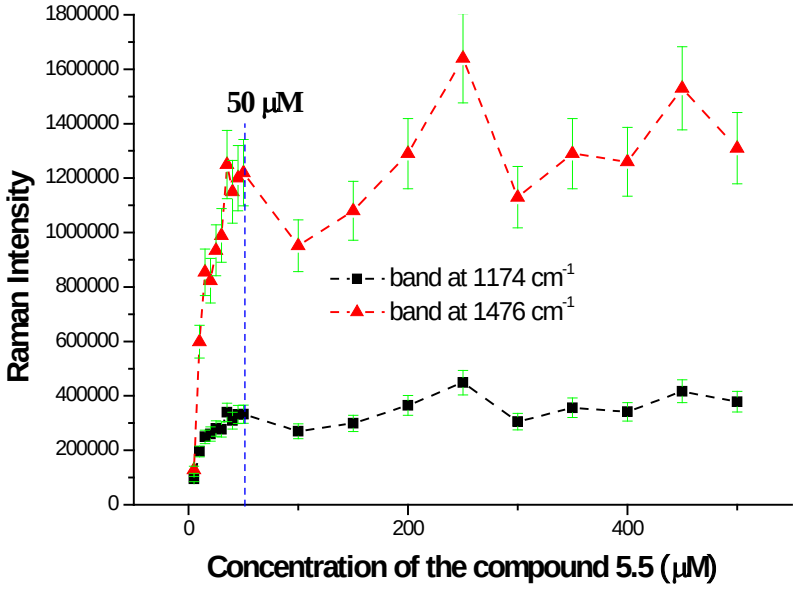

Fig 5-19: Correlation between the intensity of bands, 1174 cm^{-1} (■) and 1476 cm^{-1} (▲), and the concentration of **5.5**. All data were analysed with software of Origin 7.0. Error bar represents 10 % variation of the intensity.

were quite similar and suggested that the critical concentration, corresponding to forming a monolayer of the analyte molecules on the surface of the Au NPs, was close to 50 μM.

5.4.2.2 Oxidation caused by $FeCl_3$

Apart from the 1174 cm^{-1} band mentioned above, bands around 1387 and 1534 cm^{-1} were also associated to the terthiophene structure [142], demonstrating the oligomerization of **5.5** by Au^{3+} ions present in Au sol ($Au^{3+} + 3e^- \rightarrow Au$). $FeCl_3$ was used to increase reduction potential ($Fe^{3+} + 3e^- \rightarrow Fe$ or $Fe^{3+} + e^- \rightarrow Fe^{2+}$), and then ensure further polymerization. Fig 5-20 shows an unexpected fact that the presence of Fe^{3+} ions lowered the intensities of all these three signature bands, different from the phenomenon observed from **5.4** that further polymerization was achieved by the Fe^{3+} ions. However, the band intensity ratio of 1389 cm^{-1} to 1453 cm^{-1} was unchanged, indicating no change in polymer structure. The reduced band intensities were explained potentially with materials precipitating out of the solution caused by $FeCl_3$.

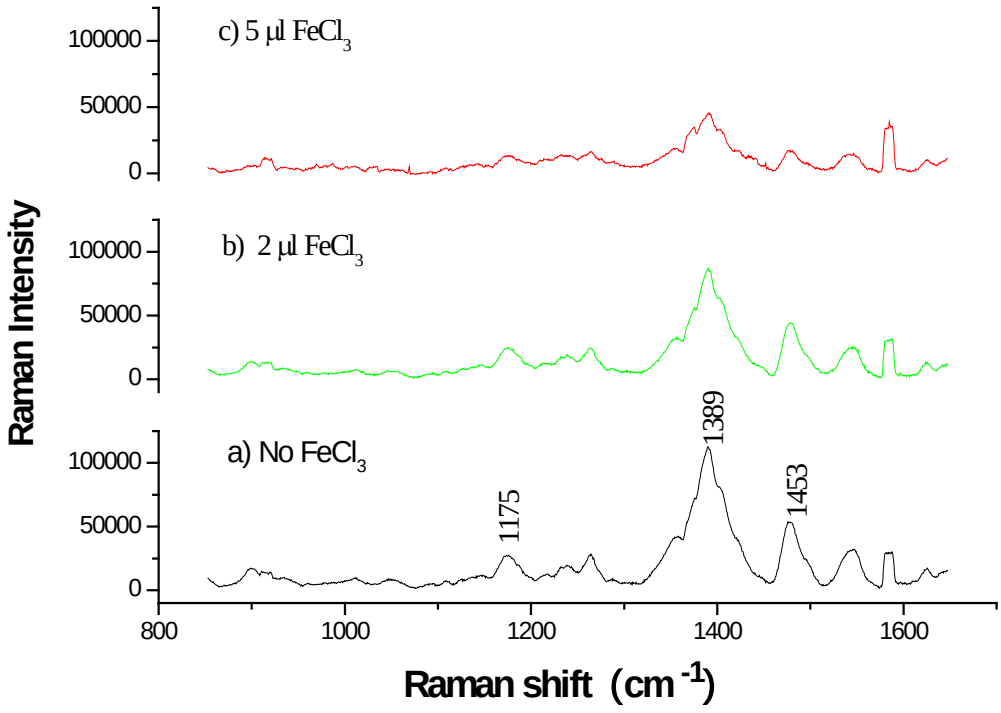

Fig 5-20: Raman spectra of **5.5** recorded a) before adding the oxidant of the $FeCl_3$, b) after adding 2 μl $FeCl_3$ (0.1 M) and c) after adding 5 μl $FeCl_3$.

5.4.3 Conclusion

As two important members of thiophene class, **5.4** and **5.5** were studied. Both of them could be partially oxidized by the Au^{3+} ions present in the Au sol and terthiophene structures as product were observed. Concentration dependence studies indicated that the critical concentration of **5.4** and **5.5** in samples, corresponding to maximum signal enhancement, were 25 and 50 μM respectively. KCl was added into the samples of **5.4** and it was found that it led to reduced signal enhancement. $FeCl_3$ was introduced to improve the reduction potential for further oxidation of both **5.4** and **5.5**. However, further polymerization was only achieved as Fe^{3+} ions were added to **5.4**.

5.5 Study of substituted terthiophene

As an important member of the conducting polymer family, terthiophene has been studied a lot with different techniques [142, 143, 149-153]. Works related to interfacial synthesizing nanostructures of conducting polymers [154, 155] as well as interfacial fabrication of nanoparticles [144, 156] show the possibility to use substituted terthiophene as RRM. Compounds **5.6-5.8** with different functional groups (Scheme I) were studied and experimental details are shown in Appendix I 4.5.5-4.5.6.

The sodium citrate reduced spherical Au NPs were also used here, of which the size was around 15.8 ± 2.66 nm confirmed by the TEM image shown in Fig 5-21 (a). They aggregated as mixing with the compounds (Fig 5-21 b), and consequently the hotspots for SERS were generated. Maximal concentration of the Au NPs was 6.02 x 10^9 NPs/ml, calculated based on the assumption that all of Au^{3+} ions have been reduced to Au^0 by the reductant.

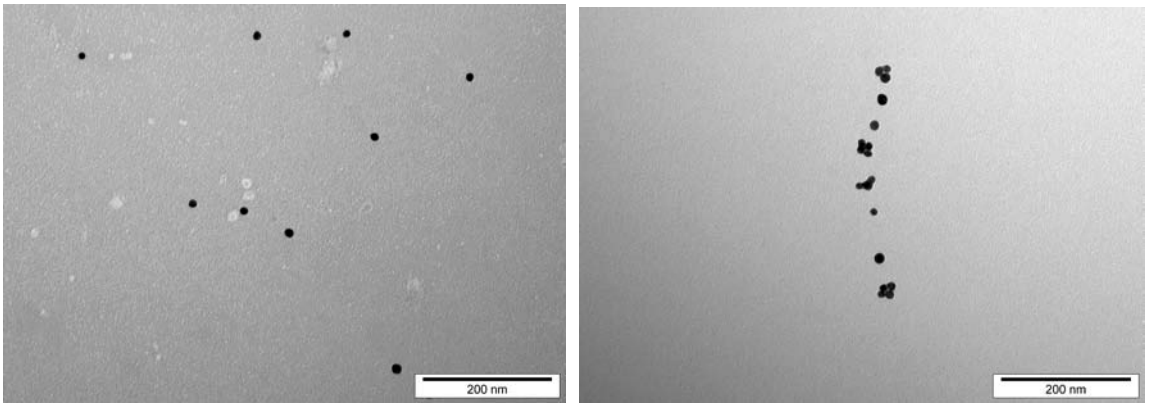

Fig 5-21: TEM images of a) the Au sol and b) aggregated Au NPs due to the interaction with the analyte molecules. The scale bars in both are 200 nm.

5.5.1 Compound 5.6

The absorption spectrum of **5.6** in $CHCl_3$ was shown in Fig 5-22 (spectrum (a)) with one intense peak at 319.5 nm and two side shoulders around 293.5 and 356 nm, corresponding to two independent chromophores in the ground state [157]. The interaction between **5.6** and the Au sol was strong, demonstrated by the

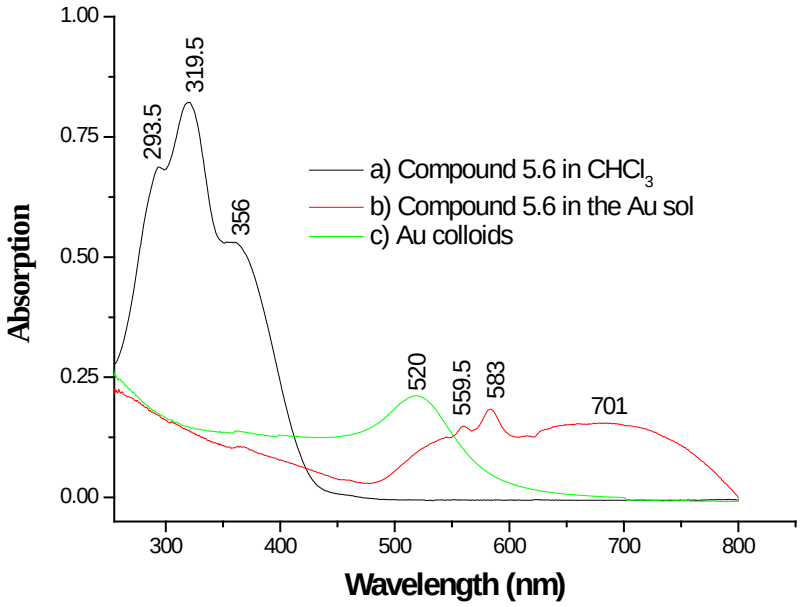

Fig 5-22: Absorption spectra of a) **5.6** in $CHCl_3$, b) the mixture of **5.6** and the Au-sol and c) the Au-sol used for study.

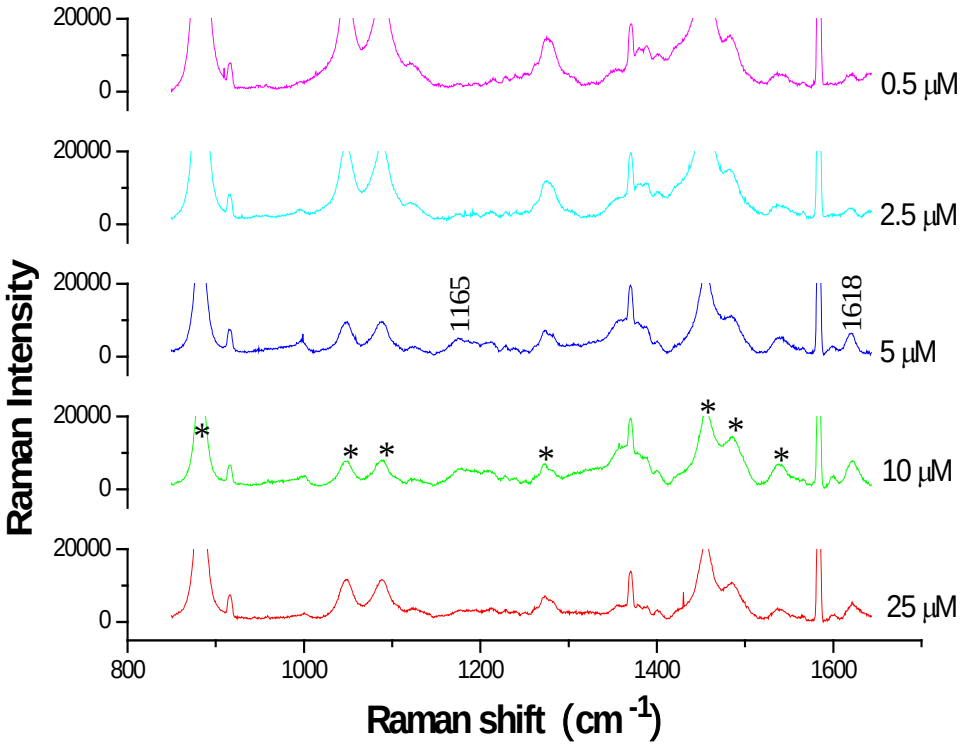

Fig 5-23: Raman spectra of **5.6** of different concentration recorded using the Au sol as substrate. The concentrations of **5.6** (from top spectrum to bottom one) were 0.5, 2.5, 5, 10, and 25 μM. Solvent bands are labelled with star..

two fresh peaks at 560 and 583 nm, the reduced plasmon resonance band of monodispersed Au NPs at 520 nm, and the fresh broad band in longer wavelength range.

Fig 5-23 showed Raman spectra of **5.6** using the Au sol as substrate. Although the band around 1165 cm^{-1} and 1618 cm^{-1} were observed in some cases, assigned to the formation of styryl sexithiophene dication [143] and ethenyl stretch linked to terthiophene and phenyl ring, **5.6** is not an ideal RRM because the signature bands were too weak compared the solvent bands labelled with star, caused by the long tail of $–OC_{10}H_{21}$ group which spaced the terthiophene structure from the Au surface.

5.5.2 Compound 5.7

Spectrum (a) shown in Fig 5-24 depicts a typical absorption spectrum of **5.7** (NO_2-pe3T) with an intense band at 344 nm and an evident shoulder around 409 nm. When **5.7** was mixed with the Au-sol, the intensity of the 344 nm band

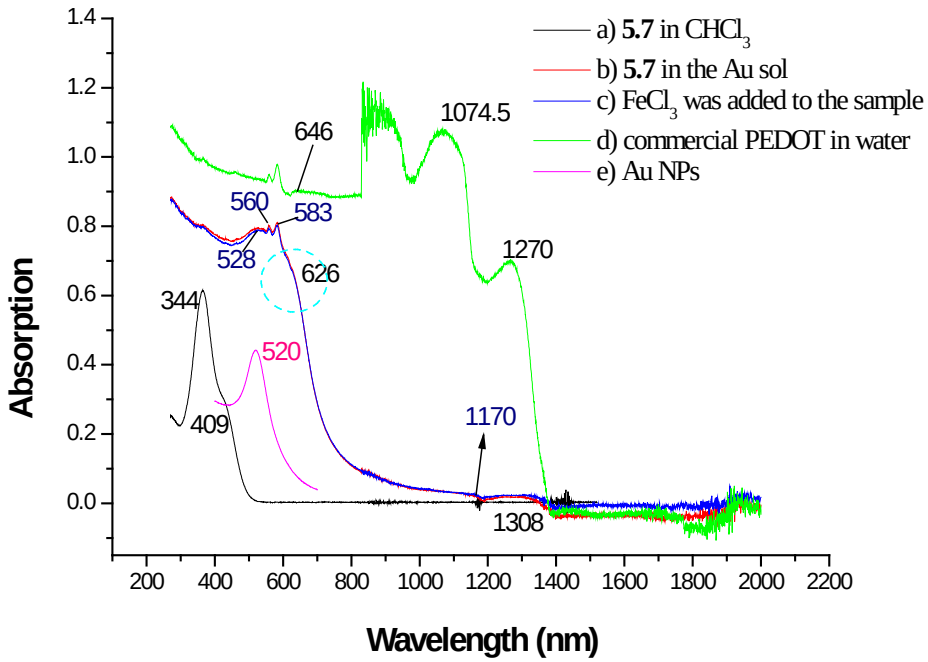

Fig 5-24: UV-Visible absorption spectra of **5.7** in CHCl3 (a), **5.7** (2.5 μM) with Au-sol before (b) and after (c) adding $FeCl_3$, commercial PEDOT (d) in Milli.Q water and Au nanospheres in Milli.Q water (e). The noise in the range of 830-970 nm (spectrum d) was caused by grating change.

related to the monomer of **5.7** dropped and the shoulder was absent (spectrum b), suggesting the consumption of monomer in the sample. Meanwhile, a red shift of 8 nm from the plasmon resonance peak of monodispersed Au NPs (520 nm, spectrum e) was observed corresponding to structures of Au NPs in polymer [158]. Two peaks on lower energy side (around 560 nm and 580 nm), compared well to those shown in spectrum (d) of the commercial PEDOT and are an indicative of sexithiophene [159]. The distinctive transitions at about 626 nm, 1170 nm and 1308 nm, once again comparable to the reference spectrum of PEDOT in which they were detected at similar frequency at 646 nm, 1074.5 nm and 1270 nm, were created by the oxidation of the NO_2-pe3T monomer [160]. Taking account of the difficulty of polymerization of terthiophene in solution, all changes in absorption spectra demonstrated that the monomers of **5.7** were oxidized by the free Au^{3+} in short time corresponding to the catalytic activity of the Au NPs. More details will be discussed with Raman spectra later.

5.5.2.1 Oxidation caused by Au^{3+}

The function of the Au-sol in the interaction was further investigated with Raman spectroscopy and the related spectra are shown in Fig 5-25. Comparing the spectrum of **5.7** and the corresponding solvent spectrum (spectrum a and b), it was believed that new peaks at 1108 cm^{-1}, 1340 cm^{-1}, 1460 cm^{-1}, 1530 cm^{-1}, 1594 cm^{-1} and 1628 cm^{-1} were caused by the neutral monomer of **5.7**. To assign them, a comparison with other terthiophenes available in literature [142, 160] was conducted. The intense band of 1340 cm^{-1} was a signature of the nitro group ($-NO_2$) which has been calculated around 1333 cm^{-1}. The peak measured at 1460 cm^{-1} related to a symmetrical C=C stretching mode localized on the terthiophene unit was calculated at 1446 cm^{-1}, and the experimental peak at 1530 cm^{-1} (calculated at 1524 cm^{-1}) represented a asymmetrical C=C stretching. The peak at 1594 cm^{-1} calculated at 1593 cm^{-1} presented the phenyl symmetrical stretching mode. C=C stretching mode of the ethenyl side-chain was exhibited by the peak at 1628 cm^{-1} that was calculated at 1620 cm^{-1}.

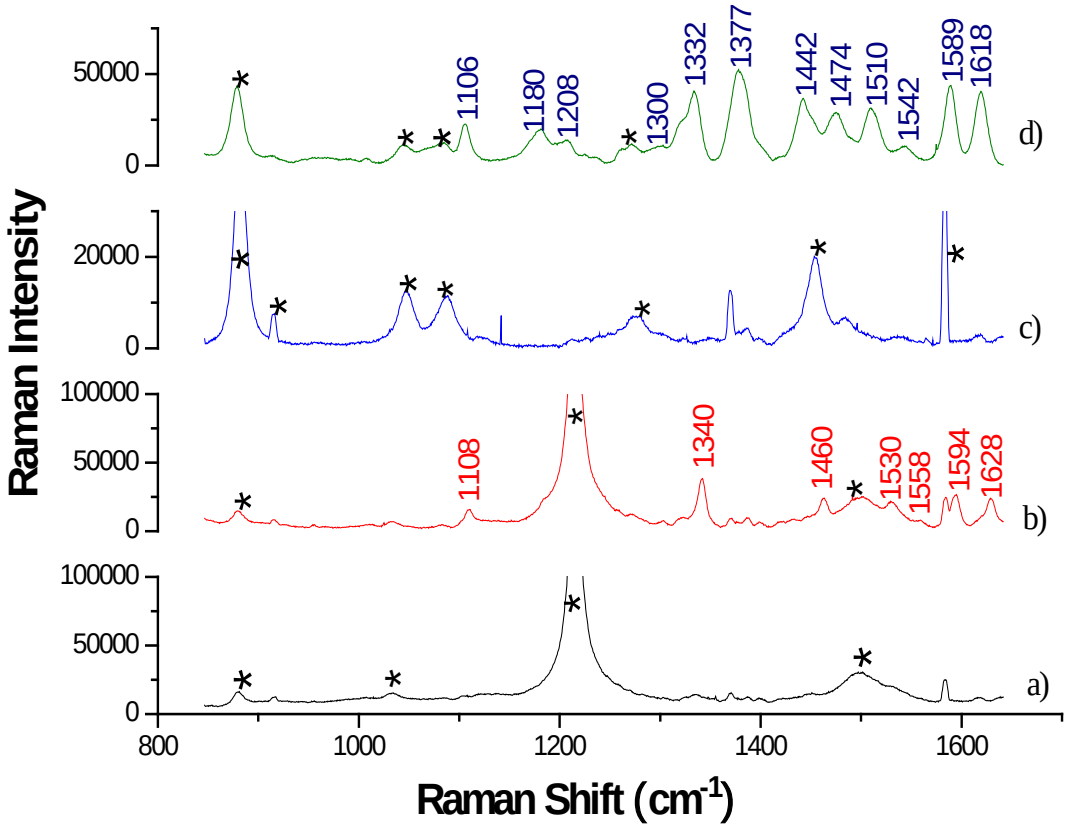

Fig 5-25: Raman spectra of a) $CHCl_3$, b) **5.7** (2 mM) in solvent of $CHCl_3$, c) 1% $CHCl_3$ in ethanol (v/v), d) **5.7** (10 μM) mixed with equivalent volume Au-sol. The solvent peaks are labelled with star.

The spectrum d (Fig 5-25) recorded in the presence of the Au sol was distinctively different from the spectrum b. The bands at 1106 cm^{-1}, 1332 cm^{-1} and 1589 cm^{-1} were still present at quite similar frequencies. Apart from these three, a fresh weak band at 1180 cm^{-1} and clear downshifts of band 1530 cm^{-1} to 1510 cm^{-1} and band 1628 cm^{-1} to 1618 cm^{-1}, representing C-S stretching of thiophene, asymmetrical C=C stretching mode and ethenyl stretching respectively, were observed and explained by the state change from neutral to radical cation reported by Clark et al. [143]. Moreover, appearance of strong band around 1377 cm^{-1} indicative of inter C-C stretching between terthiophene structure, and band around 1442 cm^{-1} coming along with the oxidation of pe3T [143], revealed that the first step oxidization of the NO_2-pe3T (to radical cation (NO_2-pe3T$^{\bullet+}$)) was achieved with free Au^{3+} ions and mediated by the Au NPs. All phenomena supported the

conclusion from UV-Vis absorption spectra (Fig 5-24) which stated the changes caused by the dimerization. The weak enhanced band of 1442 cm^{-1} also suggested the presence of dimers (sexithiophene) instead of polymers in samples before adding $FeCl_3$. Herein, the electromagnetic field enhancement generated around the hotspots was more reasonable explanation for the recorded SERS spectrum d.

5.5.2.2 Effects of the reaction conditions on the Raman signals

It has been discussed before that only information of the analyte molecules linked to the hotspots will be reported efficiently. In another word, the SERS signals will be saturated according to the numbers of NPs present in samples. To reveal that, a series of **5.7** (0.05 – 50 µM) were prepared from the stock solution of **5.7** (2 mM in $CHCl_3$) using ethanol as diluents. The peak areas of the two bands of 1180 cm^{-1} and 1332 cm^{-1} were analysed against the concentration of the compound **5.7** and are shown in Fig 5-26. The signals were still be detectable even in the case of using **5.7** of 0.05 µM suggested that less than 10 molecules

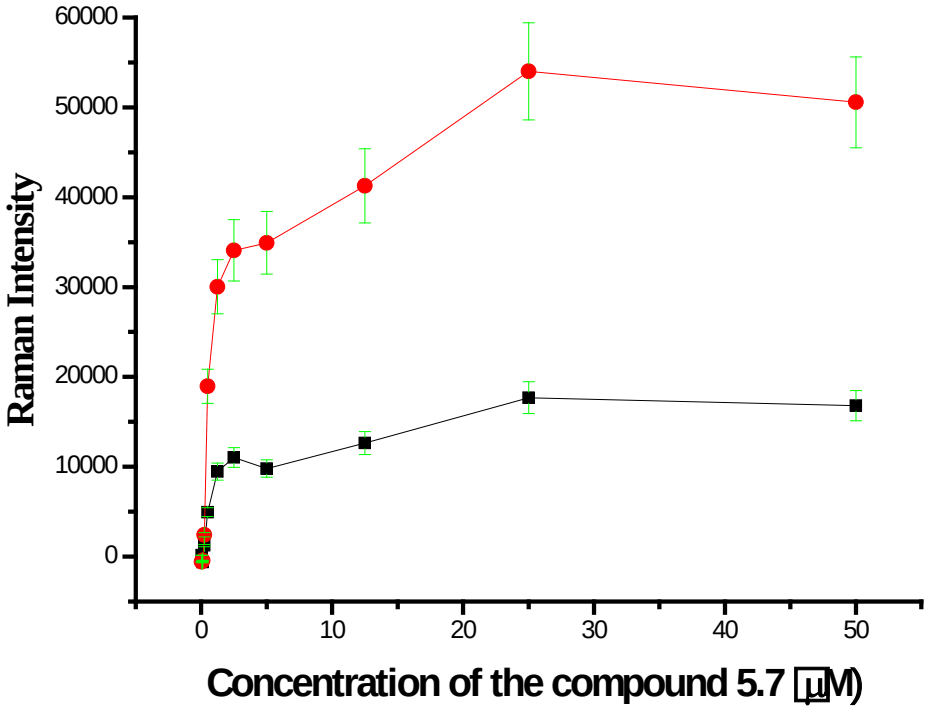

Fig 5-26: Peak areas of bands at 1180 cm^{-1} (■) and 1332 cm^{-1} (●) are plotted versus the concentration of **5.7**. Error bar represents 10 % variation of the intensity.

could be detected per Au NP (the concentration of the sample (0.05 μM) multiplied by 6.02 x 10^{23} molecules/mole and then divided by the NPs' concentration of 6.02 x 10^{9} NPs/mL), and indicated high potential of **5.7** to be an efficient Raman signal reporter. Both traces suggested that for the Au-sol (6.02 x 10^{9} NPs/mL) used currently, the maximum signal enhancement can be achieved by forming a monolayer of **5.7** on the surface of the Au NPs, of which the concentration was close to 5 μM. Maximum number of the analyte molecules adsorbed onto the surface of a 15 nm (diameter) sized sphere was assumed around 500 corresponding to the critical concentration.

Effects of oxidant diffusion on the signal enhancement were studied with stirring and sonication using the sample containing **5.7** of 5 μM, the recorded spectra were compared to the one obtained with pipetting. No evident difference was presented as very small volumes of samples were used. Reaction time dependence of the SERS signals was studied by monitoring the intensity of the

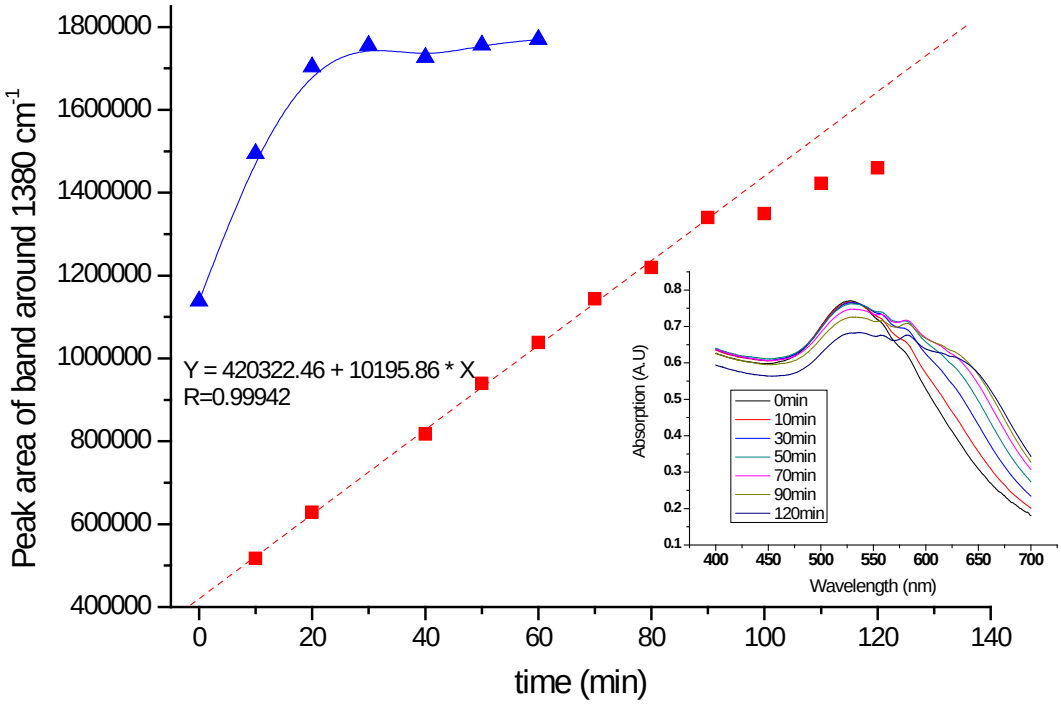

Fig 5-27: The peak areas of the band around 1380 cm^{-1}, before (■) and after (▲) adding the Fe^{3+}, are plotted versus time. The dash line was the linear fit in 90 minutes. The insert figure shows absorption spectra recorded at different time before adding the Fe^{3+}.

band of 1380 cm^{-1} over time and are plotted in Fig 5-27. Intensity of the band increased linearly up to 90 minutes, suggesting that the free Au^{3+} ions in the Au sol were used up by the sample containing 6.0 x 10^{14} analyte molecules in 90 minutes and the dimerization process of the sample stopped consequently. Independently, the insert absorption spectra recorded over time showed that the shoulder at about 630 nm, corresponding to resonance absorption of the dimers achieved by the oxidation of **5.7** [160], grew continuously for ca. 90 minutes, supporting the conclusion from the SERS spectra. If 90 minutes is required to consume all Au^{3+} present in samples, it can be understood that the absorption bands of 626 nm, 1170 nm and 1308 nm shown in Fig 5-24, associated with the oxidation of the NO_2-pe3T monomer [160], were weak because the incubation time for that sample was only 10 minutes.

5.5.2.3 Oxidation caused by $FeCl_3$

Once all free Au^{3+} ions were consumed, the oxidant of $FeCl_3$ was added. The Au NPs showed high stability in the mixture even in the presence of 1 mM $FeCl_3$ may be explained with the belief that the dimers generated by the Au^{3+} acted as stabilizers of the Au NPs here. Change of the Raman spectrum was evident once Fe^{3+} ions were added (Fig 5-28 a and b). The band around 1165 cm^{-1} indicative of a styryl sexithiophene dication [143] appeared and continuously grew, illuminating the change between radical cation to dication of **5.7** corresponding to increased amount of the oxidant (Fe^{3+}) present in the sample. Intensity of the band around 1370 cm^{-1}, in answer to the amount of dimers in solution, was also promoted as adding Fe^{3+} to the sample. Meanwhile, solvent signals were reduced, i.e. SERS enhancement has increased. Considering the resonance absorption of the dimer (630 nm) close to the excited laser wavelength (632.8 nm), it was concluded that resonant SERS spectrum (spectrum c) has been recorded in the presence of more Fe^{3+} (0.625 μmol). Due to the resonant enhancement, more structure information were obtained, such as C-C out-of-plane bending vibration of ethane (975 cm^{-1}) and C-C stretching vibration of phenyl skeletal (990 cm^{-1})

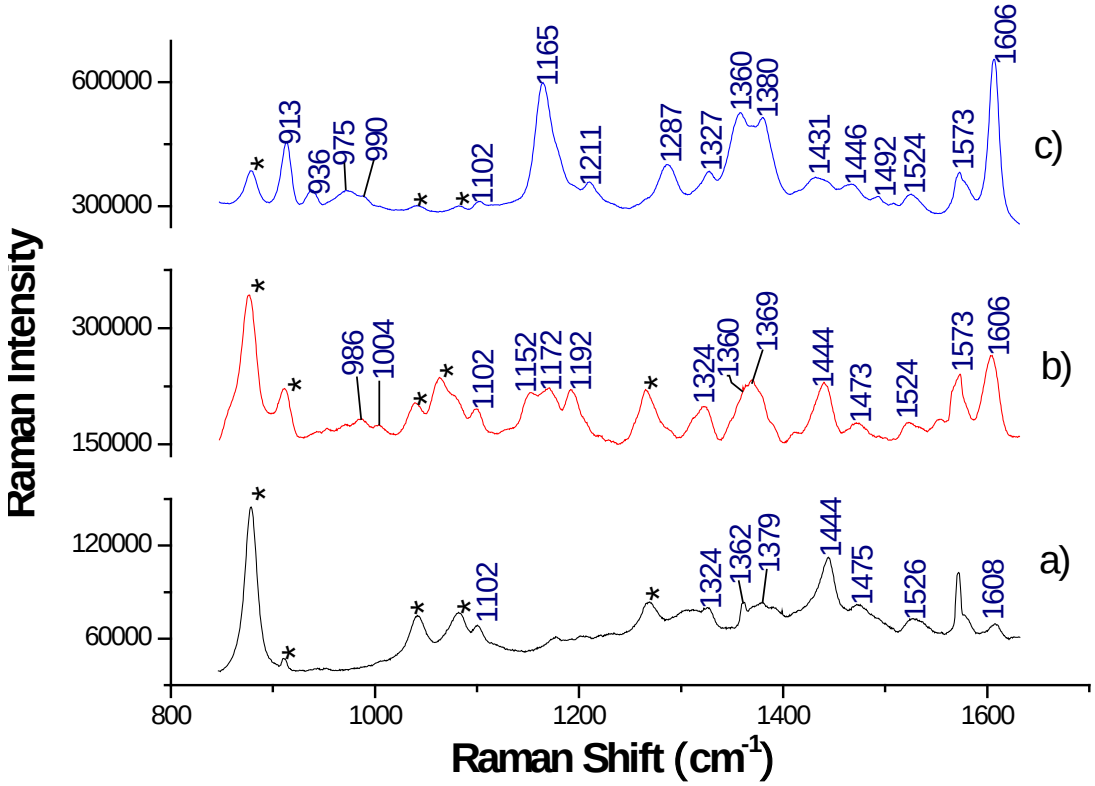

Fig 5-28: Raman spectra of a) **5.7** (5 μM) mixed with Au-sol according a volume ratio of 1:1, b) 0.125 μmol Fe^{3+} added to the mixture, c) another 0.5 μmol Fe^{3+} added to the mixture. Solvent peaks are labelled with star in each spectrum.

[142]. The band assigned to ethenyl stretch coupled to both terthiophene and phenyl ring, shifted from 1628 cm^{-1} (neutral species, spectrum b in Fig 5-25) to 1618 cm^{-1} (radical cation, spectrum d in Fig 5-25) corresponding to the oxidation caused by the Au^{3+}, and then shifted another 12 cm^{-1} down to 1606 cm^{-1} (dication) related to the further oxidation caused by the Fe^{3+} (Fig 5-28). The large down-shift seems to be induced by loss of double-bond character in ethenyl. All these changes revealed that the Fe^{3+} led to further electron loss of NO_2-pe3T$^{\bullet+}$. Similar experiments have been done to investigate the reaction rate of the further oxidation caused by the Fe^{3+} ions and result is shown in Fig 5-27. It was found that it only took about 20 minutes to arrive at steady state. The shorter reaction time can be potentially argued by the much higher concentration of Fe^{3+} and stronger ability for oxidation.

5.5.2.4 Characterization of dimer-Au nanocomposites

TEM and SEM (with EDX) were used to reveal the 3-dimensional structures of the samples. In TEM image shown in Fig 5-29, particles with a diameter around 100 nm were observed in both stages of the oxidation and were much larger than monodispersed Au NPs (circled particles). Contrast of signal to noise shown by these particles was quite similar to that shown by Au NPs. The quite dark signals suggested high electron density of the new structures. By considering brighter edge observed from image (b), the structures were assumed to be nanocomposites which were comprised of aggregated multiple NPs in the centre and outside capsule coat of the dimers of **5.7**.

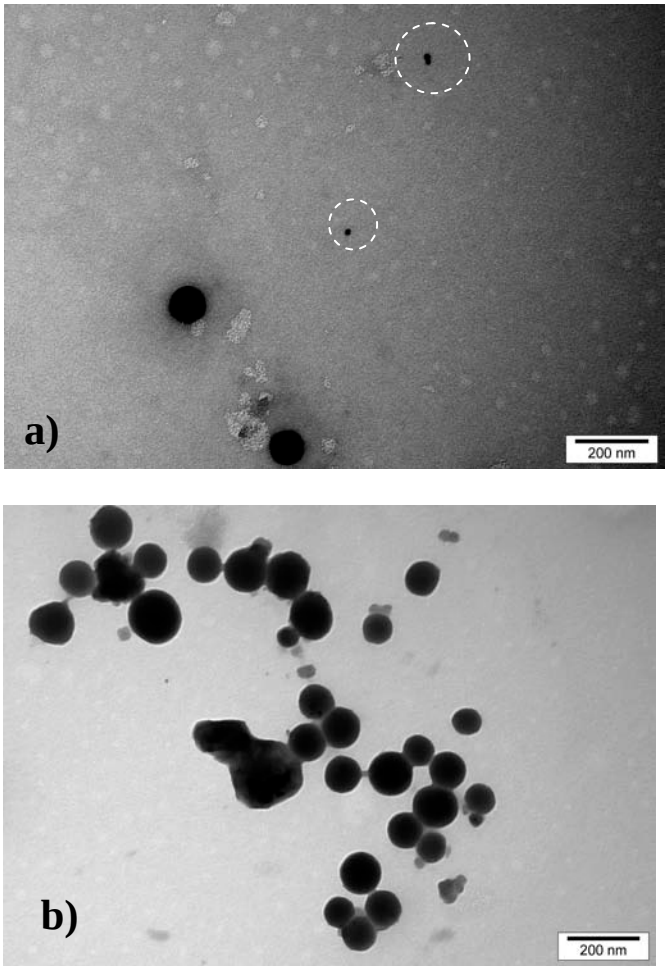

Fig 5-29: TEM images of taken before a) and after b) adding Fe^{3+} to the mixture (5 μM **5.7** and Au-sol). The scale bar in both images is 200 nm. The Au nanospheres are circled in a) image.

In SEM image taken with back scattered electron detector (BSD) (Fig 5-30 a), structures with a bright center were exhibited, suggesting the presence of heavy element which was Au validated by EDX (Fig 5-30 b). Overview image shown in Fig 5-30 c) demonstrated that transparent films were generated along with the interaction. Composition of the film can't be verified with EDX since it was too thin and the thickness was only about 100 nm (Fig 5-30 d). Image obtained with SED shown in Fig 5-30 e) stated that the general structures were leaf-shaped fractals which were assumed as a result of aggregation of the nanocomposites. High resolution image (Fig 5-30 f) showed the diameter of a single nanocomposite was in a range of 100 nm – 200 nm that was in agreement with the information obtained from TEM images.

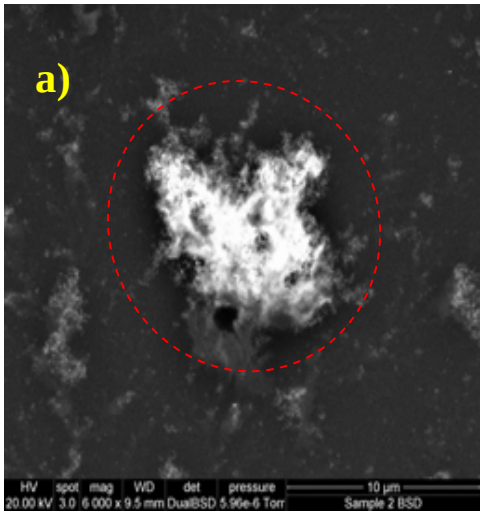

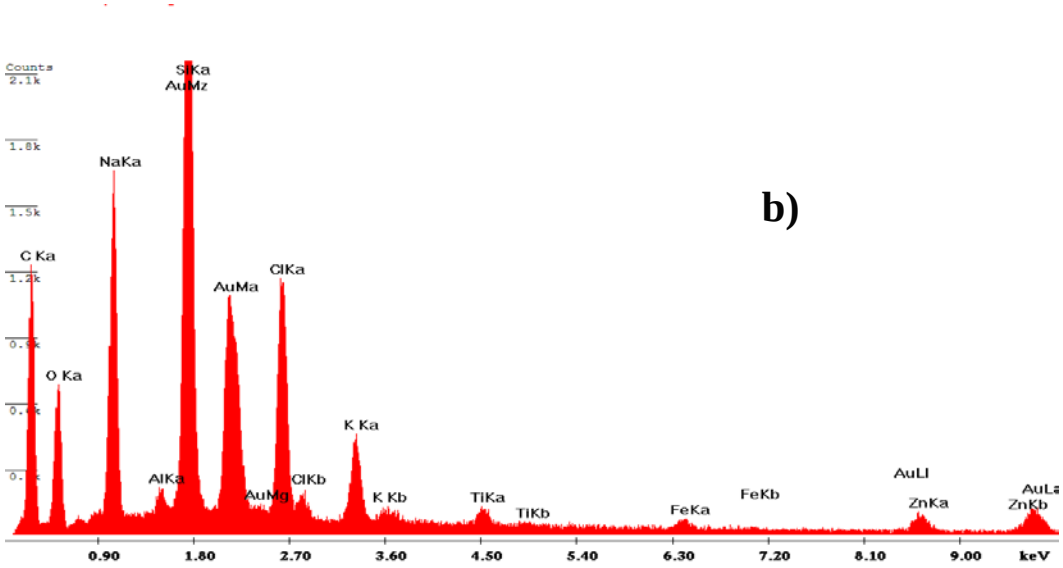

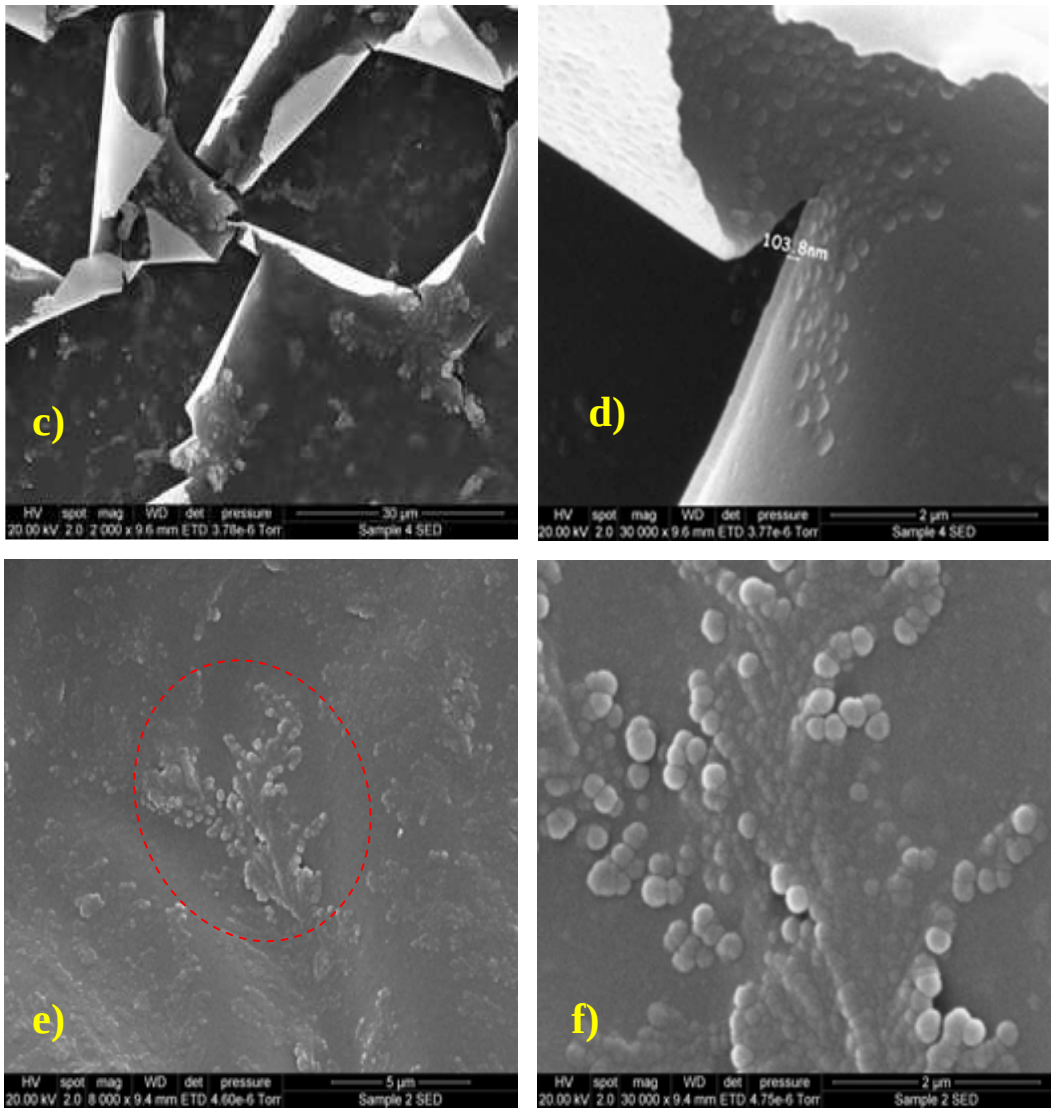

Fig 5-30: a) BSD image taken after adding Fe^{3+} to the sample composed of equivalent volume of **5.7** (5 μM) and Au-sol with a scale bar of 10 μm. The circled part was spotted for element analysis. b) EDX spectrum based on the circled part in a). c) Overview of the sample taken by SED with a scale bar of 30 μm. d) High resolution SED image of the transparent film shown in c) with a scale bar of 2 μm. e) Low resolution SED image of with a scale bar of 5 μm. d) Zoom in the circled part in c) with a scale bar of 2 μm.

In addition, dynamic light scattering was introduced to determine hydrodynamic diameters of scattering units in the sample. The diameter was monitored over time and the correlation is plotted in Fig 5-31. It was found that before adding the Fe^{3+} the initial size of the unit was about 90 nm and it continuously increased to a range of 130 nm – 140 nm in 20 minutes. In the following 100 minutes the reported size distribution was quite narrow, assigned by the lower SD. The addition of Fe^{3+} at t=120 mins led to a jump of approximately

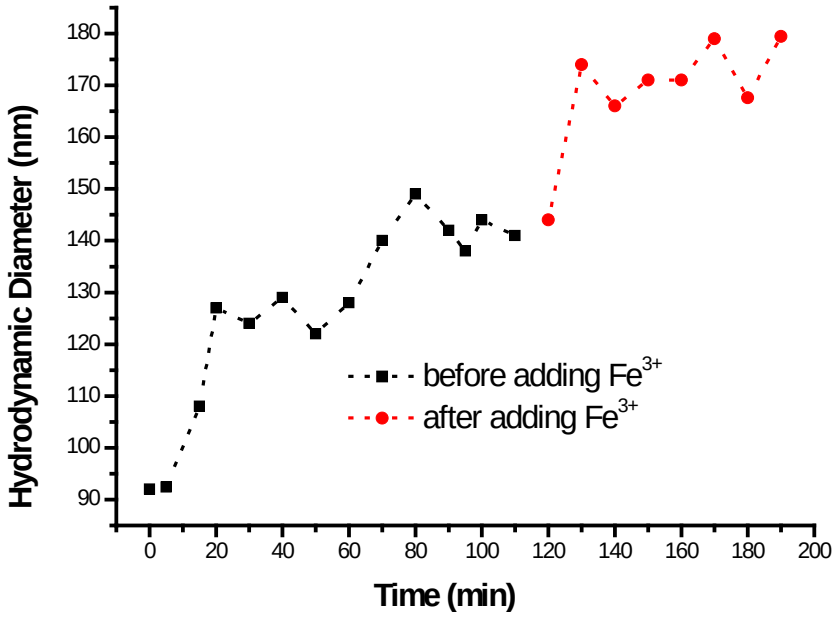

Fig 5-31: Correlation of the average hydrodynamic diameter and the reaction time. In the first 120 minutes, mixtures of the Au-sol and **5.7** (5 μM) were analyzed. $FeCl_3$ was added at t=120 minute.

40 nm (from 140 to 180 nm), assumed due to aggregation of the units. All information obtained with DLS were in consistent with those concluded from previous study.

5.5.3 Compound 5.8

5.8 was investigated following the same procedure for **5.7**. A single sharp peak at 332 nm observed in the absorption spectrum was assigned to resonance absorption of monomer of **5.8** (Fig 5-32 a). From absorption spectrum (Fig 5-32 b) taken in the presence of the Au-sol, it is observed that the plasmon resonance peak of the Au sol red shifted about 10 nm as a result of the coating dimers of **5.8**, followed by two peaks at 560 nm and 582 nm. Fresh shoulders around 630 nm, 1130 nm and 1301 nm represent oxidized **5.8**. Intensities of the last two shoulders increased obviously as the Fe^{3+} was added, different from the phenomenon observed from the spectrum (c) of the Fig 5-24. In the case of adding the Fe^{3+} into the mixture of **5.7** and the Au sol, the absorbance of the shoulders didn't increase. This difference indicated that **5.8** was easier to be oxidized, consistent with that reported by Clark et al. [142], group of $–NH_2$ is a stronger electron donator.

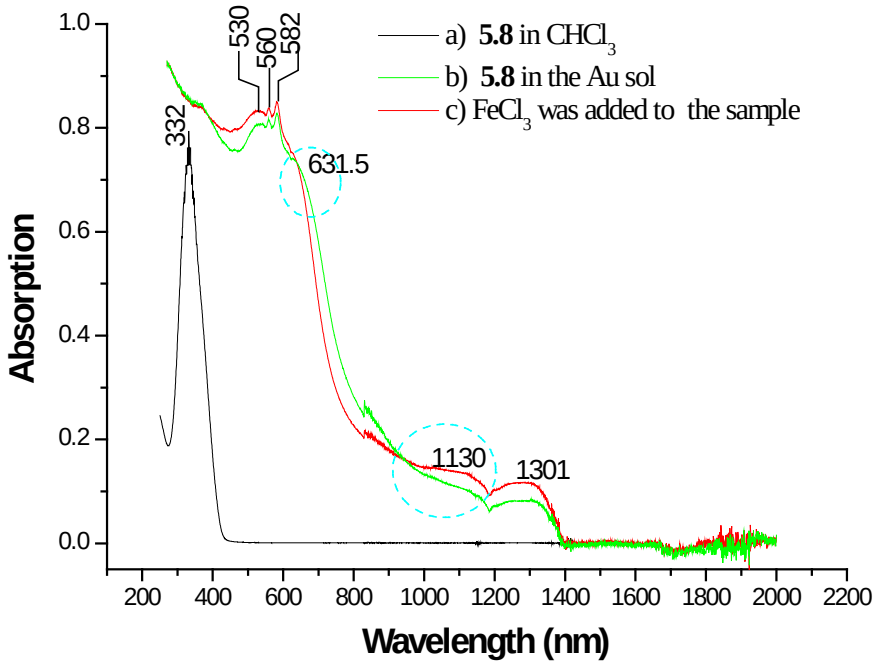

Fig 5-32: UV-Visible absorption spectra of **5.8** in CHCl3 (a), **5.8** (5μM) with Au-sol before (b) and after (c) adding $FeCl_3$.

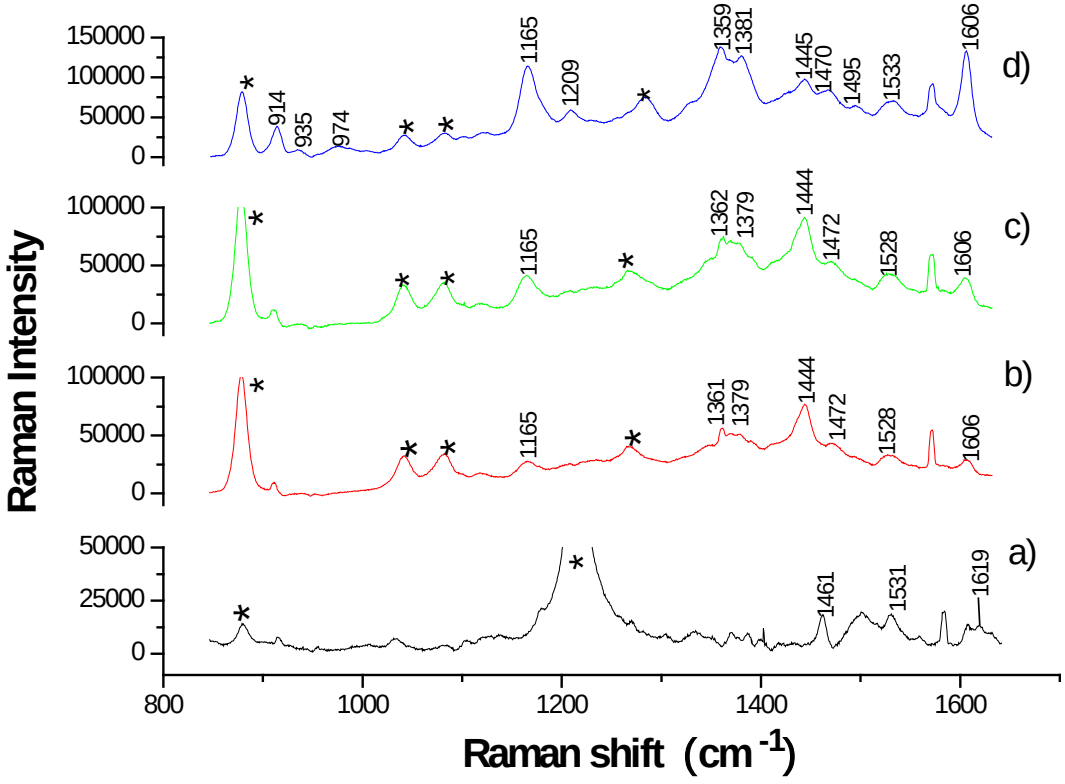

Fig 5-33: Raman spectra of a) **5.8** in $CHCl_3$, b) **5.8** mixed with Au-sol, c) 0.125 μmol Fe^{3+} added to the mixture, d) 0.625 μmol Fe^{3+} added to the mixture. Solvent peaks are labeled with star in each spectrum.

Fig 5-33 shows the Raman spectra of **5.8** collected under different conditions. Spectrum (a) shares a number of common figures with the spectrum (b) shown in Fig 5-25, such as intense bands at 1461 cm^{-1}, 1531 cm^{-1} and wide band around 1619 cm^{-1}, since the quite similar chemical structure of **5.7** and **5.8**. Absence of the band at 1340 cm^{-1}, which was present in the spectrum of **5.7,** supported that it was the fingerprint of the group of $-NO_2$. Spectrum (b) was recorded using the Au sol as the substrate. The presence of Au-sol caused the dimerization of **5.8** that was supported with fresh intense band at 1444 cm^{-1} and weak band at 1379 cm^{-1}. Moreover, from the spectrum (b) it was found that the band of 1165 cm^{-1} demonstrating a styryl sexithiophene dication [143] appeared before adding Fe^{3+} into the samples. Although it was not sufficient to cause resonant enhancement, its appearance revealed the fact again, the $–NH_2$ group is a stronger electron donator. As the amount of the oxidant was increased, the 1165 cm^{-1} band became more and more intense till to cause resonance enhancement (spectrum (c) and (d) in Fig 5-33).

Structure of NH_2-pe3T dimers coated Au nanocomposites were further studied with TEM, SEM and EDX, and confirmed to be same as the nanocomposites generated by **5.7** with an average diameter around 100 – 200 nm. They also preferred to aggregate to form fractals (Figures not shown, since they were almost same to those shown in the Fig 5-30).

Considering the high bio-activity of amine group, the NH_2-pe3T dimers coated Au nanostructures were believed to be potentially significant for the SERS biosensor development.

5.5.4 Conclusion

Study of **5.6** indicated that it will be a poor RRM since the signature bands were too weak. In the course of our investigation for **5.7** and **5.8**, it was found that the monomers of analyte molecules were oxidized, firstly by the free Au^{3+} ions present in the Au-sol, further by the stronger oxidant of $FeCl_3$, and finally coupled

to sexithiophene which have been revealed by the UV-Visible absorption and SERS spectra. The total process was catalyzed by Au NPs which accelerated the electron transfer from the oxidants to the compounds. The study carried out with Raman spectroscopy indicated that in the first stage, the Raman signals were dominated by the electromagnetic field enhancement with a LOD lower than 10 molecules / NP. In the second stage, the signals mainly responded to resonance enhancement caused by a large number of dimers achieved by the Fe^{3+}. In the meantime, new nanostructures, multiple NPs capsuled by the dimers of the analyte molecules, were observed with an average diameter of 100-200 nm by the electron microscopes and EDX, also supported by the DLS experiment. The generated nanocomposites showed high stability even in a high ionic strength environment. All these characteristics make them a potentially ideal candidate for the biological application.

5.6 Conclusion

A third sensor system is being investigated with the SERS technique using RRM covered Au NPs as the signal generator. Au sol was utilized as the substrate by considering its high surface area and its biocompatibility. Three different families of compounds, substituted porphyrin, thiophene and substituted terthiophene, were introduced for the study of the RRM. Both Ag and Au NPs have been applied as substrates to obtain SERS signals. Although the signal enhancement was more efficient as using the Ag sol, in which KCl of 2.5 mM was present, the Au sol was a better substrate by considering the biocompatibility required for biological system.

Strong Raman signals were observed using substituted porphyrin compounds (**5.1**-**5.3**) as RRM and were pH dependent. Raman studies of **5.2** and **5.3** indicated that the orientation of **5.2** was vertical to the Au surface, proving that Raman scattering is good for studying orientations.

Terthiophenes as resultant were confirmed with Raman spectra when **5.4** and **5.5** were studied, demonstrating that the oligomerization of thiophene or EDOT was achieved by the Au^{3+} ions present in Au NPs suspension. It was believed this process was catalysed by Au NPs by considering the difficulty of polymerization of thiophenes in solution.

To achieve additional stability to the SERS probe system, substituted terthiophenes (**5.6**-**5.8**) as one kind of important polymer materials were investigated. The weak finger-print bands caused by the long tail group of **5.6** precluded its application as RRM. Compound **5.7** and **5.8** (NO_2/NH_2-pe3T) were believed to be potentially good options since (1) both of them provided intense signature bands in Raman spectra, (2) the interactions between them and the Au sol were strong and thus efficient SERS signals were observed, (3) surface enhanced resonance Raman scattering was observed from dimers of the compounds, which were formed from the oxidation of monomers by Au^{3+} and

Fe^{3+}, and (4) new nanostructures with an average diameter of 100-200 nm, formed by wrapping multiple Au NPs with the dimers, showed high stability even in a high ionic strength environment. Considering the high bio-activity of the amine group, **5.8** (NH_2-pe3T) dimers coated Au nanostructures are potentially significant for SERS biosensor development. This exciting result obtained from this study, oligomerization of NO_2/NH_2-pe3T in aqueous Au suspension, shows a possibility to bridge conducting polymer and nanotechnology for applications in more areas.

Conclusions and future work

➢ Conclusions

Nanotechnology as an interdisciplinary science has developed very rapidly over the last decade and the range of applications is increasing. The aim of our work was to use Au NPs, one of the most widely investigated NPs, as functional materials to develop biosensor systems. For this, three techniques were introduced replying on their different advantages, being lateral flow immunoassay (LFIA), surface plasmon resonance (SPR) and surface-enhanced Raman scattering (SERS). In this work, two precise and reproducible immunoassays (SPR and LFIA) were developed for the rapid detection of E3-16G in adult urine samples of pregnant and non-pregnant women and can be potentially commercialized in the future. Furthermore, a new sensing system is being investigated using Raman spectroscopy. Although we are still in the early stages of this study, the exciting results obtained from substituted terthiophenes are quite encouraging and show that the new composites composed of a core of multiple NPs and terthiophene

dimers shell, due to oxidation of terthiophene monomer, could be new functional materials for future study.

As a prelude to our study, Au NPs with different sizes and shapes were formed in an aqueous solution and characterized using UV-Vis spectrophotometry and TEM. Spherical Au NPs synthesized with sodium citrate were used for subsequent studies based on their relatively narrow size distribution. Two different kinds of Au NP bioconjugates were synthesized using a partially purified polyclonal anti-E3-16G IgG raised in sheep and with a rabbit anti-sheep serum, respectively. The synthesized NRs were not used for study due to unsuccessful purification of final products.

LFIA strip assays were developed with two different strategies: a one-step assay using a pAb-Au conjugate as signal generator and a two-step assay in which 2°AS-Au produced a visible signal. It has been shown that the one-step assay was more sensitive and was less disturbed by the matrix effect of urine samples. A reproducible LOD of 3.8 ± 1.3 nmol/24 hr was firstly reported in this format indicating that the determination low levels of E3-16G in liquid samples could be potentially simplified using strip sensors by taking into account its overall speed and simple sample preparation. The strong matrix effect in adult female urine masked part of the response to E3-16G in samples and precluded the application of the strip sensor to monitoring menstrual cycle levels of E3-16G. However, its application to urinary samples from pregnancy was successful and revealed that the excretion of E3-16G rises steadily from week 14. Moreover, to optimize the two-step assay several factors have been studied including the concentration of pAb applied in the first step, the amount of 2°AS used for synthesis of the conjugates and the size of Au NPs utilized. It was found that the assay sensitivity was only clearly dependent on the concentration of the pAb. Although the standard curve performed with standards spiked in TM buffer showed a working range appropriate for application of the two-step format to clinical samples, the significant differences of the

standard curve, including the intensity of the test line, the sensitivity and the curve shape caused by the urine blank, precluded its real world application.

More sensitive determination of E3-16G in human female urine was achieved using an SPR sensor without the need for prior clean-up and minimal sample preparation. Compared to the strip sensor, the LOD was firstly improved from the ng/mL range to the pg/mL range in non-enhanced assays developed with pAb and then further reduced in the enhanced assay in which spherical Au NPs were used as high mass labels. The superior sensitivity of SPR assays allowed the matrix effect to be considerably reduced by increasing the dilution factors of the urine samples. Consequently, E3-16G quantification was more accurate. With it, reported excretion levels of E3-16G during a normal menstrual cycle agreed with other work and the obviously increasing tendency of E3-16G excretion from the feto-placental unit started from the end of the first trimester. Currently, the SPR method appears to be one of the few efficient ways available to accurately analyse E3-16G production rates in urinary samples of a normal menstrual cycle. A range of other small molecule analytes may be similarly assayed at low concentration by this method.

Urine matrix effects have to be considered when the first two techniques are applied to urine samples due to the lack of selectivity. A new sensor system is being developed with Raman spectroscopy by considering its high specificity. In the early stage of our study, work was focused on examining different compounds as Raman Reporter Molecule (RRM) **(compounds 5.1-5.8)**. Three different classes of compounds were used for study by considering their electron rich structures which promise intense signature bands in the Raman spectrum. Also the sulfur atom in compounds guarantees efficient signal enhancement, and stable monolayer formation caused by the strong interaction between sulfur and Au. Compounds **5.7** and **5.8** are believed to be ideal candidates for RRM since the Raman scattering intensities can be increased by several mechanisms, 1) by the resonance with the localized surface plasmon related to the hot spot, 2) by the

resonance caused by a charger-transfer transition corresponding to the interaction between the analyte molecules and the metallic nanostraucture (first step oxidation of **5.7** and **5.8** caused by the Au^{3+}), and 3) by the resonance resulting from the matched wavelength of the excitation laser to the absorption wavelength of the dimers of **5.7** or **5.8** caused by the further oxidation of the compounds. Moreover, new nanocomposites, composed of multiple aggregated Au NPs and an outside coat of dimers, were observed along with dimerization of terthiophenes and can be used as new functional materials for biological studies by taking into account the potential interaction of terminated amine group of 5.7 with biological molecules.

➢ Future work

The present studies have demonstrated that AuNPs can enhance the sensitivity of plasmon based biosensor techniques, in particular surface plasmon resonance. Plasmon resonance from AuNPs is also utilized in the surface-enhanced Raman effect to provide sensitive spectroscopic signatures of bioanalytes in solution. Based on the current thesis, there are a number of things that can be done in the future. Meanwhile, during the course of the work several other questions have arisen, highlighting some areas where there is still need for research and areas that the author maintains an interest in.

Firstly, successful application of LFIA in urinary samples from a pregnant woman along with the quick user friendly analysis lets it potentially to be commercialized as a home-testing device to monitor fetal-wellbeing. In the current LFIA format, assays were developed using Au NPs for visualization. It is known, many commercial available dyes could be used for visualization of the results, and it will be very interesting to see the comparison between the assays developed with different dyes.

Secondly, the SPR sensor-based sensitive detection approach to E3-16G quantification in urinary samples could be easily transferred to other

environmentally relevant substances, drug residues, or veterinary products. Although the commercial 2°Ab-Au conjugates and the antiserum have not given us the expected signal enhancement due to the strong non-specific binding to the chip surface, there are still many other options for high mass labels, such as using Au NRs. It is believed that it will be exciting work to introduce Au NRs to the SPR system by considering their different polarizations along and perpendicular to the rod axis.

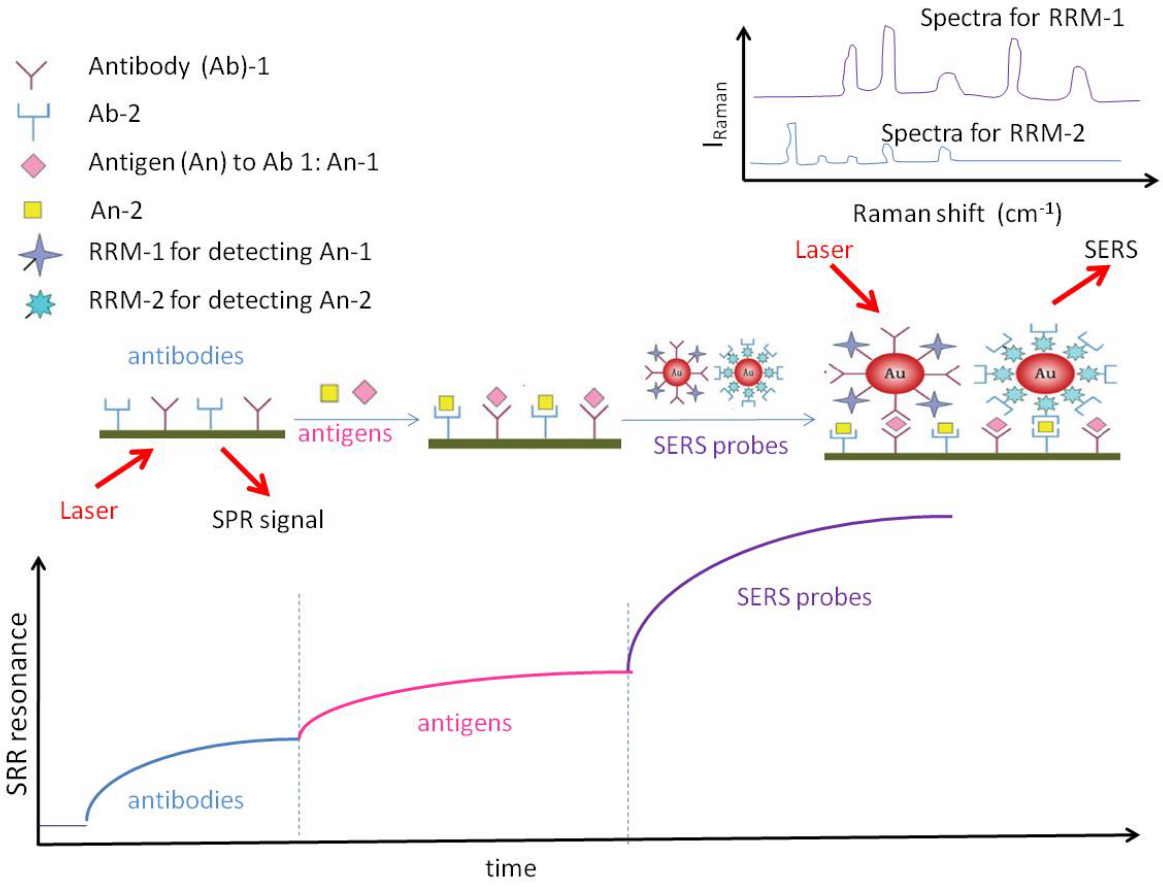

Scheme 1: Schematic illustration of multianalytes immunoassay based on a parallel application of SPR and SERS. This scheme is partially reproduced from [161]

Thirdly, in the process of developing the SERS sensor system, although we met some difficulties, surprising results obtained from NO_2/NH_2-pe3T are very encouraging and show the possibility that a new biosensor may be developed by combining the SERS and SPR work, possessing both the sensitivity of SPR and the specificity of SERS. Of course, there are several ways to utilize the

advantages of both techniques. Here I only introduce one model which will be possibly used for our work in the future and illustrated with scheme I. It is designed to use a Au chip like the CM5 chip used for the SPR work but with no dextran layer on the surface. On the Au chip surface, two different antibodies (Ab-1 and Ab-2) can be immobilized for multiple detections of antigens (An-1 and An-2) which flow through the system following the Ab coupling. They can be captured via specific interaction between the antibodies and antigens. And then, two different SERS probes, modified by corresponding antibodies to An-1 and An-2 respectively, can be passed over chip surface and captured by the immobilized antigens. SPR sensor is used to monitor the whole processes and giving signals corresponding to the mass change on the chip surface and indicating the interactions of each step, as shown in scheme I with three parts of increase of the resonance response. However, from the SPR sensorgram you could not confirm which antigen was present in solution. Raman spectroscopy is used to detect the final complex on the chip surface. Different finger-print bands in two Raman spectra help us to get final answer. Moreover, the parallel SPR test also guarantees that the Raman signals only result from the analytes immobilized on the chip surface, but not from free analytes in solution. Obviously, the analytes must have two epitopes to allow a sandwich assay to be formed between the analytes and the two antibodies.

Appendix

I : Experimental

1. Chemicals

Trisodium citrate dihydrate ($NaC_6H_5O_7 \cdot 2H_2O$), sodium borohydride ($NaBH_4$), tetrachloroauric acid trihydrate ($HAuCl_4 \cdot 3H_2O$), cetyltrimethylammonium bromide (CTAB), anti-sheep IgG (whole molecule) serum produced in rabbit, trehalose, ovalbumin (OVA), bovine serum albumin (BSA), polyvinylpyrrolidone (PVP), estriol -17- (β-D-glucuronide) sodium salt (E3-17G), 2,3-dihydrothieno[3,4-b]-1,4-dioxin (EDOT), ferric chloride (anhydrous, ≥98%) and poly(2,3-dihydrothieno-1,4-dioxin) (PEDOT) were all purchased from Sigma-Aldrich (St. Louis, MO, USA). Ascorbic acid, glacial acetic acid, octanoic acid, sucrose, sulphuric acid, Tween 20, di-sodium hydrogen orthophosphate, and ethanol (99.7-100%, v/v) were obtained from BDH Laboratory Supplies (Poole, England). Ammonium sulphate, silver nitrate and chloroform were from Merck Chemicals (Darmstadt, Germany). Triton-X 100 was purchased from Pure Science Limited (Wellington, New Zealand), sodium azide was from Serva Electrophoresis (Heidelberg, Germany), and the 0.22 μm cellulose acetate filters were from ADVANTEC MFS, Inc (Dublin, U.S.A). Hi-Flow plus 75 membrane cards (60 mm x 301 mm) and cellulose fiber sample pads (17 mm x 300 mm) were from Millipore (Massachusetts, USA). U-bottom microtiter 96 well plates were from Greiner Bio-One GmbH (Frickenhasen, Germany). The E3-16G-BSA conjugates, estrone-3-glucuronide (E1-3G) were obtained from Science Haven Limited (Palmerston North, New Zealand). The E3-16G-OEG-OVA conjugates were from Hort Research (Hamilton, New Zealand). Compounds **5.1-5.3** and **5.6-5.8** were obtained from the MacDiarmid Institute at Massey University (Palmerston North, New Zealand).

2. Instruments

All absorbance spectra were acquired with a UV-Vis-NIR spectrophotometer (UV-3101PC SHIMADZU Japan). The TEM images were taken with a Philips CM10 transmission electron microscope. Zetasizer Nano (Malvern, Worcestershire, UK) was used to analyse the size distribution of colloidal Au NPs in samples. ^{1}H and ^{13}C NMR spectra were obtained using either a Bruker Advance 400 or 500 MHz spectrometer. Chemical shifts for spectra in $CDCl_3$ are given in parts per million (ppm) down field from tetramethylsilane as internal standard (^{1}H) or relative to residual solvent (^{13}C). High resolution mass spectra were recorded using a VG7070 mass spectrometer operating at a normal accelerating voltage of 70 eV. A BIAcore X100 system (GE Healthcare, Uppsala, Sweden) was used to develop SPR assays. Reagents for SPR work, including the CM5 chip, amine coupling kit (0.1 M NHS, 0.4 M EDC and 1 M ethanolamine) and HBS-EP running buffer (0.01 M HEPES pH=7.4, 0.15 M NaCl, 3 mM EDTA and 0.005 % surfactant P20) were purchased from GE Healthcare (Uppsala, Sweden). An IsoFlow™ Reagent Dispenser (Imagenetechnology, Hanover, USA) was used to dispense control and test lines on a nitrocellulose membrane. The strips were cut with an M-70 cutter (advanced Sensor System Ltd, Ambala, India). An HP scanjet 3500c photo scanner and dedicated software were used to obtain images of the strips. FEI Quanta 200 with a tungsten filament scanning electron microscope (SEM) (Hillsboro, USA) cooperated with Energy Disperse System of X-ray (EDX) (EDAX Genesis system) (Mahwah, USA) were used to reveal nanostructures of colloidal Au and dimer-Au composites. SpectraPhysics model 165 Argon ion laser at excitation wavelength of 488nm was used for Dynamic Light Scattering measurements. 15 mW HeNe laser (ThorLabs) collection geometry was 180° back-scatter with free-space optics. Scattered light was focussed through notch-filter (Iridian) and onto the entrance slit of an Acton SpectraPro 2500i. The detection system is a Roper Scientific 100:10b CCD.

3. Software

The intensity of the control and test lines on the strips was quantified with a strip reader system (version 2.00, Simon Brown[2] Ltd, Launceston, Tasmania, Australia). For statistical analysis, all assay standard curves were fitted to a four-parameter logistic equation using Graph Pad Prism 5 (La Jolla, CA, USA). All IC_{50} values were presented as a parameter from the curve fitting. The LOD was computed with OriginPro 7.0 (OriginLab, Northampton, MA, USA). Moreover, OriginPro 7.0 was also used to analyze intensity of Raman signals.

4. Recipes

4.1 Nanoparticles

4.1.1 Spherical nanoparticles

Au nanoparticles (NPs) were synthesised via citrate reduction. Six samples were prepared by mixing citrate (170 mM) of different volumes (0.29, 0.40, 0.588, 0.60, 1.00 and 1.18 mL) and $HAuCl_4 \cdot 3H_2O$ (50mL 1mM). Mixtures were left to stand in a warm water bath (75 ºC to 80 ºC) for 15 minutes. The colloidal Au suspension was filtered through a 0.22 µm cellulose membrane and then stored at 4 ºC for further use.

Ag NPs were prepared by reducing $AgNO_3$ with sodium citrate as well. $AgNO_3$ of 1 mM (10 mL) was brought to boiling, followed by 200 µl sodium citrate of 34 mM. The NPs were synthesized around 10 minutes later, indicated by color changing to green yellow, and then characterized by UV-Vis spectrophotometry using a 1:4 dilution of the sample.

4.1.2 Rod-shaped nanoparticles

4.1.2.1 Seed mediated synthesis

The negatively charged seed solution was synthesized mixing $HAuCl_4 \cdot 3H_2O$ (5mL 0.25 mM) and $NaBH_4$ (50 µl 0.1 M) in the presence of 0.25 mM sodium citrate (5 mL). The GS were prepared by adding 50 µl freshly prepared ice-cold ascorbic acid (0.1 M) to the mixture containing an equivalent volume (5 mL) $HAuCl_4 \cdot 3H_2O$ (0.25 mM) and CTAB (0.1 M).

The seed solution of 25 µl was directly added to the growth solution to achieve NRs - 1. For NRs - 2, three same GS (GS I, GS II, GS III) were prepared. The 1st step was to add 1.0 mL of the seed solution into GS I to obtain GS I *. The 2nd step was to add mixed 1.0 mL GS I * into GS II in 15 minutes. About 3 minutes later, GS II * was formed. The last step was to add 1.0 mL GS II * to GS III to synthesize NRs - 2.

4.1.2.2 Synthesis in the presence of $AgNO_3$

The CTAB capped seed solution was synthesized by adding the surfactant of CTAB (5 mL 0.2 M) to mixture of 5 mL $HAuCl_4 \cdot 3H_2O$ (0.5 mM) and 600 µl $NaBH_4$ (0.01 M). To control the aspect ratio of the NRs, 4 mM $AgNO_3$ at different volumes (0.15, 0.20, 0.25, 0.30, 0.35, 0.40, 0.45, 0.50 mL) was added to a mixture of $HAuCl_4 \cdot 3H_2O$ (5 mL 1 mM) and CTAB (5 mL 0.2 M). Subsequently, 70 µl ascorbic acid (0.0788 M) was added and the GS was formed.

The NRs – 3 were synthesized by adding a CTAB capped seed solution (12 µl) to GS. The samples formed were left in a water bath (50 °C) for 1 hour and then centrifuged twice at 6500 rpm for 20 min. The supernatant was kept for analysis.

4.1.3 Characterization of NPs

Absorption spectra were achieved by measuring a 1:20 dilution (v/v, Au sol / Milli.Q water) of the sample with UV-Vis spectrophotometry. Size distributions of the aggregated Au NPs were determined by detecting a 1:4 dilution of the sample with a Zetasizer. Samples for TEM were first pre-diluted with Milli.Q water (around 1:100) and then stabilized by 1% BSA, of which the volume was around 1/10 of total volume of the sample, and then images taken on a carbon grid.

4.2 Gold-Antibody conjugates

4.2.1 Purification of polyclonal primary antibodies

The antibody purification started with serum harvested from the fifth bleed of a sheep inoculated with E3-16G-thyroglobulin conjugate. The sheep serum (5 mL) was added to acetate buffer (10 mL of 0.06 M pH=6.0) and the pH was adjusted to 4.8 using 0.1 M HCl. Octanoic acid (330 µl) was added dropwise to the solution (15 mL) with vigorous stirring to remove non globulin material the mixture was stirred on an ice bath for 30 minutes and centrifuged at 3345 g for 60 minutes. The resulting supernatant was transferred to a fresh tube for a second centrifugation for 35 minutes under the same conditions and dialysed against phosphate buffer (10 mM pH=7) overnight. Two further buffer changes were carried out after 1 and 2 hours respectively.

The dialysed sample was centrifuged at 3345 g for 40 minutes, and the supernatant was mixed with an equal volume of saturated ammonium sulphate solution (76 g ammonium sulphate dissolved in 100 mL Milli.Q water and pH adjusted to 7.0 using sulphuric acid) in a fresh tube. The solution was left stirring overnight at 4 ºC for complete precipitation of the immunoglobulins. The antibodies were spun down (2x 30 min at 3345 g) and washed with phosphate buffer (4.5 mL of 10 mM pH=7). The pellet was re-suspended in the phosphate buffer and dialysed for 40 hours with 7 x 1 L changes of phosphate buffer (10 mM pH=7). Finally the antibodies were spun down at 23036 g for 30 minutes and stored in 10 mM phosphate buffer.

4.2.2 Titration

Antibody solution of 0.2 mg/mL in sodium borate buffer (2 mM) were prepared using concentration of stock solution which were 4.8 mg/mL for pAb and 69 or 3.5 mg/mL for specific 2°Ab in serum. Au suspension of 10 mL were adjusted to pH of 7.0, 7.5, 8.0, 8.5, 9.0 and 9.5 using 20 mM K_2CO_3 and 10 mM HCl.

For each antibody, a matrix was set up in 1 mL cuvettes with Au NPs of different pH values and the antibody of different concentrations. Concentrations of the pAb series were 0, 23, 46.2, 69.3, 92.4, 115.5, 138.6, 161.7, 184.8, 207.9 and 230 µg/mL. The first titration for the 2°AS-Au conjugates was carried out using 69 mg/mL as the stock solution. Three solutions of 60.5, 100 and 200 µg/mL were prepared for titration. The second titration was performed with solutions of different concentrations (40, 80, 120, 160, 200 µg/mL) calculated using 3.5 mg/mL as the stock solution of the antibody. Colloidal Au solution of 500 µl at different pH values were mixed with the series of antibodies of different concentrations (50 µl) and incubated for 2 minutes at room temperature, and the 100 µl NaCl (10% w/v in Milli.Q water) was added to each tube. After 5 minutes, the mixtures were characterized with UV-Vis spectrophotometry (400-700 nm).

4.2.3 Synthesis of conjugates

Gold NPs were synthesized according to the method introduced in 4.1.1. Volumes of citrated (170 mM) and $HAuCl_4 \cdot 3H_2O$ (1 mM) were 1.47 and 50 mL, respectively. The stock concentration of Au NPs was 1 mM. The pH of Au colloids was adjusted using 20 mM K_2CO_3 and 10 mM HCl during the synthesis.

Conjugates	C_{pAb} or $C_{2°Ab}$ (µg/mL)	C_{Au} (mM)	λ_{Au} nm
pAb-Au-1	73	0.5	525
pAb-Au-2	187	0.5	525
2°AS-Au-1	91	0.5	530
2°AS-Au-2	105	0.5	530
2°AS-Au-3	216	0.5	530
2°AS-Au-4	216	0.5	537
2°AS-Au-5	91	0.25	530
2°AS-Au-6	91	1.0	530

Table A: Conjugates synthesized using Au NPs and pAb or antiserum. C_{pAb} and $C_{2°Ab}$ represent the concentration of pAb and 2°Ab in the final conjugates, respectively. C_{Au} is the concentration of Au NPs used for synthesis. λ_{Au} is the plasmon resonance wavelength of Au NPs used for synthesis.

The conjugates were formed by adding pAb (4.8 mg/mL) or antiserum (3.5 mg/mL) to the Au colloids of 20 mL (pH 8.5 for pAb and pH 8.0 for antiserum) followed by 10 % BSA (2 mL, w/v) to block unreacted sites on the surface of the NPs. The conjugates were spun down (9750 g for 60 min) using a SS-34 rotor and the pellets were resuspended in buffer (2 mL) containing 0.25 % Triton X (v/v), 0.06 M trehalose, 0.175 M sucrose, 0.154 M sodium azide, 0.05 M Na_2HPO_4, and 1 % BSA (w/v). Table A shows the information of the conjugates.

The concentration of antibodies in the mixture of Au suspension and antibodies is calculated with

$$C_{Ab} = (C_{stock\ solution} * V_{added\ Ab}) / V_{mixture}\ ,$$

where the $C_{stock\ solution}$ is the concentration of antibody stock solution (4.8 mg/mL for the pAb or 3.5 mg/mL for the 2°Ab), $V_{added\ Ab}$ is the volume of antibodies added to Au suspension and $V_{mixture}$ is the volume of the mixture. Considering the final volume of the conjugates was around 1/10 of the initial volume of mixture, therefore the concentration of antibodies in the conjugates (Table A) was estimated by multiplying a factor of 10.

4.3 Lateral flow immunoassay

4.3.1 Preparation of the test strips for LFIA

The lateral flow test strip was made up from a commercial nitrocellulose card containing a test line (E3-16G-BSA conjugates), a control line (rabbit anti-sheep IgG in serum for the one-step format and pAb for the two-step format) and an absorbent pad. The concentration of the E3-16G-BSA conjugates was 4.8 mg/mL and they were diluted to 1 mg/mL using Milli.Q water and 10 times concentrated (10x) PBS buffer before spraying onto the membrane. Half of the total volume was 10x PBS, and the other half was the required E3-16G-BSA conjugates (4.8 mg/mL) diluted to 1 mg/mL and Milli.Q water. The concentrations of the rabbit anti-sheep IgG in the serum and pAb in phosphate buffer were 3.5 and 4.8 mg/mL respectively, which were also diluted to 1 mg/mL as described above. Both the test line and control line were sprayed onto the nitrocellulose membrane at a speed of 100 mm/s. The dispense rate was 0.1 µl/mm. The distance between the test and control line was 0.5 cm. After drying at 40 ºC for 1 hour, the bottom part of a membrane card, which was designed for attachment of a sample pad and conjugate pad, was cut away. The membrane was then cut into 5 mm width strips and sealed and stored under dry conditions at room temperature.

4.3.2 Procedures for lateral flow immunoassay

4.3.2.1 One-step assay

A. Assay procedure

Assay reagents were directly pipetted into the sample wells of a low protein binding microtiter plate and allowed to migrate up the strips which were inserted vertically into the wells. The total volume of sample in the wells was kept at 75 µl. The reaction mixture in each well consisted of 5 µl of a time-diluted urine sample (or standard) mixed with 5 µl of un-diluted Au-pAb conjugates, 5 µl of TM buffer (or time diluted blank urine), 40 µl of diluent buffer (0.154 M sodium azide, 0.05

M Na_2PO_4 and 1 % BSA in Milli.Q water) and 20 µl Tween 20-PVP (2 % (v/v) Tween 20 and 1 nM PVP in diluent buffer). After 15 minutes, the test results were quantified using a strip reader. A standard curve was computed by plotting the test line intensity versus the logarithm of the concentrations of the standard samples.

B. Urine matrix effects

To estimate the matrix effect of urine samples in the LFIA, standard curves were generated using both the 10 mM TM buffer (pH=7.1) and the blank urine with the same series of E3-16G standards (0 to 100k nmol/24 hr) spiked in the TM buffer. For example, the buffer standard curve was generated from 12 solutions containing 5 µl standards, 5 µl un-diluted Au-pAb conjugates, 5 µl TM buffer, 20 µl Tween 20-PVP, and 40 µl diluent while the blank urine curve was generated by replacing the equivalent volume of TM buffer (5 µl) with time-diluted blank urine. Both standard curves were obtained using strips cut from the same nitrocellulose membrane card.

The pH and conductivity dependence of the matrix effect were studied by measuring the apparent absorbance of blank samples in triplicate containing the Au-pAb conjugates in the absence of analyte. The blank urines were adjusted to different pH values (pH=5.00, 6.77, 7.10, and 9.00) using HCl (0.5 M) and NaOH (0.5 M). The conductivity of the blank urine was adjusted to 2.17 and 3.48 mS with Milli.Q water.

C. Precision of the assay

The assay precision was determined for both intra-assay and inter-assay strips. These were evaluated by generating the standard curves with the A and B sets of Au-pAb conjugates (conjugates A1-A3 and conjugates B1-B3) using strips cut from several cards.

D. Accuracy of the assay

The accuracy of the test strips was determined by testing the recovery of

control samples of spiked E3-16G (10, 30, and 50 nmol/24 hr) in blank urine. The test was performed in triplicate (75 µl in 15 minutes) with the strips cut from the same membrane card for both the control samples and the calibration curve.

4.3.2.2 Two-step assay

A. Determination of the concentration of the pAb applied in the first step

In the well, 5 µl 2°AS-Au was mixed with 1 µl pAb of different dilutions (1:1, 1:2, 1:5, 1:10 and TM buffer), 20 µl Tween 20-PVP and 49 µl of diluent buffer. The strips with a test line of pAb were left standing in the well for 15 minutes, and then the test results were quantifies using strip reader.

B. Assay procedure for calibration curve

In the first step, the reaction mixture in each well consisted of 5 µl standard of different concentrations (0 to 100k nmol/24 hr) spiked in the TM buffer mixed with 1 µl pAb (1:5 or 1:10 dilution), 8 µl Tween 20-PVP and 16 µl diluent buffer. Strips were left in the wells for 10 minutes and then moved to the mixtures prepared for the second step, which consisted of 5 µl un-diluted 2°AS-Au conjugates, 8 µl Tween 20-PVP, and 17 µl diluent buffer. The test results were quantified using a strip reader after 10 minutes. A standard curve was computed by plotting the test line intensity versus the logarithm of the concentrations of the standard samples.

4.3.3 Determination of E3-16G using LFIA

Time-diluted sample	DF in LFIA format	DF in SPR format
Week 4	1:10	1:300
Week 6	1:5	1:60
Week 8	1:5	1:300
Week 10	1:10	1:1500
Week 12	1:50	1:4000
Week 14	1:100	1:12000
Week 18	1:100	1:12000
Week 24	1:100	1:25000

Table B：Further pre-dilution of time diluted urinary samples of volunteer C. DF: dilution factor

In order to determine the E3-16G excretion in clinical samples through a normal menstrual cycle, daily time-diluted urinary samples collected form volunteer A and B were analysed in triplicate and the profile patterned from the resulting excretion rates. The time-diluted samples of the first two trimesters collected from a pregnant woman (volunteer C) were pre-diluted according to the factors shown in the above table and then applied to the strip tests. All measurements of real samples were carried out according to the procedure of 75 µl in 15 minutes (5 µl un-diluted Au-pAb conjugates, 5 µl TM buffer, 20 µl Tween 20-PVP, 40 µl diluents, and 5 µl time-diluted urinary samples from non-pregnant women or further diluted samples from pregnant women).

4.4 SPR-based immunoassay

4.4.1 Synthesis of E3-16G-OEG-OVA (from the MacDiarmid Institute)

E3-16G (**1**) and a OEG linker **(2)** were prepared separately according to two previous methods [99, 162]. A solution of DCC (0.16 mmol) and NHS (0.16 mmol) in DMF (0.5 mL) was added to a solution of E3-16G (25 mg, 0.0538 mmol) in DMF (0.5 mL) under an atmosphere of nitrogen. The reaction mixture was stirred for 4 hours, followed by the addition of the OEG linker (0.3 mmol) in $CHCl_3$ (1 mL) and triethylamine (0.5 mL), and subsequently stirred for further 12 hours. Water (50 mL) was added and the reaction mixture extracted with

Scheme 2. Synthesis of Estriol 16-Glucuronide-Olbumin Conjugate (E3-16G-OEG-OVA)

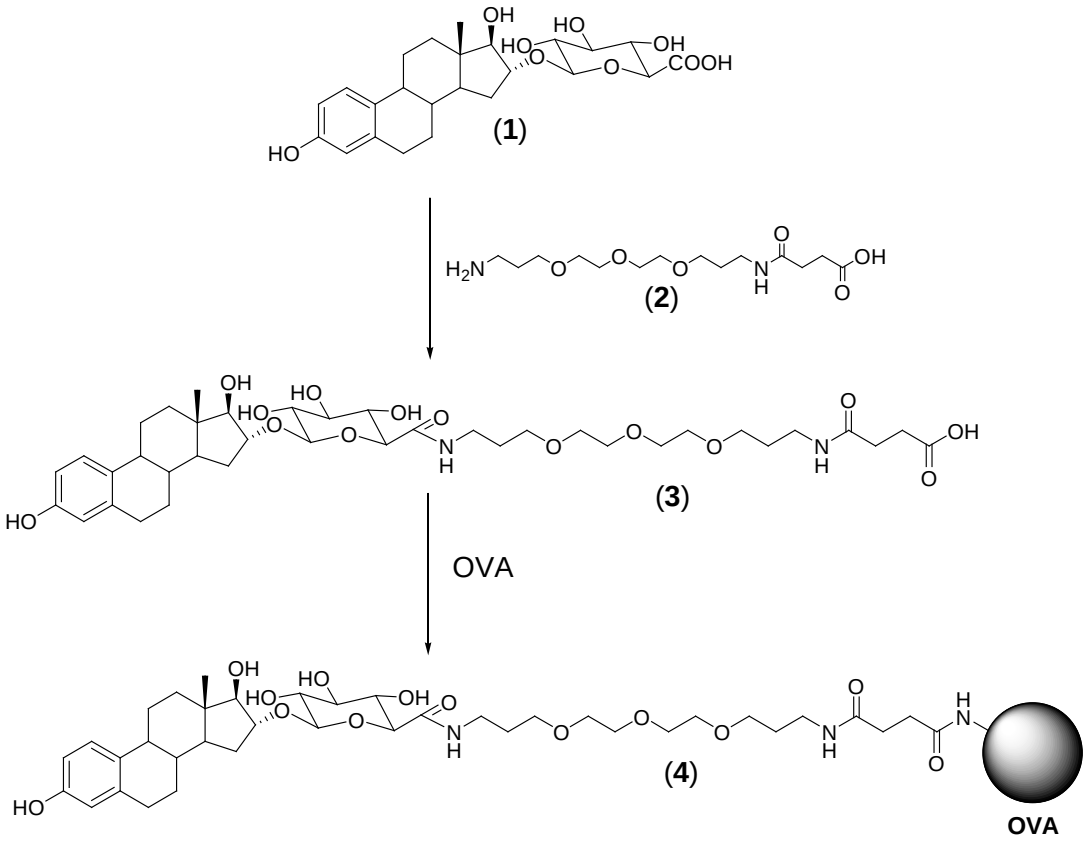

Scheme 2: how to synthesize the conjugate of E3-16G-OEG-OVA. **(1)** is E3-16G. **(2)** is heterobifunctional oligoethylene glycol (OEG) linker. **(3)** is N-(4,7,10-trioxa-1,13-tridecanyl-13-butanamidoicacid)-3,17b-dihydroxy-1,3,5(10)-estratriene-16a-yl-b-D-glucopyranosamide. **(4)** is E3-16G-OEG-OVA conjugate.

dichloromethane (DCM) (20 mL x 3). After removing the DCM layer from the aqueous phase the solution was passed through an XAD-2 column and eluted with MeOH/water (1:1). After evaporating the solvent, the residue was purified by flash column chromatography eluting with CH_2Cl_2/MeOH/HOAc (10:1:0.1) to afford the product N-(4,7,10-trioxa-1,13-tridecanyl-13-butanamidoicacid)-3,17ß-dihydroxy-1,3,5(10)-estratriene-16α-yl-ß-D-glucopyranosamide **(3)** as a colourless solid (18 mg, 44%).

^{1}H NMR (500 MHz, $CDCl_3$): □0.82 (s, 3H), 1.31-1.49 (m, 4H), 1.57 (q, J = 9.4 Hz, 1H), 1.75-1.99 (m, 7H), 2.17-2.23 (m, 1H), 2.29-2.35 (m, 1H), 2.48 (t, J = 7.2 Hz, 2H), 2.61 (t, J = 7.2 Hz, 2H), 2.78-2.82 (m, 2H), 3.25-3.35 (m, 9H), 3.44 (t, J = 8.9 Hz, 1H), 3.49 (t, J = 7.9 Hz, 1H), 3.53-3.70 (m, 10H), 3.75 (d, J = 9.4 Hz, 1H), 4.17 (q, J = 5.2 Hz, 1H), 4.39 (d, J = 7.9 Hz, 1H), 6.50 (d, J = 4.3 Hz, 1H), 6.55 (dd, J = 2.6, 6.8 Hz, 1H), 7.10 (d, J = 8.5 Hz, 1H) ppm.

^{13}C NMR (125 MHz, $CDCl_3$): 1.5, 25.8, 27.2, 28.9, 29.3, 31.0, 36.2, 36.4, 36.6, 38.6, 43.5, 43.9, 68.4, 48.5, 68.8, 70.1, 72.2, 73.3, 73.7, 76.3, 85.4, 87.3, 102.2, 112.4, 114.7, 125.8, 131.0, 154.6, 170.8, 173.1, 174.9 ppm; HRMS (EAB^+): MH^+, found 767.39630. $C_{38}H_{58}N_2O_{14}$ requires 767.39663.

N-(4,7,10-trioxa-1,13-tridecanyl-13-butanamidoicacid)-3,17b-dihydroxy-1,3,5(10)-estratriene-16a-yl-b-D-glucopyranosamide **(3)** (10 mg, 0.013 mmol) was dissolved in a mixture of DCC (0.044 mmol) and NHS (0.044 mmol) in DMF (0.26 mL), and the reaction was stirred at room temperature for 3 hours until white precipitate was formed. The solution was added to OVA (0.65 mol) in phosphate buffer (2.6 mL, 0.2 M, pH 7.4) and stirred at 4 ^oC overnight. After dialysis against deionized water for 2 days (3 changes per day) and PBS/T for one day (2 changes) at 4 ^oC, the conjugate **(4)** (2.5 mL) was further purified by passing it through a PD-10 column using PBS/T as the eluent, and the purified conjugate **(4)** (3.5 mL) was collected. The protein concentration of E3-16G-OEG-OVA **(4)** was determined by a bicinchonimic acid protein assay.

4.4.2 Procedure for SPR assay

4.4.2.1 Immobilization of E3-16G-OEG-OVA onto a CM5 chip

Both flow cell 1 (FC1) and flow cell 2 (FC2) of a BIAcore CM5 chip were activated by mounting the chip within the SPR instrument and exposing each cell to 100 µl of a 1:1(v/v) mixture of EDC (0.4 M) and NHS (0.1 M) for 20 minutes. This was followed by triplicate injection in FC2 of E3-16G-OEG-OVA (50 µl of 0.33 mg/mL) in sodium acetate (10 mM, pH=4.0) at a flow rate of 5 µl/min, and then EAH (100 µl of 1.0 M) was injected and the solution stood for 20 min. At the end, glycine (10 mM pH=2) of 10 µl were injected in triplicate at a FR of 20 µl/min to clean the chip surface. For the reference flow cell (FC1), following activation of the surface, OVA (50 µl, 0.05% (w/v)) in sodium acetate (10 mM, pH=4) was coupled to the chip surface in 20 minutes.

4.4.2.2 Binding performance of pAb and pAb-Au conjugates on chip surface

For analysis of the binding affinity of the pAb on the chip surface, samples (20 µl) containing 7 different concentrations of pAb (0, 0.1, 0.5, 1.0, 2.5, 5.0, 10.0 µg/ml) were injected for 2 minutes at a flow rate of 10 µl/min. The surface was regenerated by injecting a mixture of 100 mM NaOH and 10 % acetonitrile for 40 seconds at a flow rate of 10 µl/min. For evaluating the affinity of the pAb-Au conjugates to the surface, the conjugates (C_{pAb}=187 µg/mL) were diluted with running buffer to form 9 samples in which the pAb concentration was 0, 0.078, 0.156, 0.312, 0.623, 1.250, 2.490, 4.990 and 9.970 µg/ml respectively. These samples were also injected at 10 µl/min for 2 minutes. Regeneration was achieved using 10 µl of 200 mM NaOH and 20 % acetonitrile for 1 minute.

4.4.2.3 Inhibition assay developed with pAb

A series of E3-16G standards (in the range of 0 to 300 ng/ml) were prepared using HBS-EP buffer as diluent. Samples were prepared by mixing TM buffer (10 mM, pH = 7.0), E3-16G standards, and a constant concentration of pAb according to a volume ratio of 1:1:1 and incubating for 5 minutes at room temperature.

Samples containing pAb (15 µl of 5 µg/ml) were injected over the chip surface in 1.5 minutes while the samples containing pAb (1 µg/ml) 75 µl were injected in 7.5 minutes. Regeneration was performed with a solution of 100 mM NaOH and 10 % acetonitrile in Milli.Q water (5 µl for 30s).

4.4.2.4 Enhanced assay developed with pAb-Au

The pAb-Au NP conjugates were firstly diluted with the buffer (dilution factors were 12.5, 25, 100, and 200) and mixed with equivalent volumes of E3-16G standards and TM buffer. The mixtures were injected at a FR of 10 µl/min for 1, 1.5, 4.5, and 7.5 minutes according to the dilution factors. The chip surface was regenerated with a solution of 200 mM NaOH and 20% acetonitrile in Milli.Q water (10 µl for 60s).

4.4.2.5 Validation of non-specific binding of 2°Ab-Au conjugates and 2°AS on chip surface

In the case of using the commercial monoclonal 2°Ab-Au conjugates, 20 µl pAb of different concentrations (0, 0.04, 0.05, 0.06, 0.075, 0.0767, 0.10 and 1 µg/mL) was injected in 2 minutes, then, 20 µl 2°Ab-Au conjugates of different dilutions (1:8, 1:14, 1:16, 1:25 and 1:32) were injected at a FR of 10 µl/min. The chip surface was regenerated with a solution of 200 mM NaOH and 20% acetonitrile in Milli.Q water (10 µl for 60s).

In the case of using 2°AS as high mass probe, six different running buffers were prepared, A: HBS-EP buffer, B: 0.5 M NaCl, C: 0.05% OVA, D: 0.5 M NaCl 1% PEG, E: 0.5 M NaCl, 0.05% OVA and F: 1% PEG and F: 0.3 M NaCl, 1% PEG. To determine the best running buffer for the lowest non-specific binding of 2°AS, solutions of 2°AS, in which the concentration of specific antibody was 25 µg/mL, were prepared using the six buffers and then injected in the absence of pAb (20 µl/120s). Regeneration was performed with a solution of 200 mM NaOH and 20 % acetonitrile in Milli.Q water (10 µl for 60s).

The optimum signal enhancement from the 2°AS was determined by

injecting solutions containing the specific 2°Ab of different concentrations (5, 10 and 25 µg/mL) prepared in buffer E (20 µl/120s) after coupling the pAb (1, 5 and 10 µg/mL) onto the chip surface (20 µl/120s). A solution of 200 mM NaOH and 20 % acetonitrile in Milli.Q water (10 µl for 60s) was used to regenerate the chip surface.

4.4.2.6 Cross-reactivity of the polyclonal anti-E3-16G antibody

A non-enhanced SPR assay (using the pAb of 1 µg/mL) was used to estimate the cross-reactivity of the pAb. A series of E3-17G standards (0 to 500 µg/mL) and E1-3G standards (0 to 12.7 µg/mL) were prepared using HBS-EP buffer as diluent. Samples for injection were prepared by mixing TM buffer (1:5 dilution of 10 mM TM buffer, pH = 7.10), E3-17G or E1-3G standards, and pAb (15 µg/mL) according to a volume ratio of 1:1:1 and incubating for 5 minutes at room temperature. Then the samples (15 µl) were injected for 90 seconds. The surface was regenerated using a mixture of 100 mM NaOH and 10 % acetonitrile in Milli.Q water (5 µl for 30s). Each sample was performed in triplicate and the calculations of the IC_{50} values were performed using Graph Pad Prism.

4.4.2.7 The matrix effect of urine in the SPR immunoassay

Different dilutions (1:5, 1:10, and 1:30) of TM buffer (10 mM) or time-diluted blank urine were pre-incubated with an equivalent volume of a zero standard (HBS-EP buffer) and Au-pAb conjugates (1:100 dilution in HBS-EP buffer) at room temperature and the SPR response measured (20 µl/120 s at a FR of 10 µl/min) in triplicate. The chip surface was regenerated using NaOH (100 mM) and 20% acetonitrile in Milli.Q water (10 µl for 60s).

4.4.2.8 Accuracy of the immunoassay

Three standards were prepared by spiking blank urine with E3-16G (1.29, 3.87, and 6.45 ng/mL), and measured as unknowns in the standard SPR assay. A 1:30 dilution of each spiked urine specimen was incubated with an equivalent volume of a 1:30 diluted TM buffer (10 mM) and a 1:100 dilution of pAb-Au

conjugates for which the nominal pAb concentration was 1.87 µg/mL (187 µg/mL was divided by the dilution factor of 100). The SPR response for the mixture (20 µl for 120 seconds) was tested in triplicate at a flow rate of 10 µl/min. Between exposures the biosensor surface was regenerated with 100 mM NaOH and 20 % acetonitrile in Milli.Q water (10 µl for 60s).

4.4.3 Determination of E3-16G in the time-diluted urine samples

Mixtures (20 µl) were prepared containing equivalent volumes of the urinary samples (either diluted 1:30 from volunteer A and B or further diluted as shown in Table B from volunteer C), a 1:30 dilution of 10 mM TM buffer and a 1:100 dilution of the gold conjugates (C_{pAb}=1.87 µg/mL) flowed through the chip in 120 seconds at a flow rate of 10 µl/min. The chip surface was cleaned with 100 mM NaOH and 20 % acetonitrile in Milli.Q water (10 µl for 60s).

4.5 Surface-enhanced Raman scattering

Both the Au and Ag sol were prepared according to the procedure shown in Appendix I 4.1.1. Au NPs concentration was 1 mM calculated based on the assumption that all Au^{3+} were reduced to Au^{0}.

4.5.1 Study of 5.1

Stock solution of **5.1** (1 mM) were prepared using an organic solvent of methanol in a glass bottle and kept covered with tinfoil for further use. The absorption spectra of **5.1** were recorded in a range of 300 to 900 nm by subtracting a baseline of methanol. The Raman spectra were collected with an accumulation of 60 times for 5 seconds each.

C_{KCl} / $C_{compound}$	50mMKCl	25mMKCl	12.5mMKCl	10mMKCl	40mMKCl
0.25mM	0.5ml 1mM Ag 0.25ml 200mM KCL 0.25ml 1mM Dye	0.5ml 1mM Ag 0.25ml 100 mM KCL 0.25ml 1mM Dye	0.5ml 1mM Ag 0.25ml 50 mM KCL 0.25ml 1mM Dye	0.5ml 1mM Ag 0.25ml 40 mM KCL 0.25ml 1mM Dye	0.5ml 1mM Ag 0.25ml 200 mM KCL 0.25ml 1mM Dye
0.20mM	0.5ml 1mM Ag 0.25ml 200mM KCL 0.25ml 0.8 mM Dye	0.5ml 1mM Ag 0.25ml 100 mM KCL 0.25ml 0.8 mM Dye	0.5ml 1mM Ag 0.25ml 50 mM KCL 0.25ml 0.8 mM Dye	0.5ml 1mM Ag 0.25ml 40 mM KCL 0.25ml 0.8 mM Dye	0.5ml 1mM Ag 0.25ml 200 mM KCL 0.25ml 0.8 mM Dye
0.125mM	0.5ml 1mM Ag 0.25ml 200mM KCL 0.25ml 0.5 mM Dye	0.5ml 1mM Ag 0.25ml 100 mM KCL 0.25ml 0.5 mM Dye	0.5ml 1mM Ag 0.25ml 50 mM KCL 0.25ml 0.5 mM Dye	0.5ml 1mM Ag 0.25ml 40 mM KCL 0.25ml 0.5 mM Dye	0.5ml 1mM Ag 0.25ml 200 mM KCL 0.25ml 0.5 mM Dye
0.10mM	0.5ml 1mM Ag 0.25ml 200mM KCL 0.25ml 0.4 mM Dye	0.5ml 1mM Ag 0.25ml 100 mM KCL 0.25ml 0.4 mM Dye	0.5ml 1mM Ag 0.25ml 50 mM KCL 0.25ml 0.4 mM Dye	0.5ml 1mM Ag 0.25ml 40 mM KCL 0.25ml 0.4 mM Dye	0.5ml 1mM Ag 0.25ml 200 mM KCL 0.25ml 0.4 mM Dye
50µM	0.5ml 1mM Ag 0.25ml 200mM KCL 0.25ml 0.2 mM Dye	0.5ml 1mM Ag 0.25ml 100 mM KCL 0.25ml 0.2 mM Dye	0.5ml 1mM Ag 0.25ml 50 mM KCL 0.25ml 0.2 mM Dye	0.5ml 1mM Ag 0.25ml 40 mM KCL 0.25ml 0.2 mM Dye	0.5ml 1mM Ag 0.25ml 200 mM KCL 0.25ml 0.2 mM Dye
25µM	0.5ml 1mM Ag 0.25ml 200mM KCL 0.25ml 0.1 mM Dye	0.5ml 1mM Ag 0.25ml 100 mM KCL 0.25ml 0.1 mM Dye	0.5ml 1mM Ag 0.25ml 50 mM KCL 0.25ml 0.1 mM Dye	0.5ml 1mM Ag 0.25ml 40 mM KCL 0.25ml 0.1 mM Dye	0.5ml 1mM Ag 0.25ml 200 mM KCL 0.25ml 0.1 mM Dye
250nM	0.5ml 1mM Ag 0.25ml 200mM KCL 0.25ml 1µM Dye	0.5ml 1mM Ag 0.25ml 100 mM KCL 0.25ml 1µM Dye	0.5ml 1mM Ag 0.25ml 50 mM KCL 0.25ml 1µM Dye	0.5ml 1mM Ag 0.25ml 40 mM KCL 0.25ml 1µM Dye	0.5ml 1mM Ag 0.25ml 200 mM KCL 0.25ml 1µM Dye

Table C: Matrix designed for the determination of the optimum concentration of KCl and the LOD of **5.1**. Dye mentioned in the table represents **5.1**. C_{KCl} and $C_{compound}$ demonstrate the concentrations of KCl and **5.1**in the mixtures

To determine the optimum concentration of KCl for signal enhancement using Ag sol as a substrate and the LOD of the **5.1**, a matrix was designed as shown in Table C. Each sample contained 0.5 mL Ag-sol, 0.25 mL KCl of different concentrations and 0.25 mL **5.1** of different concentrations. Raman spectra of these samples were collected with an accumulation of 60 times in 3

minutes.

Signal enhancement from the Au sol was determined by measuring the samples containing the colloidal Au of different sizes, **5.1** (250 nM) in the absence and presence of 10 mM KCl with the Raman spectroscopy (5s/exposure, accumulated 60 times).

For the pH dependence study of the Raman signals, pH values of the Au sol were adjusted with 10 mM HCl and 20 mM K_2CO_3, and then a 1:20 dilution was characterized by a UV-Vis spectrophotometry in a range of 400-700 nm. Reaction mixtures consisting of equivalent volumes of Au-sol of different pH values and **5.1** (250 nM) were incubated for 5 minutes at room temperature, then measured with the Raman spectroscopy (5s/exposure, accumulated 60 times) and with the UV-Vis spectrophotometry from 300-900 nm.

4.5.2 Study of 5.2 and 5.3

Stock solutions of **5.2** and **5.3** (0.1 mM) were prepared using organic solvent mixtures composed of 5 % $CHCl_3$ and 95 % methanol. Absorption spectra of the two compounds were recorded in a range of 300 to 800 nm by subtracting a baseline of methanol. The stock solutions were further diluted using methanol.

Signal enhancement from the Au sol was studied with Raman spectroscopy (5s/exposure, accumulated 60 times) by measuring the samples, prepared with containing equivalent volumes of **5.2** or **5.3** (0.5 µM) and the Au-sol. Ten minutes incubation was required before Raman measurement.

The pH dependence study of signal enhancement was carried out with 0.5 µM compound **5.2** or **5.3** and the Au sol of different pH (3-10). Samples comprising the compound (**5.2** or **5.3**) and the Au sol (volume ratio =1:1) were detected by Raman spectroscopy with a 60 times accumulations (5s for each).

4.5.3 Study of 5.4

Raman information of the pure **5.4** was obtained by measuring the sample with Raman spectroscopy for 6 minutes (30s, accumulated for 12 times). A stock solution of 10 mM was prepared using ethanol, and then was further diluted to a series of solutions for concentration dependence studies. Concentrations of the solutions were $0.17x10^{-3}$, $0.5x10^{-3}$, $1.0x10^{-3}$, $1.7x10^{-3}$, $5x10^{-3}$, 0.01, 0.17, 0.05, 0.1, 0.5, 1 and 5 mM. The compound solutions of different concentrations (250 µl) were mixed with 750 µl Au sol, and then incubated for 1 hr before being detected with Raman spectroscopy (30s/exposure, accumulated for 20 times). The maximum Raman intensity of the band around 1145 cm^{-1} was analyzed against the concentration of **5.4** using the software package of OriginPro 7.0.

The contribution of KCl to signal enhancement was determined by monitoring the Raman signals over the concentration of KCl. A series of KCl solutions were prepared starting a stock solution of 100 mM (113.9 mg KCl in 15.27 mL Milli.Q water). The Au sol was mixed with KCl (150 µl) of different concentrations (0.01, 0.025, 0.05, 0.1, 0.5, 1.0, 2.5 and 5.0 mM) and left for 10 minutes at room temperature, followed by an addition of 150 µl of **5.4** (0.1 mM). The mixture was incubated for 1 hr before Raman measurement (30s/exposure, accumulated for 20 times).

Polymerization of **5.4** caused by $FeCl_3$ was determined by comparing the Raman spectra taken in the absence and presence of $FeCl_3$. Au sol (250 µl) was mixed with 250 µl **5.4** (10 µM) and incubated for 10 minutes, and then detected with a 10 times accumulations (30s/exposure). Then 0.1 M $FeCl_3$ (80.1 mg dissolved in 4.938 mL Milli.Q water) of different volumes (5 and 10 µl) was added to the sample. The sample was measured again with Raman spectroscopy (30s, accumulated for 10 times) after 10 minutes incubation.

4.5.4 Study of 5.5

Commercial compound **5.5** (1.331 g/mL) was diluted with ethanol to obtain a 10 mM stock solution (10.68 µl **5.5** in 9989.32 µl ethanol), and then the stock solution was measured by Raman spectroscopy to record a reference spectrum (0.5s, accumulated for 60 times).

The concentration dependence of the Raman signals was studied with a series of solutions prepared the stock solution (10 mM) using MIlli.Q water as diluents. The Au NPs (250 µl) were mixed with 250 µl series of **5.5** solutions, of which the concentrations was 10, 20, 30, 40, 50, 60, 70, 80, 90, 100, 200, 300, 400, 500, 600, 700, 800, 900 and 1000 µM, and then incubated for 5 minutes. Raman spectra were collected in 5 minutes with a 10 times accumulation. Peak areas of the bands around 1174 and 1476 cm^{-1} were plotted versus the concentration of **5.5** with the software package of OriginPro 7.0.

Oxidation related to $FeCl_3$ was investigated using a mixture comprising 250 µl Au sol and 250 µl **5.5** (50 µM). After incubating for 2 minutes, the Raman spectrum of the mixture was recorded with an exposure time of 30 s (accumulated for 10 times). $FeCl_3$ of 2 µl or 5 µl (0.1 M) was added to the mixture, and the sample was incubated for 5 minutes and then measured by Raman spectroscopy (30s, accumulated 10 times).

4.5.5 Study of 5.6

A stock solution (1 mM) of **5.6** was prepared by dissolving 3.3 mg **5.6** in 4.98 mL $CHCl_3$. The adsorption spectrum of **5.6** was recorded using a 1:150 dilution of the stock solution by subtracting a baseline of solvent ($CHCl_3$).

Interaction with the Au sol was studied with a series of solutions of **5.6** prepared using ethanol as diluents, of which the concentration was from nM (35, 50, 100, 250 and 500) to µM range (1, 2.5, 5, 10, 25 and 50). Samples for Raman study were composed of 250 µl Au sol and 250 µl **5.6** of different concentrations, and then were measured with Raman spectroscopy (30s, accumulated for 10

times). One of the samples comprising **5.6** of 10 μM was also detected by UV-Vis spectrophotometry to record the absorption spectrum.

4.5.6 Study of 5.7 and 5.8

Stock solution of **5.7** and **5.8** (2 mM) was prepared using an organic solvent of chloroform ($CHCl_3$) in glass bottles and kept covered with tinfoil for further use. The absorption spectra of R-pe3T were recorded in a range of 270 to 2000 nm by subtracting a baseline of $CHCl_3$. The Raman spectra were collected with an accumulation of 10 times over 5 minutes (30/exposure).

For a concentration dependence study of Raman signals, a series of R-pe3T in a range of 0.05 to 50 μM was prepared from the stock solution using ethanol as diluent. Reaction mixtures consisted of equivalent volume of Au-sol and R-pe3T were incubated for 10 minutes at room temperature and measured with Raman spectroscopy (30 seconds, accumulated for 10 times).

A time dependence study of the Raman signals was carried out with **5.7** (5 μM). In the first stage reaction, an equivalent volume (250 μl) of **5.7** (5 μM) and the Au-sol were mixed and then detected by UV-Vis spectrophotometry and Raman spectroscopy every 10 mins for 2 hours. In the second step, Fe^{3+} (5 μl 0.1 M) was added to the sample after incubating for 90 minutes, following which the sample was scattered with Raman spectroscopy every 10 minutes with an 10 times accumulations (30s for each) till the signals remained unchanged.

To investigate the dimer-Au nanocomposites, in the first stage R-pe3T of 5 μM was mixed with Au-sol according to a volume ratio of 1:1, then incubated at room temperature for 90 minutes and characterized. In the second stage, $FeCl_3$ dissolved in MIlli.Q water was added twice, 0.125 μmol and 0.5 μmol. An incubation time of 20 minutes was required before charaterization. In each step, samples were analyzed with UV-Vis spectrophotometry with a baseline of ethanol-Milli.Q water mixture (v/v=1:1), Raman spectroscopy (5 minutes accumulation = 30 s x 10). Samples prepared with same procedure were used for

DLS measurements as well.

The samples, prepared for both stages were determined with TEM, SEM and EDX. In the TEM experiments, samples were diluted with Milli.Q water with a factor around 50, stabilized with 1 % BSA (volume of BSA close to 1/10 of total volume of the sample) and observed on a carbon grid. In the SEM experiments, undiluted samples were evaporated on glass cover slips which were pre-soniccleaned with ethanol (30 minutes), then rinsed with Milli.Q water and finally dried with argon gas. The prepared samples were firstly coated with carbon for images taken using a back scattered electron detector (BSD) and elemental analysis with EDX using 15 and 20 KeV. Followed, the samples were coated with Au for three dimensional information using a secondary electron detector (SED).

The 488 nm line of a SpectraPhysics 165 argon-ion laser, operating at 150 mW was used as the excitation source, and a 90° scattering geometry to the sample well was employed. Scattered light was collected via fibre optics and correlation functions were analysed using home-built software.

II: Reference

1. Thompson, D., *Michael Faraday's recognition of ruby gold: the birth of modern nanotechnology.* Gold Bulletin, 2007. **40**(4): p. 267-269.

2. Shipway, A.N., E. Katz, and I. Willner, *Nanoparticle arrays on surfaces for electronic, optical, and sensor applications.* Chemphyschem, 2000. **1**(1): p. 18-52.

3. Yao, J.L., et al., *A complementary study of surface-enhanced Raman scattering and metal nanorod arrays.* Pure and Applied Chemistry, 2000. **72**(1-2): p. 221-228.

4. Steiner, D., et al., *Electronic structure of metal-semiconductor nanojunctions in gold CdSe nanodumbbells.* Physical Review Letters, 2005. **95**(5).

5. Cui, Y., et al., *Electrical transport through a single nanoscale semiconductor branch point.* Nano Letters, 2005. **5**(7): p. 1519-1523.

6. Rothenberg, E., et al., *Electric field induced switching of the fluorescence of single semiconductor quantum rods.* Nano Letters, 2005. **5**: p. 1581-1586.

7. Sauer, G., et al., *In situ surface-enhanced Raman spectroscopy of monodisperse silver nanowire arrays.* Journal of Applied Physics, 2005. **97**(2).

8. Gratzel, M., *Perspectives for dye-sensitized nanocrystalline solar cells.* Progress in Photovoltaics, 2000. **8**(1): p. 171-185.

9. Aslan, K., et al., *Saccharide sensing using gold and silver nanoparticles - A review.* Journal of Fluorescence, 2004. **14**(4): p. 391-400.

10. Stuart, D.A., et al., *Refractive index sensitive, plasmon resonant scattering, and surface enhanced Raman scattering nanoparticles and arrays as biological sensing platforms.* Plasmonics in Biology and Medicine, 2004. **5327**: p. 60-73.

11. Hornstein, B.J. and R.G. Finke, *Transition-metal nanocluster kinetic and mechanistic studies emphasizing nanocluster agglomeration: Demonstration of a kinetic method that allows monitoring of all three phases of nanocluster formation and aging.* Chemistry of Materials, 2004. **16**(1): p. 139-150.

12. Kukushkin, S.A. and A.V. Osipov, *Phase transitions and the nucleation of catalytic nanostructures under the action of chemical, physical, and mechanical factors.* Kinetics and Catalysis, 2008. **49**(1): p. 79-91.

13. Cao, G., *Nanostructures & nanomaterials : synthesis, properties & applications*. 2004, London: Imperial College Press. xiv, 433.

14. Gai, P.L. and M.A. Harmer, *Surface atomic defect structures and growth of gold nanorods.* Nano Letters, 2002. **2**(7): p. 771-774.

15. Jana, N.R., L. Gearheart, and C.J. Murphy, *Wet chemical synthesis of high aspect ratio cylindrical gold nanorods.* Journal of Physical Chemistry B, 2001. **105**(19): p. 4065-4067.

16. Kittel, C., *Introduction to solid state physics*. 7th ed. 1996, New York: Wiley. xi, 673.

17. Posthuma-Trumpie, G., J. Korf, and A. van Amerongen, *Lateral flow (immuno)assay: its strengths, weaknesses, opportunities and threats. A literature survey.* Analytical and Bioanalytical Chemistry, 2009. **393**(2): p. 569-582.

18. Lonnberg, M. and J. Carlsson, *Quantitative detection in the attomole range for immunochromatographic tests by means of a flatbed scanner.* Analytical Biochemistry, 2001. **293**(2): p. 224-231.

19. Oku, Y., et al., *Development of oligonucleotide lateral-flow immunoassay for multi-parameter detection.* Journal of Immunological Methods, 2001. **258**(1-2): p. 73-84.

20. Buechler, K.F., et al., *SIMULTANEOUS DETECTION OF 7 DRUGS OF ABUSE BY THE TRIAGE(TM) PANEL FOR DRUGS OF ABUSE.* Clinical Chemistry, 1992. **38**(9): p. 1678-1684.

21. Kalogianni, D.P., et al., *Dry reagent dipstick test combined with 23S rRNA PCR for molecular diagnosis of bacterial infection in arthroplasty.* Analytical Biochemistry, 2007. **361**(2): p. 169-175.

22. Fernandez-Sanchez, C., et al., *One-step immunostrip test for the simultaneous detection of free and total prostate specific antigen in serum.* Journal of Immunological Methods, 2005. **307**(1-2): p. 1-12.

23. Leuvering, J.H.W., et al., *SOL PARTICLE AGGLUTINATION IMMUNOASSAY FOR HUMAN CHORIONIC-GONADOTROPIN.* Fresenius Zeitschrift Fur Analytische Chemie, 1980. **301**(2): p. 132-132.

24. Gussenhoven, G.C., et al., *LEPTO dipstick, a dipstick assay for detection of Leptospira-specific immunoglobulin M antibodies in human sera.* Journal of Clinical Microbiology, 1997. **35**(1): p. 92-97.

25. Lou, S.C., et al., *ONE-STEP COMPETITIVE IMMUNOCHROMATOGRAPHIC ASSAY FOR SEMIQUANTITATIVE DETERMINATION OF LIPOPROTEIN(A) IN PLASMA.* Clinical Chemistry, 1993. **39**(4): p. 619-624.

26. Vanamerongen, A., et al., *COLLOIDAL CARBON PARTICLES AS A NEW LABEL FOR RAPID IMMUNOCHEMICAL TEST METHODS - QUANTITATIVE COMPUTER IMAGE-ANALYSIS OF RESULTS.* Journal of Biotechnology, 1993. **30**(2): p. 185-195.

27. Zaytseva, N.V., et al., *Multi-analyte single-membrane biosensor for the serotype-specific detection of Dengue virus.* Analytical and Bioanalytical Chemistry, 2004. **380**(1): p. 46-53.

28. Delmulle, B.S., et al., *Development of an immunoassay-based lateral flow dipstick for the rapid detection of aflatoxin B-1 in pig feed.* Journal of Agricultural and Food Chemistry, 2005. **53**(9): p. 3364-3368.

29. Klewitz, T., et al., *Immunochromatographic assay for determination of botulinum neurotoxin type D.* Sensors and Actuators B-Chemical, 2006. **113**(2): p. 582-589.

30. Liedberg, B., C. Nylander, and I. Lundstrom, *SURFACE-PLASMON RESONANCE FOR GAS-DETECTION AND BIOSENSING.* Sensors and Actuators, 1983. **4**(2): p. 299-304.

31. Ahmad, A., et al., *Use of surface plasmon resonance biosensor technology as a possible alternative to detect differences in binding of enantiomeric drug compounds to immobilized albumins.* Biosensors & Bioelectronics, 2003. **18**(4): p. 399-404.

32. Komolov, K.E., et al., *Surface plasmon resonance study of G protein/receptor coupling in a lipid bilayer-free system.* Analytical Chemistry, 2006. **78**(4): p. 1228-1234.

33. Nordin, H., et al., *Kinetic studies of small molecule interactions with protein kinases using biosensor technology.* Analytical Biochemistry, 2005. **340**(2): p. 359-368.

34. Wegner, G.J., et al., *Real-time surface plasmon resonance imaging measurements for the multiplexed determination of protein adsorption/desorption kinetics and surface enzymatic reactions on peptide microarrays.* Analytical Chemistry, 2004. **76**(19): p. 5677-5684.

35. Nygren-Babol, L., et al., *Affinity and rate constants for interactions of bovine folate-binding protein and folate derivatives determined by optical biosensor technology. Effect of stereoselectivity.* Journal of Agricultural and Food Chemistry, 2005. **53**(13): p. 5473-5478.

36. Huber, W., et al., *SPR-based interaction studies with small molecular weight ligands using hAGT fusion proteins.* Analytical Biochemistry, 2004. **333**(2): p. 280-288.

37. Miura, N., et al., *Detection of morphine in ppb range by using SPR (surface-plasmon-resonance) immunosensor.* Chemistry Letters, 1997(8): p. 713-714.

38. Yu, Q.M., et al., *Detection of low-molecular-weight domoic acid using surface plasmon resonance sensor.* Sensors and Actuators B-Chemical, 2005. **107**(1): p. 193-201.

39. Wood, R.W., *On a remarkable case of uneven distribution of light in a diffraction grating spectrum.* Philosophical Magazine, 1902. **4**: p. 396-402.

40. Fano, U., *The theory of anomalous diffraction gratings and of quasi-stationary waves on metallic surfaces (Sommerfeld's waves).* Journal of the Optical Society of America, 1941. **31**(3): p. 213-222.

41. Otto, A., *EXCITATION OF NONRADIATIVE SURFACE PLASMA WAVES IN SILVER BY METHOD OF FRUSTRATED TOTAL REFLECTION.* Zeitschrift Fur Physik, 1968. **216**(4): p. 398-&.

42. Kretschm.E and H. Raether, *RADIATIVE DECAY OF NON RADIATIVE SURFACE PLASMONS EXCITED BY LIGHT.* Zeitschrift Fur Naturforschung Part a-Astrophysik Physik Und Physikalische Chemie, 1968. **A 23**(12): p. 2135-&.

43. Weaver, M.J., S. Farquharson, and M.A. Tadayyoni, *Surface Enhancement Factors for Raman-Scattering at Silver Electrodes - Role of Adsorbate Surface Interactions and Electronic-Structure.* Journal of Chemical Physics, 1985. **82**(11): p. 4867-4874.

44. Skinner, J.G. and W.G. Nilsen, *ABSOLUTE RAMAN SCATTERING CROSS-SECTION MEASUREMENT OF 992 CM-1 LINE OF BENZENE.* Journal of the Optical Society of America, 1968. **58**(1): p. 113-&.

45. Fleischm.M, P.J. Hendra, and McQuilla.Aj, *Raman-Spectra of Pyridine Adsorbed at a Silver Electrode.* Chemical Physics Letters, 1974. **26**(2): p. 163-166.

46. Kneipp, K., et al., *Surface-enhanced Raman scattering and biophysics.* Journal of Physics-Condensed Matter, 2002. **14**(18): p. R597-R624.

47. Moskovits, M., *SURFACE-ENHANCED SPECTROSCOPY.* Reviews of Modern Physics, 1985. **57**(3): p. 783-826.

48. Jeanmaire, D.L. and R.P. Vanduyne, *Surface Raman Spectroelectrochemistry .1. Heterocyclic, Aromatic, and Aliphatic-Amines Adsorbed on Anodized Silver Electrode.* Journal of Electroanalytical Chemistry, 1977. **84**(1): p. 1-20.

49. Kneipp, K., et al., *Single molecule detection using surface-enhanced Raman scattering (SERS).* Physical Review Letters, 1997. **78**(9): p. 1667-1670.

50. Nie, S.M. and S.R. Emery, *Probing single molecules and single nanoparticles by surface-enhanced Raman scattering.* Science, 1997. **275**(5303): p. 1102-1106.

51. Krug, J.T., et al., *Efficient Raman enhancement and intermittent*

light emission observed in single gold nanocrystals. Journal of the American Chemical Society, 1999. **121**(39): p. 9208-9214.

52. Kneipp, K., et al., *Ultrasensitive chemical analysis by Raman spectroscopy.* Chemical Reviews, 1999. **99**(10): p. 2957-+.

53. Vodinh, T., *Sers Chemical Sensors and Biosensors - New Tools for Environmental and Biological Analysis.* Sensors and Actuators B-Chemical, 1995. **29**(1-3): p. 183-189.

54. Xing, Y., et al., *Bioconjugated quantum dots for multiplexed and quantitative immunohistochemistry.* Nature Protocols, 2007. **2**(5): p. 1152-1165.

55. Graham, D. and K. Faulds, *Quantitative SERRS for DNA sequence analysis.* Chemical Society Reviews, 2008. **37**(5): p. 1042-1051.

56. Yonzon, C.R., et al., *Surface-enhanced nanosensors.* Spectroscopy, 2007. **22**(1): p. 42-+.

57. Gao, X.P., J.P. Davies, and M.J. Weaver, *A Test of Surface Selection-Rules for Surface-Enhanced Raman-Scattering - the Orientation of Adsorbed Benzene and Monosubstituted Benzenes on Gold.* Journal of Physical Chemistry, 1990. **94**(17): p. 6858-6864.

58. Jarvis, R.M., A. Brooker, and R. Goodacre, *Surface-enhanced Raman spectroscopy for bacterial discrimination utilizing a scanning electron microscope with a Raman spectroscopy interface.* Analytical Chemistry, 2004. **76**(17): p. 5198-5202.

59. Moskovits, M. and J.S. Suh, *Conformation of Mono-Carboxylic and Dicarboxylic-Acids Adsorbed on Silver Surfaces.* Journal of the American Chemical Society, 1985. **107**(24): p. 6826-6829.

60. Lombardi, J.R., et al., *CHARGE-TRANSFER THEORY OF SURFACE ENHANCED RAMAN-SPECTROSCOPY - HERZBERG-TELLER CONTRIBUTIONS.* Journal of Chemical Physics, 1986. **84**(8): p. 4174-4180.

61. Allen, C.S. and R.P. Vanduyne, *ORIENTATIONAL SPECIFICITY OF RAMAN-SCATTERING FROM MOLECULES ADSORBED ON SILVER ELECTRODES.* Chemical Physics Letters, 1979. **63**(3): p. 455-459.

62. Burstein, E., et al., *GIANT RAMAN-SCATTERING BY ADSORBED MOLECULES ON METAL-SURFACES.* Solid State Communications, 1979. **29**(8): p. 567-570.

63. Otto, A., *RAMAN-SCATTERING FROM ADSORBATES ON SILVER.* Surface Science, 1980. **92**(1): p. 145-152.

64. Numata, H., *CONTRIBUTION TO SERS OF SURFACE-PLASMON POLARITON MODES ON SINUSOIDAL METAL-SURFACE.* Journal of the

Physical Society of Japan, 1982. **51**(8): p. 2575-2581.

65. Lombardi, J.R. and R.L. Birke, *A Unified View of Surface-Enhanced Raman Scattering.* Accounts of Chemical Research, 2009. **42**(6): p. 734-742.

66. Maier, S.A., *Plasmonics : fundamentals and applications*. 1st ed. 2007, New York: Springer /. xxiv, 223.

67. Link, S. and M.A. El-Sayed, *Shape and size dependence of radiative, non-radiative and photothermal properties of gold nanocrystals.* International Reviews in Physical Chemistry, 2000. **19**(3): p. 409-453.

68. Albrecht, M.G. and J.A. Creighton, *ANOMALOUSLY INTENSE RAMAN-SPECTRA OF PYRIDINE AT A SILVER ELECTRODE.* Journal of the American Chemical Society, 1977. **99**(15): p. 5215-5217.

69. Creighton, J.A., C.G. Blatchford, and M.G. Albrecht, *PLASMA RESONANCE ENHANCEMENT OF RAMAN-SCATTERING BY PYRIDINE ADSORBED ON SILVER OR GOLD SOL PARTICLES OF SIZE COMPARABLE TO THE EXCITATION WAVELENGTH.* Journal of the Chemical Society-Faraday Transactions Ii, 1979. **75**: p. 790-798.

70. Tsai, D.P., et al., *PHOTON SCANNING-TUNNELING-MICROSCOPY IMAGES OF OPTICAL-EXCITATIONS OF FRACTAL METAL COLLOID CLUSTERS.* Physical Review Letters, 1994. **72**(26): p. 4149-4152.

71. Kneipp, K., et al., *Extremely large enhancement factors in surface-enhanced Raman scattering for molecules on colloidal gold clusters.* Applied Spectroscopy, 1998. **52**(12): p. 1493-1497.

72. Inoue, M. and K. Ohtaka, *SURFACE ENHANCED RAMAN-SCATTERING BY METAL SPHERES .1. CLUSTER EFFECT.* Journal of the Physical Society of Japan, 1983. **52**(11): p. 3853-3864.

73. Poliakov, E.Y., et al., *Enhanced Raman scattering from self-affine thin films.* Optics Letters, 1996. **21**(20): p. 1628-1630.

74. Wang, D.S., H. Chew, and M. Kerker, *ENHANCED RAMAN-SCATTERING AT THE SURFACE (SERS) OF A SPHERICAL-PARTICLE.* Applied Optics, 1980. **19**(14): p. 2256-2257.

75. Derkatchova, A. and K. Kolwas, *Size dependence of dipole and quadrupole plasmon resonances in light induced sodium clusters.* 5th Workshop on Atomic and Molecular Physics, 2005. **5849**: p. 150-153.

76. Heath, J.R., *SIZE-DEPENDENT SURFACE-PLASMON RESONANCES OF BARE SILVER PARTICLES.* Physical Review B, 1989. **40**(14): p. 9982-9985.

77. Frens, G., *Controlled Nucleation for Regulation of Particle-Size in*

Monodisperse Gold Suspensions. Nature-Physical Science, 1973. **241**(105): p. 20-22.

78. Yu, Y.Y., et al., *Gold nanorods: Electrochemical synthesis and optical properties.* Journal of Physical Chemistry B, 1997. **101**(34): p. 6661-6664.

79. Brust, M., et al., *Synthesis of Thiol-Derivatized Gold Nanoparticles in a 2-Phase Liquid-Liquid System.* Journal of the Chemical Society-Chemical Communications, 1994(7): p. 801-802.

80. Turkevich, J., P.C. Stevenson, and J. Hillier, *A STUDY OF THE NUCLEATION AND GROWTH PROCESSES IN THE SYNTHESIS OF COLLOIDAL GOLD.* Discussions of the Faraday Society, 1951(11): p. 55-&.

81. Jin, R.C., et al., *Controlling anisotropic nanoparticle growth through plasmon excitation.* Nature, 2003. **425**(6957): p. 487-490.

82. Perez-Juste, J., et al., *Gold nanorods: Synthesis, characterization and applications.* Coordination Chemistry Reviews, 2005. **249**(17-18): p. 1870-1901.

83. Shankar, S.S., et al., *Biological synthesis of triangular gold nanoprisms.* Nature Materials, 2004. **3**(7): p. 482-488.

84. Jana, N.R., L. Gearheart, and C.J. Murphy, *Evidence for seed-mediated nucleation in the chemical reduction of gold salts to gold nanoparticles.* Chemistry of Materials, 2001. **13**(7): p. 2313-2322.

85. Kim, K.S., D. Demberelnyamba, and H. Lee, *Size-selective synthesis of gold and platinum nanoparticles using novel thiol-functionalized ionic liquids.* Langmuir, 2004. **20**(3): p. 556-560.

86. Raula, J., et al., *Synthesis of gold nanoparticles grafted with a thermoresponsive polymer by surface-induced reversible-addition-fragmentation chain-transfer polymerization.* Langmuir, 2003. **19**(8): p. 3499-3504.

87. Zsigmondy, R. and E. Huckel, *The reduction rate and the growth of smaller gold particles in the creation of a colloid gold solution.* Zeitschrift Fur Physikalische Chemie--Stochiometrie Und Verwandtschaftslehre, 1925. **116**(3/4): p. 291-303.

88. Turkevich, J., G. Garton, and P.C. Stevenson, *THE COLOR OF COLLOIDAL GOLD.* Journal of Colloid Science, 1954. **9**(6): p. S26-S35.

89. Kumar, S., K.S. Gandhi, and R. Kumar, *Modeling of formation of gold nanoparticles by citrate method.* Industrial & Engineering Chemistry Research, 2007. **46**(10): p. 3128-3136.

90. Gao, J.X., C.M. Bender, and C.J. Murphy, *Dependence of the gold*

nanorod aspect ratio on the nature of the directing surfactant in aqueous solution. Langmuir, 2003. **19**(21): p. 9065-9070.

91. Gole, A. and C.J. Murphy, *Seed-mediated synthesis of gold nanorods: Role of the size and nature of the seed.* Chemistry of Materials, 2004. **16**(19): p. 3633-3640.

92. Kreibig, U. and M. Vollmer, *Optical properties of metal clusters*. Springer series in materials science ; 25. 1995, Berlin New York: Springer. xx, 532.

93. Link, S. and M.A. El-Sayed, *Spectroscopic determination of the melting energy of a gold nanorod.* Journal of Chemical Physics, 2001. **114**(5): p. 2362-2368.

94. Katz, E. and I. Willner, *Integrated nanoparticle-biomolecule hybrid systems: Synthesis, properties, and applications.* Angewandte Chemie-International Edition, 2004. **43**(45): p. 6042-6108.

95. Guo, S.J. and S.J. Dong, *Biomolecule-nanoparticle hybrids for electrochemical biosensors.* Trac-Trends in Analytical Chemistry, 2009. **28**(1): p. 96-109.

96. Zheng, J., P.R. Nicovich, and R.M. Dickson, *Highly fluorescent noble-metal quantum dots.* Annual Review of Physical Chemistry, 2007. **58**: p. 409-431.

97. Bagwe, R.P., X.J. Zhao, and W.H. Tan, *Bioconjugated luminescent nanoparticles for biological applications.* Journal of Dispersion Science and Technology, 2003. **24**(3-4): p. 453-464.

98. Wu, Y.Q., et al., *Evaluation of progesterone-ovalbumin conjugates with different length linkers in enzyme-linked immunosorbant assay and surface plasmon resonance-based immunoassay.* Steroids, 2002. **67**(7): p. 565-572.

99. Yuan, J., et al., *Sensitivity enhancement of SPR assay of progesterone based on mixed self-assembled monolayers using nanogold particles.* Biosensors & Bioelectronics, 2007. **23**(1): p. 144-148.

100. Jiang, X.Q., et al., *Sensitive determination of estriol-16-glucuronide using surface plasmon resonance sensing.* Steroids, 2009. **74**(10-11): p. 819-824.

101. Jain, K.K., *Nanodiagnostics: application of nanotechnology in molecular diagnostics.* Expert Review of Molecular Diagnostics, 2003. **3**(2): p. 153-161.

102. Rembaum, A. and W.J. Dreyer, *IMMUNOMICROSPHERES - REAGENTS FOR CELL LABELING AND SEPARATION.* Science, 1980.

208(4442): p. 364-368.

103. Souza, G.R., et al., *Networks of gold nanoparticles and bacteriophage as biological sensors and cell-targeting agents.* Proceedings of the National Academy of Sciences of the United States of America, 2006. **103**: p. 1215-1220.

104. Huang, Y., et al., *Programmable assembly of nanoarchitectures using genetically engineered viruses.* Nano Letters, 2005. **5**(7): p. 1429-1434.

105. Dragnea, B., et al., *Gold nanoparticles as spectroscopic enhancers for in vitro studies on single viruses.* Journal of the American Chemical Society, 2003. **125**(21): p. 6374-6375.

106. Salomone, A., et al., *Reliability of detection of Citrus tristeza virus by an immunochromatographic lateral flow assay in comparison with ELISA.* Journal of Plant Pathology, 2004. **86**(1): p. 43-48.

107. Cekan, S.Z., et al., *The Prediction and/or Detection of Ovulation by Means of Urinary Steroid Assays.* Contraception, 1986. **33**(4): p. 327-345.

108. Goebelsm.U, et al., *Comparison of Metabolism of Oestriol-3-Glucosiduronate and Oestriol-16-Glucosiduronate in Pregnant Women.* Acta Endocrinologica, 1966. **52**(1): p. 30-&.

109. Kim, S.Y., et al., *The prediction of adverse pregnancy outcome using low unconjugated estriol in the second trimester of pregnancy without risk of Down's syndrome.* Yonsei Medical Journal, 2000. **41**(2): p. 226-229.

110. Lonning, P.E. and P. Skulstad, *Alterations in the Urine Excretion of Estrogen Metabolites in Breast-Cancer Women Treated with Aminoglutethimide.* Journal of Steroid Biochemistry and Molecular Biology, 1989. **33**(4): p. 565-571.

111. Blackwell, L.F., et al., *Hormonal monitoring of ovarian activity using the Ovarian Monitor, Part 1. Validation of home and laboratory results obtained during ovulatory cycles by comparison with radioimmunoassay.* Steroids, 2003. **68**(5): p. 465-476.

112. Cooke, D.G., J.E. Binnie, and L.F. Blackwell, *Validation of a reference ELISA for estrone glucuronide using urine samples normalized by dilution to a constant rate of urine production.* Steroids, 2007. **72**(6-7): p. 580-591.

113. Dighe, A.S. and P.M. Sluss, *Improved detection of serum estradiol after sample extraction procedure.* Clinical Chemistry, 2004. **50**(4): p. 764-766.

114. Cekan, S.Z., *BIASES IN THE ASSAYS OF STEROIDS AND THEIR BINDING-PROTEINS.* Journal of Steroid Biochemistry and Molecular

Biology, 1987. **27**(1-3): p. 95-98.

115. Reis, M.F., et al., *Quantification of urinary chorionic gonadotropin in spontaneous abortion of pre-clinically recognized pregnancy: Method development and analytical validation.* International Journal of Hygiene and Environmental Health, 2007. **210**(3-4): p. 419-427.

116. Baker, T.S., K.M. Jennison, and A.E. Kellie, *Direct Radioimmunoassay of Estrogen Glucuronides in Human Female Urine.* Biochemical Journal, 1979. **177**(2): p. 729-738.

117. Haning, R.V., et al., *Direct Radioimmunoassay for Estriol-16-Glucuronide in Urine for Monitoring Pregnancy and Induction of Ovulation.* American Journal of Obstetrics and Gynecology, 1977. **128**(7): p. 793-802.

118. Stanczyk, F.Z., I. Miyakawa, and J.R. Soares, *Radioimmunoassay of Estriol-16-Glucuronide Using Tritiated and Radioiodinated Radioligands - Direct Radioimmunoassay of Urinary Estriol-16-Glucuronide During the Menstrual-Cycle.* Journal of Steroid Biochemistry and Molecular Biology, 1979. **10**(4): p. 443-448.

119. Farre, M., et al., *Comparative study of an estradiol enzyme-linked immunosorbent assay kit, liquid chromatography-tandem mass spectrometry, and ultra performance liquid chromatography-quadrupole time of flight mass spectrometry for part-per-trillion analysis of estrogens in water samples.* Journal of Chromatography A, 2007. **1160**(1-2): p. 166-175.

120. Ying, G.G., R.S. Kookana, and Z.L. Chen, *On-line solid-phase extraction and fluorescence detection of selected endocrine disrupting chemicals in water by high-performance liquid chromatography.* Journal of Environmental Science and Health Part B-Pesticides Food Contaminants and Agricultural Wastes, 2002. **37**(3): p. 225-234.

121. Rodriguez-Mozaz, S., M.J.L. de Alda, and D. Barcelo, *Picogram per liter level determination of estrogens in natural waters and waterworks by a fully automated on-line solid-phase extraction-liquid chromatography-electrospray tandem mass spectrometry method.* Analytical Chemistry, 2004. **76**(23): p. 6998-7006.

122. Schoneshofer, M., T.K. Dhar, and D. Ioanides, *Total Urinary Estriol Determined by Online Liquid Chromatograph with Ultraviolet Detection.* Clinical Chemistry, 1986. **32**(10): p. 1948-1950.

123. Yang, Y.J., et al., *Direct determination of estriol 3-and 16-glucuronides in pregnancy urine by column-switching liquid chromatography with electrospray tandem mass spectrometry.* Biomedical Chromatography, 2003. **17**(4): p. 219-225.

124. Li, L.Y., et al., *Protein adsorption on oligo(ethylene glycol)-terminated alkanethiolate self-assembled monolayers: The molecular basis for nonfouling behavior.* Journal of Physical Chemistry B, 2005. **109**(7): p. 2934-2941.

125. Johne, B., et al., *Colloidal Gold Conjugated Monoclonal-Antibodies, Studied in the Biacore Biosensor and in the Nycocard Immunoassay Format.* Journal of Immunological Methods, 1995. **183**(1): p. 167-174.

126. Lyon, L.A., M.D. Musick, and M.J. Natan, *Colloidal Au-enhanced surface plasmon resonance immunosensing.* Analytical Chemistry, 1998. **70**(24): p. 5177-5183.

127. Hansen, C.B., et al., *ATTACHMENT OF ANTIBODIES TO STERICALLY STABILIZED LIPOSOMES - EVALUATION, COMPARISON AND OPTIMIZATION OF COUPLING PROCEDURES.* Biochimica Et Biophysica Acta-Biomembranes, 1995. **1239**(2): p. 133-144.

128. Chan, C.T.L., MA), Gravallese, Debra A. (Watertown, MA), *Method and composition for reducing the nonspecific binding of radioiodinated protein hormones*. 1982.

129. Blackwell, L.F., J.B. Brown, and D. Cooke, *Definition of the potentially fertile period from urinary steroid excretion rates. Part II. A threshold value for pregnanediol glucuronide as a marker for the end of the potentially fertile period in the human menstrual cycle.* Steroids, 1998. **63**(1): p. 5-13.

130. Fehring, R.J. and M. Schneider, *Variability in the hormonally estimated fertile phase of the menstrual cycle.* Fertility and Sterility, 2008. **90**(4): p. 1232-1235.

131. Doering, W.E. and S.M. Nie, *Spectroscopic tags using dye-embedded nanoparticies and surface-enhanced Raman scattering.* Analytical Chemistry, 2003. **75**(22): p. 6171-6176.

132. Lee, P.C. and D. Meisel, *Adsorption and Surface-Enhanced Raman of Dyes on Silver and Gold Sols.* Journal of Physical Chemistry, 1982. **86**(17): p. 3391-3395.

133. McCreery, R.L., *Symposium on Photoelectrochemical and Electrochemical Surface Science - Preface.* Langmuir, 1990. **6**(1): p. 43-43.

134. Mary, Y.S., et al., *FT-IR, FT-Raman and SERS Spectra of L-Proline.* Journal of the Iranian Chemical Society, 2009. **6**(1): p. 138-144.

135. Fischmeister, I., *RELATION BETWEEN THEFREQUENCY OF THE HYDROXYL OUT-OF-PLANE DEFORMATION VIBRATION AND THE HYDROGEN BOND LENGTH IN CARBOXYLIC ACIDS.* Spectrochimica Acta, 1964. **20**(6): p. 1071-1080.

136. Markel, V.A., et al., *Near-field optical spectroscopy of individual surface-plasmon modes in colloid clusters.* Physical Review B, 1999. **59**(16): p. 10903-10909.

137. Moskovits, M., et al., *SERS and the single molecule.* Optical Properties of Nanostructured Random Media, 2002. **82**: p. 215-226.

138. Lecomte, S., P. Matejka, and M.H. Baron, *Correlation between surface enhanced Raman scattering and absorbance changes in silver colloids. Evidence for the chemical enhancement mechanism.* Langmuir, 1998. **14**(16): p. 4373-4377.

139. Faulds, K., et al., *Comparison of surface-enhanced resonance Raman scattering from unaggregated and aggregated nanoparticles.* Analytical Chemistry, 2004. **76**(3): p. 592-598.

140. Pretsch, E., P. Bühlmann, and M. Badertscher, *Structure determination of organic compounds : tables of spectral data*. 4th, rev. and enlarged ed. 2009, Berlin: Springer. xv, 433.

141. Podstawka, E., et al., *Influence of aliphatic spacer group on adsorption mechanisms of phosphonate derivatives of L-phenylalanine: Surface-enhanced.* Surface Science, 2007. **601**: p. 4586-4597.

142. Clarke, T.M., et al., *Theoretical and spectroscopic study of a series of styryl-substituted terthiophenes.* Journal of Physical Chemistry A, 2003. **107**(51): p. 11505-11516.

143. Clarke, T.M., et al., *Raman spectroscopy of short-lived terthiophene radical cations generated by photochemical and chemical oxidation.* Chemphyschem, 2006. **7**(6): p. 1276-1285.

144. Kumar, S.S., et al., *Stabilized gold nanoparticles by reduction using 3,4-ethylenedioxythiophene-polystyrenesulfonate in aqueous solutions: Nanocomposite formation, stability, and application in catalysis.* Langmuir, 2007. **23**(6): p. 3401-3408.

145. Pringle, J.M., et al., *One-step synthesis of conducting polymer-Noble metal nanoparticle composites using an ionic liquid.* Advanced Functional Materials, 2008. **18**(14): p. 2031-2040.

146. Yohannes, T., et al., *Electrochemical and spectroscopic characteristics of copolymers electrochemically synthesized from 3-methylthiophene and 3,4-ethylenedioxythiophene.* Synthetic Metals, 1997. **88**(1): p. 15-21.

147. Chiu, W.W., et al., *Studies of dopant effects in poly(3,4-ethylenedioxythiophene) using Raman spectroscopy.* Journal of Raman Spectroscopy, 2006. **37**(12): p. 1354-1361.

148. Garreau, S., et al., *In situ spectroelectrochemical Raman studies of poly(3,4-ethylenedioxythiophene) (PEDT).* Macromolecules, 1999. **32**(20): p. 6807-6812.

149. Compagnini, G., A. De Bonis, and R.S. Cataliotti, *The effect of self-assembled nanometric spacers on surface enhanced Raman spectra of terthiophene ultrathin films.* Materials Science & Engineering C-Biomimetic and Supramolecular Systems, 2001. **15**(1-2): p. 37-39.

150. Sarkar, U.K., et al., *CLASSICAL AND CHEMICAL EFFECTS OF SERS FROM 2,2'-5,2'' TERTHIOPHENE ADSORBED ON AG-SOLS.* Chemical Physics Letters, 1992. **190**(1-2): p. 59-63.

151. Sarkar, U.K., et al., *A COMPARATIVE-STUDY OF SERS FROM ALPHA-SEXITHIOPHENE AND OTHER THIOPHENE OLIGOMERS.* Chemical Physics Letters, 1992. **200**(1-2): p. 55-59.

152. Zerbi, G., B. Chierichetti, and O. Inganas, *VIBRATIONAL-SPECTRA OF OLIGOTHIOPHENES AS MODEL OF POLYTHIOPHENES.* Journal of Chemical Physics, 1991. **94**(6): p. 4637-4645.

153. Akimoto, M., et al., *CORRELATION BETWEEN VIBRATIONAL-SPECTRA AND ELECTRICAL-CONDUCTIVITY OF POLYTHIOPHENE.* Synthetic Metals, 1986. **15**(4): p. 353-360.

154. Jang, J., J. Bae, and E. Park, *Selective fabrication of poly (3,4-ethylenedioxythiophene) nanocapsules and mesocellular foams using surfactant-mediated interfacial polymerization.* Advanced Materials, 2006. **18**(3): p. 354-+.

155. Huang, J., et al., *Nanostructured polyaniline sensors.* Chemistry-a European Journal, 2004. **10**(6): p. 1315-1319.

156. Hormozi Nezhad, M.R., et al., *Synthesis and patterning of gold nanostructures on InP and GaAs via galvanic displacement.* Small, 2005. **1**(11): p. 1076-81.

157. Wagner, P. and D.L. Officer, *Structural and electronic properties of substituted terthiophenes.* Synthetic Metals, 2005. **154**(1-3): p. 325-328.

158. Zhai, L. and R.D. McCullough, *Regioregular polythiophene/gold nanoparticle hybrid materials.* Journal of Materials Chemistry, 2004. **14**(2): p. 141-143.

159. NAGARAJAN, S., Ramaswamy Nagarajan, Mario Cazeca, Jayant Kumar, Ferdinando F. Bruno, Lynne Samuelson,. *Single Step Biocatalytic Synthesis of a Sexithiophene*. in *232nd National Meeting & Exposition of the American Chemical Society*. 2006. San Francisco, CA USA: Polymer Preprints.

160. Clarke, T.M., et al., *Modulation of electronic properties in neutral and oxidized oligothiophenes substituted with conjugated polyaromatic hydrocarbons.* Journal of Physical Chemistry A, 2007. **111**(12): p. 2385-2397.

161. Cui, Y., et al., *Multianalyte immunoassay based on surface-enhanced Raman spectroscopy.* Journal of Raman Spectroscopy, 2007. **38**(7): p. 896-902.

162. Wu, Y.Q. and L.F. Blackwell, *The Synthesis of Estriol 16-Monoglucuronide and 17-Monoglucuronide from Estriol.* Steroids, 1993. **58**(10): p. 452-456.